Ab Initio Studies of Surfaces and Interfaces

A Dissertation
Presented to the Faculty of the Graduate School
of
Yale University
in Candidacy for the Degree of
Doctor of Philosophy

by
Kevin F. Garrity

Dissertation Director: Sohrab Ismail-Beigi

May 2011

Copyright © 2011 by Kevin F. Garrity

All rights reserved.

Contents

1 Introduction **1**

2 Methods **6**

2.1 Density Functional Theory 6

2.1.1 Hohenberg-Kohn Theorems 6

2.1.2 Kohn-Sham Equations and the Local Density Approximation . 9

2.1.3 Plane Waves and Pseudopotentials 12

2.2 DFT Perturbation Theory 15

2.3 Nudged Elastic Band 16

2.4 Wannier Functions 17

2.5 Classical Monte Carlo 20

3 Phase Diagram and Kinetics of Sr on Si (001) **23**

3.1 Introduction 23

3.2 Methods 25

3.2.1 Total energies 25

3.2.2 Phonons free energies 28

3.2.3 Energy barriers 30

3.2.4 Wannier functions 31

3.3 Review of Experimental Work 32

3.4 Standard Dimerized Surfaces 34
3.5 Modified Dimer Patterns 41
3.6 Mobile Silicon Reconstructions 47
3.7 Explanation of Experimental Growth 56
3.8 Simulated STM and XRD 58
3.9 1.0 ML Silicide Structures 60
3.10 Conclusions 64

4 Phase Transition of Sr on Si (001) 66

4.1 Introduction 66
4.2 Lattice gas Hamiltonian 68
4.3 *Ab initio* calculations and parameter extraction 71
4.4 Experiment 75
4.5 Results and Discussion 76

5 Phase Diagram and STM of Sr on Ge (001) 79

5.1 Introduction 79
5.2 Description of Experiments 81
5.3 Methods 84
5.4 Low Coverage Structures 85
5.5 High Coverage Structures 90
5.6 Summary 94

6 Phases of submonolayer La on Si (001) 95

6.1 Introduction 95
6.2 Methods 97
6.3 Stoichiometric Surfaces 98

6.3.1 $\leq 1/3$ ML Chains 100
6.3.2 $> 1/3$ ML Broken Dimers. 102
6.4 Non-Stoichiometric Si surfaces. 107
6.4.1 Non-stoichiometric $\leq 1/3$ ML 108
6.4.2 Non-stoichiometric $> 1/3$ ML. 109
6.5 Phase Diagram 111
6.6 Conclusions 115

7 $LaAlO_3$ on Si (001) 117

7.1 Introduction 117
7.2 Methods 118
7.2.1 Surface and Interface Thermodynamics 119
7.3 La + Sr Template Layers 121
7.3.1 Initial Sr + O Layers 121
7.3.2 Initial Sr + La + O Layers 124
7.4 Interface Structures 127
7.4.1 Pure $LaAlO_3$ Interface Structures 127
7.4.2 Sr + $LaAlO_3$ Interface Structures 132
7.5 Proposal for Epitaxial Growth 136
7.6 Summary 140

8 Ferroelectric Surface Chemistry 141

8.1 Methods 143
8.2 Stoichiometric Surfaces 146
8.3 Non-Stoichiometric Surfaces 152
8.3.1 Surface Thermodynamics 152
8.3.2 Bare Surfaces 155

8.3.3 CO_2 binding . . . 159
8.3.4 H_2O Binding . . . 161
8.4 Epitaxial Catalytic Layers on $PbTiO_3$ . . . 164
8.5 Conclusions . . . 166

9 Resonant Phonon Coupling **168**
9.1 Introduction . . . 168
9.2 Experiments . . . 171
9.3 Zero Temperature Structures . . . 173
9.3.1 Methods . . . 173
9.3.2 Bulk Strained LSMO . . . 174
9.3.3 Supercell Calculations . . . 175
9.4 Finite Temperature Calculations . . . 178
9.4.1 Model of Octahedral Rotations . . . 178
9.4.2 Monte Carlo Sampling . . . 181
9.4.3 Effect of Temperature on Interface Structure . . . 182
9.4.4 How Structural Changes Modulate Conductivity . . . 185
9.4.5 Correlations and Phonons . . . 186
9.5 Summary . . . 191

10 Conclusions and Outlook **193**
10.1 Epitaxial Oxide Growth on Semiconductors . . . 193
10.2 Ferroelectric Surfaces . . . 194
10.3 Interface Phonon Coupling . . . 195

Bibliography **196**

List of Figures

2.1 Pseudo vs All-Electron 14

2.2 NEB Schematic 18

2.3 Wannier Function Example 19

2.4 Thermalization example 22

3.1 Slab Convergence 31

3.2 Isolated Sr on Si 36

3.3 0.5 ML Sr on Si Wannier Functions 39

3.4 DOS 0.5 ML Sr on Si A 39

3.5 DOS 0.5 ML Sr on Si D 40

3.6 Sr on Si 0-0.5 ML 42

3.7 Low energy modified dimer patterns 43

3.8 Phonon DOS 46

3.9 Submonolayer Sr and Si step-like structures 49

3.10 Submonolayer dimer vacancy structures 50

3.11 Wannier functions 1/6 ML DV structure 52

3.12 DOS for 1/6 ML DV structure 52

3.13 Schematic for 1/6 ML DV structure energy levels 53

3.14 NEB diagram 55

3.15 NEB energies 55

3.16 Phase diagram . . . 58
3.17 Sr on Si STM . . . 61
3.18 Side view of 1 ML Sr on Si structures . . . 63

4.1 Lattice gas top view . . . 70
4.2 Sr on Si and dimer buckling . . . 73
4.3 Top view Sr on Si . . . 74
4.4 Coverage vs. Temperature phase diagram and RHEED . . . 78

5.1 STM Experiments . . . 82
5.2 STM Experimental Highlights . . . 83
5.3 3×4 Ge on Sr STM . . . 87
5.4 Atomic projected density of states for 3×4 1/6 ML structure . . . 88
5.5 Structure and STM of c(8×4) structure at 3/16 ML coverage . . . 91
5.6 Calculated STM of c(8×4) structure . . . 92
5.7 Side view of high coverage Sr on Ge structures. . . . 93

6.1 Isolated La on Si . . . 99
6.2 Stoichiometric Si La surfaces . . . 101
6.3 Atomic projected density of states for 1/3 ML and 1/2 ML structures 103
6.4 DOS broken dimer structures . . . 105
6.5 Top view of high coverage La structures on a stoichiometric Si surface 106
6.6 La structures with modified Si bonding . . . 110
6.7 Broken Dimer La + extra Si . . . 112
6.8 La on Si phase diagram . . . 114
6.9 La silicide surface cluster structure . . . 115

7.1 SrO on Si . . . 122

7.2 SrO phase diagram 122
7.3 Side view of low energy Sr+La+O structures 125
7.4 La+Sr+O phase diagram 127
7.5 Pure $LaAlO_3$ phase diagram 129
7.6 Pure $LaAlO_3$ structures 130
7.7 DOS $LaAlO_3$ on Si 131
7.8 Side view of low energy interface structures with Al substituted for Si 133
7.9 LaAlO3 on SrO 134
7.10 LaAlO3 + Sr + Si phase diagram 136
7.11 Side view of low energy interface structures with Sr 137
7.12 Interface structures 138
7.13 Interface DOS 139

8.1 Schematic of simulation cell 144
8.2 Average absolute value of Ti-O z-displacement in each layer 145
8.3 Projected density of states (DOS) for the TiO_2-terminated paraelectric surface 146
8.4 Schematic of electronic reconstructions. 147
8.5 Integrated local density of states (DOS) 147
8.6 Projected density of states (DOS) for the TiO_2-terminated positively-poled surface 148
8.7 Projected density of states (DOS) for the TiO_2-terminated negatively-poled surface. 149
8.8 Binding geometry and charge transfer for 0.5 ML CO_2 on a stoichiometric TiO_2-terminated surface 150
8.9 Phase diagram of the paraelectric surface as a function of μ_O and μ_{Pb}. 156

8.10 Phase diagram of negatively poled surface as a function of μ_O and μ_{Pb}. 157
8.11 Atomic structure of negatively-poled PbO terminated surface with 0.5 ML vacancies arranged into a 4×1 reconstruction. 157
8.12 Phase diagram of the positively-poled surface as a function of μ_O and μ_{Pb}. 158
8.13 Selected thermodynamically stable structures for the positively-poled surface. 159
8.14 Binding of 0.5 ML CO_2 to selected thermodynamically stable surfaces 161
8.15 Binding of 0.5 ML H_2O to selected thermodynamically stable surfaces 162
8.16 Possible method for reversibly binding CO_2 to a $SrRuO_3$ (or SrO) monolayer on $PbTiO_3$. 165
8.17 Binding of 0.5 ML CO_2 to selected surfaces with added catalytic layers. 166

9.1 Phonon softening in STO 170
9.2 Experimental results showing enhanced phonon-scattering. 172
9.3 Top: Side view of interface geometry, with octahedral oxygen cages drawn. 177
9.4 Energy difference between tetragonal LSMO and LSMO with rotated octahedra 180
9.5 Mean rotation angle versus layer number for four temperatures 183
9.6 Correlation of layers near the interface with bulk STO layers at $T = T_c$ 187
9.7 Correlation of the two STO layers and two LSMO layers closest to the interface with bulk STO 188
9.8 Energy ($\hbar\omega$) of the lowest energy mode in the interface system 189
9.9 Spatial profile of the eigenvector 190

9.10 Resistivity of an 11 u.c. film of $La_{0.53}Sr_{0.47}MnO_3$ as a function of temperature 191

List of Tables

3.1 Comparison of Sr binding energies for different Si slab configurations. 27

3.2 Sr Si RHEED 33

3.3 Binding energies of selected standard dimer pattern structures. See Figs. 3.2 and 3.6. 41

3.4 Binding Energies Stoichiometric Si 43

3.5 Energies of non-stoichiometric reconstructions 44

3.6 Energies Submonolayer Sr and Si steps 48

3.7 Energies of submonolayer Sr and Si dimer vacancy structures 50

3.8 Hopping Rates 54

3.9 . Binding Energy per Sr of 1.0 ML structures (See Fig. 3.18). 62

4.1 Binding energies Sr on Si 73

4.2 RHEED Data 78

5.1 Energies and average distance from Sr to four nearest neighbor Ge for various Sr on Ge structures. 89

6.1 Barriers for La motion 100

6.2 Stoichiometric Si La energies 100

6.3 Energy barriers to break a Si dimer bond (see Fig 6.1) at various La coverages, and estimated hopping rates. 108

6.4 Binding energies of La at various coverages with modified Si bonding patterns. 109

6.5 Binding energies for structures with added Si on the surface. 111

8.1 Binding energy of 0.5 ML CO_2 on stoichiometric TiO_2-terminated surface. See Fig. 8.8. 151

8.2 DFT formation energies and experimental $\Delta_f H^0$ of various compounds. 153

8.3 Binding energy of 0.5 ML CO_2 to thermodynamically stable surfaces. 159

8.4 Binding energy of 0.5 ML H_2O to several surfaces 162

8.5 Binding energy of 0.5 ML CO_2 to various surfaces. 167

9.1 LSMO rotation angles and the resulting conductivities 184

Acknowledgements

It should come as no surprise to those who know me that I will keep this section brief. First, I would like to thank my adviser, Sohrab Ismail-Beigi, for his guidance, clear thinking, patience, and encouragement. His mentoring has taught me both how to do research and how to present it to others with confidence, and I am grateful for his help.

I am also grateful to the rest of the members of the Ismail-Beigi group for their help throughout my graduate career. Specifically, I would like to thank Alexie Kolpak for her help with chemistry and thermodynamics, Jie Jiang for his sense of humor, and my officemates Hanghui Chen and Hui Tang for their insightful discussions as well as their practical help running calculations. I would also like to thank my third officemate, Xiao Pan, for putting up with us for many years. Also on the theory side, I would like to thank Jay Kerwin and John Tully for their advice on surface science.

This work would not be possible without the careful experiments of many people in the CRISP collaboration at Yale, and their willingness to explain their work to me very carefully. First, I would like to thank James Reiner, Yaron Segal, Carlos Vaz, Jason Hoffman, and Myrtle-Rose Padmore, who worked under the guidance of Fred Walker and Charles Ahn. Their work on both semiconductor surfaces and oxide interfaces as well as their advice in understanding and presenting results has been crucial to my graduate school career. In addition, I would like to thank Boris

Lukanov and his adviser Eric Altman for both collaborating on the Sr on Ge system and for discussions of ferroelectric surfaces.

In addition, I would like to thank all the people who supported me outside of academics during my time at Yale. In particular, I want thank everyone in the Lost Wednesday crew for creating a great sense of community in the Physics department. I would also like to thank all of the teammates I met through ultimate frisbee during my time in New Haven for providing a friendly and competitive environment. Finally, I would like to thank my parents, for their continual support throughout my lengthy education.

Chapter 1

Introduction

Since Richard Feynman's 1959 lecture "There's Plenty of Room at the Bottom" popularized the ideas of building machines on an atomic scale, there has been an incredible growth in research and applications related to nanotechnology and nanomaterials, which consist of functional materials with dimensions on the order of 1 nm (nanometer, 10^{-9} m).[1] As materials processing techniques such as chemical vapor deposition (CVD), molecular beam epitaxy (MBE) and lithography continue to improve, and the use of bottom-up nanomaterials like carbon nanotubes becomes more widespread, the active areas in electronic devices, catalytic systems, and other materials systems will continue to decrease in size, and are already reaching atomic dimensions.[2, 1] As this process continues, the understanding of surfaces and interfaces on an atomic scale will have increasingly important implications for the design and construction of new and better transistors, memory devices, catalysts, energy storage devices, etc. For example, the smallest layer of a modern transistor has already been scaled down to 1.2 nm, which is only 5 atoms thick, and the interface between this layer and the silicon substrate is crucial to device performance.[2, 3]

In parallel with this process, as both computing power and theoretical techniques

have improved, there has been a great increase in the capabilities of first principles modeling to describe interesting surfaces and interfaces with the accuracy necessary to quantitatively study new systems. First principles techniques are well-suited for understanding new phenomena at surfaces and interfaces, as they do not require the fitting of parameters to previous experiments or similar materials, and can therefore predict and explain effects which are not present in the bulk. In conjunction with careful experimental measurements, first principles calculations have provided insight into many nanoscale structures and properties.[4] In this work, I use first principles techniques to understand and design a variety of technologically relevant interfaces and surfaces.

A large portion of this work is related to the integration of complex oxides with silicon at an atomically sharp epitaxial interface. Si-based substrates and transistors are the backbone of the modern semiconductor industry, which over the past 50 years has managed to exponentially increase the density of transistors in a given area on a Si chip (the number of transistors per area has doubled roughly every two years, a phenomenon known as Moore's law).[5] This process has proceeded by scaling down the dimensions of a transistor, which requires each individual component of the transistor to decrease in size. However, this process has begun to reach atomic dimensions, as mentioned above, and further scaling will require improved materials. In particular, the dielectric layer of a transistor, which has traditionally been made of SiO_2, has already been replaced with a Hf-based oxide in modern transistors, due to its superior dielectric constant.[2, 3] This allows the dielectric layer to be made physically thicker, reducing quantum mechanical leakage currents, while maintaining the desired electric properties. One possible application of complex oxides on Si is to replace this dielectric layer with a material with even higher dielectric constant, allowing further scaling of transistors to take place.[6, 7, 3]

More broadly, the complex oxides display a dizzying array of potentially useful properties, including ferroelectricity, ferromagnetism, multiferroic behavior, colossal magnetoresistance, and high temperature superconductivity[8, 9]. However, in order to use these properties in applications such as a non-volatile transistors, spintronics, and multiferroic memory, they frequently must be integrated with Si. Our current ability to grow epitaxial oxides on Si is limited to a few materials, and detailed understanding of the growth procedures and the materials properties which enable the formation of high quality interfaces is necessary to both improve existing interfaces as well as expand the range of materials which can be grown epitaxially on Si.[6]

In this work, I investigate the properties of Sr which make it an ideal material to form a template layer for epitaxial growth of oxides on Si. I look at Sr on both Si and Ge, and I consider the effects of temperature on the growth of these materials. These results have already improved understanding of growth techniques for high quality interfaces between Si and $SrTiO_3$.[10, 6] In addition, I compare the performance of La to Sr as a template layer for oxide growth, and then use this knowledge to propose a series of interface structures which may allow for the growth of $LaAlO_3$ on Si, which has not yet been achieved.[6]

In addition to this work, I have also investigated the surface chemistry of $PbTiO_3$, a ferroelectric. The surfaces of ferroelectrics, which are materials with a stable but switchable polarization, provide an intriguing avenue for controlling surface chemistry and catalysis with an external electric field.[11, 12, 13, 14] By switching the polarization of the substrate, one can reversibly change the surface, potentially binding or releasing an adsorbate or turning off and on a reaction pathway. In order to understand the surface chemistry of $PbTiO_3$, a technologically relevant ferroelectric, I perform the first *ab initio* thermodynamic analysis of the variation of the $PbTiO_3$ surface with polarization, and I consider the effects of the changing $PbTiO_3$ surface

on its applications for surface chemistry. Specifically, I investigate the binding of CO_2 and H_2O to the surface for different polarizations of the substrate. Finally, I attempt to design a new surface layer which is both thermodynamically stable and will maximize the variation of the surface chemistry with polarization.

Interfaces can also be used to couple materials in new ways, creating unexpected phenomena which are not present in either bulk material.[8, 9, 15, 16] For example, an epitaxial interface between a $SrTiO_3$ substrate and a thin film of $La_{1-x}Sr_xMnO_3$ (LSMO) allows phonon modes related to octahedral rotations in the $SrTiO_3$ to couple directly with the LSMO. The transport properties of LSMO, which is a correlated oxide which displays colossal magnetoresistance,[17, 18] are very sensitive to these phonons. At the $SrTiO_3$ phase transition temperature, the frequency of these octahedral rotations approaches zero, leading to the diverging occupation of these phonon modes. These modes then couple across the interface and into the LSMO, modifying its transport properties and magnetization, and therefore creating a novel method to probe the electronic structure near the interface. In order to understand this effect, I build a first principles model of octahedral rotations at this interface and analyze the behavior of the octahedral rotations at finite temperatures.

This thesis is organized as follows:

In chapter 2, I review over the theoretical techniques used in my work.

In chapter 3, I investigate the properties of a submonolayer coverage of Sr on a Si (001) surface. In collaboration with my experimental colleagues James Reiner, Fred Walker, and Charles Ahn,[10] I explain the previously unknown 1/6 monolayer (ML) structure and its role in the evolution of the 1/2 ML template layer structure for oxide growth on Si.

In chapter 4, I calculate the properties of a phase transition between a disordered lattice gas of Sr on Si and an ordered silicide structure. These findings are in agree-

ment with the measurements of my experimental colleagues Myrtle-Rose Padmore, Yaron Segal, James Reiner, Fred Walker, and Charles Ahn.[19]

In chapter 5, I calculate the phases of Sr on a Ge (001) surface, and find a series of new structures which are in agreement with the scanning tunneling microscopy images of Boris Lukanov and Eric Altman.

In chapter 6, I investigate the properties of La on Si (001), and compare the surface to the results of chapter 3. I find a series of previous unknown silicide structures that indicate La will be difficult to use as a template layer for oxide growth, and which shed further light on the performance of Sr as an oxide template.

In chapter 7, I propose a growth procedure for epitaxial $LaAlO_3$ on Si, which builds on the results of the previous chapters. The stable interface structures require the incorporation of Sr at the interface in order to prevent silicide and SiO_2 formation as well as to compensate the polar field at the stoichiometric (001) $LaAlO_3$ surface.

In chapter 8, I present my work on ferroelectric surface chemistry, done in collaboration with Alexie Kolpak. I present the first polarization dependent phase diagram for the $PbTiO_3$ surface and investigate the effect of polarization on surface chemistry in this system.

In chapter 9, I present my model of the octahedral rotations between a $SrTiO_3$ substrate and an LSMO thin film. In collaboration with Yaron Segal, Carlos Vaz, Jason Hoffman, Fred Walker, and Charles Ahn, I explain the observed resistivity cusp in LSMO at the $SrTiO_3$ phase transition temperature in terms of dynamic cross-interface phonon coupling.

Chapter 2

Methods

2.1 Density Functional Theory

2.1.1 Hohenberg-Kohn Theorems

The central goal of electronic structure calculations is to solve the many-body Schrödinger's equation (under the Born-Oppenheimer approximation, in atomic units):

$$\hat{H}\Psi(r_1, r_2, ...) = E\Psi(r_1, r_2, ...) \quad (2.1)$$

$$(\hat{T} + \hat{V}_{ee} + \hat{V}_{eI})\Psi(r_1, r_2, ...) = E\Psi(r_1, r_2, ...) \quad (2.2)$$

$$-\frac{1}{2}\sum_{l=1}^{N}\nabla_l^2\Psi + \sum_{l<l'}\frac{1}{|r_l - r_l'|}\Psi + \sum_l U_{ion}(r_l)\Psi = E\Psi(r_1, r_2, ...) \quad (2.3)$$

where $\Psi(r_1, r_2, ...)$ is the full many-body wavefunction, which depends on the positions and spins of all N electrons in the system, E is the energy, $\hat{T}$ is the kinetic energy operator, $\hat{V}_{ee}$ is the electron-electron interaction operator, and $\hat{V}_{eI}$ is the potential due to the nuclei. Unfortunately, the space required just to store $\Psi(r_1, r_2, ...)$ numerically grows exponentially with the number of electrons in the system, making a direct solution of Schrödinger's equation impossible for all but the smallest number

of electrons. However, many approximate methods for solving Eq. 2.1 exist, and one of the most successful for investigating materials systems is density functional theory (DFT)[20, 21, 22] under the local density approximation (LDA),[21, 23, 24] which is used extensively in this work.

The main motivation for DFT is the realization that a direct attempt to solve for $\Psi(r_1, r_2, ...)$ is asking for too much information. When answering materials science questions, we are usually interested in far simpler quantities, like the energy, forces, and electron density of a given configuration of atoms. The great insight of DFT is that the ground state electron density, in principle, contains all of the information in the ground state wavefunction, $\Psi_0(r_1, r_2, ...)$,[20] where the electron density is defined as

$$n(r) = N \int dr_1 dr_2 ... dr_N \Psi_0^*(r_1, r_2, ...) \delta(r - r_1) \Psi_0(r_1, r_2, ...). \tag{2.4}$$

The electron density, $n(r)$, is a real function of only three spatial degrees of freedom, as opposed to Ψ_0, which is a complex function of $3N$ degrees of freedom; solving for $n(r)$ will greatly simplify the solution of the many-body problem.

In order to prove the claim that we can solve for $n(r)$ instead of Ψ_0, we first note that the ground state energy of a system can be written

$$E_0 = \langle \Psi_0 \mid \hat{T} + \hat{V}_{ee} + \hat{V}_{ext} \mid \Psi_0 \rangle \tag{2.5}$$

$$E_0 = \langle \Psi_0 \mid \hat{T} + \hat{V}_{ee} \mid \Psi_0 \rangle + \int dr\, n(r) v(r) \tag{2.6}$$

where the first two terms are the same for any system, and all of the differences between any particular material system comes from $v(r)$, the external potential, which is due to the nuclei and any external fields. Normally, one is given $v(r)$ and

solves for Ψ_0 and then computes $n(r)$. In order to show that $n(r)$ contains all the information of Ψ_0, we will show that for any given $n(r)$, there is a unique $v(r)$ (up to an additive constant), and therefore we can proceed from $n(r)$ to $v(r)$ to Ψ_0 without losing information. We proceed via proof by contradiction. Assume there are two different external potentials $v(r)$ and $v'(r)$ which produce the same $n(r)$. Then, we solve for Ψ_0 and Ψ_0' for the two potentials, and we note that due to the variational principle,

$$\begin{aligned} E_0 = \langle \Psi_0 \mid \hat{H} \mid \Psi_0 \rangle &< \langle \Psi_0' \mid \hat{H} \mid \Psi_0' \rangle & (2.7) \\ E_0 &< \langle \Psi_0' \mid \hat{H}' \mid \Psi_0' \rangle - \langle \Psi_0' \mid \hat{H} - \hat{H}' \mid \Psi_0' \rangle & (2.8) \\ E_0 &< E_0' + \int dr\, n(r)\Big(v(r) - v'(r)\Big), & (2.9) \end{aligned}$$

where in the second line we add and subtract $E_0' = \langle \Psi_0' \mid \hat{H}' \mid \Psi_0' \rangle$. However, if we switch the prime and unprimed variables and follow the same steps, we find

$$E_0' < E_0 + \int dr\, n(r)\Big(v'(r) - v(r)\Big). \quad (2.10)$$

Adding Eq. 2.9 and 2.10, we find that

$$E_0 + E_0' < E_0 + E_0' \quad (2.11)$$

which is a contradiction. Therefore, $v(r) = v'(r)$, up to a constant, and there is a one-to-one mapping between the external potential and the ground state electron density.

In order to make use of this result, we must find a way to solve for $n(r)$ given

$v(r)$. This can accomplished by minimizing the energy functional:[20]

$$E[n] = \langle \Psi_0[n] \mid \hat{T} + \hat{V}_{ee} \mid \Psi_0[n] \rangle + \int dr\, n(r) v(r). \tag{2.12}$$

In order to prove that the minimum of this function is the ground state electron density, we again make use of the variational principle. For some trial electron density $\tilde{n}(r)$:

$$E[n] = \langle \Psi_0[n] \mid \hat{H} \mid \Psi_0[n] \rangle \leq \langle \Psi_0[\tilde{n}] \mid \hat{H} \mid \Psi_0[\tilde{n}] \rangle \tag{2.13}$$

with equality achieved when $\tilde{n}(r) = n(r)$, the ground state electron density.

2.1.2 Kohn-Sham Equations and the Local Density Approximation

In order to make use of this formalism, we must find an explicit way to calculate

$$\begin{aligned} E[n] &= \langle \Psi_0[n] \mid \hat{H} \mid \Psi_0[n] \rangle & (2.14) \\ &= F[n] + V_{ext}[n] & (2.15) \\ &= T[n] + V_{ee}[n] + \int dr\, n(r) v(r), & (2.16) \end{aligned}$$

where $F[n] \equiv T[n] + V_{ee}[n]$ is a universal functional of $n(r)$ which includes both the kinetic energy and the Coulomb energy of the full many-body system. Following Kohn and Sham,[21] we will use approximations to $F[n]$ and create a single particle framework. First, we will write the kinetic energy, $T[n]$, by introducing a set of N orthogonal single particle states $\psi_i(r)$, where N is the number of electrons, which

are constrained to add up to $n(r)$:

$$T[n] = -\frac{1}{2}\sum_{i=1}^{N}\langle\psi_i \mid \nabla^2 \mid \psi_i\rangle \tag{2.17}$$

$$n(r) = \sum_{i=1}^{N}|\psi_i(r)|^2 \tag{2.18}$$

$$\langle\psi_i \mid \psi_j\rangle = \delta_{ij} \tag{2.19}$$

$$\tag{2.20}$$

The ψ_i are chosen to give the minimum of Eq. 2.17 while obeying Eqs. 2.18-2.19.

Next, we will rewrite V_{ee} by separating the classical Hartree electrostatic interactions from the rest:

$$V_{ee}[n] = \frac{1}{2}\int dr \int dr' \, \frac{n(r)n(r')}{|r_l - r'_l|} + E_{xc}[n] \tag{2.21}$$

where $E_{xc}[n]$, called the exchange and correlation energy, is defined to include all interactions beyond the mean-field Hartree term and the single particle kinetic energy (Eq. 2.17). One contribution to $E_{xc}[n]$ is classic (Fock) exchange, which is due to the fact that electrons are antisymmetric under exchange of indicies (this term is included exactly in Hartree-Fock theory). A second contribution is the correlations between the electrons, which are due to the fact that electrons repel each other, and therefore, each electron tends to have a lower instantaneous density of neighboring electrons around it than would be predicted by mean field theory. In addition, $E_{xc}[n]$ in principle includes any many-body kinetic energy effects which are not captured in Eq. 2.17, as well as self-interaction correction terms, which compensate for the fact that the Hartree term includes interactions between an electron and itself (these effects are not included accurately in the approximations used in this work).

With the explicit forms of Eqs. 2.17 and 2.21, we can take a functional derivate

of $E[n]$ with respect to $n(r)$, resulting in the Kohn-Sham equations, which can be solved self-consistently for the ground state energy and electron density:[21]

$$\Big[-\frac{1}{2}\nabla^2 + v(r) + \int dr' \frac{n(r')}{|r_l - r'_l|} + v_{xc}(r) \Big] \psi_j(r) = \epsilon_j \psi_j \tag{2.22}$$

$$v_{xc}(r) \equiv \frac{\delta E_{xc}[n]}{\delta n(r)} \tag{2.23}$$

$$n(r) = \sum_{i=1}^{N} |\psi_i(r)|^2 \tag{2.24}$$

Up until this point, DFT is exact; however, the exact forms of $E_{xc}[n]$ and $v_{xc}(r)$ are unknown, and approximations are required to continue. While many approximations of varying complexity exist, a simple and widely used approximation is the local density approximation (LDA), in which $E_{xc}[n(r)]$ is approximated at a given point in space by the value of the exchange and correlation terms of a uniform electron gas (jellium) at the same density:[21, 23, 24]

$$E_{xc}^{LDA}[n] = \int dr\, n(r) \epsilon_{xc}(n(r)) \tag{2.25}$$

where $\epsilon_{xc}(n)$ is the exchange and correlation energy per electron of an electron gas at density n with a uniform compensating positive background. The exchange contribution to $\epsilon_{xc}(n)$ can be calculated exactly,[25] while the correlation contribution has been computed to high accuracy via quantum Monte Carlo.[26, 27]

The success of LDA in describing materials systems is somewhat surprising, given how simple the approximation is and how far from a uniform electron gas the electron density most materials systems are. For instance, DFT using LDA can calculate semiconductor lattice constants to within 1-2%, and bulk moduli and phonon frequencies to within 5%.[22] More significant errors are found in solid cohesion energies and molecular atomization energies, which are frequently overestimated by >1.0

eV.[22, 28, 29] Much of the success of LDA is due to the fact that it gives the exact exchange and correlation energy for a physical system (the uniform electron gas), and therefore obeys a series of sum rules which are also obeyed by any real system under study.[30, 28]

My work also uses the generalized gradient approximation (GGA),[31, 32, 33, 28] which is closely related to LDA. In GGA, the approximation for E_{xc} includes gradients of the electron gas density:

$$E_{xc}^{GGA}[n] = \int dr\, n(r)\epsilon_{xc}^{GGA}(n(r), |\nabla n(r)|) \tag{2.26}$$

where $\epsilon_{xc}^{GGA}(n, |\nabla n|)$ is the exchange and correlation energy per electron of a uniform electron gas with a electron density n and a electron density gradient $|\nabla n|$. This is not a unique definition, and different GGAs exist that are chosen to reproduce various sum rules and scaling laws in addition to reproducing the exchange and correlation energy of a slowly varying electron gas.[28, 33] GGAs tend to improve total energies, atomization energies, energy barriers, and energy differences between structures compared to LDA but give similar lattice constants and structural properties.[28] For instance, compared to LDA, GGA reduces errors in the atomization energies of small molecules by a factor of four, and cohesive energies are also greatly improved.[28]

2.1.3 Plane Waves and Pseudopotentials

In order to solve the Kohn-Sham equations (Eq. 2.23) numerically in a solid-state environment, we expand our Bloch single particle wave functions in terms of plane waves:

$$\psi_{nk}(r) = e^{ikr} \sum_{G}^{|G| \leq G_{cut}} c_{nk}(G) e^{iG \cdot r}/\Omega \tag{2.27}$$

where $c_{nk}(G)$ are our expansion coefficients, and Ω is the unit cell volume. Our expansion in truncated at finite G_{cut}, usually specified as $E_{cut} = \frac{|G_{cut}|^2}{2}$. This basis has many nice properties, including: 1) it can be systematically improved by increasing E_{cut}, with convergence ensured as the Fourier basis is complete, 2) the kinetic energy is very simple in Fourier space, and 3) it naturally includes the periodic boundary conditions present in crystals. Unfortunately, the number of plane-waves required to accurately describe wavefunctions near the nuclei, which have many high frequency oscillations (see Fig. 2.1), is prohibitively high. This makes a straightforward application of a plane-wave expansion to any large system impossible.

In order to use a plane wave basis set, a technique must be used to describe the regions around the nuclei at low computational cost; in this work, we use pseudopotentials.[34, 35] In pseudopotential calculations, the core electrons are removed from the calculation, and the atomic potential felt by the valence electrons is modified so that it reproduces the correct wavefunctions outside of a cutoff radius (r_c), and the wavefunctions and potentials are smooth inside r_c (see Fig. 2.1). In practice, *ab initio* pseudopotentials are constructed from atomic all-electron calculations so that the all-electron and pseudo wavefunctions a) have the same eigenvalues ϵ_{nl}, b) are equal for $r > r_c$ and match smoothly at $r = r_c$, c) have matching logarithmic derivatives at $r = r_c$ and $\epsilon = \epsilon_{nl}$.[36] The last requirement ensures that the scattering properties of the pseudopotential match the all-electron potential at the chosen energy. When constructing and testing pseudopotentials, parameters such as r_c and the number of core versus valence states are adjusted in order to obtain the required accuracy for atomic and solid-state calculations, where the pseudopotential must reproduce the effective all-electron potential in a chemical environment which is not known *a priori*.

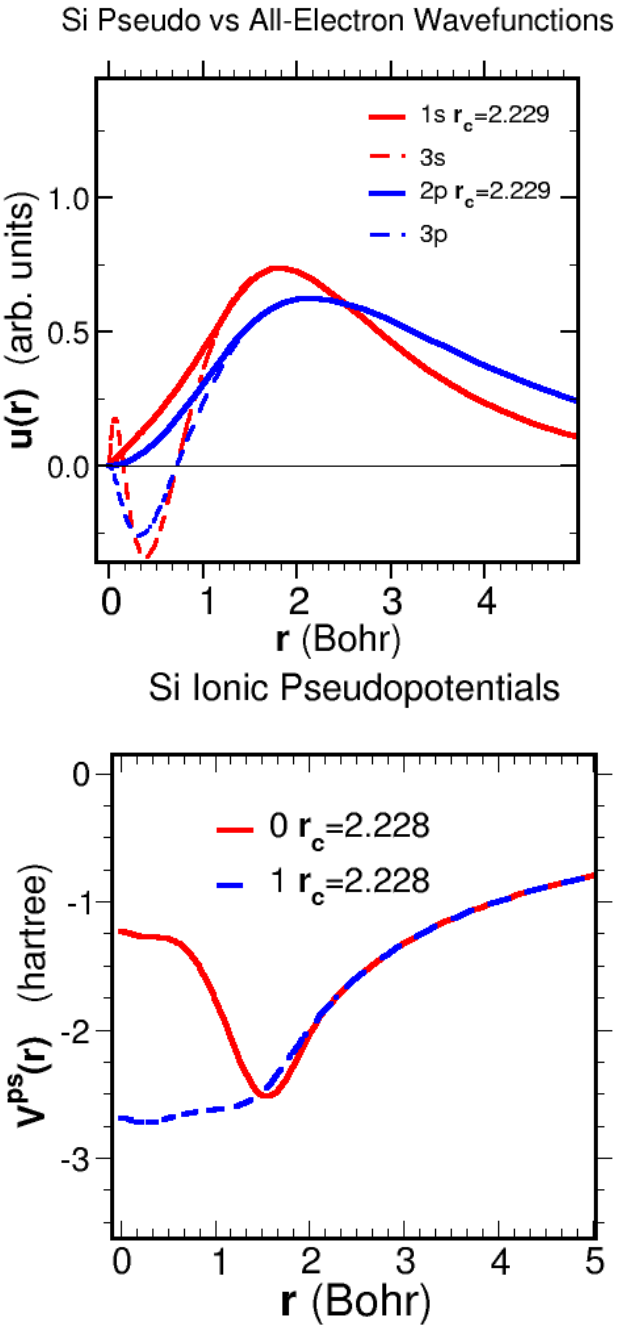

Figure 2.1: Top: Si all-electron (dashed) and pseudo (solid) wavefunctions, for the $3s$ and $3p$ valence orbitals. Bottom: Si pseudopotentials. $r_c = 2.23$ Bohr. This is example uses the norm-conserving Troullier-Martin's pseudoization scheme[34].

2.2 DFT Perturbation Theory

In order to calculate phonon frequencies and other properties that depend on derivatives of the total energy with respect to ionic positions, we need to calculate derivatives of the total energy:

$$E[n, \mathbf{R}] = T[n] + V_{ee}[n] + \int dr\, n(r) V_{ion}[\mathbf{R}] + V_{II}[\mathbf{R}] \tag{2.28}$$

where we emphasize the dependence of terms in the energy on $\mathbf{R}$, the ionic positions (see Eq. 2.16). The first two terms, the electron kinetic energy and electron-electron interactions, do not depend explicitly on $\mathbf{R}$, and do not directly affect the following analysis. The forth term, $V_{II}[\mathbf{R}]$, contains the ion-ion electrostatic interactions, computed with Ewald sums, and its derivatives with respect to the ionic positions are straightforward. However, the third term, the electron-ion interactions, will require additional analysis. We proceed by computing derivatives of E with respect to $\mathbf{R}$, which are necessary to calculate the spring constant matrix:

$$\frac{\partial E[n, \mathbf{R}]}{\partial \mathbf{R}} = \int dr\, n(r) \frac{\partial V_{ion}[\mathbf{R}]}{\partial \mathbf{R}} + \frac{\partial V_{II}}{\partial \mathbf{R}} \tag{2.29}$$

$$\frac{\partial^2 E[n, \mathbf{R}]}{\partial \mathbf{R} \partial \mathbf{R}'} = \int dr\, \frac{\partial n(r)}{\partial \mathbf{R}'} \frac{\partial V_{ion}[\mathbf{R}]}{\partial \mathbf{R}} + \int dr\, n(r) \frac{\partial^2 V_{ion}[\mathbf{R}]}{\partial \mathbf{R} \partial \mathbf{R}'} + \frac{\partial^2 V_{II}}{\partial \mathbf{R} \partial \mathbf{R}'} \tag{2.30}$$

Due to the Hellman-Feynman theorem, the first derivative of the energy, $\frac{\partial E[n, \mathbf{R}]}{\partial \mathbf{R}}$, does not require derivatives of the electron density. However, the second derivative, $\frac{\partial^2 E[n, \mathbf{R}]}{\partial \mathbf{R} \partial \mathbf{R}'}$, requires knowledge of $\frac{\partial n(r)}{\partial \mathbf{R}'}$, which we will compute with first order perturbation theory on the Kohn-Sham equations (see Eqs. 2.23 and 2.31):[37, 38, 39]

$$H \mid \psi_n \rangle = \epsilon_n \mid \psi_n \rangle \tag{2.31}$$

$$\frac{\partial \epsilon_n}{\partial \mathbf{R}} = \langle \psi_n \mid \frac{\partial H}{\partial \mathbf{R}} \mid \psi_n \rangle \tag{2.32}$$

$$(H-\epsilon_n)\mid \frac{\partial\psi_n}{\partial\mathbf{R}}\rangle = -(\frac{\partial H}{\partial\mathbf{R}}-\frac{\partial\epsilon_n}{\partial\mathbf{R}})\mid\psi_n\rangle \quad (2.33)$$

$$\frac{\partial H}{\partial\mathbf{R}} = \frac{\partial V_{ion}(r)}{\partial\mathbf{R}}+\int dr\,\frac{\partial n(r)}{\partial\mathbf{R}}\frac{1}{|r-r'|}dr'+\frac{dv_{xc}(n)}{dn}\frac{\partial n(r)}{\partial\mathbf{R}} \quad (2.34)$$

$$\frac{\partial n(r)}{\partial\mathbf{R}} = 2\,\mathbf{Re}\sum_{n=1}^{N}\psi_n^*(r)\frac{\partial\psi_n}{\partial\mathbf{R}}(r) \quad (2.35)$$

Eqs. 2.32-2.35 form a self-consistent set, which can be solved for $\frac{\partial n(r)}{\partial\mathbf{R}}$. Then, $\frac{\partial n(r)}{\partial\mathbf{R}}$ can then be used in Eq. 2.30 to calculate the spring constant matrix $\frac{\partial^2 E[n,\mathbf{R}]}{\partial\mathbf{R}\partial\mathbf{R}'}$.

2.3 Nudged Elastic Band

The nudged elastic band method (NEB)[40, 41] is a technique for finding the minimum energy path (MEP), and therefore the saddle point, between two local energy minima. For instance, it can be used to find the energy barrier for the motion of an adatom between two binding sites on a surface. Using transition state theory,[42, 43] the energy barrier for motion from site 1 to site 2 can be used to calculate the hopping rate:

$$R_{1\to 2} = \nu\exp(-E_b/k_BT)) \quad (2.36)$$

where E_b is the energy barrier, the highest point along the MEP, ν is an attempt frequency, T is the temperature, and k_B is Boltzmann's constant.

The NEB method works by first creating a series of images (usually around 7) which are an initial guesses for steps along the MEP between the two local minima in the atomic positions. The initial guess is frequently very high in energy, and must be relaxed to the MEP; however, naive force minimization will result in all of the images returning to one of the two local minima. In order to prevent this, the images are connected with fictitious springs, with spring constant k (see schematic in Fig.

2.2). Then, the forces on all of the images are relaxed, except in the direction parallel ($\|$) to the current MEP. Motion in this direction is relaxed according to the fictitious springs:

$$F_i = F^s_{i\|} + \nabla E(R_i)_\perp \tag{2.37}$$

$$\nabla E(R_i)_\perp = \nabla E(R_i) - (\nabla E(R_i) \cdot \hat{\tau}_i)\hat{\tau}_i \tag{2.38}$$

$$F^s_{i\|} = k(|R_{i+1} - R_i| - |R_i - R_{i-1}|)\hat{\tau}_i \tag{2.39}$$

where F_i is the total force on image i, $\hat{\tau}_i$ is the local tangent to the current MEP, $\nabla E(R_i)$ are the physical forces on an image, and F^s_i are the fictitious spring forces, with spring constant k. The projection of the F_i into perpendicular and parallel components is necessary to prevent the springs from distorting the MEP by pulling the images towards the shortest distance between the minima.[40]

2.4 Wannier Functions

While DFT is very good at calculating the Bloch states $\psi_{nk}(r)$ and the band energies ϵ_{nk} in reciprocal space for a given configuration of atoms, we frequently wish to understand the chemistry between atoms in terms of localized atomic bonds. One tool for achieving this is a Wannier function basis, which is a Fourier transform of the Bloch wavefunctions:

$$w_n(R, r) = \langle r \mid R_n \rangle = \frac{1}{\sqrt{N_k}} \sum_k e^{ik \cdot R} \psi_{nk}(r) \tag{2.40}$$

where N_k is the number of lattice sites and also the number of k-points in the first Brillouin zone over which the sum is performed. R is the lattice site about

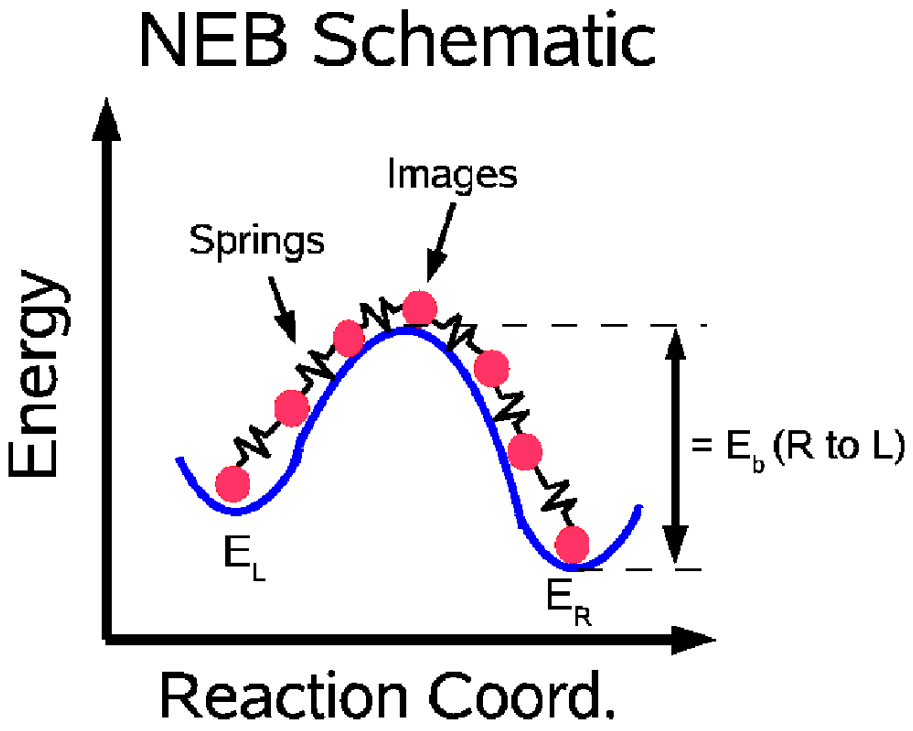

Figure 2.2: (Color Online) Schematic of Nudged Elastic Band (NEB) method. The plot is of the energy versus reaction coordinate (the minimum energy path), with images (red circles) along the path connected by springs, which prevent them from moving downhill to the local minima. The barrier E_b for transitions from the right minimum to the left minimum is marked.

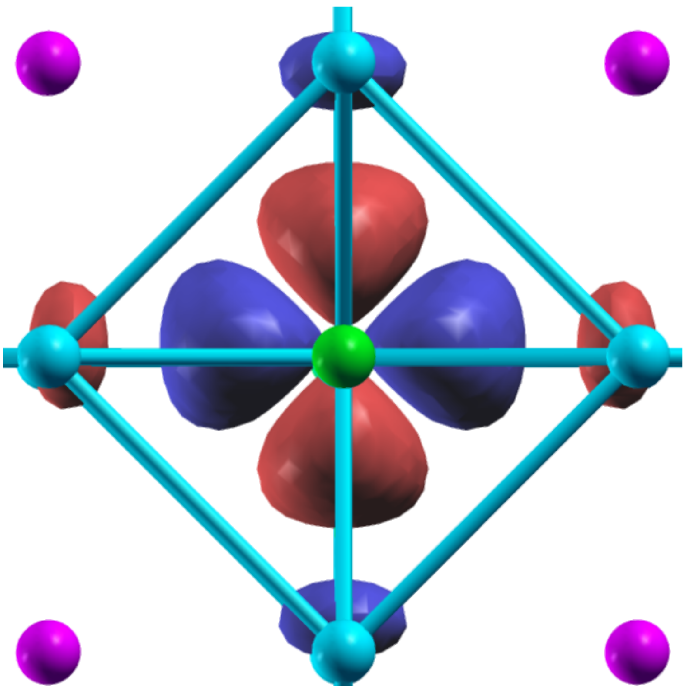

Figure 2.3: (color online) Top view of an isosurface plot of a Wannier function with $d_{x^2-y^2}$ character centered on a Mn atom in $La_{0.5}Sr_{0.5}MnO_3$. The Mn is green and in the center, the O are cyan with O-O bonds drawn, and the La/Sr are magenta. The red regions are positive, and the blue regions are negative. The function is largely localized on the Mn, but extends to neighboring O atoms due to bonding interactions.

which $w_n(R, r)$ is localized. Like the Bloch states $\psi_{nk}(r)$, Wannier functions form an orthonormal set, but rather than extending periodically throughout the crystal, $w_n(R, r)$ are typically localized at a particular lattice site R, which allows us to visualize and develop intuition for chemical interactions (see Fig. 2.3). In addition, by rewriting the reciprocal space Hamiltonian $H_{nm}(k, k') = \epsilon_{nk}\delta_{nm}\delta_{kk'}$ in a Wannier function basis, $H_{nm}(R, R')$, we can create an exact tight-binding Hamiltonian which reproduces the *ab initio* band structure ϵ_{nk}. In fact, if $H_{nm}(R, R')$ is localized (i.e. the matrix elements decay quickly as $|R - R'|$ increases), we can truncate our expansion in R-space and then inverse Fourier transform to any k with losing accuracy, allowing us to interpolate to a much higher k-point density than can easily be achieved with straight-forward DFT calculations.

In order for Wannier functions to be a useful description of the electronic structure, they must be localized in space. While this is always possible in one dimension,[44] and is frequently possible in higher dimensions,[45] some care is needed. In particular, a unitary transformation ($\psi'_{nk} = \sum_m U^k_{nm}\psi_{mk}$) between any set of overlapping bands in Eq. 2.40, which cannot change the results of the calculation of any physical quantities, will nevertheless have a dramatic effect on the resulting Wannier functions and their locality. In this work, we choose the U^k that minimizes the quadratic spread functional (Ω):[46]

$$\Omega = \sum_n \left[\langle r^2\rangle_n - \langle r\rangle_n^2\right] \tag{2.41}$$

$$\langle r\rangle_n = \langle R_n \mid \hat{r} \mid R_n\rangle \tag{2.42}$$

$$\langle r^2\rangle_n = \langle R_n \mid \hat{r}^2 \mid R_n\rangle. \tag{2.43}$$

This choice leads to maximally-localized Wannier functions, which are related to the modern theory of polarization.[47]

2.5 Classical Monte Carlo

In order to calculate the finite temperature properties of the systems described in this work, we would like to sum the partition function and also calculate the expectation value of operators:

$$Z = \sum_i e^{-\beta E_i}, \tag{2.44}$$

$$\langle O\rangle = \frac{1}{Z}\sum_i O_i e^{-\beta E_i} \tag{2.45}$$

where the sums are over all states of the system, Z is the partition function, E_i is the energy of state i, $\langle O \rangle$ is the average value of operator O and $\beta = \frac{1}{k_B T}$ is the inverse temperature. The number of terms in these sums grows exponentially with the number of particles in the system, making direct summation impossible. In addition, many unphysical states (i.e. with many broken bonds, or atoms on top of each other) are included in the sum, but have vanishing contributions. A computationally tractable method for dealing with high-dimensional sums is to use the Metropolis Monte Carlo method.[48, 49, 50] Rather than directly sum Eq. 2.44, we calculate the average value of observables by sampling from the Boltzmann distribution:

$$\langle O \rangle \approx \frac{1}{n} \sum_{i \propto p_i}^{n} O_i, \tag{2.46}$$

$$p_i = e^{-\beta E_i}/Z \tag{2.47}$$

where the states in the sum are drawn randomly, with probability p_i according to the Boltzmann distribution, and the sum has manageable number of terms. In order to do this summation, we need to be able to sample the Boltzmann distribution, which can be done by generating new states from prior states while obeying the detailed balance condition:

$$c_{ij} p_i = c_{ji} p_j \tag{2.48}$$

where c_{ij} is the probability of proposing a step from state i to state j. We impose this condition because it ensures that if the system is at equilibrium, then the stochastic evolution of the system maintains equilibrium. The Metropolis algorithm is a way of generating new states of the system while maintaining detailed balance, which allows us to calculate the average values of observables with Eq. 2.46. The algorithm

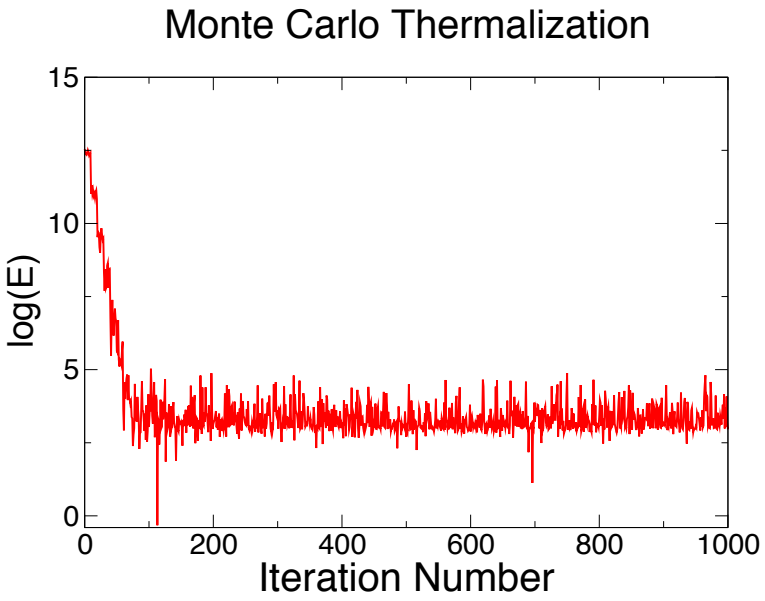

Figure 2.4: (color online) Example of thermalization in a Monte Carlo run. The log of the energy of the system is plotted versus iteration number. The initial configuration of the system is very high energy, but it quickly relaxes to random variations around its equilibrium value at the chosen temperature.

consists of repeating the following steps:

1) Propose a trial move from the current state (i) to a new state (j).

2) Calculate the energy of the current state (E_i) and the new state (E_j).

3) Accept the move with probability $\mathbf{min}\left[1, \frac{c_{ji}}{c_{ij}} e^{-\beta(E_j - E_i)}\right]$.

The proposed moves from one state to another are often chosen at random (i.e. move a random atom in a random direction by some step size), in which case, $\frac{c_{ji}}{c_{ij}} = 1$. In Sec. 9.4.2, we discuss a more complicated scheme, where the current state of the system (i.e. the forces on the atoms) is used to increase the chance that a move is accepted, which can increase computational efficiency.

In order to start the algorithm, a random initial state can be chosen, and then the algorithm is run until the average values of the observables stabilize. This process is called thermalization, and must be completed before sampling can begin (see Fig. 2.4).

Chapter 3

Phase Diagram and Kinetics of Sr on Si (001)

3.1 Introduction

The integration of new materials with current microelectronics technology is an important prerequisite for both improving many current technologies as well as creating new ones. In particular, the growth of epitaxial oxides on silicon is a key goal for the continuation of Moore's law in current CMOS transistors as well as a necessary component for many proposed devices.

As the electronics industry strives to pack higher densities of faster transistors onto a silicon wafer, the area of all the transistors must decrease. Despite this scaling, due to limitations on the charge and voltage, the capacitance across the dielectric layer of a transistor must remain constant.[2] In the past, the solution to this problem has been to decrease the thickness of the dielectric layer, currently made primarily of silicon dioxide, in order to maintain the desired capacitance per unit area. Unfortunately, current dielectric layers are only a few atomic layers thick

and further decreases in the thickness of this layer will result in unacceptably large quantum mechanical tunneling (leakage) currents through the dielectric.[2]

One solution is to replace the silicon dioxide dielectric with a material which has a higher dielectric constant, thus allowing the dielectric layer to be physically thicker but still have the desired capacitance.[7, 51, 6] In order for this approach to be successful, the new material must have a high quality interface with silicon which minimizes the scattering of electrons in the channel region of the transistor. Complex transition metal oxides deposited epitaxially on Si are one class of materials which can fulfill both requirements.

Beyond current technological concerns, the epitaxial integration of complex oxides with silicon would also allow the many interesting and potentially useful properties of oxides to be used in new devices, including but not limited to ferroelectricity, ferromagnetism, multiferroic behavior, and high-T_c superconductivity. In principle, these properties could be used in memory applications, improved transistors, or other novel spin-based devices; however, integrating these properties into practical devices will require atomic level control over oxide interfaces with silicon.

Currently, all examples of complex oxides grown epitaxially on silicon have required the deposition of a submonlayer template layer of Sr, Ba, or Ca on the silicon as a first step.[52, 53] During this initial deposition, experiments with *in situ* sample characterization observe several different surface reconstructions. However, the role of these reconstructions in preparing the surface as an oxide growth template which forms the eventual interface[54, 55, 6] with the complex oxide is unknown. Here, we propose several new submonolayer Sr on Si (001) structures which explain these reconstructions and which enable us to clarify the role temperature plays in creating an effective oxide template. Our knowledge of Sr on Si (001) has allowed us to predict an experimentally verified low temperature path to oxide epitaxy.[10]

In addition to understanding this particular oxide growth method, we hope that, over longer time scales, the knowledge acquired by studying Sr on Si will help explain the failure of other elements to provide an effective template layer for oxide growth. La, in particular, would be very intriguing as an oxide template due to the high dielectric constant and large band offsets of $LaAlO_3$ with Si (see Chapters 6-7). Unfortunately, La has thus far failed as a template layer for epitaxial growth on Si.[56, 6]

This chapter is organized as follows. In Sec. 3.2 we describe our calculational methods. In Sec. 3.3 we present a review of experimental work on Sr on Si (001). In Sec. 3.4 we present results for Sr deposited on a standard dimerized surface: these findings are largely in agreement with previous theoretical work[57] but fail to explain many of the experimental results. In Sec. 3.5 we present new results for Sr on modified dimer surfaces which allow us to rule out this entire class of structures. In Sec 3.6, we present new results for Sr on submonolayer silicon surfaces. In Sec. 3.7 we use the results of Secs. 3.4-3.6 to explain the experimental data and present a phase diagram for submonolayer Sr on Si (001) up to 0.5 ML coverage. In Sec. 3.8 we present computed STM images for the most stable 1/6 monolayer (ML) structure which also turn out to compare well with experimental findings, and briefly discuss recent XRD results. In Sec. 3.9, we present results on 1.0 ML Sr silicides. Finally, in Sec. 3.10, we present our conclusions.

3.2 Methods

3.2.1 Total energies

Our calculations were based on first-principles density functional theory calculations using a plane wave basis set.[20, 21] We used the PBE GGA to approximate the

exchange correlation functional.[28] In order to minimize the number of electrons in our calculations, we employed norm-conserving Troullier-Martins pseudopotentials to simulate the valence electrons.[34] For silicon, we used $3s$, $3p$, and $3d$ projectors (d local) with cutoff radii of r_s=r_p=r_d=2.25 Bohr and the reference atomic configuration $3s^2 3p^2 3d^0$. For Sr, we treated the semicore $4s$ and $4p$ states as valence electrons in addition to the valence $3d$, $5s$, and $5p$ states ($3d$ local) with cutoff radii of r_s=1.3 Bohr, r_p=r_d=2.0 Bohr and reference configuration $5s^1 4d^1 5p^0$. The semicore states are necessary to properly describe the physics of Sr. With semicore states, our calculated Sr lattice constant was 6.05 Å, in excellent agreement with experiment, but when we did not include semicore states in our Sr pseudopotentials, we found poor transferability between different atomic states and a lattice constant that varies 5% depending on apparently irrelevant numerical choices in for our reference configuration or cutoff radii.

All our calculations were run at the theoretical lattice constant of silicon, which we calculated to be 5.456 Å, and with a plane-wave cutoff energy of 60 Ryd. We used a slab geometry with periodic boundary conditions in the x and y directions and a finite thickness in the z direction, which is the (001) direction in the Si crystal. This geometry creates two surfaces, one on each side of the slab. We treated the surfaces symmetrically by adding Sr to both sides to create two physically identical surfaces (see the next paragraph for why this is important). The slab was simulated with at least 8 layers of silicon plus an equivalent of 8 silicon layers of vacuum. We found binding energies to be converged to within 0.01 eV/Sr using a 6x6 k-point sampling per 1x1 surface unit cell of silicon with a Fermi-Dirac smearing temperature of 0.1 eV. In this work, the z direction is the surface normal, x is by default the direction in which a clean Si (001) surface doubles it periodicity by dimerizing, and y is orthogonal to both x and z.

Table 3.1: Comparison of Sr binding energies for different Si slab configurations. All energies are relative to the 8 layer symmetric configuration used in this work which has the same atomic configuration on both sides of the slab. For the unreconstructed configurations, each Si in the bottom layer is frozen to its bulk position and two H atoms per surface Si are used to passivate its dangling bonds. In the reconstructed configurations, the bottom of the slab is dimerized with one H atom per surface Si.

Sr Coverage (ML)	Slab configuration	ΔE_{bind} (eV)
1/4	4 layers unreconstructed	-0.33
1/4	4 layers reconstructed	0.10
1/4	8 layers reconstructed	-0.04
1/4	8 layers symmetric	$\equiv$ 0.00
1/2	4 layers unreconstructed	-0.22
1/2	4 layers reconstructed	0.13
1/2	8 layers reconstructed	-0.02
1/2	8 layers symmetric	$\equiv$ 0.00
1/2	12 layers symmetric	0.01

Initially, we attempted to decrease the size of our calculation by only using one Sr on Si surface and passivating the opposite slab surface with hydrogen, as per Ashman *et al.*[57] and Stekolnikov*et al.*,[58] among others. However, we found that these configurations were insufficient to converge binding energies to within 0.01 eV/Sr. Table 3.1 compares the results of several different methods of approximating a Si slab to our 8 layer symmetric surface method. The reason for the insufficiency is the following: an examination of the electric potentials of the asymmetric calculations revealed significant long range electric fields through the vacuum. Due to the different charge densities at the two surfaces, this electric field is unavoidable, and the energy associated with it seems sufficient to change the computed total energy in an uncontrolled fashion.

Sr binding energies were calculated relative to a bare silicon surface in the p(2×2) configuration and an isolated Sr atom at rest in vacuum. More positive binding energies mean stronger binding. In this work, we considered many surfaces with non-stoichiometric Si coverages, *i.e.* less than a full monolayer (ML) of Si on the

surface, which required the use of a bulk Si reservoir to calculate binding energies. The chemical potential of the bulk reservoir was determined by subtracting the two nearest full monolayer silicon slab calculations and dividing the difference by the number of silicon atoms. For example, to determine the binding energy of a structure with 8 full layers of Si plus 2 extra Si atoms per side, we used a chemical potential determined from the 8 and 10 layer Si slab calculations. This method was used to approximate the energy of bulk Si to the same accuracy as the rest of the slab and to remove an ambiguity as to whether a structure with a partial Si layer should be considered as adding bulk atoms to a thinner reference slab or subtracting bulk atoms from a thicker reference slab. For a sufficiently thick reference slab, this method for determining the chemical potential will give the same result as the more intuitive method of using a *ab initio* bulk Si calculation to determine the chemical potential, but our method converges faster for finite-sized slabs.

3.2.2 Phonons free energies

Most first principles calculations assume that contributions to the free energy from the vibrational degrees of freedom of similar structures are either too small or too similar to be relevant at experimental temperatures. However, since we were examining temperature dependent effects and small energy differences, we were forced to consider phonon contributions to the free energies. Phonon calculations require the first derivative of the charge density with respect to the nuclear positions, which we calculated using DFT perturbation theory.[37, 38, 39]

Our method for calculating the free energy of large slabs with periodic boundary conditions in the x and y directions depended on the locality of the dynamical matrix in real space. First, we calculated the dynamical matrix on a coarse grid in (k_x, k_y) space. Next, we Fourier transformed to get the dynamical matrix in (x, y)

space and we checked to see if the matrix elements between atoms which were well separated in real space had decayed to negligible values. Once we had the real space dynamical matrix with sufficient range such that any further matrix elements would be negligible, we could Fourier transform back to (k_x, k_y) space exactly and therefore calculate the dynamical matrix at any k-point essentially exactly. We found that real space matrix elements typically converged within three 1x1 unit cells of silicon. In order to ensure the convergence of low frequency modes in a computationally efficient manner (see discussion in Mounet and Marzari[59]), we enforced the translational acoustic sum rule by editing the diagonal elements of the real-space dynamical matrix D,

$$D_{ij}^{\alpha\alpha} = -\sum_{\beta\neq\alpha} D_{ij}^{\alpha\beta}\,, \tag{3.1}$$

where α and β label the atoms in the system and i and j label the x, y, or z directions. Enforcing the acoustic sum rule ensures that moving all the atoms collectively results in exactly zero restoring force, and therefore that the frequencies of the three acoustic modes do in fact go to zero at Γ.

Once we had the real-space dynamical matrix, we used the above method to sample the phonon dispersion on for a dense k-point grid sufficient to converge the free energy. The free energy was calculated with the standard formula for quantum harmonic oscillators,

$$F = E_0 + \sum_i \frac{1}{2}\hbar\omega_i + \ln(1-\exp(-\hbar\omega_i/k_bT)) \tag{3.2}$$

where E_0 is the total ground state energy of the system as determined by the plane wave calculation, ω_i are the phonon frequencies, k_b is Boltzmann's constant, and T is the absolute temperature. For a slab system, the sum over i represents both the

sum over both the $3N_{atoms}$ modes in the unit cell as well as (k_x, k_y) space.

While the Sr atoms on the surface only interacted significantly with the first three to four layers of Si directly, we still needed to converge our free energies with respect to the thickness of our slab in order to properly capture the differences between low frequency modes in the z direction. In order to accomplish this in a computationally efficient manner, we attached additional layers of bulk Si to the *ab initio* slab and converged free energy differences as a function of the number of added bulk layers (see Figure 3.1). Specifically, we first derived an accurate *ab initio* second nearest neighbor model for the dynamical matrix of bulk Si. Second, we computed the *ab initio* dynamical matrix elements of all atoms comprising the surface and and first four layers of Si of the slab. Third, to connect this slab data to the added bulk Si layers, we replaced the dynamical matrix elements connecting the third and fourth Si slab layers to the added bulk by those appropriate to the bulk second nearest neighbor model. The free energy differences are converged to 1 meV after attaching 10 layers of bulk silicon to 4 layers of slab data as shown in Fig. 3.1.

3.2.3 Energy barriers

Another potential source of temperature effects are kinetic barriers which prevent the system from reaching true thermodynamic equilibrium. In order to estimate these kinetic effects for key configurations, we performed energy barrier calculations for typical atomic motions. Energy barriers (E_{bar}) were determined using the Nudged Elastic Band method plus Climbing Images, which determines the energy of the transition state between two local minima.[40, 41] We then used simple transition state theory to estimate transition rates:

$$R = \nu \exp(-E_{bar}/kT)) \tag{3.3}$$

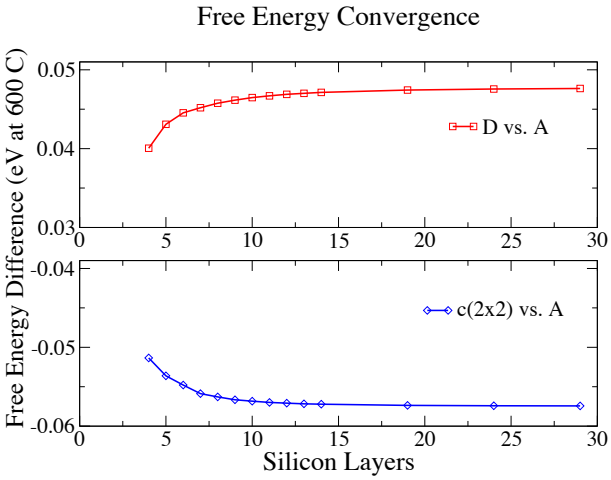

Figure 3.1: (Color online) Convergence data for vibrational free energies versus number of bulk silicon layers added to the slab for 1/2 ML structures (see Figs. 3.2 and 3.6 for all the A and all D structures and Fig. 3.7 for the c(2×2) structure). Top: Vibrational free energy of all A structure minus all D structure. Bottom: Vibrational free energy of all A structure minus c(2×2) structure. We found that convergence to 1 meV/Sr at 600^{o}C is achieved after 10 layers of Si were added to a 4 layer *ab initio* calculation.

The exponential prefactor (ν) was estimated from our phonon calculations. We expect these rates to give a good order of magnitude estimate for the rate limiting steps which dominate the motion of surface atoms.

3.2.4 Wannier functions

Finally, maximally-localized Wannier function calculations were performed in order to analyze electronic structure and surface chemistry.[46] We considered several different Wannier function schemes to analyze the surface bonding. To get a qualitative understanding of our surfaces, we used a basis consisting of Sr s and d orbitals plus sp^3-like dangling bonds on surface silicon atoms. In order to get a more quantitative understanding of the surface, we also considered a full sp^3 basis for the silicon. Using the full sp^3 basis allowed us to create an exact first-principles tight binding model of the surface near the Fermi level, but the additional Wannier functions did not

change our qualitative interpretation of the surface bonding. All of the density of states plots in this work were obtained by projecting onto Wannier states. The advantage of projecting onto Wannier functions rather than the more commonly used atomic orbitals is that Wannier functions are orthonormal, maximally localized, and complete within the chosen Hilbert space, which we generally set to be a few eV around the Fermi level.

3.3 Review of Experimental Work

The first step of the only known pathway to epitaxial oxide growth on Si (001) is to deposit submonolayer coverages of an alkaline earth metal on silicon near 600^oC. The first structures of this type used Sr,[52] but the method as been expanded to Ba and Ca.[53] Experiments indicate that Sr coverages between 1/4 ML and 1/2 ML are suitable for oxide growth,[60] but the role of high temperature Sr deposition in promoting epitaxial growth is unclear.

Previous high temperature RHEED,[52, 60] LEED,[61] and STM[62, 63] studies of the surface found that the surface evolves from the 2× reconstruction exhibited by the bare silicon surface to a 3× structure at 1/6 ML, which is then replaced by a 2× structure at 1/4 ML. The final 2× structure is observed to be stable up to 1/2 ML Sr coverage. These shifting diffraction patterns are often used for calibration in oxide growth procedures. Unfortunately, their origin has up to now been largely unknown.

Diffraction experiments on the silicon surface typically suffer from the fact that the standard Si (001) surface displays terraces separated by single height steps with reconstructions rotated by 90 degrees, resulting in diffraction data which contain a mixture of the two terminations. This mixture of surface termination prevents a

Table 3.2: Experimental symmetry patterns observed with RHEED on miscut silicon wafers.[10]

Sr Coverage (ML)	T = 25^{o}C	T = 600^{o}C
0	2×1	2×1
1/6	disordered 2×1	2×3
1/2	2×1	1×2

clear determination of the relative alignments of the observed reconstructions. New data from the experiments of our collaborators Reiner *et al.*[10] avoided this issue by using specially prepared silicon wafers. They deposited Sr on a 4 degree miscut silicon wafer using molecular beam epitaxy (MBE) and analyzed the surface using RHEED. The large miscut angle decreases the size of the silicon terraces, which both reduces the influence of strain effects and increases the influence of step energies.[64] The combination of these two effects causes all of the silicon dimer rows to align on all terraces, removing an ambiguity in the interpretation of RHEED results.

This new RHEED data showed an unexplained temperature dependence (see Table 3.2). At low temperatures (25^{o}C), the experiments indicated that from 0 ML up to 1/2 ML of Sr coverage, the surface retains the 2×1 symmetry of the initial dimerized silicon surface. However, at high temperatures (600^{o}C), more complicated phases emerged. The surfaces started with 2×1 symmetry at 0 ML, but transitioned to a 2×3 pattern at 1/6 ML. As the Sr coverage was further increased, at around 1/4 ML the pattern again changed to a 1×2 pattern, which continued until 1/2 ML. These high temperature measurements cannot be explained by existing theory work of Sr on Si (001), as we explain below.

3.4 Standard Dimerized Surfaces

To orient the reader, we first summarize key facts concerning the bare Si (001) surface (see ref. [65] and references therein). The atoms of the top layer of the unreconstructed Si (001) surface are each missing two covalent bonds. The surface has a first order reconstruction whereby each surface Si atom pairs with a neighbor and forms a strong dimer bond. Due to the highly directional sp^3 bonding with the second layer Si atoms, all of the dimers are forced to lie in the same direction, perpendicular to the bonds between the first and second layer atoms. These dimers prefer to arrange themselves into rows, which minimizes bond stretching. This symmetry breaking dimerization causes the periodicity of the surface to double in the x direction, leading to a 2×1 reconstruction. After dimerization, each surface atom still has one half-filled dangling bond. In order to further reduce the energy of the surface, each dimer has a further and weaker symmetry breaking reconstruction: each dimer buckles in the z direction, creating an upper atom and a lower atom (see Figure 3.2). This reconstruction pushes the upper atom towards a more bulk-like sp^3 geometry with a lower energy dangling sp^3-like orbital, and it pushes the lower atom into a more planar sp^2 geometry with a higher energy p_z-like dangling orbital. Then one electron is transfered from the dangling orbital of the lower atom to the upper atom, partially opening a surface band gap. Furthermore, the dimers alternate buckling direction going down each row. Despite these reconstructions, the silicon surface still features one unpassivated dangling orbital per surface silicon and tends to accept electrons.

In our first attempt to understand low coverages of Sr on the surface, we assumed that the silicon remains in its canonical dimer row pattern and that the Sr simply sits "on top" of this silicon surface. We calculated the binding energies of several

different structures and found the results to be in agreement with Ashman *et al.*[57] In general, we found the binding energy per Sr to be at least 3.5 eV/Sr at coverages of up to 1/2 ML (a more positive binding energy indicates strong binding). This shows that almost all of the deposited Sr will remain on the surface for typical deposition temperatures of 600^oC. In fact, at 600^oC and 1/2 ML coverage, the pressure of an ideal gas of Sr above the surface would be 9×10^{-12} Pa, well below typical experimental pressures of $\sim 10^{-8}$ Pa.

To begin our search for submonolayer Sr surface structures, we compared possible binding sites for Sr adatoms. We found that isolated Sr atoms have two local minima on the silicon surface, which we called site A and site D in accordance with Ashman *et al.*[57] (see Figure 3.2 and Table 3.3). We found that site A is most stable, with a binding energy of 3.64 eV. Site D was 0.41 eV less stable; therefore, we expect all the Sr atoms to occupy A sites at low coverages. For both the A and D site, one of the silicon dimers next to the Sr atom becomes flattened and elongated. This effect has been attributed to the Sr donating 2 electrons to the dangling bonds on the silicon surface, which causes both dangling bonds on the dimer to become filled.[57] When both dangling bonds are filled, the charge transfer mechanism which is responsible for stabilizing the Si buckling reconstruction (summarized above) is eliminated, which causes the dimer to flatten.

Due to the importance of double height silicon steps in the experiments of Reiner *et al.*[10] (see section 3.3), we also considered the binding of a Sr atom to a double height silicon step (D_B in Chadi's notation [64]) which we found to be 3.75 eV. While this binding energy is larger than the binding of an isolated Sr atom to the dimerized surface, it is smaller than the most stable 1/6 ML chain structures presented below (see Table 3.3); therefore, we do not expect Sr atoms to bind preferentially to step edges nor step edges to necessarily be important sites of nucleation for the observed

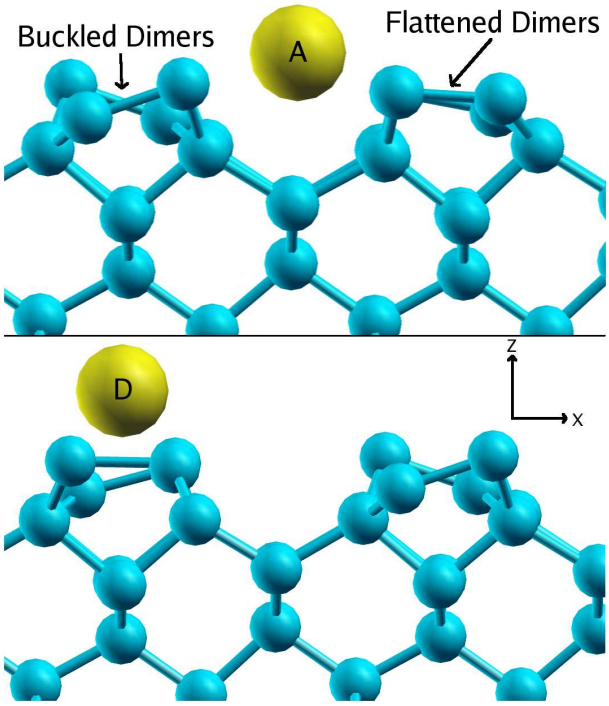

Figure 3.2: (Color online) Side view of A site (top) and D site (bottom) isolated Sr. Both figures feature both flattened and buckled dimers. The single large (gold) sphere in each figure is the Sr adatom while the Si atoms are the smaller (blue) spheres.

changes of surface structures.

Following Ashman *et al.*,[57], we began to search the phase space for higher coverages of Sr on the surface. We found that the most stable structures were those where the surface silicon atoms were able to arrange their buckling such that as many raised surface silicon atoms were nearest neighbors of the Sr as possible, without the Sr aggregating into locally high coverage patches. This condition is generally met by diagonal chains of Sr atoms, which allow the Sr atoms in adjacent rows to be linked by flattened dimers and also allow the remaining buckled dimers near the Sr to arrange their buckling to both keep raised Si atoms near the Sr and maintain an alternately buckled pattern in each row.

For example, at 1/6 ML, we found the most stable structure to be chain-like pat-

terns of Sr atoms occupying the A site (see Figure 3.6a and Table 3.3). This structure has a very strong binding energy of 3.81 eV/Sr. It is important to note that while in principle this structure will be ordered at zero temperature, there exist zig-zag chain structures which are essentially isoenergetic with the straight chains. In fact, we found that the zig-zag chains are 0.014 eV/Sr more stable than the straight chains at 1/6 ML. This energy difference is essentially within our convergence threshold and likely beyond the accuracy of the PBE GGA functional, but were it accurate, we would expect the chains to be disordered well below room temperature. This near degeneracy between straight and kinked chains causes the positions of Sr atoms in second nearest neighbor rows in the 2× direction to be very weakly correlated; therefore, we expect the Sr pattern for this reconstruction to appear disordered, in contrast to the ordered 2×3 reconstruction observed at 600^{o}C in RHEED experiments (Table 3.2).

As we increased the Sr coverage, the next coherent phase on silicon dimer rows was the double chain structure at 1/4 ML (see Figure 3.6b and Table 3.3). This structure is similar to the single chain structure, but with each chain having two consecutive A sites filled, which again maximizes the number of raised dimer atoms near each a surface Sr. For the same reasons as the single chain, this structure also will be disordered at finite temperatures.

Finally, at 1/2 ML Sr coverage, we found the most stable structure to have every A site filled, which produces a coherent 2×1 diffraction pattern (see Figure 3.6c and Table 3.3). If each Sr atom fully donated 2 valence electrons to the silicon surface, this structure would have every Si dangling bond passivated, and we did find that the surface has a band gap (see Figure 3.4). However, our Wannier function calculations indicated that the bonding is more covalent than previously thought, as there was significant hybridization between the Si dangling bonds and the Sr orbitals (see

Figures 3.3a-c). This strong overlap between Si and Sr states pushes the Sr states out of the silicon band gap. We can understand this process better by examining the Wannier functions for the D site 2×1 ML structure. By comparing Figures 3.3a-c with Figures 3.3d-f, we can see that while the silicon states are very similar, the lowest energy Sr state for the D structure is much farther from the surface and has much less overlap with the dangling bonds than in the A site case. This difference results in Sr states interacting less with the silicon and remaining in the middle of the silicon band gap (compare Figures 3.4 and 3.5), which accounts for the large difference in binding energies between the A site and D site (Table 3.3). Additionally, in both cases, there is a significant contribution to the density of states below the Fermi level which has Sr character. A pure ionic model would have no occupied Sr valence states. Thus, these contributions indicate a hybridization between the silicon dangling bonds and the Sr orbitals in a covalent bonding picture. By comparing our Wannier function calculations with and without Sr d orbitals, we found that both Sr s and d orbitals contribute to this bonding.

Because of the importance of the 1/2 ML A site structure in epitaxial oxide growth and interface formation, we were interested in determining how disordered it might become at finite temperatures. Namely, we wanted to know the lowest energy localized excitations of this surface. Due to the ordered Sr pattern, with all of the A sites filled, as well as the highly directional nature of silicon sp^3 bonding, the only available low energy surface excitation is to move a single Sr atom from an A site to a D site. In order to calculate this energy, we compared the energy of a 4×4 patch of the 1/2 ML all A site structure to the same 4×4 patch except with a single A site Sr atom moved to a neighboring D site. We found that this excitation requires 0.25 eV of energy. While this D site excitation energy is much less than the 0.60 eV/Sr required to move all of the A sites to D sites at 1/2 ML coverage, it is still several

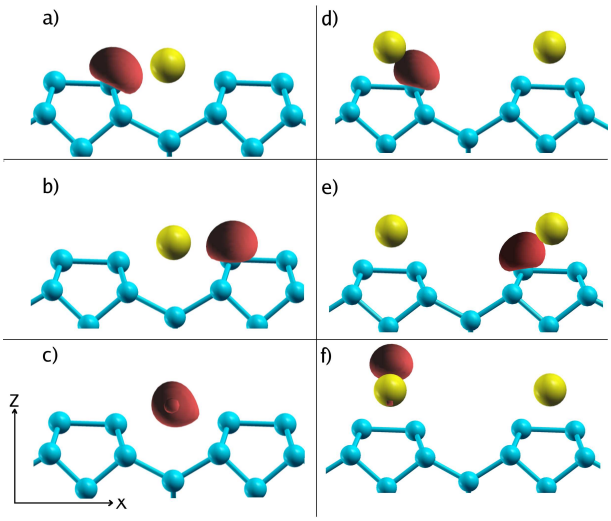

Figure 3.3: (Color online) Isosurface plots of bonding state Wannier functions at 1/2 ML coverage (red regions are positive). a-b) A site Si dangling bonds c) A site low energy Sr state. d-e) D site Si dangling bonds. f) D site low energy Sr state. Note: the Sr states in c) and f) are centered between the Sr atoms along the y direction, perpendicular to the plane of the figure.

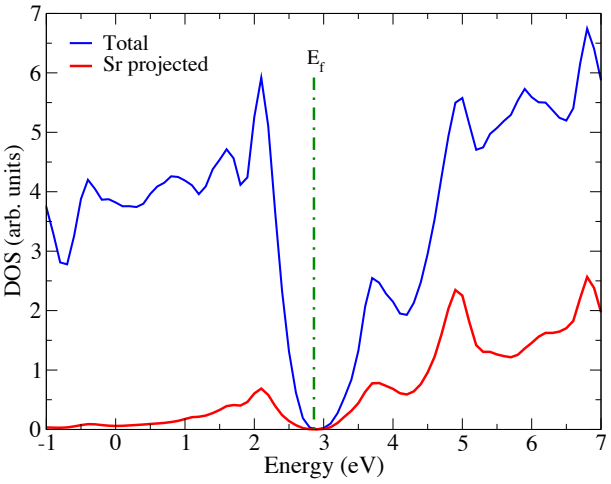

Figure 3.4: (Color online) Total density of states (DOS) in blue (upper curve) and Sr projected DOS from sp^3 Wannier function calculations in red (lower curve) for the 1/2 ML all A site structure. The strong interaction between the Sr states and Si states (see fig. 3.3 a and b) pushes the Sr levels away from the Fermi level (vertical dashed), opening a band gap.

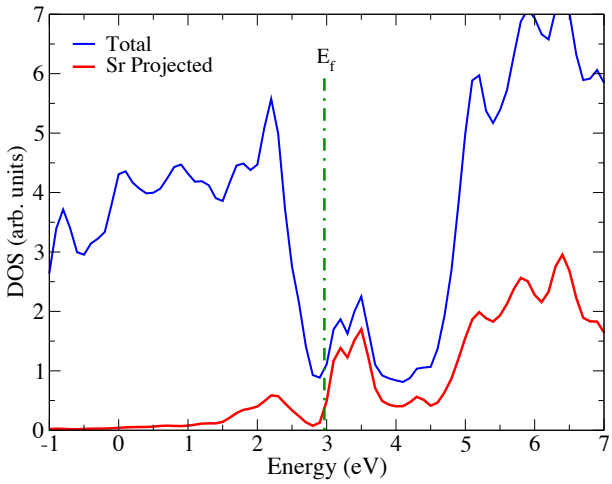

Figure 3.5: (Color online) Total density of states (DOS) in blue (upper curve) and Sr projected DOS from sp^3 Wannier function calculations in red (lower curve) for the 1/2 ML all D site structure. The weaker interaction between the Sr states and Si states ((see fig. 3.3 c and d) results in Sr levels in the silicon band gap and less hybridization between Sr states and Si states. The Fermi level is the vertical dashed line.

times k_bT (0.075 eV at 600^{o}C, a typical deposition temperature). If we make the simple approximation that each Sr atom on the 1/2 ML surface can occupy either an A site or a D site and is uncorrelated with the other Sr atoms, we find that less than 4% of the Sr will be in D sites. While calculations with a higher density of defects (e.g. AAAD in Figure 3.6 and Table 3.3) indicate that there is an attraction between second nearest neighbor D sites which partially stabilizes higher densities of D sites, due to the low density of defects at deposition temperatures, these interactions will not occur frequently enough to change our simple estimate significantly.

The 2×1 all A site structure is consistent with the low temperature RHEED results and is the most stable structure at 1/2 ML coverage we found in our work. However, while this 2×1 pattern has the correct size unit cell, it cannot by itself explain the 1×2 pattern seen at high temperatures because the 1×2 pattern is perpendicular to the original dimers (see Table 3.2). The only reasonable way the surface dimers can change orientation is for an entire layer of silicon to leave the surface,

Table 3.3: Binding energies of selected standard dimer pattern structures. See Figs. 3.2 and 3.6.

Sr Coverage (ML)	Pattern	Figure	E_{bind} (eV/Sr)
Isolated	A site	3.2 top	3.64
Isolated	D site	3.2 bottom	3.23
Isolated at step edge	D_B[64]		3.75
1/6	Single Chain	3.6a	3.82
1/4	Double Chain	3.6b	3.78
1/2	All A site	3.6c	3.54
1/2	AAAD	3.6d	3.50
1/2	Single D, remainder A		3.29

exposing the second layer of silicon atoms, which then naturally reconstructs into perpendicular dimers. Unfortunately, standard dimerized surface silicon structures provide no thermodynamic driving force for the 2×1 to 1×2 transition: the starting point and ending point have identical free energies by rotational symmetry. This lack of driving force, together with the failure to explain the observed 2×3 pattern at 1/6 ML, forces us to rule out this entire class of structures when attempting to explain the high temperature growth experiments.

3.5 Modified Dimer Patterns

When the silicon surface was constrained to be in the original dimer pattern (section 3.4), the calculated reconstruction patterns could not explain the observed high temperature surface symmetries of Table 3.2. In this section, we detail how we considered and then ruled out the possibility that the experimentally observed 2×3 and 1×2 symmetries could be due to the influence of configurational or vibrational entropy on a stoichiometric silicon surface. (This ruling out was necessary to justify the explanation of the experimental data presented in section 3.7. As we show below in this section, none of the structures we found in this class were thermodynamically stable under growth conditions when compared to those of section 3.6.)

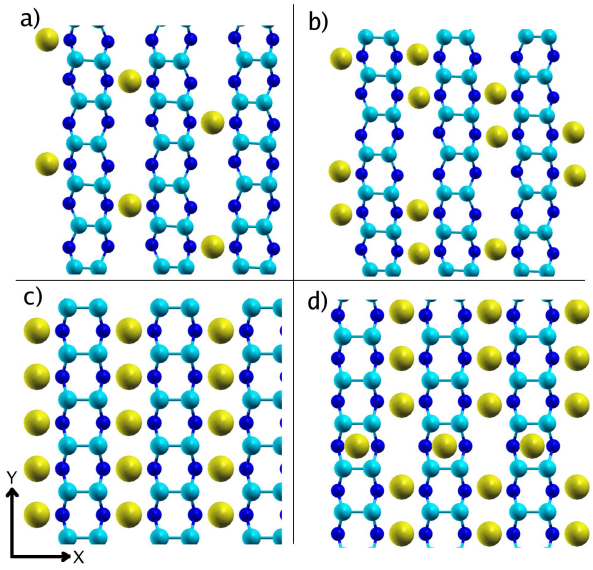

Figure 3.6: (Color online) Top view of a) 1/6 ML chain b) 1/4 ML double chain c) 1/2 ML all A site d) 1/2 ML AAAD structure. Sr are the largest atoms and are in yellow, the silicon dimers are medium sized and in light blue, and the 2nd level Si atoms are in smallest and in dark blue.

We began by searching modified dimer patterns that have similar local silicon bonding to the standard dimerized silicon surface but allow greater numbers of Sr configurations. These patterns consist of Sr atoms adsorbed on Si surfaces where all surface Si form dimers, but the dimers themselves are not arranged into rows (see Figure 3.7 for some examples). For bare silicon surfaces, these silicon patterns are all unfavorable when compared to the normal 2×1 pattern, but only by about 0.06 eV/1x1 surface area, which is small compared to typical Sr binding energies and on the order of k_bT at typical deposition temperatures (see Table 3.4 and parts of Table 3.5).

We began our search by moving every other silicon dimer out of the row alignment, creating a c(2×2) silicon reconstruction. When we placed 1/4 ML of Sr on this surface, we found an unfavorable binding energy of 3.37 eV/ Sr; however, there were several 1/2 ML structures with binding energies which were nearly competitive with

Table 3.4: Binding energies of selected modified dimer pattern structures. See Figure 3.7. All modified dimer patterns are less energetically favorable than the lowest energy 2×1 dimer reconstructions at the corresponding Sr coverages (see Table 3.3); however, they can be stabilized by entropic effects at high temperatures.

Si pattern	Sr coverage (ML)	Sr pattern	Figure	E_{bind} (eV/Sr)
2×1	1/2	A site	3.6c	3.53
c(2×2)	1/2	c(2×2)	3.7a	3.45
c(2×2)	1/2	Rows	3.7b	3.44
c(2×2)	1/2	Columns		3.02
c(2×4)	1/2	Rows	3.7c	3.48
c(2×4)	1/2	c(2×4)	3.7d	3.41
c(2×6)	1/2	AAA		3.45
c(2×6)	1/3	Rows		3.51
c(2×6)	1/3	AA		3.43
2×3	1/2	AAA_{shift}		3.42
2×3	1/2	Row+A		3.41

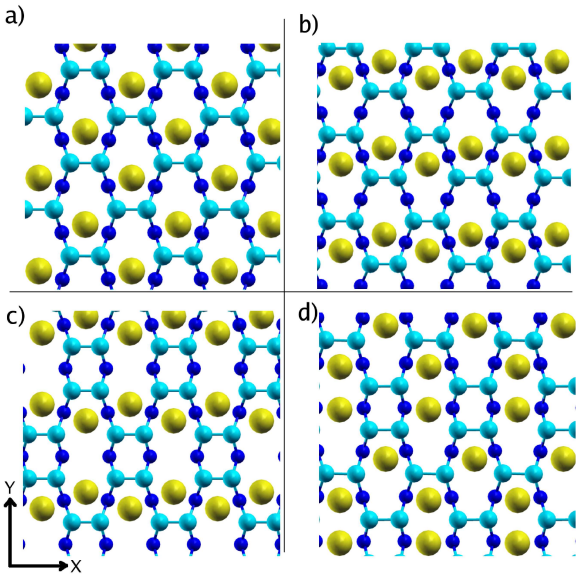

Figure 3.7: (Color online) Top view of some low energy modified dimer pattern reconstructions. a) c(2×2) silicon with 1/2 ML Sr in a c(2×2) pattern; b) c(2×2) silicon with 1/2 ML Sr in rows; c) c(2×4) silicon with 1/2 ML Sr in rows; d) 2×3 pattern with 1/2 ML Sr. Same nomenclature as Figure 3.6.

Table 3.5: Surface energies of various bare silicon reconstructions. All surface energies are given per 1x1 silicon area relative to the p(2×2) buckled dimer row reconstruction. Any submonlayer silicon is assumed to come from a bulk reservoir. All these silicon only structures considered are less stable than the p(2×2) bulked row reconstruction. The Fig. column refers to figures with the indicated silicon pattern (when Sr is removed).

Si coverage (ML)	Symmetry	Fig.	E_{surf} (eV/1x1)
0	c(2×4)	3.7c	0.07
0	c(2×6)		0.025
0	c(2×2)	3.7a	0.08
0	2×3		0.08
1/3	2×3 DV-2	3.10a	0.09
1/2	2×4 DV-2		0.09
1/2	S_a 2	3.9b	0.03
2/3	S_a 1	3.9a	0.03

the previously considered 2×1 all A site structure (see Table 3.4 and Figure 3.6).

While these c(2×2) silicon structures are less stable than the 2×1 all A structure, their geometries allow a greater number of Sr configurations than are possible when the dimers are forced to be in rows and only A sites are occupied. For instance, some combination of Figures 3.7a and 3.7b could coexist on the c(2×2) silicon surface. This configurational entropy should eventually stabilize this structural class relative to the more ordered 2×1 pattern. We made an optimistic estimate of this effect by assuming that each 1×2 surface area had 2 allowed Sr configurations with energies E_1 and E_2 that were uncorrelated with the other Sr atoms. With these simplifying assumptions, we had the following formula for the configurational free energy:

$$F_{config} = kT \ln \left(\sum_{i=1,2} \exp(-E_i/kT) \right) \tag{3.4}$$

In the limit where $E_1 = E_2 \approx$ -3.45 eV/Sr, we got the simpler formula $F = -3.45 \text{ eV} - kT\ln(2)$. This model gives a transition to the c(2×2) silicon dimer pattern at 1200^{o}C, which is much higher than the temperature where the 1×2 RHEED

reconstruction is first observed (Table 3.2).

Using the same techniques, we also investigated several other modified dimer patterns at various coverages, the most stable of which was the c(2×4) silicon configuration with 1/2 ML of Sr arranged into rows parallel to the dimers (Figure 3.7c), with a binding energy only 0.05 eV/Sr less favorable than the 2×1 all A structure. However, our simple estimate indicated that the transition to this would be above 1000^{o}C, again far too high to explain the experiments.

Encouraged by the relatively close energies of these structures, we considered the possibility that the different vibrational modes of these surface structures explained the temperature dependences observed in experiment. While most first principles calculations assume that the differences in the vibrational free energies of similar structures are negligible, the different bonding geometries combined with the possibility of low frequency modes associated with the relatively heavy Sr atoms created the possibility for strong vibrational effects.

To estimate the size of these vibrational effects, we first calculated the differences in vibrational free energy between the 1/2 ML 2×1 all A site structure and the 1/2 ML 2×1 all D site structure. We found that the contribution from the vibrational free energy favors the D site over the A site (see Figure 3.1). The free energy difference between the two structures is primarily due to the low frequency mode corresponding to Sr motion parallel to the dimers (see the lower panels of Figure 3.8 in particular). We found that the frequency of this mode is much lower for the D site than for the A site, which can be explained by the fact that D site Sr is sitting above the dimer rows so there is little to prevent it from moving parallel to the dimers. However, despite this low frequency mode, we found that at 600^{o}C, the difference in vibrational free energy is only 0.057 eV/Sr in favor of the D site which is obviously not enough to offset the 0.60 eV/Sr difference in binding energies between the structures.

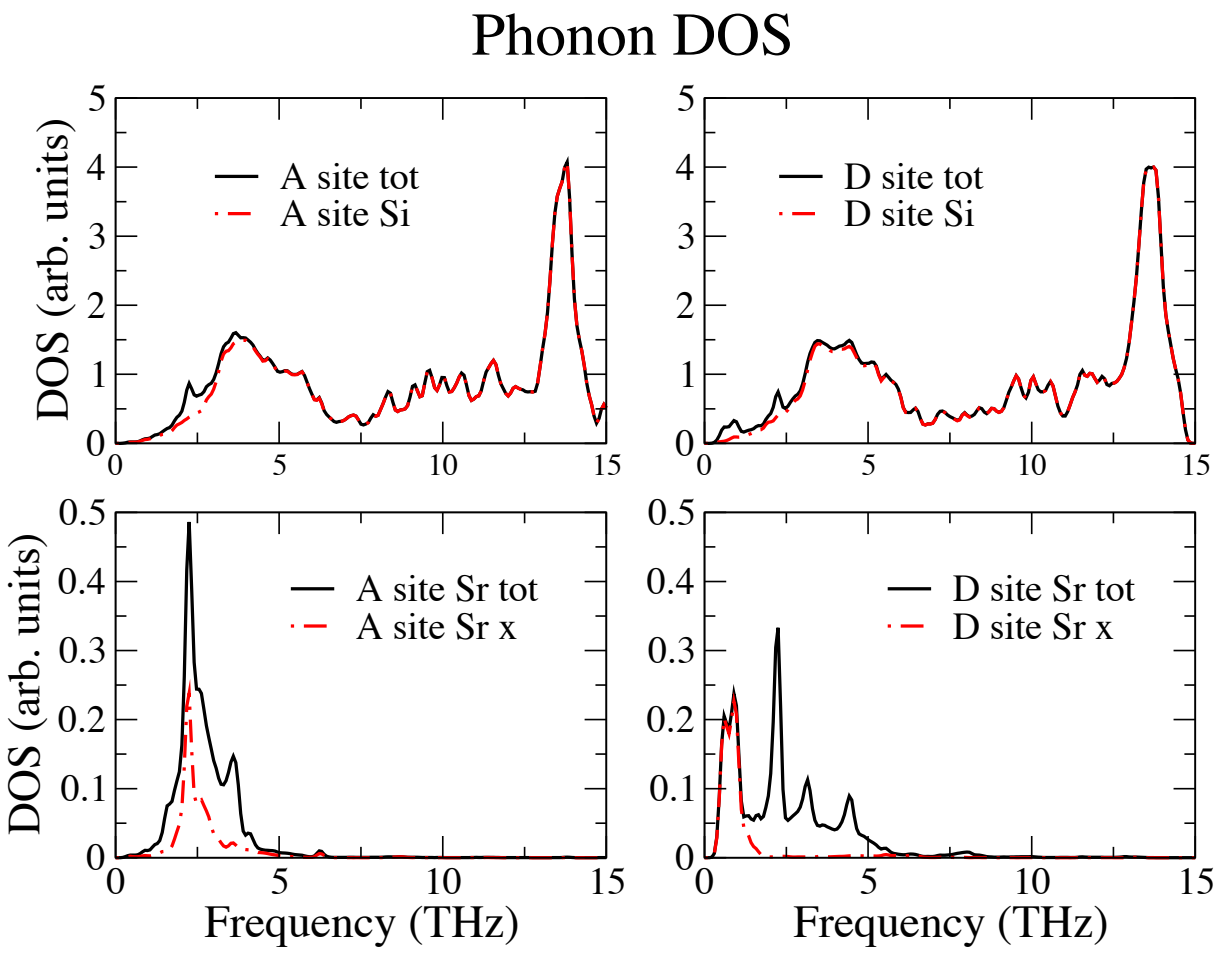

Figure 3.8: (Color online) Phonon density of states (DOS) of 1/2 ML all A and all D site surfaces with 14 layers of silicon. Top: A site (left) and D site (right) total phonon DOS (black solid) and silicon projected DOS (red dash-dotted). Bottom: A site (left) and D site (right) phonon DOS projected onto all Sr motion (black solid) and Sr x-direction motion, parallel to the dimers (red dash-dotted). The differences in the frequencies of the Sr x mode account for the majority the difference in the vibrational free energy between the A site and D site (see text).

Encouraged by the magnitude and sign of this result, we considered the differences in vibrational entropy between the 1/2 ML 2×1 all A structure and the 1/2 ML c(2×2) structure which should be typical of the bonding scheme in the modified dimer pattern structures. We found that the 2×1 all A structure is further stabilized over the modified dimer pattern by 0.047 eV/Sr at 600^{o}C due to vibrational effects.

On the basis of these test cases, we concluded that while the differences in vibrational free energy between the 2×1 all A structure and the modified dimer pattern structure are not entirely negligible compared to their binding energy differences, the effects have the wrong sign to explain the temperature dependent reconstructions observed experimentally. More generally, we expect that even for significantly different structures, the vibrational contributions to the free energy would tend to give a correction of at most 0.05 eV/Sr to the difference in ground state binding energies at typical deposition temperatures.

3.6 Mobile Silicon Reconstructions

After exploring the phase space of Sr atoms sitting on a surface with a full monolayer of silicon, we were still unable to explain the periodicity and the temperature dependence of either the 2×3 or the 1×2 reconstruction observed experimentally. Therefore, we were forced to explore surfaces with submonolayer coverages of silicon.

Structures featuring silicon atoms with less than three Si-Si bonds were quickly ruled out as very unstable, as the Sr binding energies tended to be about 2.2 eV/Sr. Additionally, any structures that created more than one Si dangling bond per 1×1 surface area were found to be very unstable. For example, a naive attempt to create a 1/2 ML Sr structure with 1×2 symmetry for the Sr atoms involves removing a column of Si dimers and replacing it with 1/2 ML Sr. However, due to the dangling

Table 3.6: Sr binding energies of submonolayer silicon S_a structures (see explanation of notation for S_a and other possible steps in Chadi [64]). Sr fill A sites, but relative to the second layer silicon. See Figure 3.9.

Si coverage (ML)	Sr coverage (ML)	Pattern	Figure	E_{bind} (eV/Sr)
2/3	1/6	2×3 A_	3.9a	3.56
2/3	1/3	2×3 AA		3.30
1/2	1/4	c(2×8) A_A	3.9b	3.58
1/2	1/4	c(2×8) AA_		3.56
1/2	3/8	c(2×8) AAA		3.42

bonds on the newly exposed second layer Si, this structure has 3 dangling bonds per 2×1 area and a correspondingly poor binding energy of 2.95 eV/Sr.

Due to these constraints, we were forced to look for structures where any exposed second layer silicon atoms were able to reconstruct into subsurface dimers. By searching structures fitting this constraint, we found two relatively stable classes of structures with submonolayer Si coverages. The first class of structures can be thought of as variations of the most stable type of single height steps (denoted as S_a by Chadi [64]). In these structures, rows of dimers are separated by areas of exposed second layer silicon atoms. The exposed silicon atoms then reconstruct into second-layer dimers, creating a 2× periodicity perpendicular to the original dimers (see Figure 3.9). While these structures are surprisingly stable, none of them are more stable than the standard dimer row structures at the same coverage, and furthermore, they quickly become unfavorable at coverages approaching 1/2 ML (compare Tables 3.6 and 3.3). Hence, we excluded these structures from further consideration.

The second structure class, on the other hand, features several structures that are more thermodynamically stable than any of those we or others considered previously. These structures are created by removing two adjacent dimers in a row (*i.e.*, removing two dimers along the original 1× or y direction), reconstructing the exposed silicon atoms into new dimers perpendicular to the original dimers, and placing a Sr atom

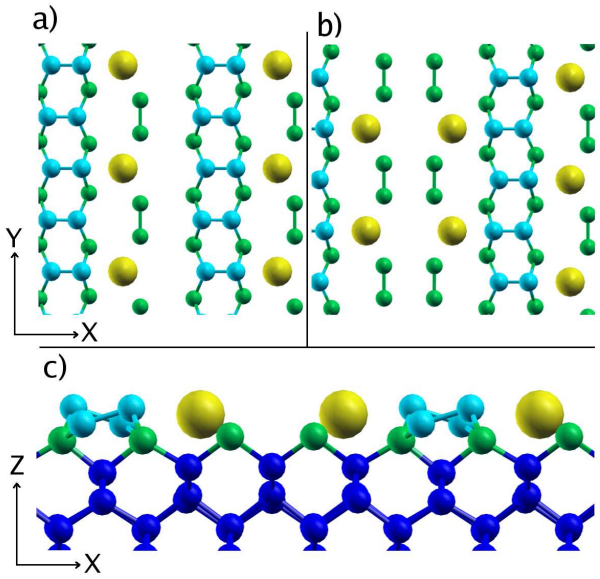

Figure 3.9: (Color online) Top and side view of selected S_a structures. a) Top view of 3×2 1/6 ML structure. b) Top view of c(8x2) 1/4 ML structure. c) Side view of 4x2 or c(8x2) 1/4 ML structure. The Sr atoms are pictured in yellow, the original silicon dimers (1/3 ML silicon) are in light blue, the second layer silicon atoms are in green, and lower level silicon are in dark blue.

in the created hole. (These structures are similar to the DV-2 dimer vacancy defect studied by Wang *et al.* [66]) In particular, both the 2×3 and c(2×6) 1/6 ML dimer vacancy reconstructions are more stable than the single chain 1/6 ML reconstruction previously considered as the most favorable (compare Tables 3.3 and 3.7). The energy differences of 0.1 eV/Sr or more between these new structure and the single chain at 1/6 ML are larger than any likely difference in vibrational free energy at deposition temperatures.

In order to understand the unusual stability of these structures, we explored the electronic density of states of these structures and were surprised to find that these 1/6 ML surfaces are insulating (see Figure 3.12). This is despite the fact that in the limit of pure ionic Sr–Si electron transfer, there are 6 dangling Si orbitals with only 8 electrons to fill them (see Figure 3.13 before interaction). In order to

Table 3.7: Sr binding energies of submonolayer silicon dimer vacancy structures. See Figure 3.10.

Si coverage (ML)	Sr coverage (ML)	Pattern	Figure	E_{bind} (eV/Sr)
1/3	1/6	c(2×6)	3.10a	3.96
1/3	1/6	2×3	3.10b	3.90
1/3	1/6	4×3		3.80
1/3	1/3	2×3		3.42
1/2	1/8	2×4		3.62

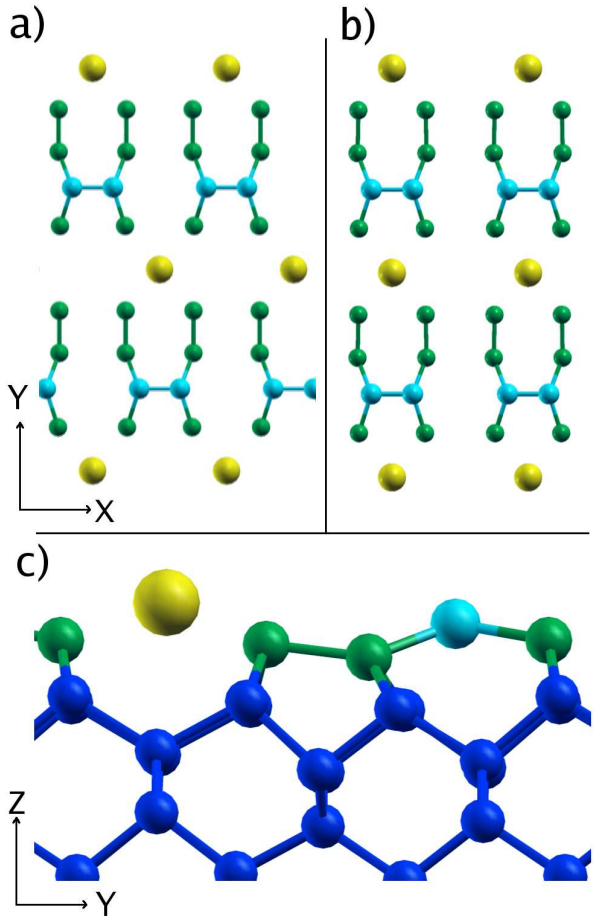

Figure 3.10: (Color online) Top view and side view of selected dimer vacancy structures. a) Top view of c(2×6) 1/6 ML structure. b) Top view of 2×3 1/6 ML structure. c) Side view of 2×3 or c(2×6) 1/6 ML structure. The Sr atom is large and yellow, the original silicon dimer (1/3 ML silicon) is in light blue, the second layer silicon atoms are in green, and lower level silicon are in dark blue.

understand this behavior, we employed maximally-localized Wannier functions to project the contributions of various orbitals to the density of states. In all of our Wannier function calculations, we used s and d Sr states. To obtain a qualitative understanding of the surface, we only added the surface silicon states. For a more quantitative understanding of the band structure and density of states, we added an sp^3 basis for the surface and subsurface silicon in our calculations.

We found that the Sr s and d states (Figure 3.11D) interact strongly with the orbitals belonging to the four Si atoms surrounding the Sr atom (Figures 3.11A and 3.11B). This interaction pushes these Sr states much higher in energy and so these Sr-derived states donate their electrons to the Si-derived orbitals (note the red curve in Figure 3.12 that shows some hybridization below the Fermi level). Figure 3.13 shows a schematic explanation of the energy levels and Figure 3.12 displays the density of states.

More surprisingly, we found that the dangling bond states on the original surface dimer were rather high energy unoccupied states with strong p_z character (Figure 3.11C). This effect is due to a significant flattening of the original dimer: the dimer unbuckles and both atoms move closer to the surface due to the stretching of neighboring bonds. This results in a planar sp^2-like bonding scheme with a high energy dangling p_z-like state. These p_z-like states also donate their electrons to the second layer Si dangling orbitals, which opens a band gap: see the magenta line in Figure 3.12, which is pushed above the Fermi level, and the schematic picture in Figure 3.13. The band gap is widened by the very strong interaction between the dangling Si states (Figure 3.11A) and the original dimer states (Figure 3.11C). This electron donation and interaction by the original surface dimer accounts for the unexpected electronic structure.

While these 1/6 ML structures are thermodynamically stable, their formation will

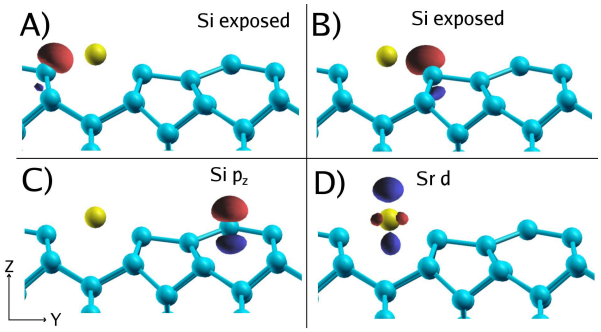

Figure 3.11: (Color online) Side view of 2×3 1/6 ML dimer vacancy structure with Wannier functions of selected surface states when using the minimal basis for the Si surface. Red and blue lobes show positive and negative isosurfaces of the Wannier functions. A) and B): dangling orbitals of exposed silicon atoms adjacent to the Sr. C): unoccupied p_z state on the original surface dimer. D): one of many unoccupied Sr d-character states.

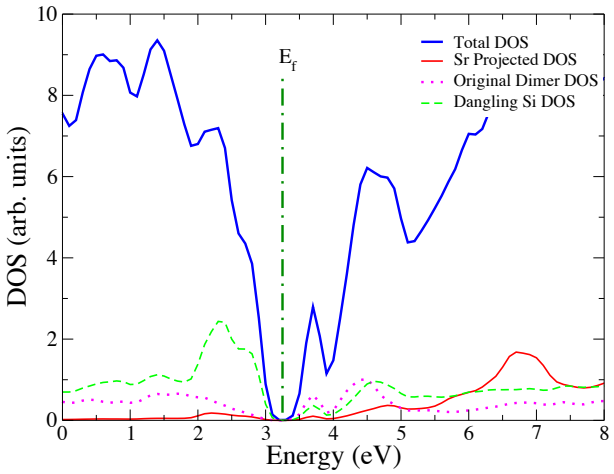

Figure 3.12: (Color online) Electronic density of states (DOS) for the 2×3 1/6 ML Sr structure, projected using Wannier functions with an sp^3 basis for the silicon. See Figure 3.13 for a schematic explanation. The upper solid blue line is the total DOS, the lower solid red line is Sr projected DOS (Figure 3.11D), the dashed green line is exposed silicon projected DOS (Figures 3.11A and B), and the dotted magenta line is the original dimer projected DOS (Figure 3.11C).

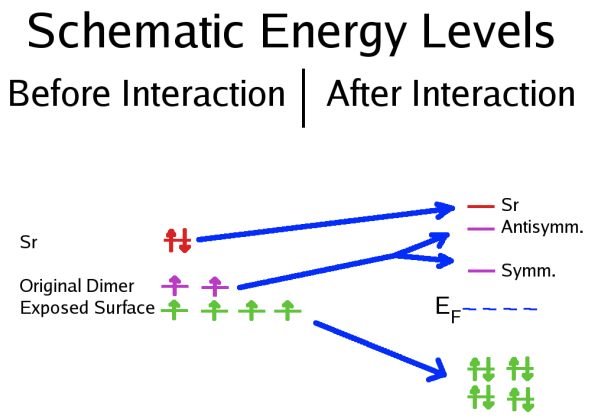

Figure 3.13: (Color online) Schematic Energy Level diagram for 2×3 1/6 ML structure. Strong interactions push the exposed surface silicon levels (Figures 3.11A and 3.11B) down in energy and the Sr (Figure 3.11D) and original dimer (Figure 3.11C) levels up. The original dimer levels also form symmetric and antisymmetric combinations, while the exposed surface atoms interact and form low energy occupied bands. See Figure 3.12, which has matching colors, for the projected DOS, and Figure 3.11 for real space plots of the Wannier functions.

Table 3.8: . Nudged elastic band and simple transition state theory results. We calculated the energy barrier to break a silicon dimer and used simple transition state theory to estimate the rate at both low and high deposition temperatures. See Figure 3.14.

Sr coverage (ML)	$E_{barrier}$ (eV)	Rate at 0^oC (Hz)	Rate at 600^oC (Hz)
0	1.29	7×10^{-12}	2×10^5
1/4	0.92	5×10^{-5}	2×10^7
1/2	0.63	1×10^2	1×10^9

be suppressed at low temperatures by the kinetic barrier required to move 2/3 ML of silicon from the surface to step edges, where it can join the bulk silicon. Because silicon adatoms are mobile at typical deposition temperatures, [67] we expected that the energy barrier to break a dimer should provide an order of magnitude estimate for this kinetic barrier. We performed Nudged Elastic Band calculations of a dimer breaking on the surface with various Sr coverages (see Table 3.8 and Figure 3.15). All of our calculations were done in a 2×2 surface cell with the silicon beginning in dimer rows (see Figure 3.14). Next, one of the dimer bonds broke as its two silicon atoms move apart. Once the silicon atoms passed the transition state where the bond was broken, they reformed into a c(2×2) pattern due to the periodic boundary conditions. We preformed this calculation with no Sr, one Sr in an A site, and two Sr — one in an A site and one in a D site (see Figure 3.2). We found that the barriers are large (0.5-1.0 eV) compared to the relevant thermal energy scales and that the barriers were greatly reduced by the presence of Sr (see Table 3.8). We attribute this lowering to the electrons from the Sr atom passivating the dangling Si orbitals present in the transition state and thus reducing its energy.

By using simple transition state theory, we could make an estimate of the rate of dimer breaking, which was our rate limiting step (see Table 3.8). Our estimate for the prefactor for our transition state theory calculations was 4×10^{12} Hz, which we calculated to be a typical frequency of a dimer vibrating in the x direction.

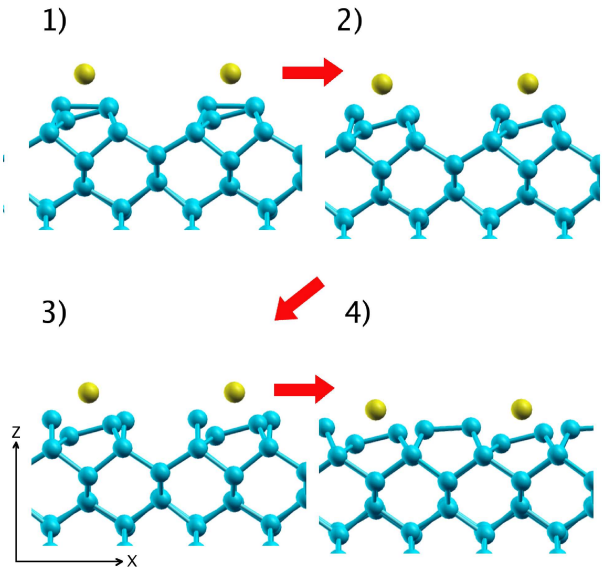

Figure 3.14: (Color online) Transition from silicon 2×1 dimer pattern to c(2×2) pattern with 1/4 ML Sr on surface. The silicon begins in a 2×1 dimer pattern, which is a local minimum, in 1). The dimer breaks in 2) and continues to the transition state in 3). Due to periodic boundary conditions, the dimer then reforms in 4) in the c(2×2) pattern, another local minimum. On a real surface, the now separate silicon adatoms would be able to diffuse freely after 3). The energy barrier for this process is 0.92 eV.

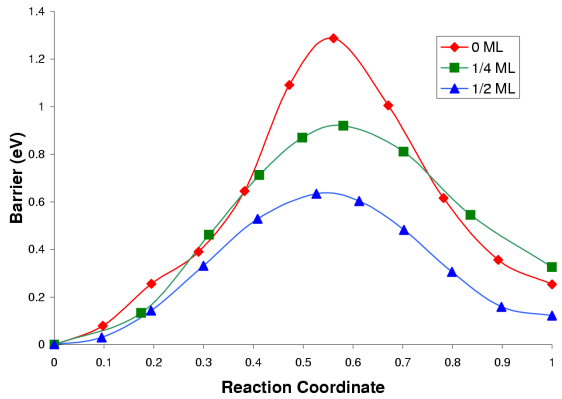

Figure 3.15: (Color online) Energy barrier versus reaction coordinate for Nudged Elastic Band calculations of dimer breaking (see Figure 3.14 and Table 3.8). Red diamonds are for the bare silicon surface, green squares are for 1/4 ML Sr on surface, and blue triangles are for 1/2 ML Sr. The lines are guides for the eye. The reaction coordinate goes from 0, where the dimer is in its equilibrium position, through the transition state near 0.5 and continues to 1, where the dimer atoms recombine with periodic copies into a metastable modified dimer row structure.

By comparing these rates to an average experimental deposition time of one minute, we could determine whether the silicon was mobile at any given temperature. According to the rates in Table 3.8, we expect that the surface silicon should be frozen for room temperature deposition but highly mobile at 600^{o}C. Also, by looking at the variation of energy barriers with coverage, we find that submonolayer coverages of Sr on Si strongly encourage the motion of silicon on the surface (see Figures 3.15).

3.7 Explanation of Experimental Growth

With the addition of the results on mobile silicon surfaces (section 3.6), we can now understand and explain the symmetries observed during Sr deposition under both high temperature and low temperature conditions. Figure 3.16 shows a schematic that organizes the discussion. Both high and low temperature depositions begin with a 2×1 dimer pattern on the bare silicon surface. At low temperatures, in accordance with our dimer breaking rate results, this dimer pattern is frozen in place and the Sr sit on top of the dimerized surface and settle into A sites. We expect these A sites to arrange themselves locally into the single chain structure at 1/6 ML and the double chain structure at 1/4 ML. However, both of these patterns will be disordered, explaining the lack of a coherent diffraction pattern at these coverages. When the Sr coverage reaches 1/2 ML, all the A sites will be filled, and the surface will display a 2×1 reconstruction consistent with experiment.

On the other hand, when the deposition is conducted at high temperature, the surface will not be frozen into a dimer pattern. In particular, as a coverage of 1/6 ML of Sr is approached, we expect the surface to transition into one of the low energy dimer vacancy patterns with 2/3 of the silicon dimers moving to step edges (see Figure 3.16). While our lowest energy 1/6 ML structure has a c(2×6) reconstruction,

the very similar 2×3 reconstruction is only 0.06 eV/Sr less stable (see Table 3.7) and matches the experimental observations.[10, 63] We speculate that the 2×3 structure is stabilized experimentally due to step edge effects, as the step edges appear straight in STM images,[63] which is incompatible with a c(2×6) reconstruction. These step edge effects will be especially large for the 4 degree miscut silicon wafers used in RHEED experiments[10] since these wafers have terraces that are only 10 silicon (001) unit cells wide.

As Sr coverage is further increased at high temperatures, the extra Sr will begin to form patches of the 1/4 ML double chain reconstruction (see Figures 3.6 and 3.16). As these patches of 1/4 ML dimerized surface grow, the remaining 1/3 ML of silicon must also move to step edges. When this process is complete, one full monolayer of silicon has been removed from the surface, and the dimers will now be oriented perpendicular to the original surface dimers, accounting for the observed 1×2 surface symmetry. As more Sr is deposited, from 1/4 ML to 1/2 ML, the double chain patches will change continuously into 1/2 ML all A site patches. Therefore, the high temperature 1/2 ML reconstruction will have the same atomic structure as the low temperature 1/2 ML reconstruction but rotated 90 degrees with respect to the original dimers. The rotation simply reflects the geometry of bulk Si: atoms in successive (001) planes have identical surroundings except for a 90 degree rotation around [001].

Since the low and high temperature reconstructions are identical up to a rotation, it should be possible to grow an oxide on both surfaces equally well. In order to investigate this possibility, our colleagues grew BaO on both the high temperature 1×2 and low temperature 2×1 1/2 ML Sr template layers.[10] As expected, both template layers promoted excellent epitaxy between the Si and BaO. This experimentally demonstrates that the 2×1 and 1×2 1/2 ML Sr surfaces are physically identical.

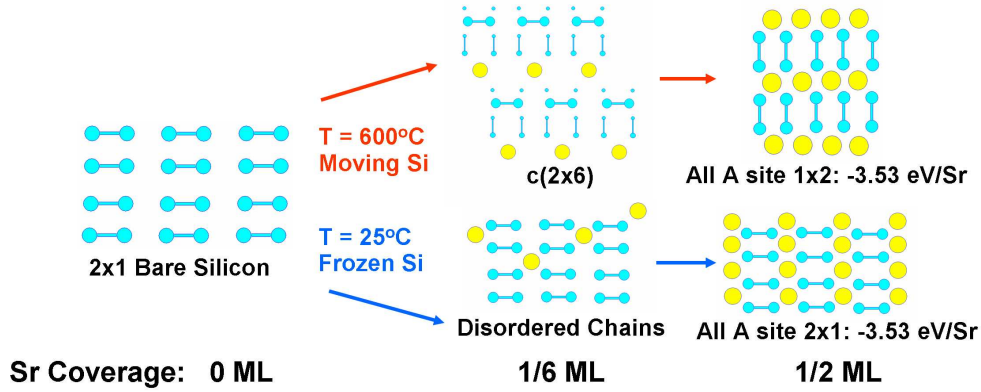

Figure 3.16: (Color online) Schematic phase diagram of submonolayer Sr on Si (001). Each diagram shows a top view of the surface with silicon surface atoms and dimers in light blue and the larger Sr in yellow. Both the low and high temperature systems begin with a 2×1 dimerized bare silicon surface, but as Sr coverage increases they follow different paths. At 600°C, the silicon is free to move on the surface, and the surface remains in thermodynamic equilibrium. However, at 25°C, silicon motion is prevented by a kinetic barrier, and the lowest energy dimerized surface structure is formed.

Furthermore, a sample grown at an intermediate temperature which displayed an incomplete transition to the 2×3 pattern displayed poor epitaxy. We believe this is caused by the intermediate temperature template layer failing to change completely from a 2×1 to a 1×2 dimer pattern, which prevents large scale epitaxy. These experiments both confirm our calculations and demonstrate a previously unknown low temperature path to silicon epitaxy.

3.8 Simulated STM and XRD

A recent paper by Du *et al.*[63] features high resolution scanning tunneling microscopy images of the 2×3 1/6 ML Sr on Si (001) surface as well as a proposal for its atomic structure based on DFT calculations. We considered that proposed theoretical structure, and we found that its binding energy was 1.93 eV/Sr, which is

considerably less stable than any of the 1/6 ML structures considered in this work (compare to Table 3.7). We also computed simulated STM images using the method of Tersoff and Hamann[68, 69] to compare with the experimental images. We found very good agreement between our low energy 2×3 dimer vacancy structure (Table 3.7 and Figure 3.10) and the experimental STM images, and also similar images for the Ba on Si system.[70, 71]

In agreement with experiment, our filled state image (Figure 3.17a) had a single large protrusion, which corresponded to the four filled Si dangling bonds surrounding the Sr atom, which were too close together to be resolved experimentally. Wannier function plots of these states can be seen in Figures 3.11A and B. Also in agreement with Du *et al.*,[63] the shape of this protrusion depended only weakly on the applied tip-sample bias.

In contrast to the filled state image, but also in agreement with experiment, our empty state images (see Figures 3.17b-d) had two protrusions. One of these protrusions corresponded to the empty p_z orbitals on the original dimer, which are depicted in Figure 3.11C. The other protrusion corresponded to the empty Sr s and d states, one of which is shown in Figure 3.11D. The relative size and shape of these two protrusions depended sensitively on the applied bias (compare Figures 3.17b/c/d). This behavior can be understood by looking at the projected electronic density of states (Figure 3.12). At low bias (0.5 V in our theory and 1.0 V in experiment), the image is dominated by the empty p_z orbitals, which form the majority of the bottom of the conduction band (see Figure 3.12). However, at higher bias, the image is dominated by the Sr orbitals, which are higher in energy and extend further from the surface than the p_z orbitals. Additionally, the protrusion corresponding to the empty Sr states changes shape from elliptical at low bias to circular at high bias (compare Figures 3.17b and 3.17d). Both this change in brightness and the change

in shape agrees with the experimental images of Du *et al.*[63] All qualitative features of the calculated STM images, including the image shapes and bias dependence, agree with the experimental images, which provides further proof that our 1/6 ML 2×3 dimer vacancy structure is the experimentally observed structure.

Quantitatively, the change in ellipticity in the images happens at approximately 0.5 V lower bias in our theoretical calculations than in the experimental images. We attribute this fact to the well-known underestimation of the band gap in DFT calculations. In our calculation, the band gap of silicon is only 0.6 eV, as compared to the experimental value of 1.2 eV. We believe that this is the reason for the ≈ 0.5 V offset in conduction band features between theory and experiment.

In another experimental work, our experimental collaborators J. W. Reiner, Y. Segal, H. Hong, C. H. Ahn, and F. J. Walker measured anomalous synchrotron x-ray diffraction (XRD) from the 1/6 ML Sr on Si structure for deposition at both 25°C, where we expect to find a stoichiometric Si surface with chains, and at 650°C, where we expect to find the 2×3 DV structure.[72] While a complete structural determination is not possible, they find results consistent with our calculated structures.

3.9 1.0 ML Silicide Structures

In addition to the 0.5 ML Sr on Si structure, > 0.5 ML Sr on Si structures are used in growth procedures for Sr on Si.[6, 52, 53, 60, 10] Normally, 0.5 ML Sr is deposited at high temperature, and then another 0.5 ML is deposited at low temperature, which is believed to prevent the formation of Sr silicides[52]. This need to prevent silicide formation is initially surprising, as according to our naive electron counting arguments, the 1×1 1.0 ML Sr structure in Fig. 3.18a should be stable and semiconducting. This is because each surface Si, which is in a bulk-like 1×1 configuration with no dimer

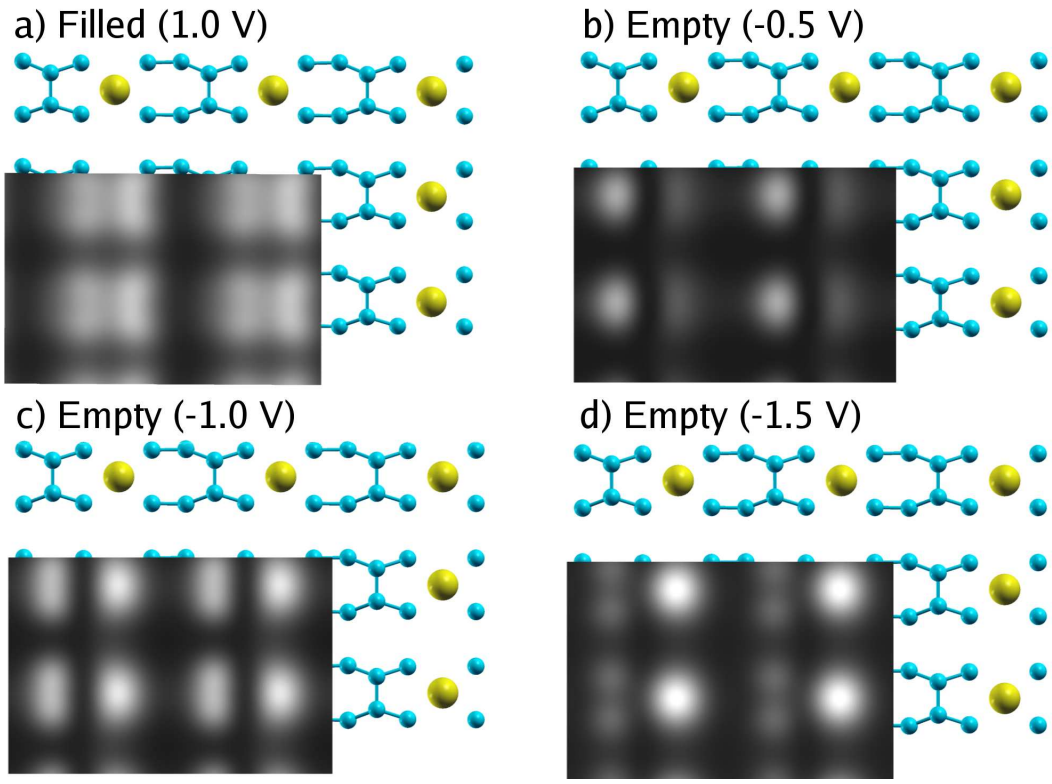

Figure 3.17: (Color online) Simulated STM images of the 2×3 dimer vacancy structure (Figure 3.10) overlayed on atomic coordinates. a) Filled states at 1.0 V bias. b-d) Empty states at -0.5 V, -1.0 V, and -1.5 V, respectively. The images show the local density of states integrated from the Fermi level to the desired voltage at a constant height of about 5 Å above the surface. The scale runs linearly from zero intensity (black) to the maximum value at the chosen height (white).

Table 3.9: . Binding Energy per Sr of 1.0 ML structures (See Fig. 3.18).

Symmetry	Si coverage (ML)	E_{bind} (eV/Sr)	Fig.
1×1	0.0	2.63	3.18a
2×1	0.0	2.71	3.18b
2×2	0.25	2.86	
2×2	0.5	2.88	3.18d

bond, has two dangling bonds, and each Sr can donate two electrons to the surface. However, this surface is actually metallic, as the Sr are too close together (3.86 Å, versus 4.31 Å in bulk Sr), and the normally empty Sr valence bands cross the filled surface Si bands. In fact, the surface can lower its energy by forming surface dimers, which reduces the distance between Sr in the x direction (see Fig. 3.18b and table 3.9). The most stable structure with a stoichiometric Si surface is either a 3×1 or 4×1 combination of the the two structural motifs in Figs. 3.18a-b.[57]

The fact that the 2×1 1.0 ML Sr structure (Fig. 3.18b) is relatively stable, despite the excess of electrons which are forced to remain in high energy Sr states, suggests that we could lower the energy of the system by adding Si atoms to the surface, creating additional low energy electron acceptors. As shown in table 3.9 (see Fig. 3.18c), this is the case since structures with either 1/4 ML or 1/2 ML added Si atoms are more stable the 2×1 structure with no added Si. These extra Si, which have 4 valence electrons, form a covalent bond with the Si below them. This passivates one dangling surface bond by creating a filled bonding and empty anti-bonding state, and allows the surface with extra Si to accept two additional electrons, relative to the original Si surface.

These structures with extra Si on the surface show that silicide formation, which will impede oxide epitaxy of Si, will begin thermodynamically for Sr coverages at or above 1.0 ML. Therefore, care must be taken when growing oxides on a Sr template layer to avoid heating the system when coverages of Sr exceed 0.5 ML in order

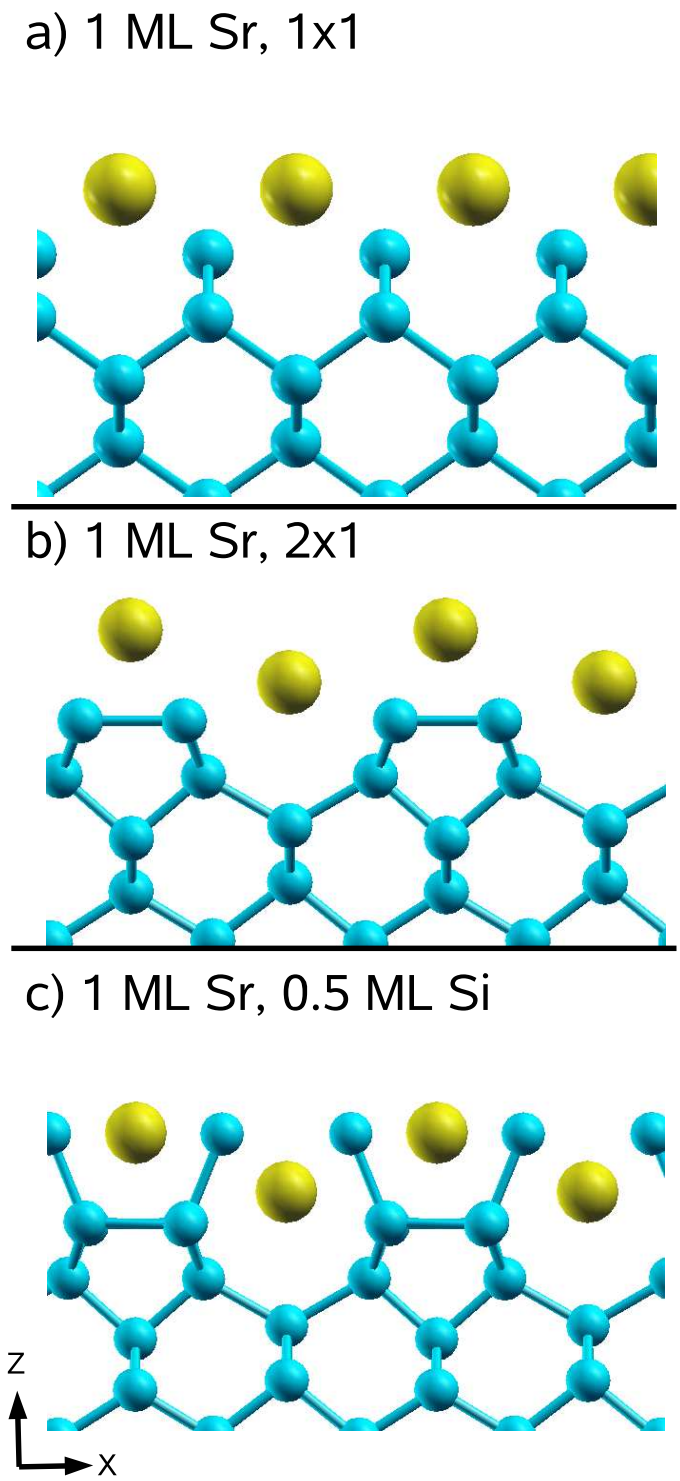

Figure 3.18: (Color online) Side view of 1 ML Sr on Si structures (see table 3.9). a) 1 ML Sr 1×1 b) 1 ML Sr 2×1 c) 1 ML Sr 2×2 + 0.5 ML Si, in a $c(2\times2)$ configuration.

to impede silicide formation kinetically, as can be done with the 1/6 ML silicide structure.[10] Similar structures with extra Si on the surface are more important for transition metals like La which have more valence electrons than Sr and which begin to form silicides at lower coverage (see Chapter 6).

3.10 Conclusions

We have presented the surface reconstructions of submonolayer coverages of Sr on Si (001) at both low and high deposition temperatures. Our findings explain the previously unknown 2×3 reconstruction observed experimentally at high temperature and 1/6 ML Sr coverage. This structure, which agrees with RHEED, STM, and XRD data, is key to understanding the effects of temperature on the 1/2 ML phase, which is important in epitaxial oxide growth. At low temperatures, this 1/2 ML phase is created by filling Sr into spaces between the dimer rows, which remain intact. At high temperatures, the formation of the 2×3 phase at 1/6 ML Sr coverage disrupts the original dimer pattern and forces the motion of 2/3 of the surface Si to step edges. The deposition of additional Sr causes the rest of the original surface Si layer to move to the step edges and a dimer pattern to reform on the now exposed second silicon layer. This new dimer pattern is rotated 90 degrees relative to the original dimers since an entire monolayer of silicon has moved.

In addition, we have presented low energy Sr-silicide structures at 1.0 ML Sr coverage, demonstrating that silicide formation must be prevented kinetically for coverages of 1 ML Sr or higher. This result explains the need for low temperatures during high coverage Sr deposition, and has implications for improving growth procedures.

Understanding this process has clarified the role of temperature in the deposition

of epitaxial oxides on Si (001) and has predicted an experimentally verified low temperature path to oxide epitaxy on Si. Further work must be done to compare the quality of the interfaces achieved via the low temperature and high temperature deposition paths. Furthermore, understanding the reconstructions of Sr on Si at the atomic level helps explain the role of Sr in promoting oxide epitaxy on Si and provides important information for future work on oxide epitaxy on Si.

Chapter 4

Phase Transition of Sr on Si (001)

4.1 Introduction

A unique feature of the epitaxial growth of oxides on Si (001) is the formation of a reconstructed submonolayer alkaline earth metal layer (usually Sr) on the clean Si surface that occurs before deposition of the oxide itself [52]. The structure and kinetics of this phase have been the subject of much attention [57, 54]. Recently, it was shown that there are two deposition paths for Sr on Si (001) which depend on the deposition temperature[73, 10, 74] (see also Chapter 3). In both cases, the Si surface begins in its canonical 2×1 dimerized pattern. At temperatures from 0°C to 400°C, the Si is kinetically limited, and Sr adatoms bind to the valleys between Sr dimer rows. This process continues until all the low energy binding sites are filled at 1/2 ML, and the surface still has 2×1 symmetry due to the Si dimers. On the other hand, at temperatures from 400°C to 600°C, Si motion is not kinetically limited. The surface again starts with 2×1 symmetry; however, as the Sr coverage is increased, an ordered 2×3 phase is observed at 1/6 monolayer (ML) coverage, which then is replaced by a 1×2 phase at 1/2 ML. The 2×3 structure results from a reorganization

of the Si surface catalyzed by the Sr adatoms and is the thermodynamic ground-state at 1/6 ML. This phase was identified using RHEED[52, 60, 10], and it has also been studied with scanning tunneling microscopy (STM)[62, 63] and x-ray diffraction (XRD)[72]. In our recent density functional theory work[73], we provide details of the structures which explain the RHEED data up to 600°C as well as simulated STM images of the 2×3 structure, which are in good agreement with experiment.

Understanding of these two pathways for Sr deposition on Si (001) has provided two experimentally verified routes for creating an appropriate template layer for oxide epitaxy [10, 74]. In the low temperature (0–400°C) deposition route, the Si dimers remain in place, and the oxide is grown on a 2×1 template layer. In the high temperature (400-600°C) route, the initial Si dimers are replaced by the 2×3 structure at 1/6 ML, and then rearranged again into a 1×2 structure at 1/2 ML, which also provides a template for oxide growth.

Our aim is to predict and understand the temperature-coverage phase diagram in the high temperature region, 500-800°C (see Fig. 4.4), for the interesting and important Si/Sr surface system. In particular, we wish to understand the order-disorder transition near 1/6 ML between the ordered 2×3 phase and a disordered lattice gas, which consists of Sr adatoms distributed with no long-range order on top of a dimerized Si surface. In order to model the transition, we use first principles density functional theory (DFT) to analyze the surface chemistry and grand canonical Monte Carlo methods to evaluate the thermodynamics. We also use reflection high energy electron diffraction (RHEED) to map out the transition and show quantitative agreement with theory.

4.2 Lattice gas Hamiltonian

First principles results and experiments show that the ground state of Sr on Si (100) has an interesting behavior versus Sr coverage: For coverages below 1/6 ML, the Si surfaces is the usual 2×1 dimerized one with the Sr forming disordered chains (a lattice gas); however at 1/6 ML the ground state changes to an ordered 2×3 structure (formed by creating dimer vacancies) [10, 73]. Although not relevant to our present work, a kinetic barrier to the Si motion prevents the formation of the 2×3 structure unless the temperature is above 400°C. In this work, we are concerned with the behavior of the surface at higher temperatures and for Sr coverages close to 1/6 ML. Therefore, it is safe to assume that the system will be in thermal equilibrium. For temperatures below 500°C, we expect the lower energy 2×3 phase to dominate. However, as we discuss below, this phase has a very low entropy because perturbations to it cost a great deal of energy. On the other hand, while structures with Sr chains on a 2×1 surface have higher energy than the 2×3 structure, the configurational entropy for the Sr leads to a much larger entropic contribution to the free energy. Thus we expect a phase transition between the ordered 2×3 and the 2×1 lattice gas phases as temperature is raised for coverages close to 1/6 ML Sr.

Calculating the thermodynamics of dimerized Si with Sr adatoms requires sampling the canonical distribution for all the possible configurations accessible to the Sr lattice gas. Preferably, one should compute the energy of each configuration from first principles, but due to disorder and the large simulation cells required, this is impractical with current computational methods and infrastructure. Therefore, we resort to using a model lattice gas Hamiltonian which can be evaluated over many Sr configurations. The form chosen for the Hamiltonian, as well as its key parameters, are dictated from first principles results (next section), with no fitting parameters.

In our lattice gas Hamiltonian, we consider only the Sr degrees of freedom, with the surface Si remaining in a 2×1 dimerized configuration, as we find that all isolated defects of the Si surface are high in energy. For example, a Sr atom in an isolated unit cell of the 2×3 structure on an otherwise 2×1 dimerized silicon surface has a binding energy of 3.60 eV, which is significantly less favorable than the lattice gas, which has a typical binding energy 3.75 eV/Sr. The form for our model Hamiltonian H_{LG} is an anisotropic interacting coverage dependent lattice gas model where each Sr binding site i on the dimerized Si surface has occupancy n_i where $n_i = 0, 1$:

$$H_{LG} = \sum_i n_i \left[\epsilon_i + \sum_\alpha J_\alpha(z_i) n_{i+\alpha} + E_i^{Si} \right], \tag{4.1}$$

$$z_i = \sum_\alpha n_{i+\alpha}\,. \tag{4.2}$$

The lattice is rectangular so each lattice site i has eight nearest neighbors, and α ranges over the intersite vectors. Specifically, for any site i with integer coordinates (x, y), α ranges over the eight vectors $\pm(1, 0)$, $\pm(0, 1)$, $\pm(1, 1)$, and $\pm(1, -1)$. The number of occupied nearest neighbor sites for i is z_i. The nearest neighbor interactions $J_\alpha(z_i)$ are anisotropic. Due to rectangular symmetry, there are only three independent interactions $J_{10}(z_i)$, $J_{01}(z_i)$, and $J_{11}(z_i)$, and they depend on the local coverage (z_i) (see Fig. 4.1 for examples).In addition to the Sr site interaction terms, there is an additional term, E_i^{Si}, which imposes an energy cost for every instance of two Sr atoms with a single unoccupied site between them in y direction. The physical origin of this term is that this configuration frustrates the Si dimer buckling, as discussed below (see also Fig. 4.1).

In order to find the phase transition between our lattice gas model and the ordered 2×3 structure as a function of temperature and coverage, we evaluate the grand

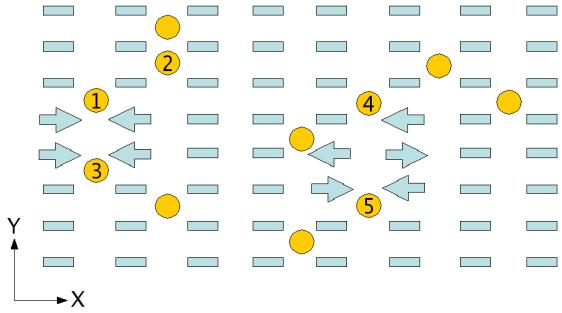

Figure 4.1: Schematic top view of a typical lattice gas configuration. All Sr atoms (yellow circles) are in the A binding sites (see Fig. 4.2 and section 4.3) between the Si dimers (light blue rectangles and arrows). The Sr labeled 1 has a single corner nearest neighbor, and the Sr labeled 2 has both a corner nearest neighbor and a nearest neighbor in the y direction. Most dimers are buckled, but are shown as flat for simplicity, and arrows are used to highlight particular buckling. The cluster of arrows on the left show dimers pinned in an unfavorable configuration by Sr atoms 1 and 3. The cluster of arrows in the center show that the dimers between Sr 4 and Sr 5 can have the more energetically favorable alternate-buckling pattern.

canonical partition function for the lattice gas,

$$Z = \sum_{\{n_i\}} \exp\Big[-(H_{LG}[n_i] - \mu_{2\times3} N[n_i])/k_b T \Big], \tag{4.3}$$

$$N[n_i] = \sum_i n_i \tag{4.4}$$

where k_b is Boltzmann's constant, T is the temperature, the sum is over all possible combinations of n_i, and the Sr chemical potential, $\mu_{2\times3}$, is set to the binding energy per Sr of the 2×3 1/6 ML structure. We choose $\mu_{2\times3}$ to be temperature independent because excitations of the 2×3 structure are much higher in energy than $k_b T$ for temperatures considered in this work (see below).

Due to the relatively long-ranged and coverage-dependent anisotropic interactions in the model Hamiltonian, the grand canonical partition function cannot be summed

exactly. However, this model lends itself to grand canonical Monte Carlo analysis using the Metropolis algorithm to sample the partition function[48, 49]. We find that the correlation function between Sr adatoms on the surface decays exponentially with a correlation length of approximately two lattice constants at the temperatures and coverages of interest. As a result, we can safely run our calculations in a 30×30 lattice with periodic boundary conditions. We sample our partition functions until the sampling error is much smaller than all other uncertainties.

We use Monte Carlo sampling to determine, as a function of temperature, the coverage of the lattice gas in equilibrium with the 2×3 structure. This set of coverages and temperatures, which forms the phase boundary between the 2×3 structure and the lattice gas, is plotted in Fig. 4.4.

4.3 *Ab initio* calculations and parameter extraction

We use first principles theory to determine the structure and energetics of a variety of stable Sr on Si (001) configurations in order to extract the parameters for the lattice gas Hamiltonian. Binding geometries and energies are obtained using density functional theory [20, 21], the details of which are presented elsewhere [10, 73]. Briefly, we employ a plane wave basis set, norm-conserving Troullier-Martins pseudopotentials [34], and the PBE GGA exchange-correlation functional. Calculations are run at the theoretical lattice constant of silicon, which we find to be 5.456 Å. We use a slab geometry, with periodic boundary conditions in the x and y directions and a finite thickness in the z direction, which is the (001) direction of the Si crystal. The z direction is the surface normal; x is the direction in which a clean Si (001) surface doubles its periodicity by dimerizing; and y is orthogonal to x and z.

We begin with isolated Sr adatoms. They adsorb on the standard dimerized Si

surface in two inequivalent sites, called site A and site D [57] (as shown in Fig. 4.2a and Table 4.1). Site A, where Sr sits in the trough between dimer rows, is most stable, with a binding energy of 3.64 eV. Site D is 0.41 eV less stable. As a result, we expect all the Sr atoms to occupy A sites at low coverages, and the sites i in our lattice gas thus only range over the rectangular array of A sites.

The bonding between the surface and Sr involves primarily charge transfer from the Sr adatom to the dangling bonds of a neighboring Si dimer [57]. This means that other positively charged Sr adatoms prefer to sit near the now negatively charged silicon dimer, creating correlations between Sr atoms at low coverage. This is evident in Table 4.1 and Fig. 4.2d, which show the interaction between two otherwise isolated Sr adatoms. The interaction between Sr adatoms in neighboring binding sites is both highly directional and much larger than k_bT=0.075 eV at 600°C (a typical deposition temperature). The strong Sr-Sr interaction makes a simple non-interacting model inadequate, and we thus resort to an anisotropic lattice gas Hamiltonian.

With increasing Sr coverage, the highly directional interactions between neighboring Sr atoms persist, but their strengths change with coverage. As with lower coverages, corner nearest neighbors are preferred at 1/6 ML (Table 4.1 and Fig. 4.3). In agreement with these predictions, scanning tunneling microscopy measurements show a diagonal chain structure adsorption pattern at low coverages [62]. In addition to the electrostatic correlations between neighboring Sr adatoms, we find another longer range interaction which causes the surface to avoid a single unoccupied site between Sr atoms in the y direction (E_i^{si} in the model Hamiltonian). This is due to the natural buckling of the silicon dimers; they are frustrated from reaching their preferred alternate buckling reconstruction if second nearest neighbor Sr sites in the y direction are occupied (see Fig. 4.1 as an example). Based on these Sr-Sr interactions, we expect a lattice gas with short range correlations between Sr atoms, but

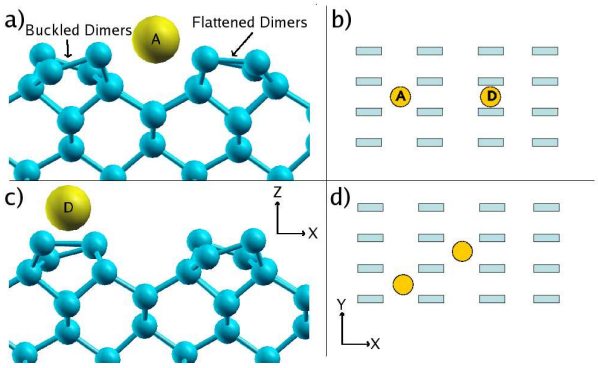

Figure 4.2: a) Side view of a Sr atom (yellow) on Si (001) surface in the A site. Both buckled and flattened dimers are labeled. b) Schematic top view of Sr (yellow circles) in both A and D sites on surface with Si dimers (light blue rectangles). c) Side view of the higher energy D binding site. d) Schematic top view of two otherwise isolated Sr atoms that are diagonal nearest neighbors. See Table 4.1 for energies. Dimer buckling is captured in the calculations, but not shown in the schematics for simplicity.

no long range order at finite temperatures.

As detailed elsewhere [73, 10], while the 1/6 ML chain structure discussed above is the lowest energy Sr adatom configuration on the dimerized Sr surface, it is not the ground state of the system. The lowest energy structure at 1/6 ML Sr coverage has a different Si bonding scheme: it is formed by removing 2/3 of the Si dimers in every dimer row, reconstructing the now exposed second layer Si atoms into subsurface

Sr configuration	Figure	E_{bind} (eV/Sr)
Isolated A site	4.2b	3.64
Isolated D site	4.2b	3.23
x dimer		3.65
Diagonal dimer	4.2d	3.83
y dimer		3.79
$\frac{1}{6}$ ML rows	4.3a	3.48
$\frac{1}{4}$ ML column	4.3c	3.51
$\frac{1}{6}$ ML chain	4.3b	3.81
$\frac{1}{4}$ ML combination	4.3d	3.75

Table 4.1: Binding energies for isolated Sr adatoms, Sr dimers, and submonolayer Sr coverages on a dimerized Si surface. See Figs. 4.2 and 4.3.

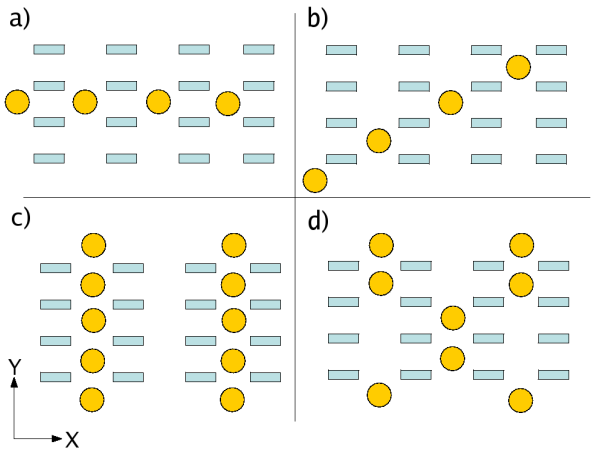

Figure 4.3: Top view of low coverages of Sr atoms (yellow circles) on a dimerized silicon surface (silicon dimers represented as blue rectangles). a) 1/6 ML A site rows, b) 1/6 ML A site diagonal chains, c) 1/4 ML A site columns, d) 1/4 ML combination of corner and y direction nearest neighbors. See Table 4.1 for energies.

dimers, and placing the Sr atom into the vacancy that is created. In contrast to the dimerized Si surface, this 2×3 submonolayer Si surface has only one low energy Sr binding site per 2×3 area. The Sr configurational degrees of freedom are high in energy and are completely frozen out at typical deposition temperatures. We have considered the effects of alternate Si bonding schemes for such submonolayer Si surfaces, and we find that all such excitations of the 2×3 structure are high in energy and have a negligible contribution to the thermodynamics.

In the case of interest here, we focus on the low coverage and low energy surface phases, and we consider in detail the interactions between Sr in A sites at local coverages of z_i=0 to 3. For z_i=1, we extract the interactions J_x, J_y, and J_{xy} from the Sr dimer calculations in Table 4.1. We find that for z_i=2 and 3, the interactions J are similar, and so we combine all of our first principles calculations with z_i=2 and 3 and perform a least squares fit to get J_x, J_y, and J_{xy} for z_i=2 or 3 nearest neighbors. Our local coverage-dependent Hamiltonian model can reproduce all of our first principles results for $0 \leq z_i \leq 3$, with errors of 0.01–0.02 eV/Sr. For $z_i > 3$, we find that

such configurations are physically unimportant for two reasons. First, the energies of such configurations are much higher than those with $z_i \leq 3$, so that they do not play a relevant role in the Monte Carlo sampling. Second, since the coverages we simulate to find the 2×3-lattice gas transition are close to 1/6 ML, $z_i > 3$ represents an unusually high local coverage and such configurations are unlikely in the sampling. For completeness, we incorporate them into the Hamiltonian in the following manner: for $z_i > 3$ the interaction terms are isotropic but z_i dependent, and the interactions are chosen to reproduce binding energy trends up to 1/2 ML of Sr.

4.4 Experiment

In order to experimentally determine the phase diagram for Sr growth on Si as a function of temperature [75] and compare with theory, out experimental colleagues Myrtle-Rose Padmore, Yaron Segal, J.W. Reiner, F.J. Walker and C.H. Ahn[19] follow the procedure used for the growth of epitaxial oxides on Si (001) [52, 53]. Sr is evaporated from an elemental source in an oxide MBE chamber with a base pressure of 1×10^{-10} Torr at a rate of ~ 1 ML/min, as measured by a quartz crystal microbalance. They calibrate the rate by matching the peak intensity of the 2×3 and 1×2 RHEED patterns to 1/6 and 1/2 ML respectively. The substrate temperature is monitored with a thermocouple, calibrated using an optical pyrometer sensitive to 0.91-0.97 μm wavelengths. A silicon wafer is introduced into the chamber and heated to to desorb the native oxide, until sharp 2×1 spots are observed in RHEED, indicating dimerization of the clean surface. Sr is then deposited onto the substrate, while RHEED images are recorded at a rate of 15 frames per second. The deposition and RHEED characterization were performed at the CRISP Teaching MBE facility.

From the recordings, they measure intensity of the 3× RHEED spots as a function

of coverage (shown in Fig. 4.4b). We determine the coverage of condensation from lattice gas to the 2×3 phase by noting the coverage at which the 3× intensity begins to rise (see phase diagram in Fig. 4.4a, and Tab. 4.2). In order to accurately and consistently determine this point, we extrapolate the linear portion of the intensity rise in the curves of Fig. 4.4b to zero. The coverage of the intersect is the beginning of condensation [76]. Uncertainty in the coverage at the point of condensation is mainly due to the uncertainty in flux measurement and is estimated to be 0.05 ML/min.

4.5 Results and Discussion

The results of our model under experimental conditions (600-750°C) involve a lattice gas consisting predominately of Sr atoms with 1-2 corner nearest neighbors, but with no long range order. A characteristic configuration of Sr adsorption is shown in Fig. 4.1. Our predicted phase equilibrium between this lattice gas and the ordered 2×3 structure is in agreement with the experimental results (see Fig. 4.4). This agreement between theory and experiment is in contrast to a simple non-interacting lattice gas model based on the isolated Sr binding energies, which underestimates the coverage of the phase equilibrium line by 50%. The effect of the interaction is to stabilize the lattice gas phase by increasing the binding energy in that phase.

While the experimental values for the magnitude of the coverage as a function of temperature agree well with theoretical predictions, the slope of the dependence of coverage on temperature is steeper in the measurement than that predicted by theory. To account for this discrepancy, we discuss several potential sources of error in the theory and experiment. The predictions follow the system in equilibrium, and kinetic limitations, such as a barrier preventing the Si atoms from rearranging into the lower energy phase, will have less effect as the temperature increases and

thus cannot explain the observed trend. One quantity that is not considered in the calculation is the difference in vibrational free energy between the 2×3 dimer vacancy structure and the disordered lattice gas. An estimate of the magnitude of this error over this temperature range can be found in ref. [73], which finds that the difference in vibrational free energy between competitive low energy Sr on Si (001) structures is at most 0.04 eV/Sr at 600°C. However, this difference is found to be nearly constant over our temperature range, so that this uncertainty shifts the theoretical curve up or down by a constant and does not change its slope. An additional source of uncertainty is the fitting of the lattice gas Hamiltonian to the first principles data, which we find to be on the order of 0.01-0.02 eV/Sr. In order to get an estimate of how these errors affect our predictions, we find the solution to our lattice gas Hamiltonian for Sr chemical potentials of 3.88 eV/Sr and 3.92 eV/Sr (instead of the calculated 3.90 eV/Sr). At a given temperature, we find that this ±0.02 eV/Sr uncertainty between the ordered 2×3 dimer vacancy structure and the disordered lattice gas changes the phase boundary by about 0.01 ML (see Fig. 4.4). Experimentally, both a thermal Debye-Waller factor and a decrease in 2×3 domain size with increased temperature will reduce the measured intensity of the 3× RHEED reflection, causing an increase in the coverage at which the reflection can be detected. This experimental effect reproduces the observed trend and could contribute to the discrepancy between the experiment and the theory.

In summary, we used first principles calculations together with Monte Carlo methods to predict the phase equilibrium line between a lattice gas of Sr on Si(100) and an ordered 2×3 structure. We also measure the phase equilibrium line using RHEED and find good agreement with theory. Anisotropic interactions between Sr in the lattice gas phase are required to reproduce experimental results. The details of the phase condensation observed here are important for controlling the epitaxy of oxides

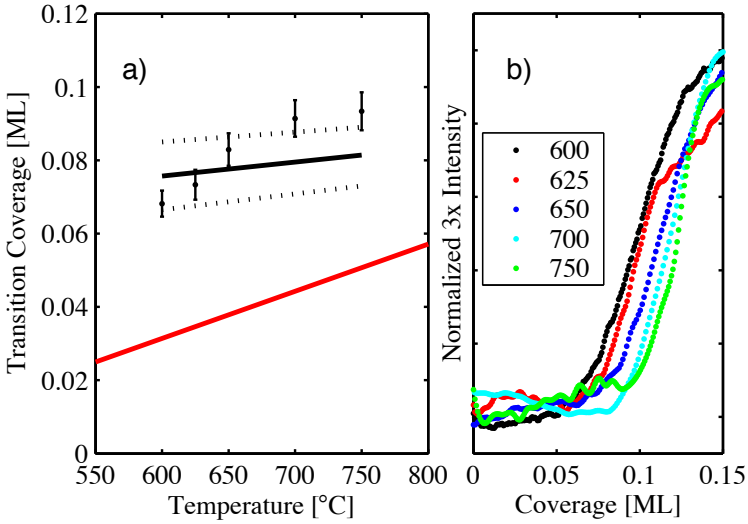

Figure 4.4: a) Coverage versus temperature phase diagram of the Sr on Si system, showing the lattice gas to 2×3 structural transition. The solid lines represent theoretical predictions with Sr-Sr interactions (black) and without interactions (red). Dotted lines are an estimate of the theoretical uncertainty (see text). The points with errors bars are RHEED data (see Tab. 4.2). b) 3× RHEED spot intensity for depositions at different temperatures.

on silicon, especially in light of the importance of the Sr template layer for the new low temperature route to epitaxy discovered by Reiner *et al.* [10] and its effect on the structure of subsequent oxide layers [77, 78].

Temp. (C)	Cov. (ML)
600	0.0682 ± 0.0036
625	0.0733 ± 0.0040
650	0.0829 ± 0.0044
700	0.0914 ± 0.0050
750	0.0934 ± 0.0052

Table 4.2: . Coverages at which the 3× RHEED spot intensity begins to rise, as a function of temperature (see Fig.4.4).

Chapter 5

Phase Diagram and STM of Sr on Ge (001)

5.1 Introduction

As has been discussed previously (see Sec. 3.1), growing complex oxides epitaxially on semiconductors is of great technological and scientific interest.[6] In addition to expanding the range of oxides which can be grown on Si, there is also great interest in expanding the range of semiconductors which can serve as the substrate. Germanium, which has the same diamond structure and 2×1 dimerized surface as Si, is especially interesting as a substrate due to its high mobility (relative to Si) because moving to high mobility materials is a long-term goal of the semiconductor industry to improve transistor performance.[2, 79] As with Si, the first step in growing epitaxial oxides on Ge requires the deposition of an alkaline earth metal on the surface.[80] We seek to understand this step in detail in order to clarify the role of the metal atoms in preparing the surface for oxide epitaxy.

In addition to being a high mobility substrate, oxide growth on Ge is also in-

teresting because $BaTiO_3$ has been grown epitaxially on Ge (001)[80], which both proves that epitaxial growth is possible for this system and provides a further motivation for study of this interface as $BaTiO_3$ is a ferroelectric material. Replacing the dielectric layer of transistor with a ferroelectric would allow for the creation of a non-volatile transistor, where the state of the transistor could be stored in the ferroelectric without need of a continuous external voltage.[6] Interface structure and quality is crucial in the ability of the ferroelectric layer to both switch polarization as well as to modify the carrier density in the channel region, making the details of the initial surface and interface layers key to eventual device performance.[80, 6, 55]

More broadly, comparing the phase diagram of Sr on Ge to our previous Sr on Si results will help elucidate the similarities and differences between these two substrates, which should help us understand the qualities which are shared by systems which can serve as template layers for oxide growth. In addition, this comparison will help us understand how generic the 1/6 ML Sr silicide structure is to alkaline earth-semiconductor interfaces.

A major part of this work depends on the high quality scanning tunneling microscopy (STM) images of low coverage Sr on Ge surfaces provided by our experimental colleagues Boris Lunkov and Eric Altman. These images provide direct confirmation that low Sr coverages cause Ge to become mobile on the surface and form non-stoichiometric structures, much like the 1/6 ML Sr on Si surface (see chapter 3); however, many details of these images are difficult to interpret directly. In order to help explain the atomic structures that create these images, we perform first principles density functional theory (DFT)[20, 21] calculations to explore the phase diagram of Sr on Ge. We find low energy structures which agree with all features of the STM images of the 3×4 structure observed near 1/6 ML Sr coverage. These structures share many features with the 3×2 1/6 ML dimer vacancy structure ob-

served in the Sr on Si system; however, there are also differences. In addition, we provide an explanation of the higher coverage Sr on Ge structures which is consistent with experiment.

5.2 Description of Experiments

Our colleagues use molecular beam epitaxy (MBE) to deposit Sr on Ge at various temperatures and then perform scanning tunneling microscopy (STM) measurements on the surface, generating a series of atomically resolved images of the surface. In addition, they use reflection high energy electron diffraction (RHEED) to analyze the symmetry of surface reconstructions.

For deposition at room temperature, and for low coverages of Sr, the STM shows the characteristic 2×1 pattern of Ge dimers on the surface, with bright spots corresponding to adatoms of Sr, which appear to sit above a normal Ge surface. However, when deposition occurs at higher temperatures, dramatically different reconstructions occur. Fig. 5.1 shows the structure at Sr coverages slightly above 1/6 ML at four different STM tip-sample biases. The large flat area on the right side of the four images has regions of 3×4 symmetry (Fig. 5.1a has a 3×4 unit cell marked). In addition, there are regular rows of defects, examples of which are marked by the yellow dotted lines in Fig. 5.1c-d. The empty state images vary sensitively with bias, while the filled state images are relatively insensitive to bias (only one is shown) and look very different than the empty state images.

Fig. 5.2 shows selected areas of Fig. 5.1 which highlight characteristics which we explore below. The top row of Fig. 5.2 shows regions of the surface with 3×4 symmetry. The filled state image (panel c) appears to show the 3×4 regions to be made from two 3×2 blocks, which form rows in the x direction (the 3× direction),

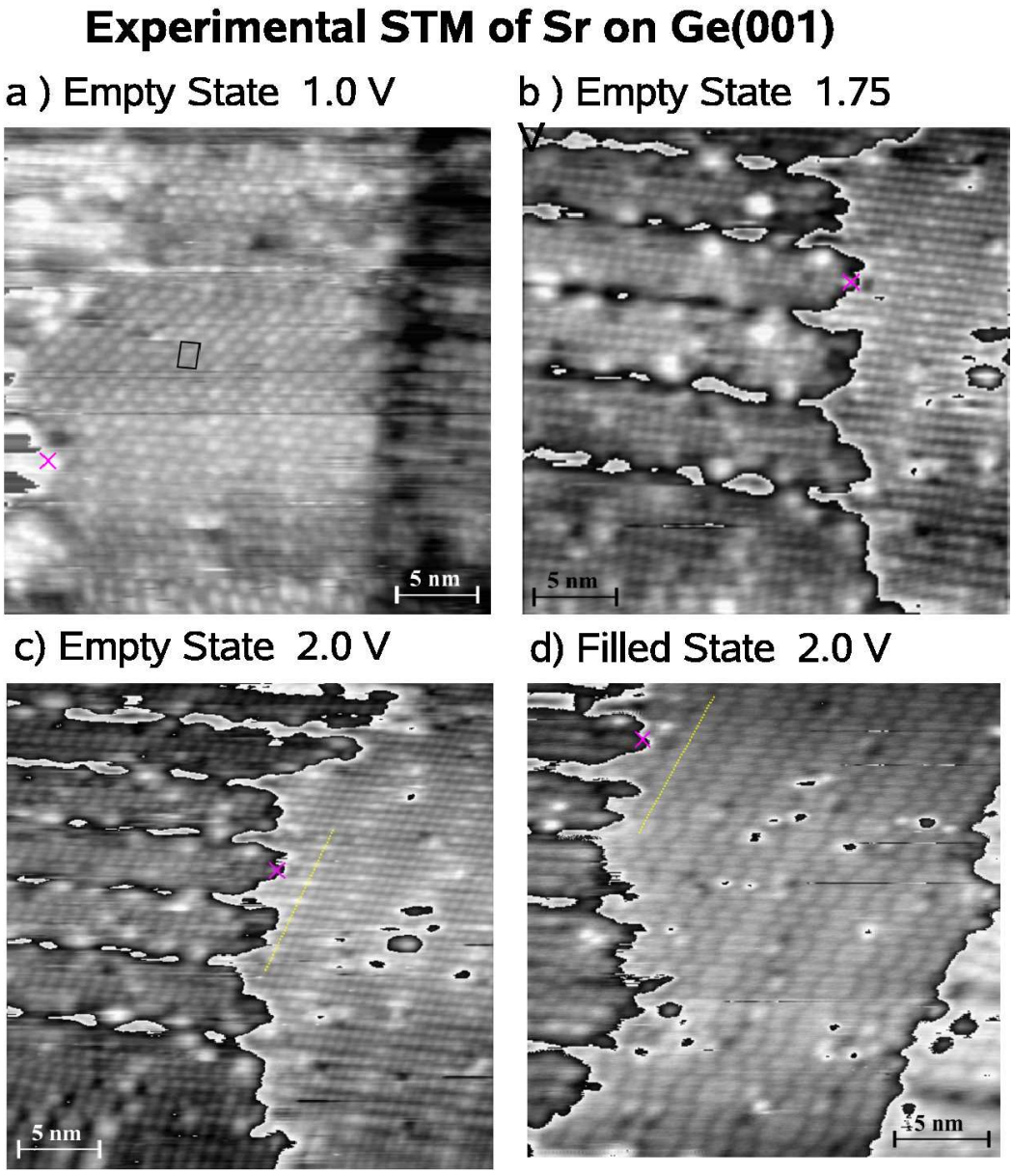

Figure 5.1: (color online) Experimental images of Sr on Ge near 1/6 ML. a-c) empty state images at 1.0V, 1.75V, and 2.0 V. d) Filled state image at 2.0 V. The yellow line and magenta $\times$ are in the same place on the surface in each image.

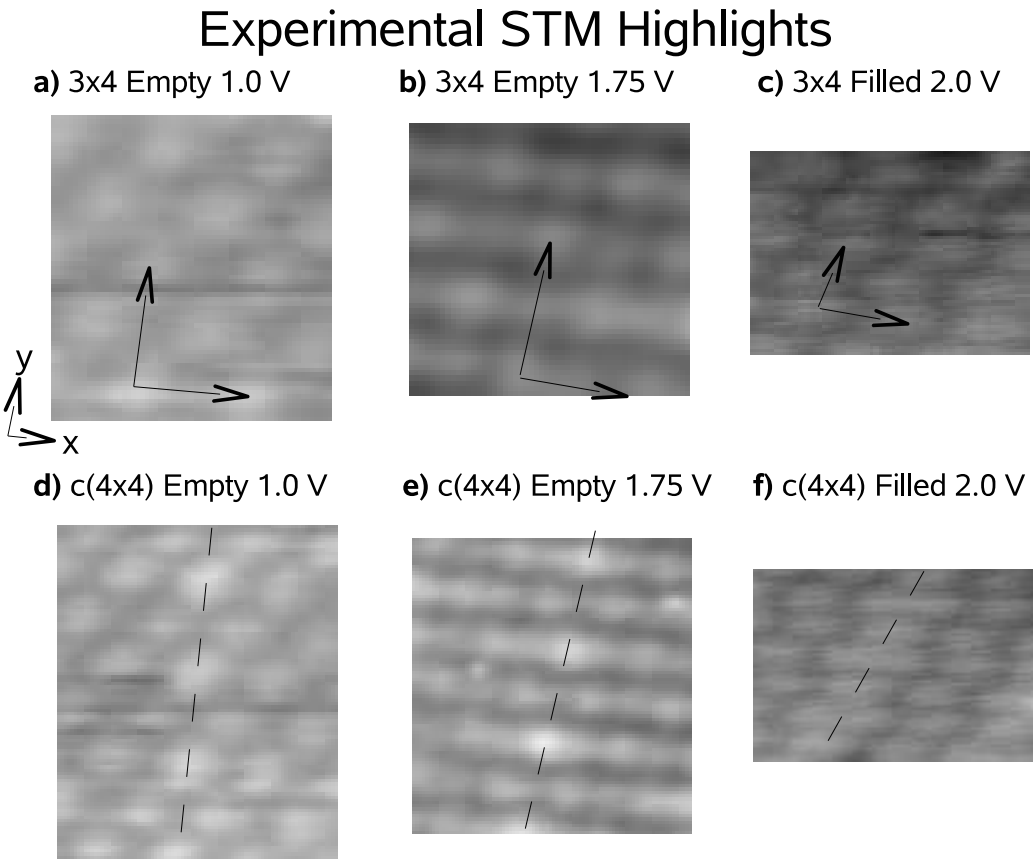

Figure 5.2: (color online) Zoomed in regions of Fig. 5.1. a-c) Regions displaying 3×4 symmetry (surface lattice vectors marked with arrows). d-f) Regions displaying defect lines (marked with dashed lines). a) and d) are from Fig. 5.1a, b) and e) are from Fig. 5.1b, c) and f) are from Fig. 5.1d.

but with the neighboring rows offset, creating a wavy pattern in the y direction (the ×4 direction). On the other hand, at low bias, the empty state images (panel a) appear to show a centered pattern. This is very unusual for a surface with 3× symmetry, as it requires the same feature to appear shifted by 1.5 unit cells along the x direction, in addition to the more typical 2 unit cells along the y direction. At higher bias (panel b), new features appear between the previous features, so that there now appear to be 2 features along the x direction per 3 unit cells, which form an almost regular grid.

In addition to the regular 3×4 regions, the flat regions on the right of Fig 5.1

also have regular lines of defects along the y direction, which we highlight in Fig. 5.2d-f. In the filled state image (panel f), these defects appear to be extra wide wavy lines. In the empty state images (panel d-e), the defects appear to be unusually bright spots, with darker regions between them. The defect lines can be interpreted as anti-phase defects between the regions of 3×4 symmetry, as the 3×4 regions on either side are misaligned by 1 unit cell (u.c.). Also, we note that there is some ordering between neighboring defect lines in the x direction, as the bright spots in the empty state images are always offset by 2 u.c's in the y direction, suggesting that the defect lines may actually be part of a stable surface reconstruction with a large unit cell.

In addition to all of the details we extract from the flat regions on the right side of the images in Fig. 5.1, the images also show very interesting behavior on their left sides. These structures, which appear at Sr coverages above 1/6 ML, consist of what appear to be raised regions with 3×2 symmetry, which are only 2-3 unit cells thick in the x direction, and which are separated by lowered trough regions of unknown origin. These trough regions appear dark at all biases, indicating that they are likely physically lower on the surface. There are additional images, not shown, in which the raised 3×2 sections of the surface appear to connect to the 3×4 regions discussed above, indicating that the 3×2 regions consist of the same building blocks as the 3×4 regions, but are arranged with a 3×2 symmetry which is stabilized by the troughs.

5.3 Methods

In order to investigate the microscopic structure of the system, we perform first-principles density functional theory (DFT) calculations using a plane-wave basis set and ultrasoft pseudopotentials.[20, 21, 35]. For Ge, we include $4s$ and $4p$ projectors

which are in the reference state $4s^{1.44}4p^{2.56}$, and have cutoff radii of $r_s = r_p = 1.8$ Bohr, and we include a non-local core correction.[81] The Sr pseudopotential was presented earlier (see chapter 3). We use a slab geometry with 8-10 layers of Ge and symmetric surfaces (see discussion in Ref. [73] and chapter 3). We use the PBE GGA to approximate the exchange correlation functional,[28] and the method of Tersoff and Hamann[68, 69] to simulate STM images, which consists of integrating the local density of states from the Fermi level to the bias voltage.

We note that all of our empty state simulated STM images have different voltages than the corresponding experimental images. This is due to the well-known underestimation of band gaps in DFT under LDA or GGA.[82, 83, 84] This problem is especially severe in Ge, which has a vanishing band gap in DFT but a value of 0.67 eV experimentally.[25] In order to interpret our calculations, the empty state images must be shifted upward in voltage by an unknown amount. In addition, several of our images would agree with experiment better if the empty Sr states were higher in energy relative to the empty Ge states, which we attribute to the same problem. Due to the size of the surface reconstructions, applying a theory with more reliable band alignment (e.g. the GW approximation[85, 86]) would be prohibitively expensive computationally.

5.4 Low Coverage Structures

We begin by investigating isolated (1/16 ML) Sr atoms on a dimerized Ge surface. Similar to our study of Sr on Si, we find that Sr prefers to sit in the trough site between 4 Ge dimers and donate its two valence electrons to dangling bonds on the Ge dimers,[57, 73] and our simulated STM images of this system (not shown) agree well with experiment.

Next, we consider 1/6 ML Sr coverage. As in the case of Sr on Si,[57, 73, 19] if we assume that the Ge surface atoms are in the same dimerized configuration as the bare Ge surface, then the lowest energy structure has Sr atoms sitting in the same binding site as the isolated the Sr atoms, but these binding sites are arranged in disordered chain-like structures with a binding energy of 3.47 eV/Sr (see Tab. 5.1, and Fig. 4.1). However, based on the similar Sr on Si system,[10, 73] we expect Ge will be mobile at experimental deposition temperatures, requiring us to consider surfaces with non-stoichiometric Ge coverages.

Again using our knowledge of Sr on Si, we consider two additional structural motifs which have non-stoichiometric Ge coverages: 1) a 2×3 single dimer vacancy structure (see Fig. 3.9), and 2) a 3×2 double dimer vacancy structure.[10, 73] Both structures are more stable than the chain-like structure considered above, and as in the case of Sr on Si, the most stable structural motif at 1/6 ML is the 3×2 double dimer vacancy structure (see Tab. 5.1 and Fig. 5.3b). However, unlike the case of Sr on Si, the most favorable way of arranging these 3×2 units is into a 3×4 pattern, with the two 3×2 building blocks arranged as in Fig. 5.3a.

The unusual bonding pattern of the 3×4 structure explains both the appearance and bias dependence of the STM images (see also discussion of 2×3 Sr on Si bonding in Sec. 3.6 and STM in Sec. 3.8). In this structure, like in the case of isolated Sr on Ge, the Sr donates its two valence electrons to two of the low-energy half-filled dangling bond states on the surrounding Ge atoms. More surprisingly, the uppermost Ge dimer, which is in an unusual planar sp^2 bonding geometry rather than the typical tetrahedral sp^3 geometry, also donates two electrons from its high-energy dangling p_z-like states to the low-energy sp^3-like dangling bond states on the Ge atoms near the Sr (see Fig. 3.13 for schematic). This can be seen in the density of states shown in Fig. 5.4, which shows filled sp^3-like dangling bond states (dark green line) just

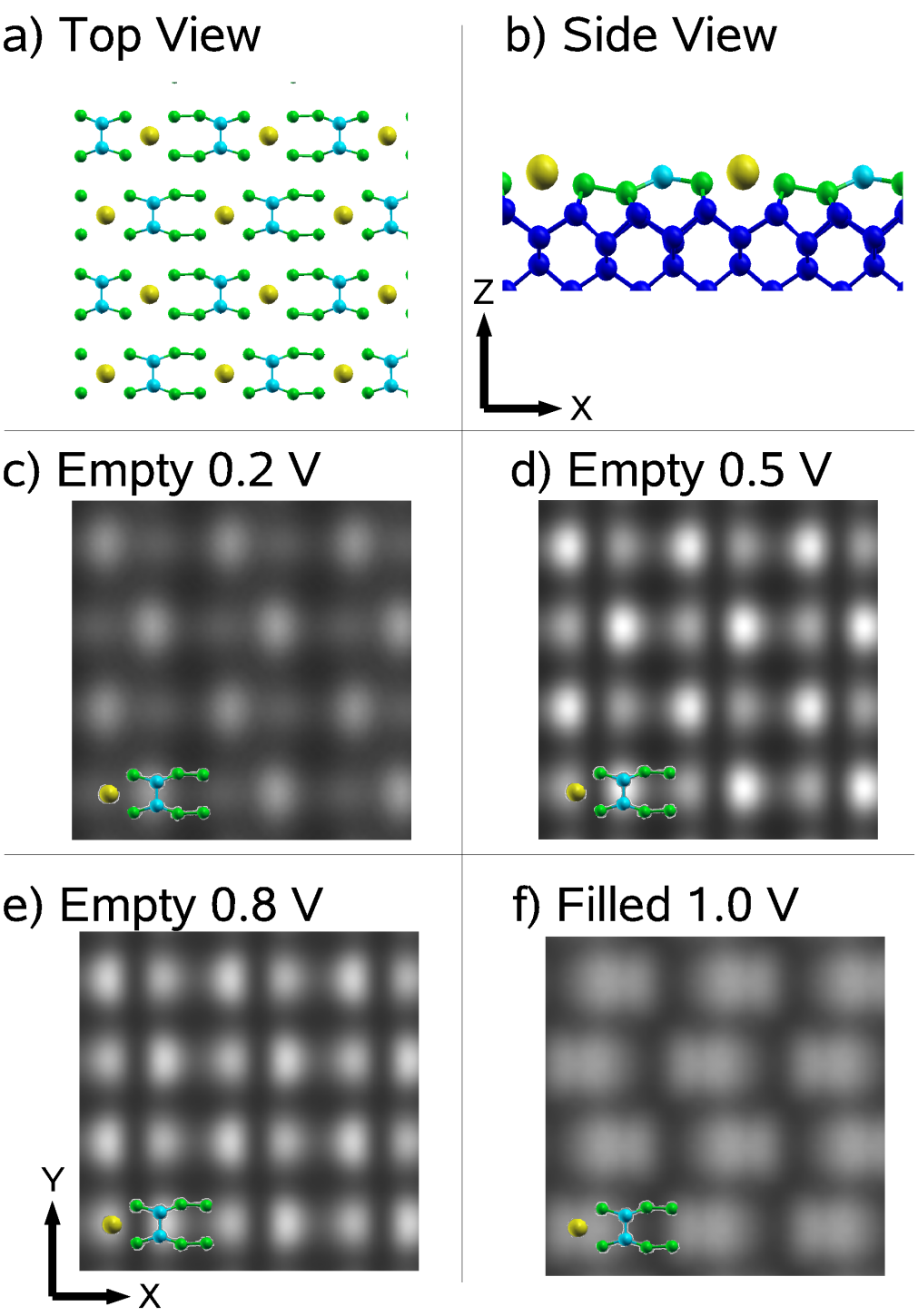

Figure 5.3: (color online) a) top view and b) side view of the 3×4 structure, the lowest energy 1/6 ML structure (see Tab. 5.1). Key: Sr-large yellow, uppermost Ge dimers-cyan, second layer Ge-green, and lower layer Ge-dark blue. c-e) simulated empty state images at 0.2 V, 0.5 V, and 0.8 V above the Fermi level. Compare to Fig. 5.2a-b, f) simulated filled state image 1.0 V below the Fermi level. Compare to Fig. 5.2c. Each image has the 3×2 building block of the 3×4 reconstruction superimposed.

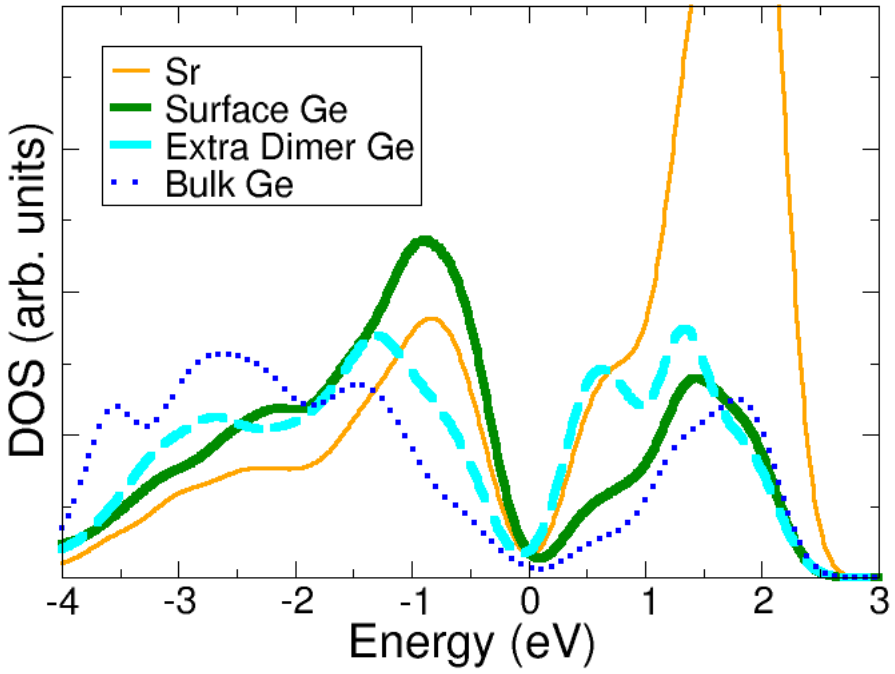

Figure 5.4: (color online) Atomic projected density of states for 3×4 1/6 ML structure (see Fig. 5.3), with the Fermi level at 0 eV. Filled state images show surface Ge (thick dark green line) while empty state images show the uppermost Ge dimer (dashed cyan) at low bias and Sr (thin orange) at high bias.

below the Fermi level and empty p_z states from the uppermost Ge just above the Fermi level (dashed cyan line). The net result of this electron transfer is that the highest energy occupied states are the four passivated dangling bond states next to each Sr, and the lowest energy unoccupied states are not Sr states, but rather the dangling p_z-like states on the raised dimer, which opens a surface band gap.

Based on this understanding of the electronic structure of the 3×4 structure, we can understand the appearance of our simulated STM images of the surface, which are in excellent agreement with experiment. The filled state images (compare Fig. 5.2c to Fig.5.3f), which are relatively insensitive to bias, show the 4 passivated dangling bond states near each Sr. The empty state images, on the other hand, are

Table 5.1: Energies and average distance from Sr to four nearest neighbor Ge for various Sr on Ge structures.

Sr Cov(ML)	Unit Cell	Ge Cov(ML)	E_{bind} (eV/Sr)	Sr-Ge(Å)	Fig.
1/16	4×4	0	3.07	3.46	
1/6	Chain	0	3.47	3.37	
1/6	2×3	2/3	3.50		
1/6	3×2	1/3	3.53	3.29	
1/6	3×4	1/3	3.54	3.27	5.3a-b
3/16	c(8×4)	3/8	3.55	3.18	5.6a
1/2	2×1	0	3.29	3.43	5.7a
2/3	3×1	0	3.33	3.23	5.7b
1	1×1	0	2.81		

strongly bias dependent. At low bias (compare Fig. 5.2a to Fig. 5.3 c-d), the images are dominated by empty p_z-like states on the raised Ge dimer, which are at relatively low energy. The combination of the displacement of these dimers from their ideal position by about 1/4 u.c. in the x direction with the way the 3×2 building block structures are arranged into a 3×4 structure on the surface causes the bright spots at this bias to appear centered (see discussion in Sec. 5.2). At higher bias (compare Fig. 5.2b to Fig. 5.3e), we begin to see the empty s and d orbitals on the Sr atoms, which appear as additional spots between the raised dimer atoms.

In addition to explaining the 3×4 STM images at 1/6 ML, we can also explain the regular lines of defects in this structure, which appear as unusually bright spots in the empty state images (see Fig. 5.2d-e) and a seemingly disordered wavy pattern in the filled state images (see Fig. 5.2f). We find that these features can be explained as either an anti-phase defect between regions of 3×4 structure, or equivalently as a mixture of a c(8×4) structure at 3/16 ML with the 3×4 structure at 1/6 ML. The atomic geometry of this structure, which we find the be thermodynamically stable (see table 5.1) is presented in Fig. 5.5a, a schematic of the resulting STM images are presented in Fig. 5.5b-d, and the calculated STM is presented in Fig. 5.6. We find that the prominent bright spots in the low bias empty state images (compare Fig.

5.2d-e to Fig. 5.6a-b) correspond to the p_z states on the isolated extra Ge dimers. These isolated extra Ge dimers are both geometrically and electronically similar to the raised dimers in the 3×4 structure, except that the empty states in this dimer are slightly lower in energy, and therefore appear to be brighter defects at low bias.

5.5 High Coverage Structures

In addition to structures near 1/6 ML coverage, we also consider all of the thermodynamically stable Sr on Si structures up to 1 ML. Unlike Sr on Si, which features a stable 2×1 structure at 0.5 ML Sr coverage,[57, 73] we find that the Ge on Sr system has no thermodynamically stable structures between 3/16 and 2/3 ML Sr coverage. We believe that this difference between Si and Ge is related to their difference in lattice constant; the surface lattice constant of Si is 0.16 Å smaller than Ge.[25] At 1/2 ML Sr coverage in the 2×1 structure, the Ge-Sr distance is 3.43 Å, but the Si-Sr distance is only 3.31 Å in the equivalent Si structure (see Fig. 5.7a, and also Fig. 3.3), resulting in weaker overlap between the Sr and Ge orbitals. In fact, all of the thermodynamically stable Ge on Sr structures have average Ge-Sr distances between 3.18 and 3.27Å, which are all shorter than any of the Ge-Sr distances for dimerized surfaces (see Tab 5.1).

According to our calculations, the Sr should phase-separate into a low coverage structure near 1/6 ML (detailed above) and a 3×1 structure at 2/3 ML (see Fig. 3.18b). As discussed in Sec. 5.2, experiments do find a surface which appears to be a mixture of rows of 1/6 ML 3×2 units, which appear as raised ordered structures to the left of images in Fig. 5.1, which are separated by troughs of an indiscernible higher coverage structure. While this large unit cell is too big to simulate directly in DFT, we believe that the ordered 3×2 units are the same 1/6 ML structure

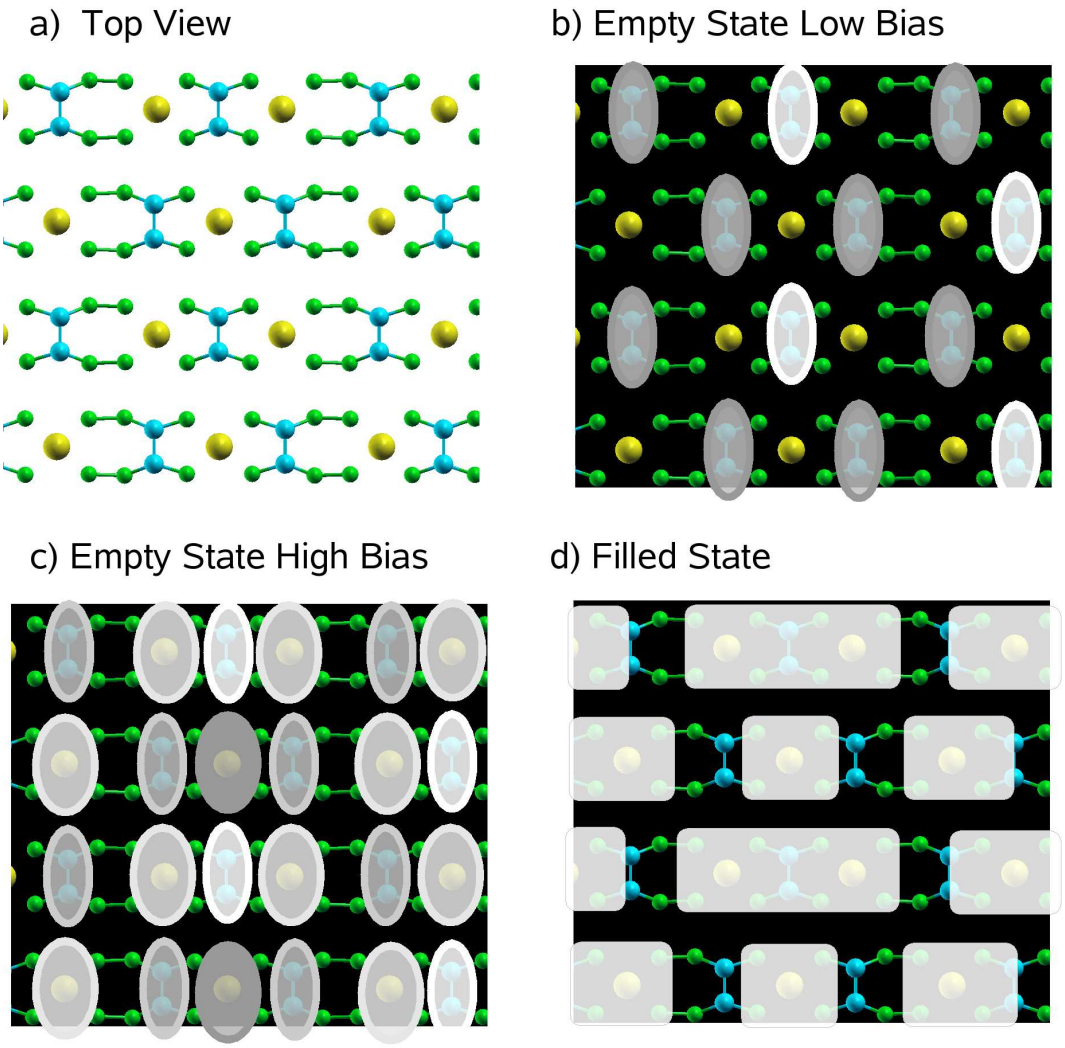

Figure 5.5: (color online) Structure (a) and schematic STM images (b-d) of c(8×4) structure at 3/16 ML coverage. See Fig. 5.6a-c for calculated versions, and compare to experiments in Figs. 5.2d-f. b) Empty state image at low bias, which shows isolated Ge dimers in bright white and other Ge dimers with less intensity c) Empty state image at higher bias; Sr is visible. c) Filled state image, dominated by the four Ge which surround each Sr.

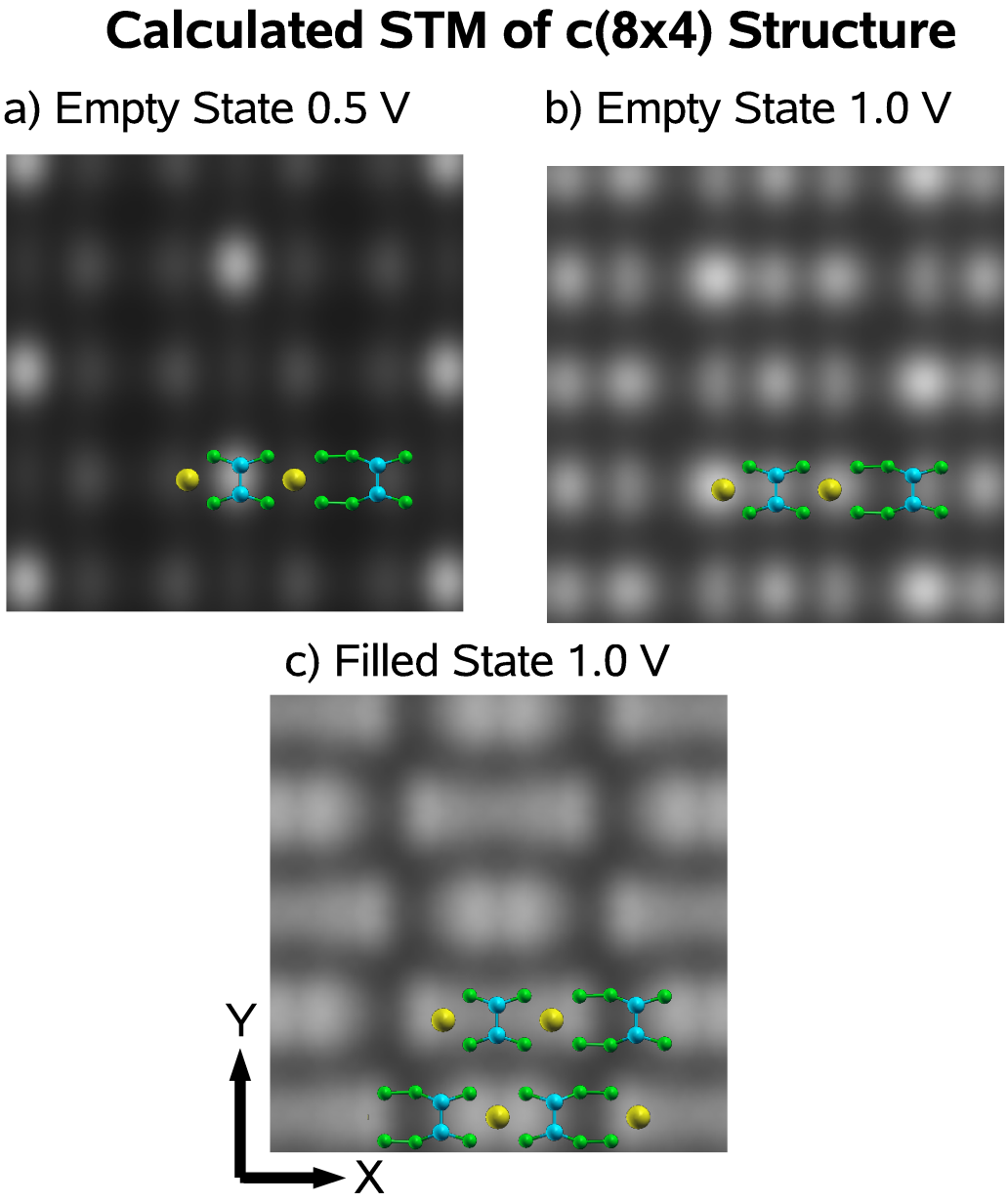

Figure 5.6: (color online) Calculated STM for c(8×4) structure. See Fig. 5.5b-c for schematic versions. a) Empty state 0.5 V. Compare to Fig. 5.2d b) Empty state 1.0 V. Compare to Fig. 5.2e c) Filled state 1.0 V. Compare to Fig. 5.2f

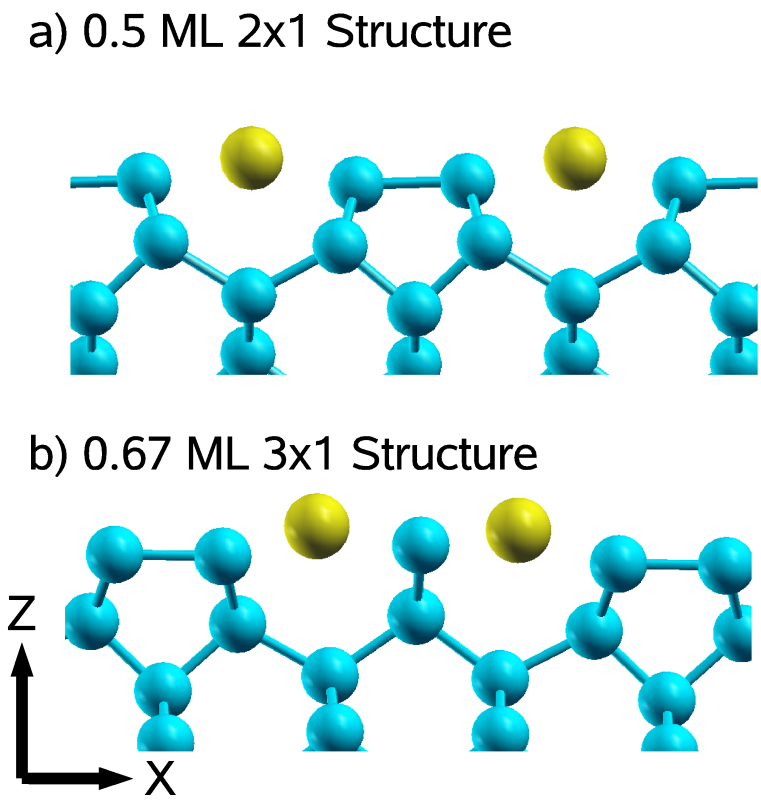

Figure 5.7: (color online) Side view of high coverage Sr on Ge structures. a) 1/2 ML structure, which is not thermodynamically stable b) 2/3 ML structure, which is stable.

which forms the building block of the 3×4 structure discussed above. While the 3×2 structure is 0.01 eV/Sr less stable than the 3×4 structure (see Tab. 5.1), we expect that the 3×2 structure is stabilized by the high density of step edges in the observed mixed structure. In particular, there is no obvious way to create a step edge which runs parallel to the y direction from the 3×4 structure without disrupting surface bonds or creating a zig-zagged step, either of which is likely to be costly in energy. The origin of the high coverage trough structure and why it prefers a high density of steps on the surface is still unclear.

5.6 Summary

We use first principles calculations to analyze the phase diagram of Sr on Ge (001). At low coverage, we find thermodynamically stable non-stoichiometric structures at 1/6 ML and 3/16 ML which are related to our previously studied 1/6 ML Sr on Si structure.[73] We have simulated STM images of these structures, and we find them to be in excellent agreement with experiment. In addition, we have investigated higher coverage Sr on Ge structures, and we find no stable structures between 3/16 and 2/3 ML Sr coverage. In particular, the 0.5 ML 2×1 structure which is commonly observed during the growth of Sr on Si, and which is a key feature of some interfaces between Si/Ge and complex oxides,[77, 87] does not form for Sr on Ge. Due to the fact that complex oxides can be grown on Ge,[80] this shows that the stability of the 0.5 ML Sr structure is not a prerequisite to form an epitaxial interface between a semiconductor and a complex oxide. The origin of the interesting mixed phase observed instead of the 0.5 ML 2×1 structure will require further study.

Chapter 6

Phases of submonolayer La on Si (001)

6.1 Introduction

Complex oxides provide a wide range of potentially useful properties, including ferromagnetism, ferroelectricity, superconductivity, multiferroic behavior, colossal magnetoresistance, high dielectric constants, etc. However, integrating these properties into useful devices has proved challenging. Many applications depend crucially on having a defect-free epitaxial interface between the oxide and a semiconductor substrate, usually silicon.[2, 6] For instance, replacing the SiO_2 layer in a field effect transistor with a complex oxide and using an electric field to modify conduction in the channel requires a direct defect-free interface with a silicon substrate for good device performance.[6]

Unfortunately, relatively few complex crystalline oxides have been grown epitaxially on silicon; the most successful example is $SrTiO_3$.[52, 53, 6] During the growth procedure for $SrTiO_3$, a crucial initial step involves the deposition of 0.5 ML Sr,

which forms an ordered 2×1 reconstruction that passivates the silicon surface and provides resistance to oxidation, as well as providing an ordered template for oxide growth.[52, 53, 60, 10, 57, 73]. Expanding the list of materials which can be used to form this initial layer beyond the alkaline earth metals would be an important step towards increasing the variety of complex oxides which can be grown directly on Si.

One particular material which would be particularly desirable to grow on silicon is $LaAlO_3$. Due to its large band gap and high dielectric constant, $LaAlO_3$ is a promising material for high-k dielectric applications, and it is thought to have favorable band offsets with silicon.[51, 88] However, despite having the same perovskite structure as $SrTiO_3$ and a well-matched lattice constant, no direct method is known for growing $LaAlO_3$ on Si. However, $LaAlO_3$ can be grown indirectly on a buffer layer of SrO or $SrTiO_3$,[89, 90, 91, 92] and Si can be grown epitaxially on a $LaAlO_3$ substrate,[93, 94] suggesting that a direct procedure for growing $LaAlO_3$ on Si may be possible.

Using our experience in studying Sr on Si,[73, 19, 10] (see chapter 3), we calculate the properties of submonolayer coverages of La on Si (001). First, we investigate the (001) surface with Si frozen into its original positions on the surface, and find results in agreement with Ashman *et. al* [95]. This surface appears to be promising as a buffer layer for oxide growth; however, when we allow the Si to move, the surface presents several complications to its use in oxide growth. In particular, at coverages above 1/5 ML, we find that the surface prefers to form silicide structures, with Si atoms above a La layer, rather than maintaining a flat surface. These findings represent a challenge for oxide growth using a La template layer.

6.2 Methods

We perform first-principles density functional theory calculations using a plane wave basis set and ultrasoft pseudopotentials.[20, 21] We used the PBE GGA to approximate the exchange correlation functional.[28] For silicon, our pseudopotential has $3s$, $3p$, and $3d$ projectors with d local, our cutoff radii were $r_s = r_p = 1.7$ Bohr, and we used the reference atomic configuration $3s^2 3p^2$. For La, we include the semicore $5s$ and $5p$ states, in addition to the valence $5d$, $6s$, $6p$, and $4f$ states. The cutoff radii are $r_s = r_p = r_d = r_f = 2.2$ Bohr. We use a reference configuration of $5d^1 6s^{1.5} 6p^{0.5} 4f^0$.

Our calculations are all run at the theoretical lattice constant of silicon, which we calculate to be 5.47 Å. We use a slab geometry, with periodic boundary conditions in the x and y directions and a finite thickness of at least 8 layers in the z direction, which is the (001) direction in the Si crystal. This geometry creates two surfaces, one on each side of the slab. In order to treat the surfaces accurately, we create identical surfaces on each side.[73] Binding energies are calculated relative to a bare silicon surface in the $p(2 \times 2)$ configuration and a La atom at rest in vacuum. For configurations with less than 1 ML of silicon on the surface, the energy of any extra silicon is compared to a bulk reservoir, determined from slab calculations.[73]

We use the Nudged Elastic Band (NEB) plus Climbing Images method[40, 41] to calculate energy barriers (E_{bar}) for La and Si motion on the surface. We then use simple transition state theory to estimate transition rates,

$$R = \nu \exp(-E_{bar}/k_B T) \tag{6.1}$$

where k_B is Boltzmann's constant and T is the temperature. The exponential prefactor (ν) is estimated from previous phonon calculations.[73] We expect these rates to

give a good order of magnitude estimate for the rate limiting steps which dominate the motion of surface atoms.

6.3 Stoichiometric Surfaces

We begin by reviewing the bonding of an isolated (1/16 ML) La atom on the Si surface. On an ideal Si (001) surface, each surface atom, which would normally have two dangling bonds, reconstructs into a dimer with a neighboring Si atom in the x direction, doubling the surface periodicity.[65] These dimers arrange themselves into rows (see Fig. 6.1). In addition to dimer formation, each dimer, which has two half-filled dangling bonds, has a further symmetry breaking reconstruction in which one atom raises and the other lowers. This reconstruction pushes the upper atom towards a more bulk-like sp^3 geometry with a low energy dangling bond, and it pushes the lower atom into a more planar sp^2 geometry with a higher energy p_z-like dangling bond. Then, one electron is partially transfered from the dangling bond of the lower atom to the upper atom, partially opening a surface band gap, although the bands still cross.

Similar to the binding of Sr on Si,[57, 73] and in agreement with the work of Ashman *et. al.*,[95] we find that La prefers to bind to a trough site between four Si dimers (see Fig. 6.1). The La atom has a large binding energy of 6.57 eV to the surface. There is a second La binding site on top of the dimer row, which is 0.25 eV less stable. In both cases, the La donates electrons to the dangling bonds on the Si dimers. La has three valence electrons, all of which can be donated to dangling bonds on the Si. This electron donation causes one or two of the dimers surrounding the La to become flat (the exact number depends on La coverage and binding site), because filling the dangling bond states eliminates the energy gained via the buckling

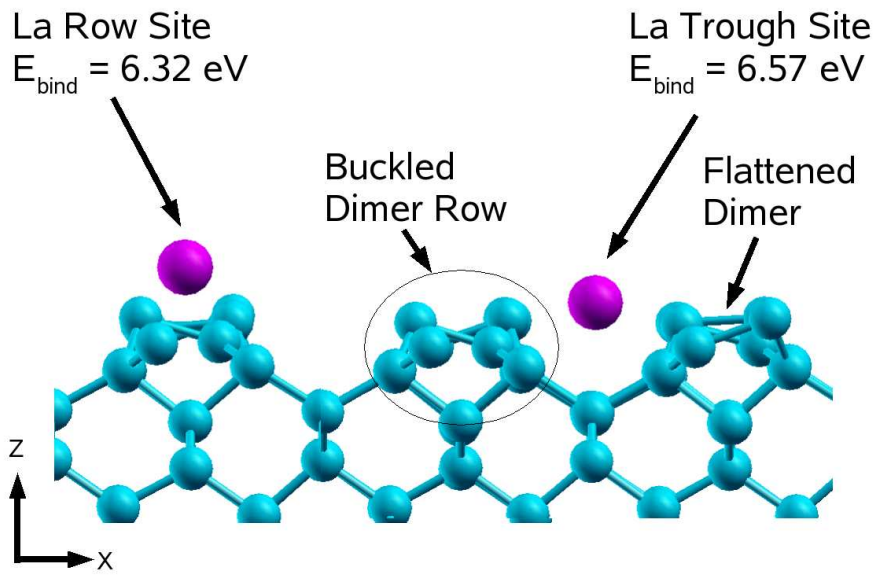

Figure 6.1: (color online) Side view of reconstructed Si (001) surface showing isolated La binding sites. The La is the larger magenta atom and the Si is in cyan. The left La is in the row binding site, which is 0.25 eV less stable than the right La, which is in the trough binding site. Between the La is an alternately buckled dimer row.

interaction described above. In addition to creating flattened dimers, any remaining buckled dimers adjacent to the La orient so that their raised atoms are closer to the La, which decreases the distance between the positively charged La and the more negatively charged Si atoms in the dimers.

The binding energy of an isolated La to the surface is more than 50% larger than Sr, which is due to a) the extra valence electron on La, which increases the charge transfer bonding, and b) the increased overlap of La d and f states with the Si surface, as compared to Sr d states, which increases the hybridization between La and Si.

We calculate the energy barrier for a La to move between binding sites on the surface. We perform the calculations at 0.25 ML La coverage in a 2×2 cell. In addition, we calculate the trough-row barriers at 1/8 ML in a 4×2 cell, and we find only a 0.14 eV difference with the 1/4 ML results. Results are reported in table

Table 6.1: Energy barriers for La motion at low coverage (see Fig. 6.1).

Start	End	Barrier (eV)	Hop Rate 300 K (Hz)	Hop Rate 800 K (Hz)
Trough	Trough	0.43	2×10^{5}	8×10^{9}
Row	Trough	1.12	6×10^{-7}	4×10^{5}
Trough	Row	1.41	8×10^{-12}	5×10^{3}
Row	Row	1.87	2×10^{-19}	7×10^{0}

Table 6.2: Binding energies for different coverages of La on a stoichiometric Si surface.

La Coverage(ml)	Configuration	$E_{bind}(eV)$	Figure
1/16	Iso. trough site	6.57	6.1a
1/16	Iso. row site	6.32	6.1b
1/10	Single Chain	6.94	6.2a
1/5	Single Chain	6.81	6.2c
1/3	Double Chain	6.70	6.2d
1/2	2×1	6.41	6.5a
8/15	5×3	6.47	6.5b
3/5	5×1	6.40	
2/3	3×2	6.32	6.5c
1	1×1	5.80	6.5d

6.1. We find that a La in a trough site should be able to move parallel to the dimer rows (along the y direction) even at room temperature. However, in contrast to Sr, which is mobile at room temperature, any the motion of a La atom which initially binds to the surface in a row site will be kinetically limited at room temperature. Therefore, low coverage La systems will not reach equilibrium at room temperature during the typical deposition time scale of minutes, reducing the effectiveness of low temperature deposition in producing an ordered surface for oxide growth.

6.3.1 $\leq$ 1/3 ML Chains

Next, we investigate low coverage La structures on a surface with all the silicon dimer bonds in place. In agreement with the work of Ashman et. al.,[95] we find that for La coverages of $\leq 1/5$ ML, all La atoms occupy the low energy trough binding sites described above, and these La arrange themselves into a series of diagonal chains

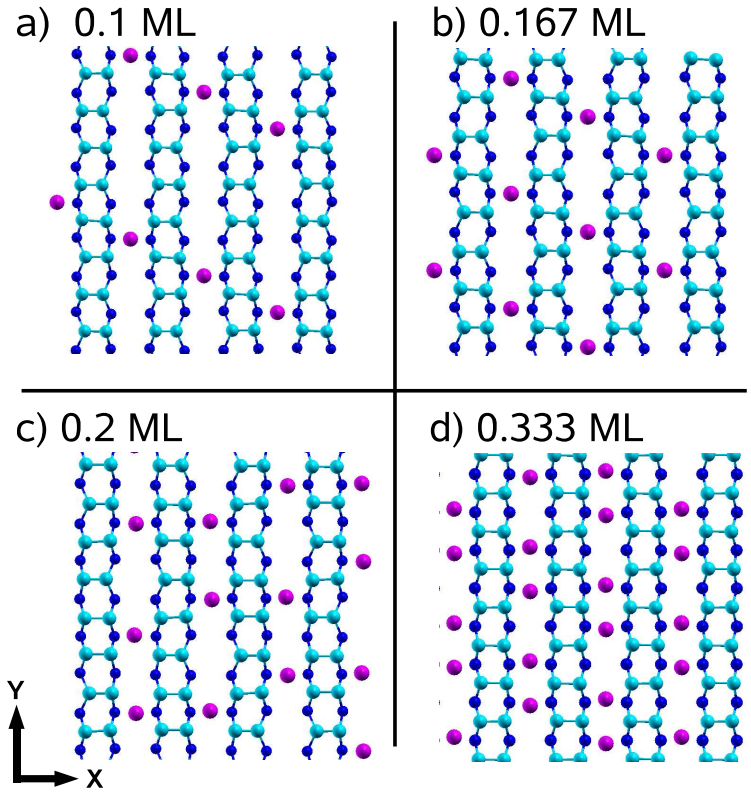

Figure 6.2: Top views of chain-like La structures on dimerized Si at a) 1/10 ML b) 1/6 ML c) 1/5 ML d) 1/3 ML coverage (see table 6.2). La is the large atom in magenta, top layer Si dimers are in cyan, and second layer Si are smaller and in blue. All La are in trough binding sites (see Fig. 6.1)

on the surface (see Fig 6.2). The correlations between La are due the La donating electrons to neighboring dimers, leaving the La positively charged and the dimer negatively charged. This causes a second positively charged La atom to prefer to be near the negatively charged dimer, but avoid the positively charged La.

In Fig. 6.2 a-c, we show examples of low energy chains between 1/10 ML and 1/5 ML; however, the energy cost to disorder the chains is very low (for example, the chain in Fig 6.2b is only 0.03 eV/La less stable than the chain in Fig. 6.2c). Therefore, we expect disordered chains on the surface at finite temperature.

For coverages higher than 1/5 ML, it is no longer possible to fit single chains on the surface while maintaining favorable dimer buckling, and the La atoms condense into double chains at 1/3 ML coverage, with two adjacent trough binding sites filled in each row (see Fig. 6.2d). Due to repulsion between the positively charged La atoms, each La moves 0.3 Å away from its neighboring La (along the y direction). At 1/3 ML La coverage, there is one half-filled Si dangling bond state per La valence electron, which leads to a stable passivated surface. This can be seen in the atomic projected density of states (DOS) in Fig. 6.3a, which shows that despite the significant hybridization between surface Si and the La, there is a gap at the Fermi level. In analogy to the 0.5 ML 2×1 Sr on Si surface, which is isoelectronic to this 1/3 ML La structure, this double chain structure has been proposed as a possible template layer for oxide growth on Si, due to its relative chemical inertness and potential for oxidation resistance.[95]

6.3.2 $>$ 1/3 ML Broken Dimers.

For coverages greater than 1/3 ML, there are no longer enough dangling Si states on the dimerized Si surface to accommodate the three valence electrons per La atom, as each dimerized Si has one half-filled dangling bond, and each La has three valence

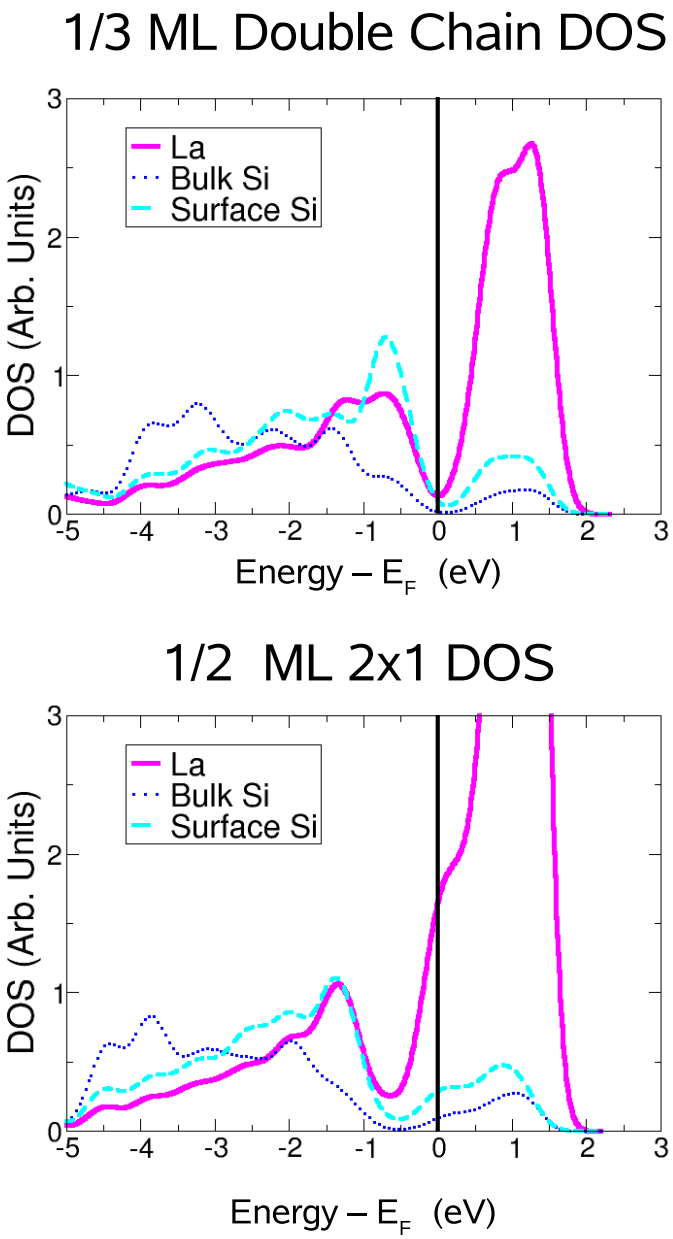

Figure 6.3: (color online) Atomic projected density of states for a) 1/3 ML double chain structure (see Fig. 6.2d) and b) 1/2 ML 2×1 structure (see Fig. 6.5a).

electrons.[95] This can be seen by comparing Fig. 6.3a, which shows the projected DOS for the 1/3 ML chain (see Fig. 6.2d) to Fig. 6.3b, which shows the projected DOS for the 2×1 1/2 ML structure (see Fig. 6.5a). In Fig. 6.3b, there is significant occupation of the La states above the valence band of Si, indicating that La is partially changing its oxidation state from La^{+3} at 1/3 ML to La^{+2}.

This shortage of partially-filled Si dangling states to bind with the La significantly reduces the binding energy of La at 1/2 ML relative to the lower coverage structures (see table 6.2). Therefore, instead of forming the 1/2 ML 2×1 structure, as seen for Sr on Si, the system prefers structures like those in Fig. 6.5 b-d, at 8/15 ML, 3/5 ML, and 2/3 ML, which consist of a combination of both dimerized and undimerized Si atoms (see Fig. 6.7a for a side view). The undimerized Si have two half-filled dangling bond states and can accept two electrons; however, the surface is still electron rich, and the extra electrons remain on La atoms, causing a transition from a La^{+3} configuration to a La^{+2} configuration as the coverage increases. This can be seen in Fig. 6.4a, which shows the projected DOS for the 2/3 ML structure in Fig. 6.5d. Despite the broken dimers, this structure has six valence electrons from the two La but only four half-filled dangling bonds per 3×1 unit cell, leading to significant occupation of La states above the Si valence band.

The the stability of the somewhat unusual 8/15 ML structure is due to the repulsion between La atoms in adjacent trough sites along the y direction, which was mentioned in Sec. 6.3.1. In this structure, there is a La vacancy every third atom along the trough, allowing the adjacent La space to move apart an additional 0.2 Å similar to what happens in the 1/3 ML chain.

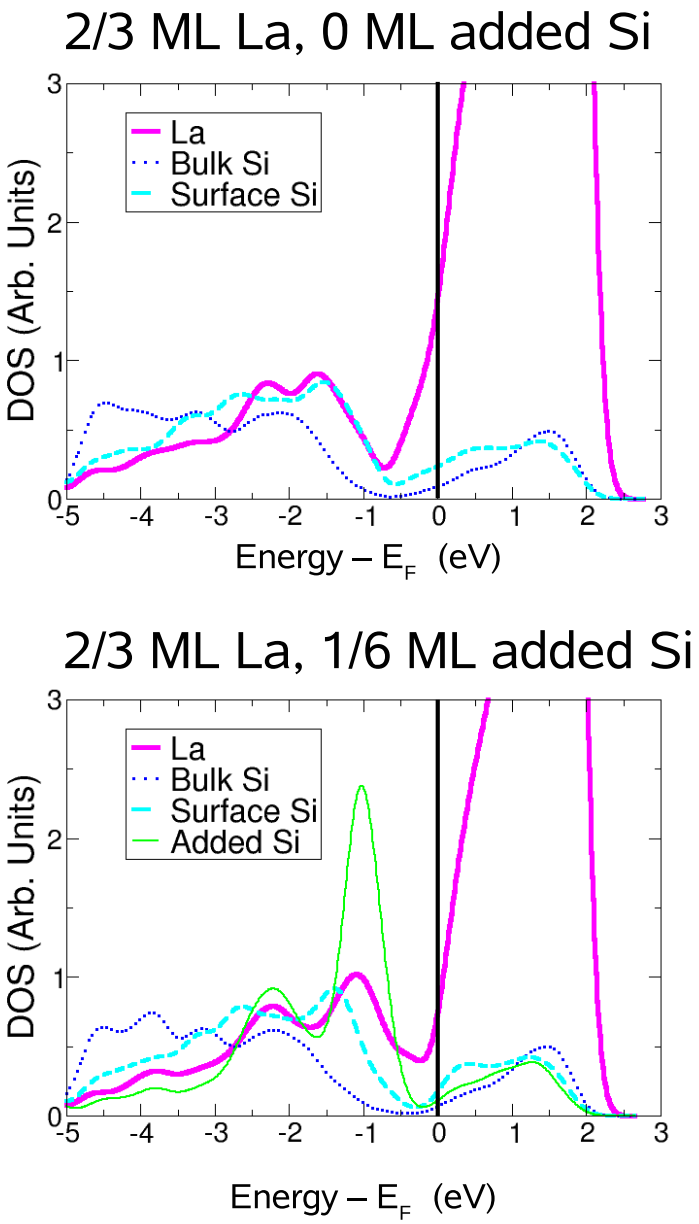

Figure 6.4: (color online) Atomic projected density of states for a) 2/3 ML La broken dimer structure with 0 ML added Si (see Figs. 6.5c and 6.7a), and b) 2/3 ML La broken dimer structure with 1/6 ML added Si (see Fig. 6.7b-d).

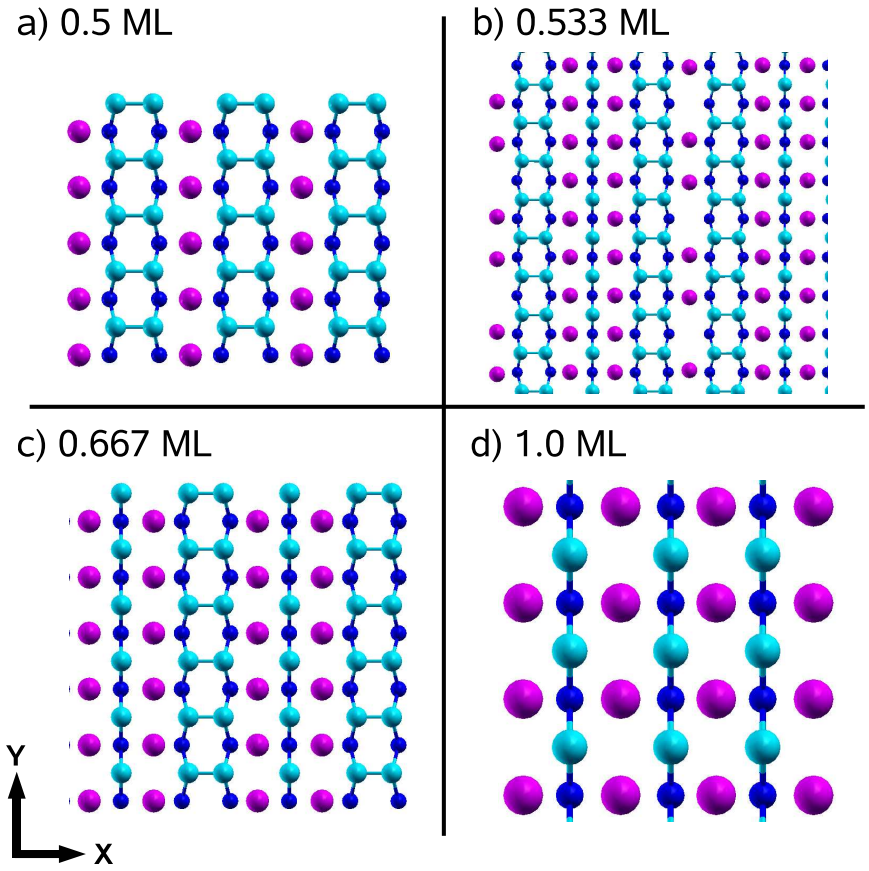

Figure 6.5: (color online) Top view of La structures on a stoichiometric Si surface with a) 1/2 ML b) 8/15 ML c) 2/3 ML and d) 1.0 ML coverage. See table 6.2.

6.4 Non-Stoichiometric Si surfaces.

Based on our experience with Sr on Si[73, 19, 10] and Sr on Ge (see chapters 3-5) we expect that a) Si will be mobile on the surface at typical oxide deposition temperatures of 800K, and b) increasing La coverage will increase Sr mobility at a given temperature. In order to get a rough estimate of the surface mobility of Si at different La coverages, we calculate the energy barrier for a Si dimer to break on the surface. We do these calculations in 2×2 and 2×3 units cells with different La coverages. Due to unphysical periodic boundary conditions, this unit cell allows the dimer to reform after breaking; however, we are only interested in getting an energy scale for Si motion on the surface, and once the dimer is broken, the resulting Si adatoms will be mobile at typical deposition temperatures.[67]

We find that La greatly reduces the energy required to break to Si dimer bond (see table 6.3). In fact, La is significantly more effective in reducing the Si energy barrier than Sr, which only lowers the Si dimer breaking barrier to 0.63 eV at 0.5 ML Sr coverage.[73] We attribute the large reduction in energy barrier to the three electrons donated per La, which help to passivate the additional dangling bonds present in the transition state structures. We use simple transition state theory (see Eq. 6.1) to calculate that even at room temperature, Si will be mobile on the surface for La coverages near 0.5 ML. This barrier lowering effect will limit the effectiveness of low temperature La deposition in kinetically limiting Si motion, a technique which has been successfully used to deposit Sr on Si without forming intermediate silicide structures.[10]

Table 6.3: Energy barriers to break a Si dimer bond (see Fig 6.1) at various La coverages, and estimated hopping rates.

La Cov. (ML)	Barrier (eV)	Hop Rate 300 K (Hz)	Hop Rate 800 K (Hz)
0	1.29	8×10^{-10}	3×10^{4}
1/6	0.65	5×10^{1}	3×10^{8}
1/4	0.53	5×10^{3}	2×10^{9}
1/2	0.37	2×10^{6}	2×10^{10}

6.4.1 Non-stoichiometric $\leq$ 1/3 ML .

Both Sr on Si[73, 10] and the similar Sr on Ge have structures at 1/6 ML Sr coverage based on a 2×3 unit cell with two dimer vacancies (see Fig. 6.6a,b, and Secs. 3.5 and 5.4). This unusually stable structure for these materials inspires us to consider a variety of La structures with unusual Si coverage or bonding. Four of the lowest energy structures we find are in Fig 6.6, and their energies are in table 6.4; however, none of these structures are more stable than the variety of chain structures in Sec. 6.3.1. In particular, the 1/6 ML dimer vacancy structure (Fig. 6.6a-b), which is insulating for a Sr adatom, has too many electrons when Sr is replaced with La, resulting in La changing to its unfavorable (+2) oxidation state. Similar structures with lower La coverage, like Fig. 6.6c, require too many unfavorable Si bonds to be stable.

In addition to dimer vacancy structures, we also consider a variety of structures with modified Si dimer rows. The best of these structures is shown in Fig 6.6d, and it is the most stable structure we find at 1/4 ML. The stability of this structure is due to the extra space afforded by the skewed dimer rows, which allow the La to avoid occupying nearest neighbor trough sites while maintaining favorable dimer buckling, despite the high coverage (see discussion in Sec. 6.3.1). However, this structure is not thermodynamically stable, as the system can lower its energy by 0.03 eV/La by phase separating into the 1/5 and 1/3 ML chains discussed in Sec. 6.3.1 (see Fig.

Table 6.4: Binding energies of La at various coverages with modified Si bonding patterns.

La Coverage (ML)	Si Coverage (eV)	E_{bind} (eV)	Fig.
1/12	2/3	6.64	6.6c
1/6	1/3	6.79	6.6a-b
1/4	0	6.73	6.6d

6.8a).

6.4.2 Non-stoichiometric > 1/3 ML.

As mentioned in Sec. 6.3.2, for structures with La coverage above above 1/3 ML, even after adopting structures with broken dimers, all of the structures we find to be thermodynamically stable lack sufficient low energy Si states to accommodate the three valence electrons per La added to the surface. Therefore, we consider structures with extra Si on the surface, and we find a series of structures that are significantly lower in energy than the stoichiometric structures mentioned in Sec. 6.3.2 (see table 6.5, and also Sec. 3.9).

These new structures can be constructed by adding extra Si to the various broken dimer structures in Fig. 6.5 b-d. As seen in Fig. 6.7 a-b, the extra Si sits above one of the surface atoms without a dimer bond. The p_z orbital of this additional Si forms a covalent bond with the Si below it, which normally has two dangling bonds. This bonding creates a filled bonding and an empty antibonding state, and leaves the p_x and p_y orbitals half-filled and able to accept electrons from the La. This process can be seen in Fig. 6.7 c and d, which shows the process of charge transfer from La to the extra Si. When the extra Si is added to the surface, charge leaves the red areas of Fig. 6.7c around the La^{+2} and moves to the blue donut-shaped region in Fig. 6.7d, which is a combination of the p_x and p_y orbitals of the extra Si.

The same process can be seen in the projected DOS in Fig. 6.4a and b. Fig.

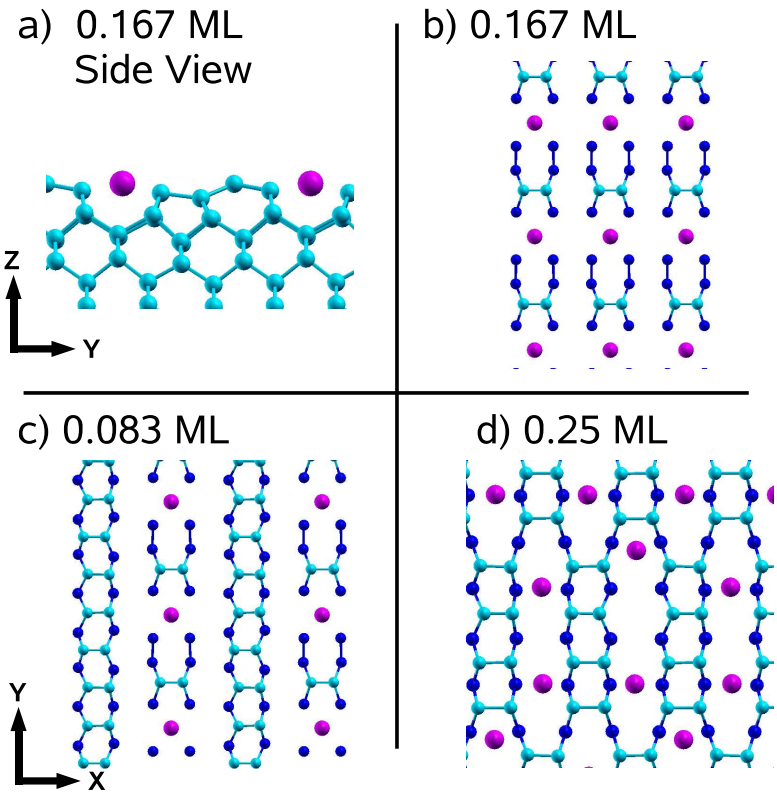

Figure 6.6: (color online) La structures with modified Si bonding patterns (see table 6.4. a-b) Side and top view of 1/6 ML La structure with two dimer vacancies c) 1/12 ML La dimer vacancy structure d) 1/4 ML La with skewed dimer rows.

Table 6.5: Binding energies for structures with added Si on the surface.

La Coverage(ML)	Si Coverage (ML)	$E_{bind}(eV)$	Fig.
2/3	0	6.32	6.5a
2/3	1/6	6.62	6.7b
2/3	2/9	6.64	
2/3	1/4	6.63	
2/3	1/3	6.62	
1	0	5.80	6.5d
1	1/4	5.98	
1	1/3	6.02	
1	1/2	6.13	
1	2/3	6.01	

6.4a shows the DOS for the structure without the extra Si, which has occupied La valence states. Adding 1/6 ML Si to the surface results in Fig. 6.4b, which shows less La occupation as well as the additional Si states, shown in green, which are localized near the top of the valence band of Si. The result of this extra binding can be seen in table 6.5, which shows that the surface can reduce its energy by more than 0.3 eV/La by adopting these structures. We find that at 2/3 ML La coverage, the system prefers slightly less Si than the simple electron counting argument above would predict (2/9 ML instead of 1/3 ML), due to the unfavorable state of the Si bonding; however, there is a wide range of structures with nearly identical energies.

6.5 Phase Diagram

We summarize our findings in the form of a zero temperature phase diagram of La on Si. We begin by looking only at the surface with stoichiometric Si, as shown in the top of Fig. 6.8. As the La coverage increases, the stoichiometric Si surface progresses first through the structures discussed in Sec. 6.3.1. The stable structures consist of chains at 1/10 ML (Fig. 6.2a), 1/5 ML (Fig. 6.2c), and 1/3 ML (Fig. 6.2d). After this point, when the surface no longer has sufficient dangling bonds to

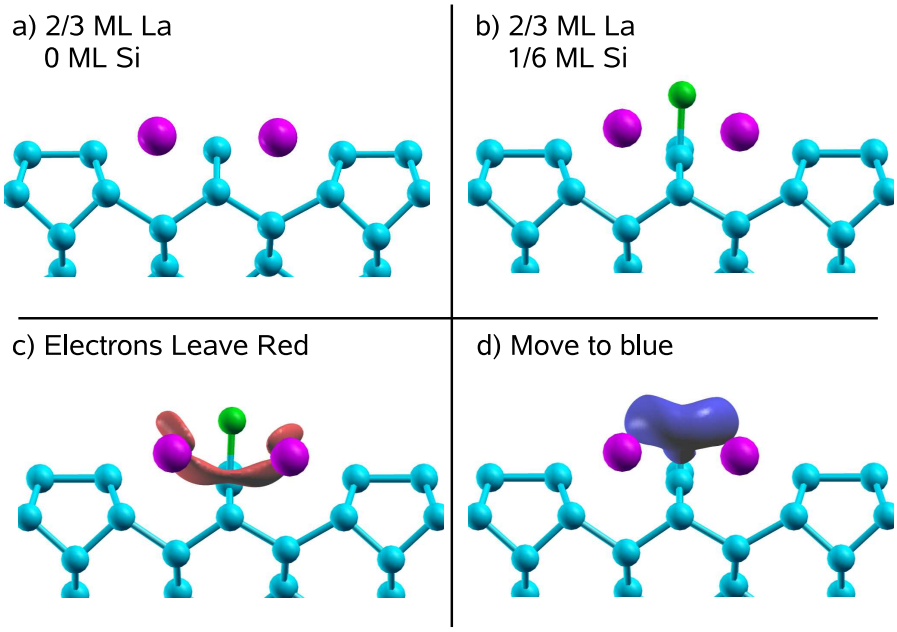

Figure 6.7: (color online) Side views of: a) 2/3 ML La broken dimer structure, 0 ML Si added b) 2/3 ML La broken dimer structure 1/6 ML Si added (added Si in green) c-d) Smoothed charge transfer plots of structure in b). When the extra Si is allowed to interact with surface, charge leaves the red regions around the La in c) and moves to the blue regions in around the added Si in d).

satisfy additional La, there is a reduction in binding, as indicated by change in slope of the phase diagram at 1/3 ML. The surface then progresses through the broken dimer structures of Sec. 6.3.2, at 8/15 ML (Fig. 6.5 b), 3/5 ML, 2/3 ML (Fig. 6.5 c), and 1 ML (Fig. 6.5 d). While this series of surfaces seems relatively promising for oxide deposition, unless the Si is kinetically limited, we should also consider the structures with non-stoichiometric Si coverage.

When we allow our the Si on the surface to become mobile, which according to our energy barrier calculations (see table 6.3) will happen at room temperature for high La coverage, the surface phase diagram changes dramatically (see Fig. 6.8b). At low coverage, the structures are the same; however, the phase diagram no longer has a large change in slope at 1/3 ML, as the surface can continue to accommodate the additional electrons at higher La coverage by adding more Si to the surface. In fact, the 1/3 ML structure is no longer thermodynamically stable, and the surface will begin forming silicide structures once the surface passes 1/5 ML La coverage. In addition, there are a variety of silicide structures with coverages between 1/3 ML and 2/3 ML which are not thermodynamically stable, but have energies only slightly above the bottom of the phase diagram (see the empty blue squares in Fig. 6.8b). These structures consist of dimerized surfaces with La clumped around Si added to the surface (see Fig. 6.9 for an example). For coverages higher than 1 ML, it is likely the surface will begin to form structures which look more like bulk silicides, like the 2 ML silicide structure discussed by Ashman et. al.[95] which consists of two layers of La with Si ions in between.

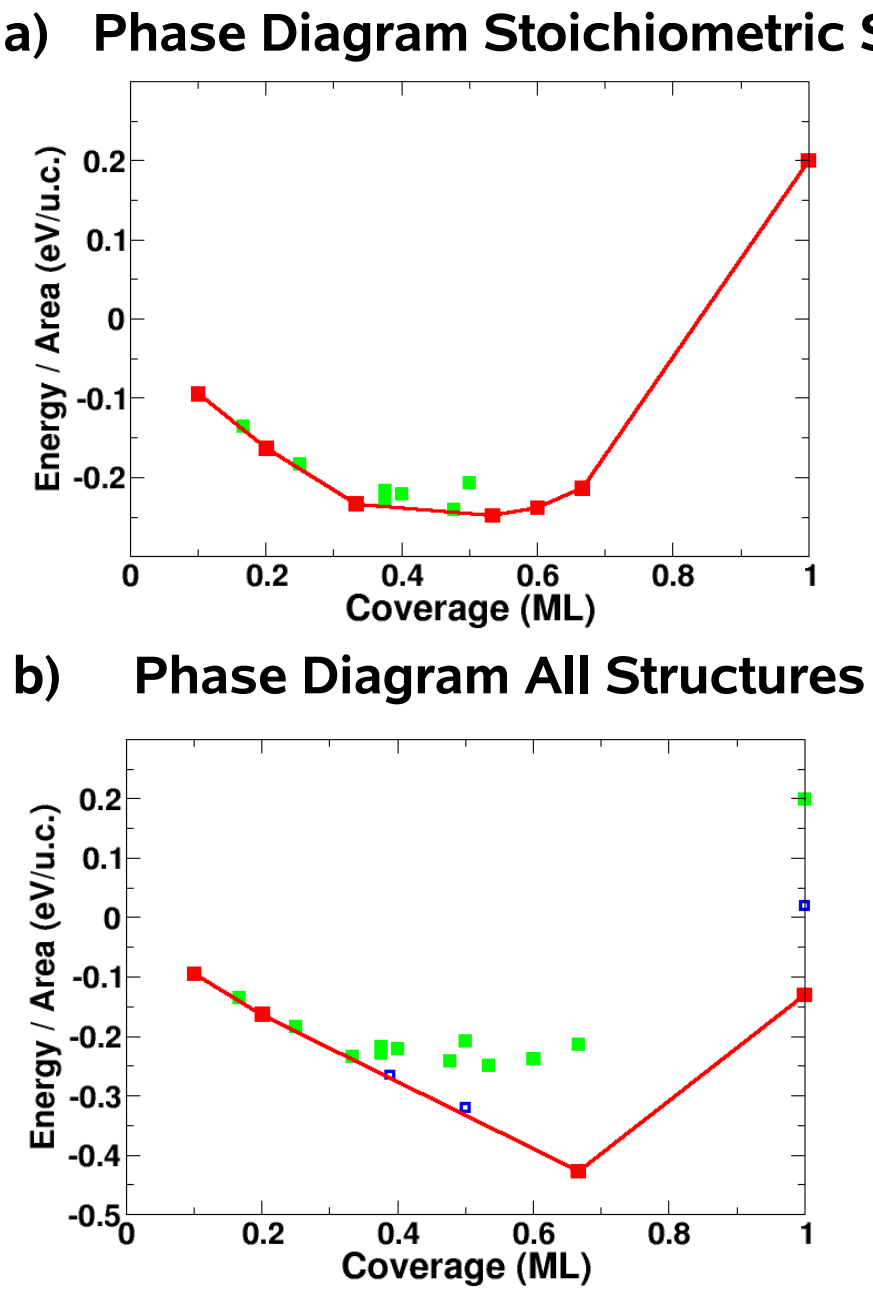

Figure 6.8: (color online) Zero temperature phase diagram. Top: Stoichiometric Si surface. Bottom: All structures. The red lines connect thermodynamically stable structures; other coverages will be a mix of the two nearest thermodynamically stable surfaces. The green filled squares show the stoichiometric surfaces which are near thermodynamically stability, while the blue empty squares show additional silicide structures (see Fig. 6.9).

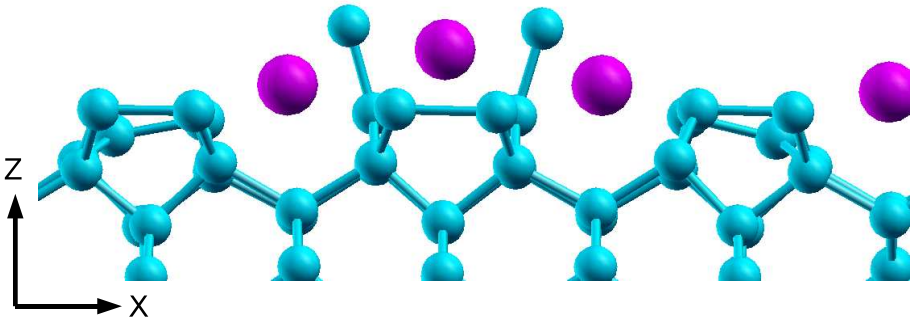

Figure 6.9: (color online) Example of a structure at 0.39 ML La coverage consisting of a high density La cluster surrounding extra surface Si on an otherwise dimerized surface. This structure is not thermodynamically stable at zero temperature, but has a competitive binding energy of 6.69 eV/La (compare to table 6.2).

6.6 Conclusions

We have presented a La on Si phase diagram for both fixed Si bonding (see Fig. 6.8 top) as well as for mobile surface Si (see Fig. 6.8 top). Our phase diagram (see Fig. 6.8, combined with our the results on energy barriers (see Tabs. 6.1 and 6.3) has unfortunate implications for the viability of using La as a replacement for Sr in the epitaxial growth of oxides on Si. In particular, the phase diagram with mobile Si shows that the surface will begin forming silicide structures at coverages greater than 1/5 ML, even before it reaches the 1/3 ML structure which has been proposed[95] as a template for oxide growth. If formed, these silicides will make growing an atomically-sharp epitaxial interface without an interfacial SiO_2 layer essentially impossible. One possible way to suppress silicide formation would be to lower the temperature and kinetically trap the Si; however, that could also be very difficult. First, any La atoms that initially stick to a binding site on top of a dimer row (see Fig. 6.1) will become stuck there at low temperature, preventing the formation of an orderly structure (see table 6.1). Second, and even more worrying, it is likely that Si becomes mobile as the La coverage increases (see table 6.3), even for room temperature deposition, making silicide formation difficult to avoid. Therefore, in chapter 7, we consider methods for

achieving epitaxial growth of La-containing oxides on Si without the deposition of an initial 0.5-1.0 ML of La on the surface.

Chapter 7

$LaAlO_3$ on Si (001)

7.1 Introduction

As mentioned in the previous chapter, there is great scientific and technological interest in growing complex oxides on semiconductors, and $LaAlO_3$ is a particularly interesting material due to possible high-K applications; however, $LaAlO_3$ cannot be grown on epitaxially on Si, and previous attempts to understand the interface that forms when Si is grown on $LaAlO_3$ have not led to growth procedure.[93, 94, 96, 97] In analogy with the successful growth procedure for $SrTiO_3$ on Si, the obvious method for growing $LaAlO_3$ on Si would begin with La deposition; however, the previous chapter has shown that depositing La on Si will result in La silicides for coverages above 0.2 ML, which will prevent a clean interface from forming. Another interesting option would be to begin growth with Al.[96] Unfortunately, although Al forms an ordered surface on Si at low temperatures, it is known to be unstable on Si at high temperatures (although Al remains an interesting possibility for carefully kinetically controlled growth).[98, 99, 100, 101, 102, 103, 104, 105] In order to avoid these difficulties, $LaAlO_3$ is sometimes grown indirectly on a buffer layer of SrO or

$SrTiO_3$[89, 90, 91, 92] although the interfaces are typically not stable when processed at high temperature.

In this work, we seek to understand the difficulties associated with $LaAlO_3$ growth on Si, and we investigate how epitaxial growth may be achieved. In particular, we seek to further understand the technique of using an initial Sr layer to passivate the Si surface and prevent reactions between Si and the desired oxide, and we want to see if this technique can be expanded to $LaAlO_3$ growth. In addition, we want to investigate the issues associated with achieving epitaxial growth of $LaAlO_3$ on the Si (001): in contrast to $SrTiO_3$ (001), the $LaAlO_3$ (001) surface is polar. We concentrate on interfaces with low Sr content (i.e. without several SrO layers). In addition, while $SrTiO_3$ has been used as a buffer layer between $LaAlO_3$ and Si, we wish to avoid using Ti in order to maintain large band offsets with Si, as the relatively low energy Ti-d states form the bottom of the $SrTiO_3$ conduction band and lead to its small band gap and poor band offsets with Si.[106, 107, 108, 109]

7.2 Methods

We perform first-principles density functional theory calculations using a plane wave basis set.[20, 21] We used the PBE GGA to approximate the exchange correlation functional.[28] We simulated the atomic potentials using a combination of norm-conserving and ultrasoft pseudopotentials.[34, 35] In addition to the potentials detailed in chapters 3 and 6, for oxygen, we use $r_s = r_p = 1.1$ Bohr and for aluminum we use $r_s = r_p = 1.76$ Bohr. In both cases, d is local and the atoms are in neutral ground state configurations.

We perform calculations in a slab geometry, with periodic boundary conditions in the x and y directions, and repeated slabs plus vacuum in the z direction. To avoid

spurious electrostatic coupling between periodic slab copies across the vacuum, we perform calculations with 8 layer Si slabs with identical atomic configurations and geometry on both surfaces.[73]

7.2.1 Surface and Interface Thermodynamics

In order to compare the relative thermodynamic stabilities of surfaces with differing numbers of Sr, La, O, Al, and Si, we compare the zero temperature surface free energy per area,

$$F = E_{tot} - \sum_i N_i \mu_i \tag{7.1}$$

where E_{tot} is the total energy of the surface per unit area, N_i is the number of atoms of species i, and μ_i is the chemical potential of species i (the considered species are La, Al, O, Sr, Si). The chemical potential of a species is the energy required to take an atom of that type from a reservoir in order to add it to the surface.

Our goal is to grow $LaAlO_3$ on Si; therefore, we only consider interfaces where both bulk Si and bulk $LaAlO_3$ are stable phases. This places the following constraints on the chemical potentials:

$$E_{Si} = \mu_{Si} \tag{7.2}$$

$$E_{LaAlO_3} = \mu_{La} + \mu_{Al} + 3\mu_O, \tag{7.3}$$

the second of which allows us to eliminate μ_{Al} and only consider μ_{La} and μ_O in our phase diagrams. Here, E_{si} and E_{LaAlO_3} are the energies of bulk Si and $LaAlO_3$, respectively. In addition, we place other limits on the chemical potentials in order to ensure that our structures are stable versus phase separation or decomposition into

various bulk materials. We require that

$$E_{La} > \mu_{La} \tag{7.4}$$

$$E_{O_2} > 2\mu_O \tag{7.5}$$

$$E_{Al} > \mu_{Al} = E_{LaAlO_3} - \mu_{La} - 3\mu_O \tag{7.6}$$

$$E_{Al_2O_3} > 2\mu_{Al} + 3\mu_0 = 2E_{LaAlO_3} - 2\mu_{La} - 3\mu_O \tag{7.7}$$

$$E_{La_2O_3} > 2\mu_{La} + 3\mu_O \tag{7.8}$$

$$E_{SiO_2} > \mu_{Si} + 2\mu_O \tag{7.9}$$

$$E_{Sr} > \mu_{Sr} \tag{7.10}$$

$$E_{SrO} > \mu_{Sr} + \mu_O \tag{7.11}$$

$$E_{SrSiO_3} > \mu_{Si} + \mu_{Sr} + 3\mu_O \tag{7.12}$$

$$E_{SrAl_2O_4} > \mu_{Sr} + 2\mu_{Al} + 4\mu_O \tag{7.13}$$

These limits are apparent in the phase diagrams presented in this chapter. In the La-O phase diagrams (e.g. Fig. 7.4), the area inside the solid red lines is where $LaAlO_3$ is stable with respect to La_2O_3, Al_2O_3, bulk La, bulk Al, and molecular O_2. In addition, the dotted red line marks onset of SiO_2 formation. When plotting the La-O phase diagrams which also contain Sr, we set $\mu_{Sr} = min(E_{Sr}, E_{SrO} - \mu_O) - E_{offset}$. $E_{offset} = 0$ would correspond to the highest possible Sr chemical potential at a given μ_O; however, we also consider lower Sr chemical potentials when considering overall thermodynamic stability of our library of structures.

7.3 La + Sr Template Layers

In order to grow $LaAlO_3$ on Si without an interfacial layer of SiO_2 or another silicate, the structure at every step during the deposition must be either thermodynamically stable or kinetically trapped. We begin by considering the stability of the initial 1-2 layers of SrO on Si, as we know that epitaxial growth of SrO on Si is possible experimentally.[110] Then, we will consider the effects of adding adding La to the system.

7.3.1 Initial Sr + O Layers

The known interfaces for perovskites grown epitaxially on Si have either 0.5 ML Sr (BaO)[77] or 1.0 ML Sr ($SrTiO_3$)[111, 55] at the interface. Growth typicically begins with 0.5-1.5 ML Sr being deposited on a clean Si surface, and then the resulting surface is exposed to oxygen. Here, we consider the formation of the initial Sr and SrO layers.

From both first principles calculations and experiment, we know that 0.5 ML Sr is thermodynamically stable on Si, and that 1.0 ML of Sr is kinetically stable at room temperature (at high temperatures 1.0 ML of Sr forms a silicide, see Sec. 3.9).[73, 10, 6] We consider structures with 0.0-1.5 ML Sr and 0.0-2.0 ML O; some of the thermodynamically stable configurations are shown in Fig. 7.1. The resulting phase diagram is shown in Fig. 7.2.

We find that 0.5 ML Sr with 0.0-1.0 ML O (Figs. 7.1 b-c) are stable versus the formation of bulk Sr, SrO, and SiO_2, which can be seen from Fig. 7.2 because a) each structure is the lowest energy structure in a region of phase space, which is represented by a solid colored region, and b) a portion of this phase space is to the left of both the SrO and SiO_2 phase stability lines (in red), and below the stability line

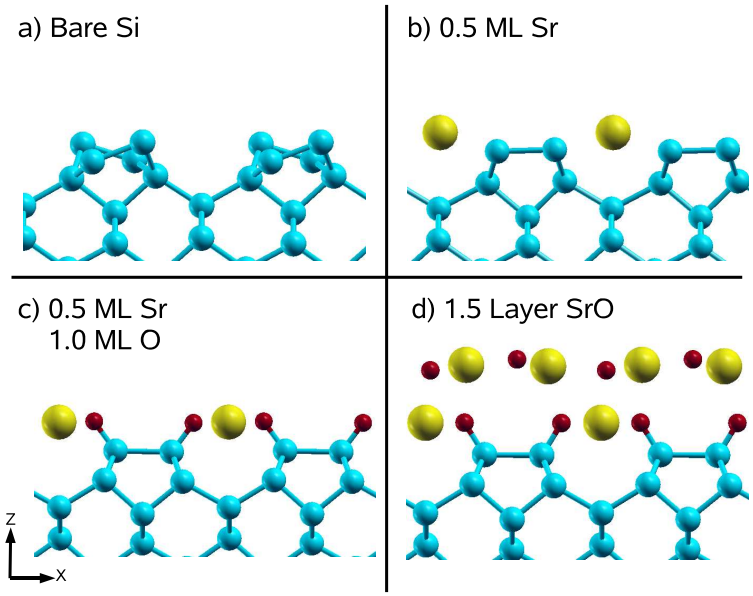

Figure 7.1: (color online) Side view of thermodynamically stable structures with Sr (large yellow atom) + O (small red atom) on the Si(001) surface (see Fig. 7.2). a) Bare Si surface, showing characteristic $2x1$ buckled dimer reconstruction b) 0.5 ML Sr, with flat passivated dimers c) 0.5 ML Sr with 1.0 ML O d) SrO interface structure, with 1.5 ML Sr and 2.0 ML O.

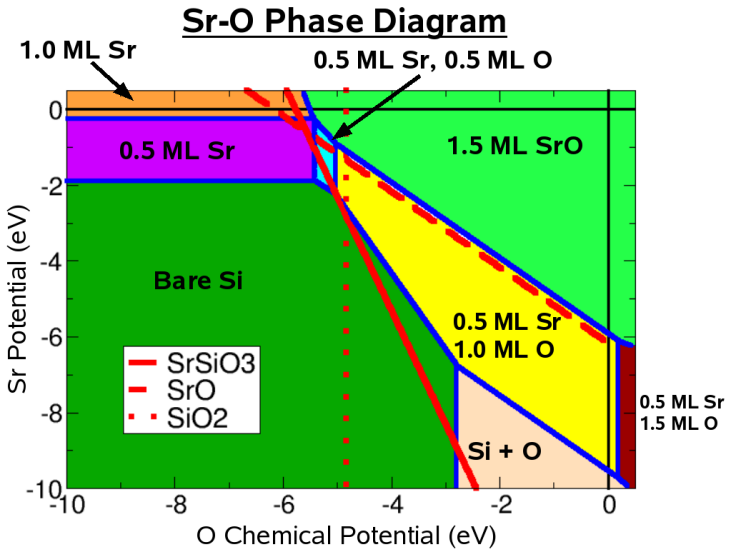

Figure 7.2: (color online) Sr-O phase diagram for structures with $\leq$ 1.5 ML Sr and $\leq$ 2 ML O on an Si (001) surface (see Fig. 7.1). The solid colored areas show the lowest energy structure at each region of phase space. The red lines show phase boundaries of bulk SrO, SiO_2, and $SrSiO_3$; thermodynamically stable surfaces are to the left of these lines.

for bulk Sr, which is the black horizontal line at $\mu_{Sr} = 0$. In addition, the structures with $<$ 1.0 ML O are stable versus the formation of $SrSiO_3$. The structure with 1.0 ML O (Fig. 7.1 c) is not stable versus the formation of bulk $SrSiO_3$. It is likely that the formation of bulk $SrSiO_3$ will be kinetically suppressed at typical deposition temperatures, and the surface will be able to reach 1.0 ML oxygen coverage with 0.5 ML Sr on the surface without forming bulk oxides. This surface is the building block of many of the stable interfaces considered in this work.

We also find that the 1.5 ML SrO structure (Fig. 7.1 d), which has the same structure as the first 1.5 ML of BaO on Si,[77] is not thermodynamically stable. Thermodynamically, even if Si motion is kinetically limited to prevent SiO_2 and $SrSiO_3$ formation, this structure will phase separate into bulk SrO and the 0.5 ML Sr + 1.0 ML O structure (Fig. 7.1c) at all chemical potentials. This instability is likely due to the rumpling in the surface layer required to accommodate the uneven interface layer, in addition to the lattice mismatch of 5% between Si (001) and SrO. Due to the fact that SrO can be grown in a layer-by-layer fashion on Si,[110] it is likely that the formation of bulk SrO (as well as bulk $SrSiO_3$ and SiO_2) is suppressed kinetically during the deposition process. However, if this structure is heated sufficiently to allow full thermodynamic equilibrium, the epitaxial interface will be destroyed, resulting in a combination of $SrSiO_3$, SrO, and SiO_2 on the surface, plus regions of 0.5 ML Sr coverage (Fig 7.1b-c). This instability has been seen experimentally, as SiO_2 and $SrSiO_3$ are formed when a SrO interface is heated above 500°C.[110]

The stability of these Sr-O surfaces is expected, because experimentally the epitaxial growth of oxides on a Sr-based template layer is believed to proceed through the formation of these initial structures. However, due to the unrealistically low μ_O required to keep SiO_2 from forming thermodynamically (-4.8 eV, which corresponds

to roughly 10^{-150} atm at room temperature), these structures are only metastable during typical procedures for the growth of oxides on Si.[52, 6] The fact that these structures can be grown despite the relatively high oxygen chemical potential in experiments the highlights the role of Sr in passivating the surface and kinetically limiting the formation of SiO_2.

7.3.2 Initial Sr + La + O Layers

Next, we investigate similar structures, but with La substituted for 1-2 Sr/2×1 area. We begin by looking at structures without O on the surface. For 1.0-1.5 ML of metal atoms, the surface is more stable with La bonded to the Si, as in Fig. 7.3a, which is 0.7 eV/2 × 1 lower in energy than having the Sr next to the Si. This is not surprising, as the binding energy of an isolated La on Si is nearly 3 eV higher than Sr, due largely to its extra valence electron (see Sec. 6.3). The strong binding of La to Si is problematic for the creation of an ordered interface starting with a Sr-La metallic template layer, as La is not thermodynamically stable at high coverage on Si, and will form various La-silicides even at low temperature (see Sec 6.4.2). However, La-silicide formation might be prevented by adding O to the system, which will allow for the formation of an La oxide layer rather than a silicide layer.

When we add O to the La/Sr system, we find improved interface structures. For sufficient oxygen coverage, we find that that La prefers to bind with oxygen, rather than Si, leaving Sr closest to the Si surface. For example, for structures with 0.5 ML Sr and 1.0 ML La, we show the lowest energy surface with increasing oxygen coverage in Fig. 7.3 a-c. When the surface reaches 2.5 ML O (panel c), the location of the Sr and La switches, and the structure with Sr at the interface and La at the surface becomes more stable by 0.9 eV/2 × 1. This structure consists of a stoichiometric, albeit highly distorted, La_2O_3 layer on top of an interface with 0.5 ML Sr and 1.0

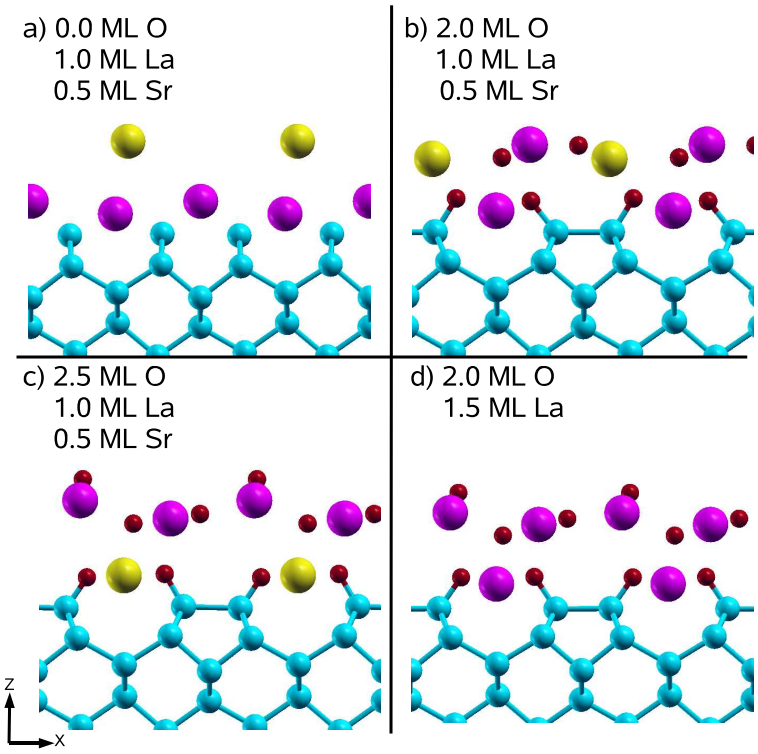

Figure 7.3: (color online) Side view of low energy Sr+La+O structures (Sr is yellow, La is magenta, O is the small red atom). a-c) 0.5 ML Sr, 1.0 ML La, and increasing oxygen coverage. d) 1.5 ML La and 2.5 ML O, with 0.0 ML Sr.

ML O, which we found to be stable in Sec. 7.3.1 (see Fig. 7.1c).

These structures initially appear promising for application as the initial layers of oxide growth, as the interfacial Sr and the La-O bonding will prevent the La from moving to and reacting with the Si surface. Unfortunately, none of these structures are thermodynamically stable with respect to the formation of bulk La_2O_3 plus a surface with 0.5 ML Sr + O (see Fig. 7.1 c). This can be seen in Fig. 7.4, which shows the La-O phase diagram for structures with 0.5 - 1.5 layer of metal (Sr/La) plus oxygen under high μ_{Sr} conditions. This diagram shows that throughout the region where $LaAlO_3$ is stable (bounded by solid red lines), none of the proposed Sr+La+O structures are stable; instead, the surface prefers structures with only Sr and O. All of the Sr+La+O structures with Sr at the interface are grouped in the lower right corner of the phase diagram, due to their high O and low La content. Reducing the Sr chemical potential does not result in any of the structures with La becoming stable, expect for the 1.5 ML La, 2.5 ML O, 0.0 ML Sr structure in Fig. 7.3d. While this structure becomes favorable relative to a bare Si surface and La_2O_3, it is still unstable relative to SiO_2 formation. In addition, it will be very difficult to form an good interface with this material, as both La and O alone are unstable on Si.

While the thermodynamic analysis above suggests that these Sr+La+O interface structures probably will never be useful for epitaxial oxide growth, it is possible that they can be stabilized kinetically if the formation of bulk SrO and La_2O_3 can be prevented, in the same way that the 1.5 ML SrO structure (Fig. 7.1d) is kinetically stabilized during growth despite being thermodynamically unstable. In particular, the structure in Fig. 7.3c is 0.6 eV/1 $\times$ 1 less stable than the 0.5 ML Sr + 1.0 ML O surface layer and bulk La_2O_3. This is only 0.3 eV/1 $\times$ 1 worse than the 1.5 ML SrO structure and bulk SrO (Fig. 7.1d).

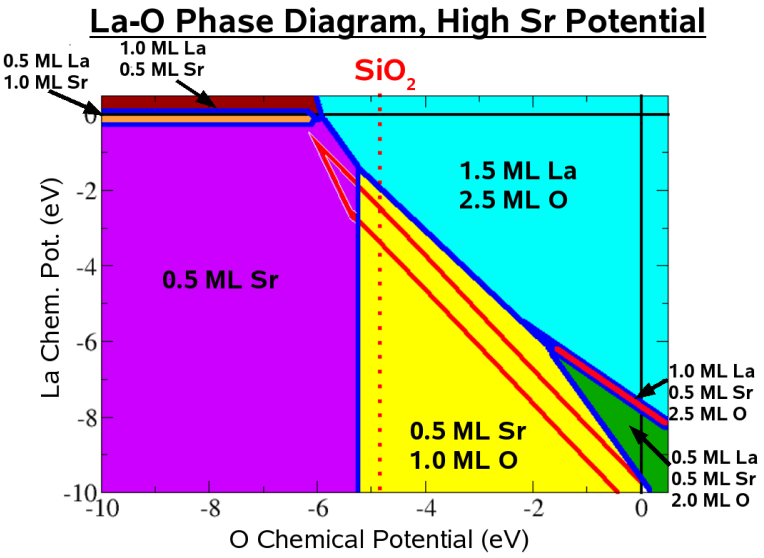

Figure 7.4: (color online) La-O Phase diagram for structures with La, Sr, and O. The Sr chemical potential is set to the highest value that will not result in bulk Sr or SrO formation at a given μ_O (high Sr conditions). $LaAlO_3$ is stable in the area between the red solid lines (which are due to La_2O_3, Al_2O_3, and bulk Al), and the line dotted red line indicates the onset of SiO_2 formation.

The extra instability of the La_2O_3 structure, relative to the SrO structure, is likely due to the incompatible interface between hexagonal La_2O_3 and cubic Si (001). In addition, it is possible that there is a more stable interface structure for these materials in a larger unit cell than we are able to study computationally; therefore, the 0.6 eV/1×1 is an upper limit to the instability.

7.4 Interface Structures

7.4.1 Pure $LaAlO_3$ Interface Structures

After achieving either a thermodynamically stable or kinetically stable template layer for oxide growth (see Sec. 7.3), the next step in $LaAlO_3$ growth is to begin depositing $LaAlO_3$ in a way that will result in a stable interface structure. We begin by examining possible pure $LaAlO_3$ interfaces (without Sr) and highlighting

the difficulties with using them for epitaxial oxide growth.

We consider structures with a stoichiometric Si surface in a 2×1 unit cell with 0.5-1 ML La at the interface, in analogy with the BaO and $SrTiO_3$ interfaces with Si, as well as structures in a 3×1 unit cell with 0.67 ML La at the interface, which is the symmetry and coverage observed experimentally during the growth of Si on $LaAlO_3$[93, 94]. All of our structures consist of some sort of interface layer capped with a full $LaAlO_3$ layer, with the AlO_2 plane closer to the Si, and the LaO plane on the surface. We considered adding an additional AlO_2 layer to the surface, but we find only the LaO-termination results in low energy structures in the region of phase space where $LaAlO_3$ is stable.

The resulting phase diagram is in Fig. 7.5, and some of the low energy structures are detailed in Fig. 7.6. The low energy structures in the region of $LaAlO_3$ stability have either a 2×1 reconstruction and with 0.5 ML La and 0-1.5 ML O at the interface (see Fig. 7.6b-d), or a 3×1 structure pictured in Fig. 7.6a, without O at the interface.[93] While these are the lowest energy structures from the class we investigated, none of them are thermodynamically stable; all of them will lower their energy by decomposing into a bare Si surface and bulk oxides or metals. This is consistent with the three-dimensional growth observed for Si on $LaAlO_3$.[93] Therefore, none of these structures appear to be suitable for oxide growth on Si.

Part of the instability of the interfaces considered in Fig. 7.6 is due to the fact that all of them have too many electrons at the interface layer, resulting in electrons occupying both high energy La valence states and the Si conduction band. This can be seen by looking at the top two panels in Fig. 7.7, which show the projected density of states (DOS) for the interface atoms in Figs. 7.6b-c (the 3×1 structure has a similar DOS as well). The Fermi level of both structures is in the Si conduction band, and both structures have partially occupied La states at the interface. Each

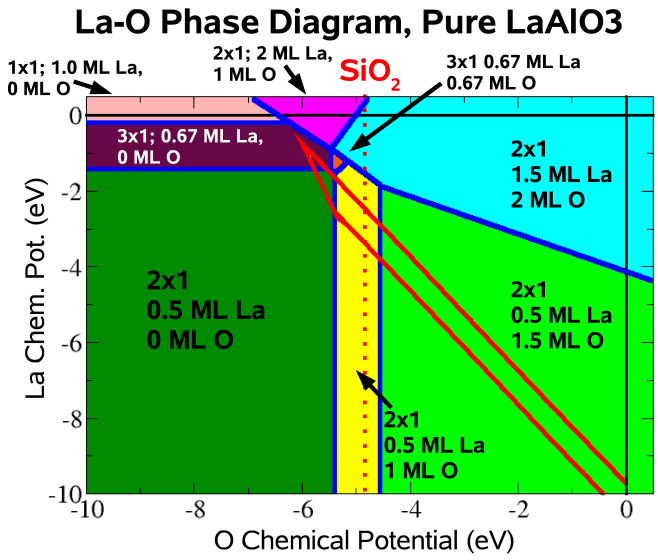

Figure 7.5: (color online) La-O Phase diagram for interface structures with La, Al, and O, and a stoichiometric Si surface (see Fig. 7.6). Structures are labeled by their interface symmetry and stoichiometry. The region between the solid red lines is where $LaAlO_3$ is thermodynamically stable, and SiO_2 is stable to the right of the red dotted line.

structure has 1 La per 2×1 area at the interface, which contributes three valence electrons, but only two half-filled Si dangling bonds to accept electrons, resulting in an excess of electrons. In addition, the structure in Fig. 7.6c has an additional 1 ML of oxygen at the interface; however, somewhat counter-intuitively, the number of oxygen bound to surface Si does not affect the electron counting at the interface.[94] This is due to the fact that each O binds to a dangling half-filled Si bond. This creates a low energy bonding state, which is filled, and high energy anti-bonding state, which remains empty. Therefore, the oxygen, which would normally accept two electrons, instead passivates the Si dangling bond and can only accept one electron, which is the same number as the original half-filled dangling Si bond.

While changing the amount of oxygen at the interface has no effect on the electron counting, it is possible to add holes to the system by substituting Al for Si, as Al has one fewer electron but similar sp^3 bonding.[94] While controlling the substitution of

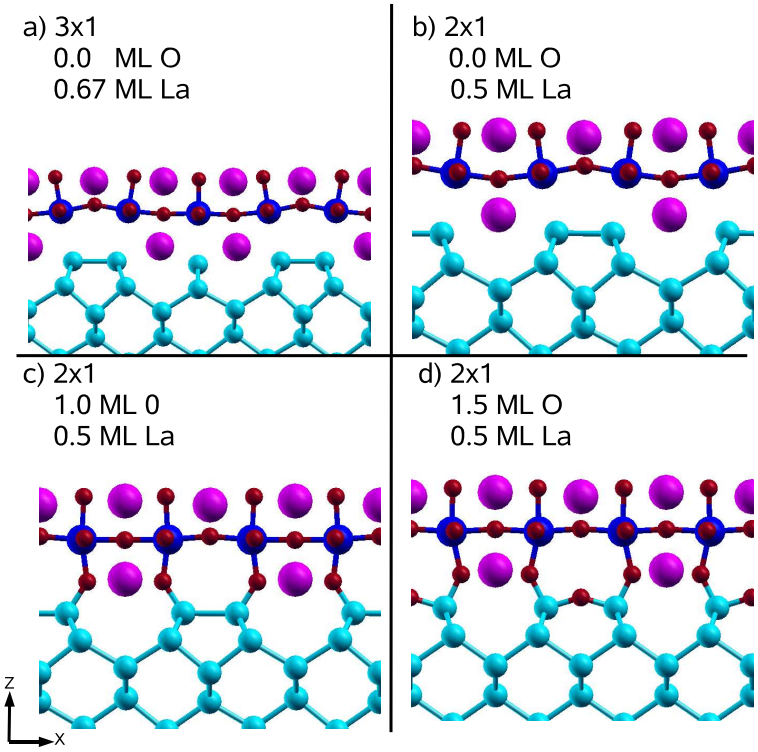

Figure 7.6: (color online) Side view of $LaAlO_3$ interfaces plus 1 ML $LaAlO_3$. a) 3×1 structure with 0.67 ML La at the interface. b-d) 2×1 structures with 0.5 ML La and increasing O coverage. Al is in dark blue.

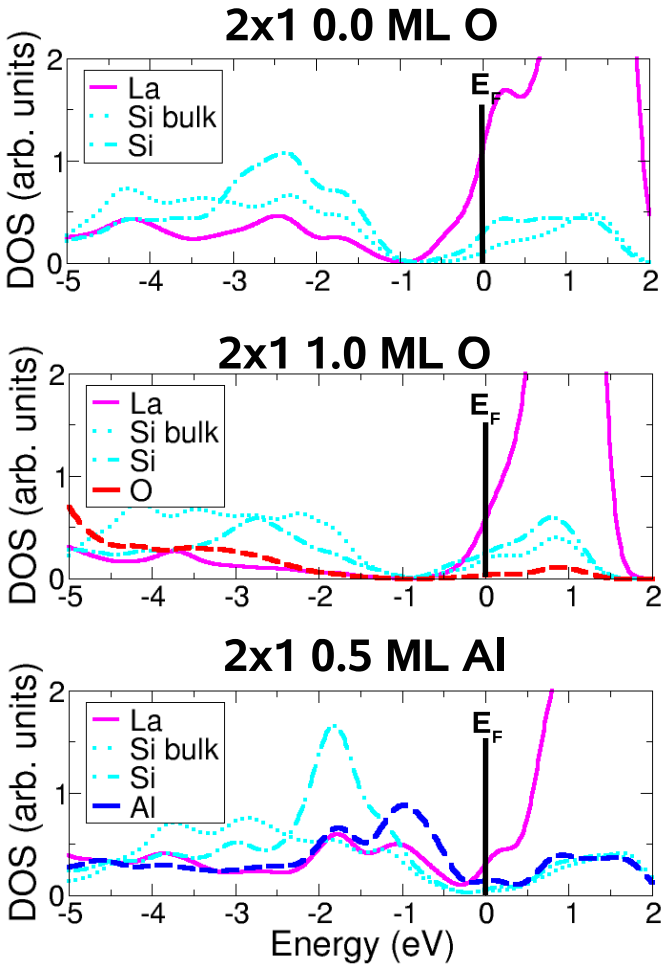

Figure 7.7: (color online) Atomic projected density of states (DOS) of the interface atoms (and bulk Si) of $LaAlO_3$ interface structures. Top: DOS for Fig. 7.6b. Center: Fig. 7.6c. Bottom: Fig. 7.8b

Al for Si without forming unwanted silicides at the interface during deposition of $LaAlO_3$ on Si would be very difficult experimentally, we consider the effects of Al substitution on our structures with 1 ML $LaAlO_3$.

By allowing Al substitution, we find that the structure in Fig. 7.8a becomes one of the low energy structures in the region where $LaAlO_3$ is stable, and other similar structures, like Fig. 7.8b-c become low energy structures in high Al regions of phase space. As expected, the substitution of 0.5 ML Al for 0.5 ML Si reduces the Fermi level at the interface, which can be seen by comparing the Fermi level of the bottom panel of Fig. 7.7 to the other two panels. Al substitution reduces Fermi level to below the bottom of the silicon conduction band; however, we find that the interface is still metallic, as the interfacial Al and La bands cross. While these interfaces with Al substitution are the lowest energy structures in parts of phase space, like the structures considered above, none of these structures is thermodynamically stable, and the system will lower its energy by decomposing into bulk oxides and a bare Si surface rather than form these structures.

7.4.2 Sr + $LaAlO_3$ Interface Structures

Due to the fact that Sr is already necessary to passivate a Si surface, as explained in Sec. 7.3, it is natural to consider whether the substitution of Sr for La in an $LaAlO_3$ film can be used to improve the stability of its interface with Si. The first possible benefit of Sr incorporation into the interface would be to add holes to the system, in analogy with how Al for Si substitution improves film stability (see Sec. 7.4.2). A second benefit of Sr would be to provide a mechanism to compensate the polar surface of LaO-terminated $LaAlO_3$.

Along the (001) direction, each atomic plane of $LaAlO_3$ is charged (i.e. it is polar). In particular, in the ionic limit, each LaO plane donates one electron per

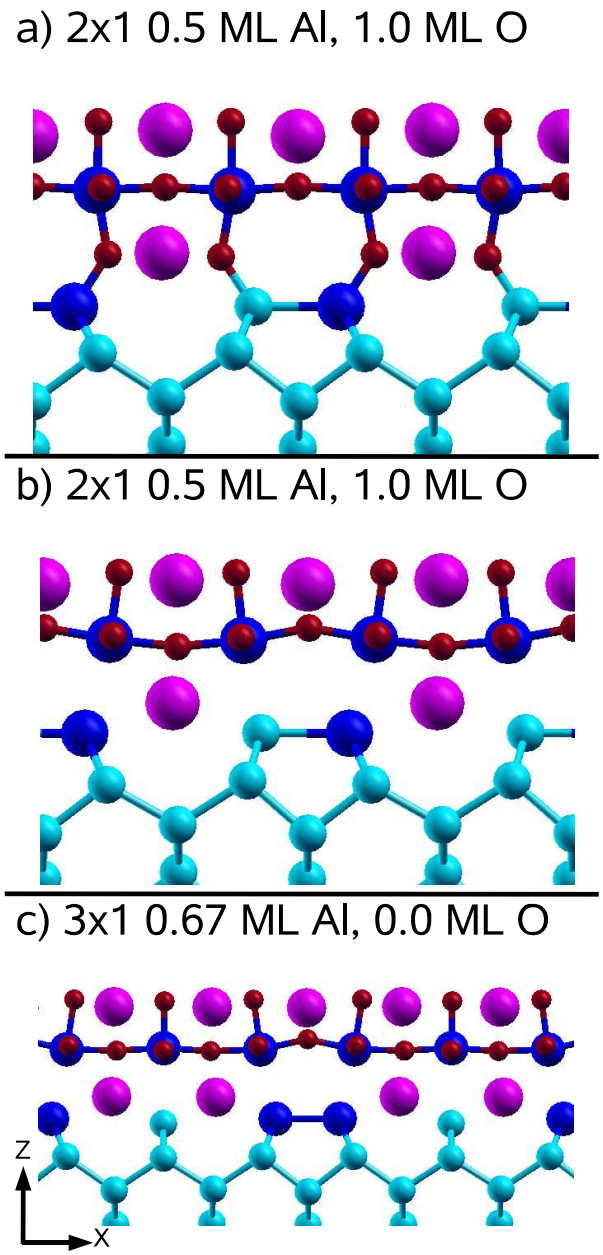

Figure 7.8: (color online) Side view of low energy interface structures with Al substituted for Si, and 1 ML $LaAlO_3$. a) 2×1 structure with 0.5 ML La, 0.5 ML Al, and 1.0 ML O. b) 2×1 structure with 0.5 ML La, 0.5 ML Al, and 0.0 ML O. c) 3×1 structure with 0.67 ML La, 0.67 ML Al, and 0.0 ML O.

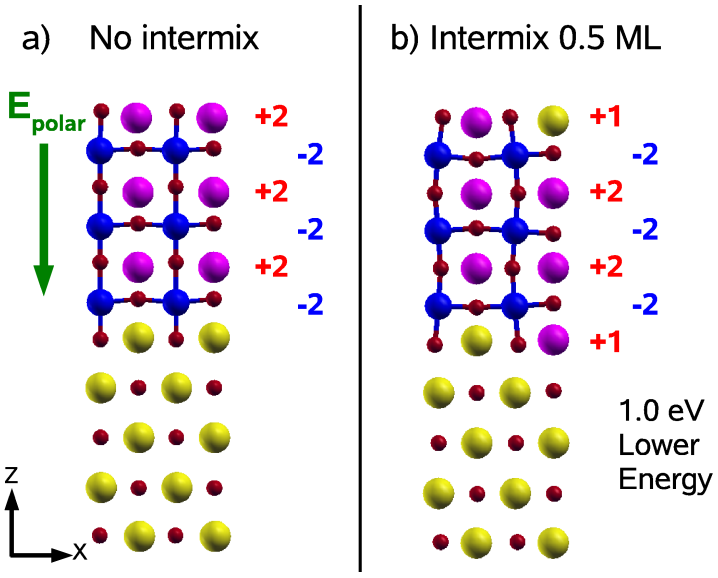

Figure 7.9: (color online) 3 layers of $LaAlO_3$ on an SrO substrate with a 2×1 unit cell. a) No intermixing. Both the LaO surface layer and AlO_2 interface layer are charged, leading to a polar field through the film. b) By intermixing 0.5 ML Sr and La, the charge distribution becomes symmetric, which cancels the long range polar field and reduces the energy of the structure by 1.0 eV/2×1 area.

1×1 area, and each AlO_2 plane accepts one electron. For a stoichiometric $LaAlO_3$ film terminated on one side by an LaO plane, and the other side by an AlO_2 plane, this creates an electric field through the film. Because the energy associated with this field scales with film thickness, continuing oxide growth will require either an electronic or atomic reconstruction at each surface to cancel the field (see Fig. 7.9a). For growth on an SrO substrate, one way achieve this cancellation and stabilize the surface would be to substitute Sr for La at both the surface and interface (see Fig. 7.9b). Finding structures with the 0.5 ML Sr at the surface and interface as $LaAlO_3$ growth proceeds should improve crystal quality and stability.

Keeping in mind the need for both interface and surface stability, we again search for films in 2×1 and 3×1 unit cells, but with Sr substituted for La. In Fig. 7.10, we show the resulting phase diagram under high Sr conditions (E_{offset} = 0.25 eV). Several of the structures which are the lowest energy structures in a region of phase

space where $LaAlO_3$ is stable are shown in Fig. 7.11.

Unlike all of the interface structures considered in section 7.4.1, the structures in Figs. 7.11a-c are more stable than forming bulk oxides plus a bare Si surface. The 1×1 $SrTiO_3$-like[111, 55] interface in Fig. 7.11c is also stable against SiO_2 and $SrSiO_3$ formation; however, as discussed in Sec. 7.3.1, the oxygen chemical potential required to achieve this is unrealistically low. The related structure in 7.11d is also stable against SiO_2 formation; however, it will decompose into $SrAl_2O_4$ thermodynamically. The stability of the structures in Figs. 7.11a-d suggests that these structures are excellent candidates for growth of an epitaxial interface of $LaAlO_3$ on Si. In principle, these interfaces will still decompose into the 0.5 ML Sr surface structures (see Fig. 7.1a-b) and bulk oxides. However, they are all as stable or more stable than the 1.5 ML SrO structure, which can be grown experimentally, and the best $LaAlO_3$ interfaces with Sr incorporated are more than 0.6 eV/1×1 eV more stable than the best interfaces without Sr.

In addition to being thermodynamically stable, the interfaces of Fig. 7.11b-c can accommodate additional $LaAlO_3$ layers without creating a polar field (see Fig. 7.9). In order to do avoid a polar field, the additional $LaAlO_3$ layers must be incorporated into the middle of the slab, as demonstrated in our proposed interface structures in Fig. 7.12, while a layer with 0.5 ML Sr, 0.5 ML La, and 1.0 ML O remains on the surface. As discussed above, the 0.5 ML Sr will compensate for the normally polar LaO-terminated surface and provide a flat, neutral surface to continue layer-by-layer $LaAlO_3$ growth. This can be seen in Fig. 7.13, which shows the atomic projected DOS for the 2×1 interface structure in Fig. 7.12a. The Fermi level is in the band gap of both Si and $LaAlO_3$, the film is insulating throughout, and the polar field is canceled.

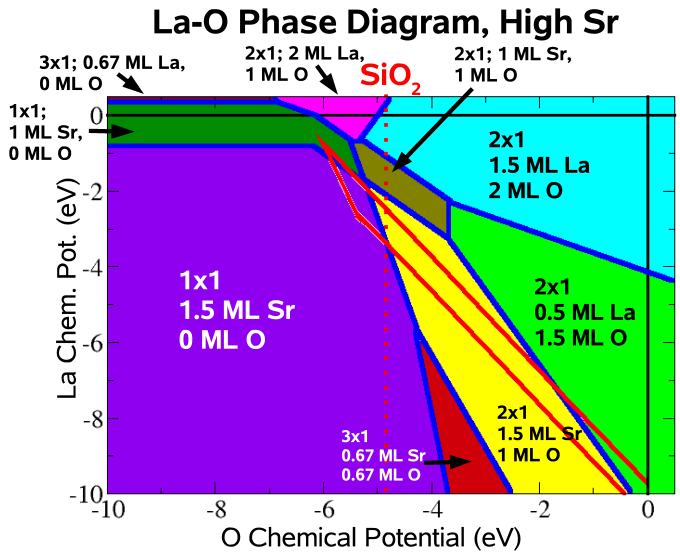

Figure 7.10: (color online) La-O phase diagram of $LaAlO_3$+Sr interfaces, under high Sr conditions (0.25 eV below maximum μ_{Sr}). Structures are labeled by O at interface and total Sr content, or La at the interface if they have no Sr. Some of the low energy structures are shown in Fig. 7.11.

7.5 Proposal for Epitaxial Growth

Based on our calculations, the following example growth procedures should result in epitaxial growth of $LaAlO_3$ on a minimal SrO buffer layer.

Growth Procedure for 2×1 O-rich interface (Fig. 7.12a), starting with a clean Si (001) substrate:

1. Deposit 0.5 ML Sr at high temperature (500°C).

2. At low temperature (25°C), deposit 1.0 ML Sr + O to get 1.5 ML SrO (Fig. 7.1d).

3. Still at low temperature (25°C), deposit 1.0 ML $LaAlO_3$, then anneal at a moderate temperature to get to Fig. 7.11b.

4. Continue depositing $LaAlO_3$ at high enough temperature to allow 0.5 ML Sr to remain mobile and on the surface.

Growth Procedure for 1×1 O-poor interface (Fig. 7.12b), starting with a clean

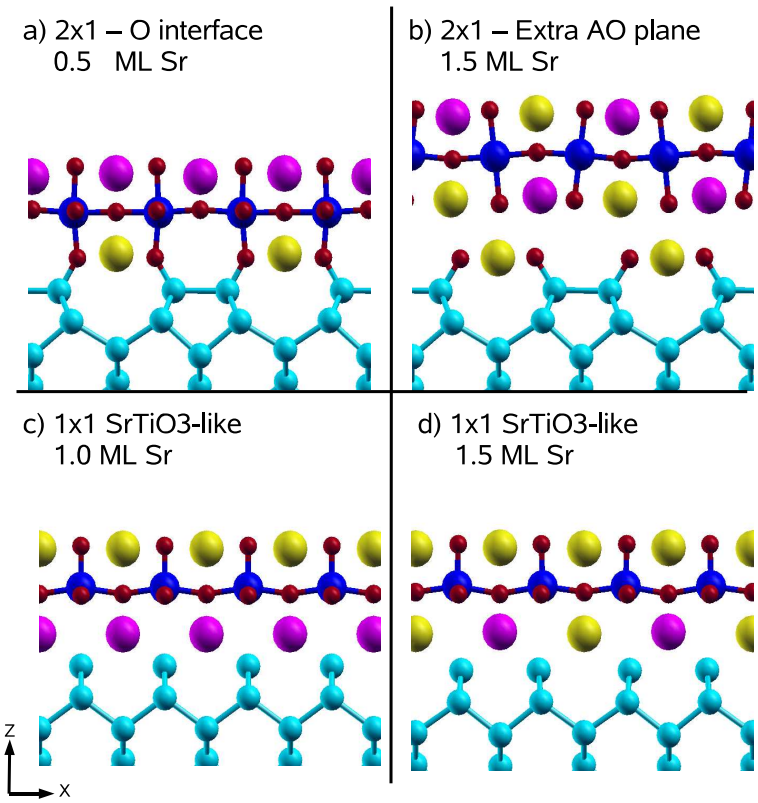

Figure 7.11: (color online) Side view of low energy interface structures with Sr. a) 2×1 0.5 ML Sr and 1.0 ML O at interface b) 2×1 with extra AO atomic plane, 1.5 ML Sr, c-d) 1×1 $SrTiO_3$-like interfaces, with 1.0 and 1.5 ML Sr

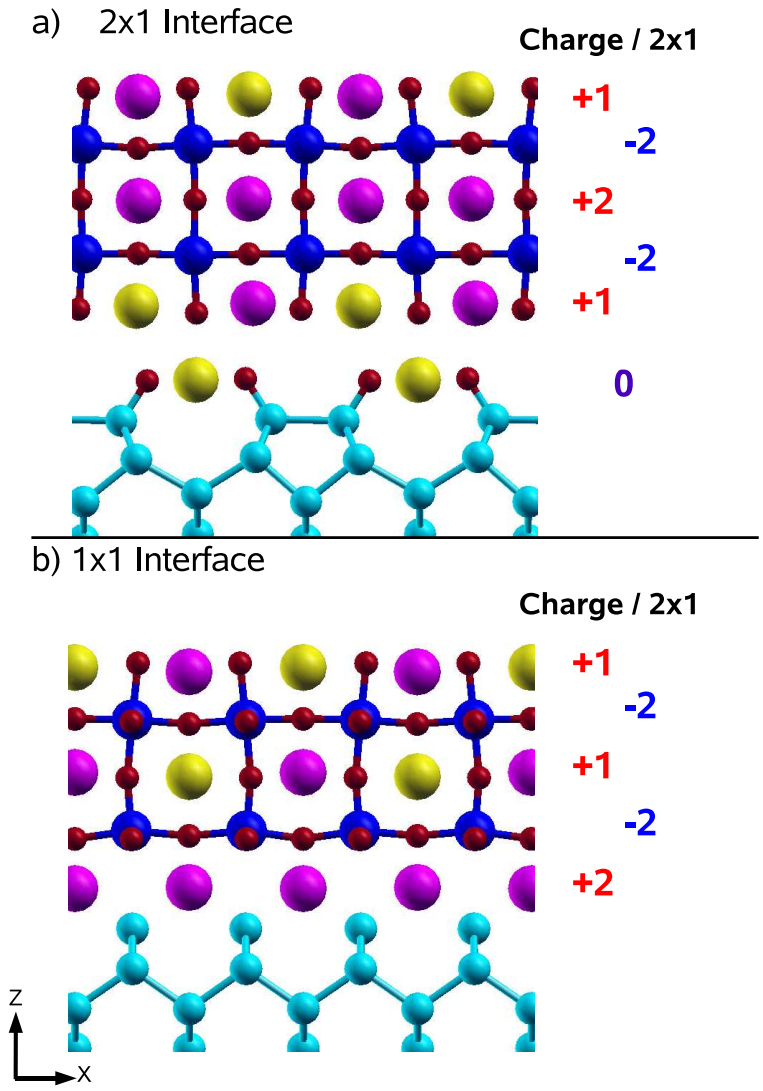

Figure 7.12: (color online) Side view of two proposed interface structures, as well as the formal ionic charge per 2×1 layer. a) 2×1 BaO-like interface b) 1×1 $SrTiO_3$-like interface.

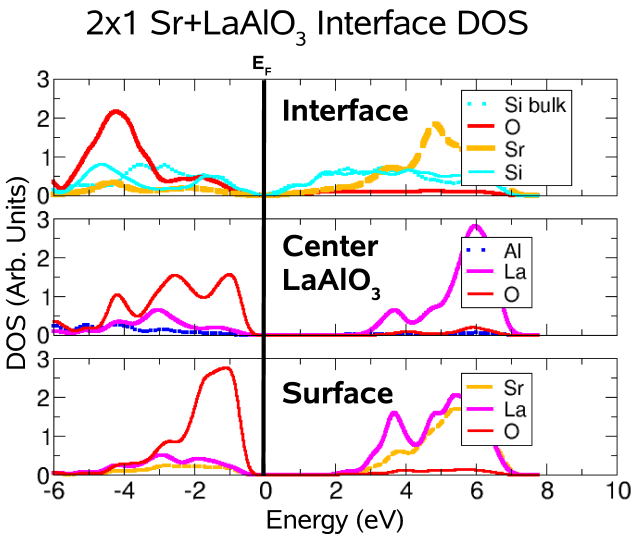

Figure 7.13: (color online) Atomic projected density of states (DOS) for structure in Fig. 7.12a. The top panel shows the interface layer (and bulk Si), the center panel shows the $LaAlO_3$ layer, and the lower panel shows the surface atoms.

Si (001) substrate:

1. Deposit 0.5 ML Sr at high temperature (500°C).

2. At low temperature (25°C), expose to oxygen and deposit 1.0 ML La to reach Fig. 7.3b or c.

3. Deposit 1.0 ML Al and 0.5 ML Sr and anneal at moderate temperature to reach 7.11c.

4. Continue depositing $LaAlO_3$ at high enough temperature to allow 0.5 ML Sr to remain mobile and on the surface.

In both procedures, it is important initially to carefully control growth kinetics in order to get to the stable structures in Fig. 7.11 without creating SiO_2, silicides, or unwanted three-dimensional oxides, and then raise the temperature to ensure Sr incorporation into the interface and surface, which can compensate for the polar field (see Fig. 7.9).

7.6 Summary

First, we investigated the initial 0.5-1.5 ML of SrO on Si. We find that the 1.5 ML SrO on Si structure will decompose into 0.5 ML Sr on Si plus bulk SrO thermodynamically, but can be stabilized kinetically. We find that similar structures containing La can also be stabilized with sufficient oxygen, and act as precursors for the growth of $LaAlO_3$. We find that interfaces with only $LaAlO_3$ are not thermodynamically stable, but by incorportating Sr into the interfaces, we can both add holes to the interface and cancel the polar field, which should allow for the epitaxial growth of $LaAlO_3$ on Si with an insulating interface. Using the results of our thermodynamic analysis of the surface structures, we propose growth procedures for two possible interfaces for $LaAlO_3$ on Si.

Chapter 8

Ferroelectric Surface Chemistry

Due to a large, persistent response to electric fields, ferroelectric substrates offer a unique opportunity to tune the properties of a surface via an external field, potentially providing an avenue for advanced surface chemistry. By using an electric field to change the polarization direction of a ferroelectric substrate, one can potentially reversibly modify the surface Fermi level, atomic geometry, or even stoichiometry, all of which can alter the performance of the surface in applications.[13, 14] This extra control over surface chemistry could potentially allow one to bind and release molecules from the surface or to turn reaction pathways on and off, enabling a new level of control over surface catalysis.[112, 113]

Despite the promise of this approach, relatively little work has been done to understand the effects of polarization on the surface chemistry of ferroelectrics, and in particular on the binding of molecules to ferroelectric surfaces. Yun, *et al.* performed a temperature programmed desorption (TPD) study of a variety of molecules on positively and negatively-poled $LiNbO_3$ (0001) and found significant differences in desorption peak temperatures as well as pre-exponential factors.[114, 115] In addition, Vohs *et al.* investigated small molecule adsorption on $LiNbO_3$, $BaTiO_3$ and

lead-zirconate titante, finding that adsorption rates are affected by the substrate polarization, but that adsorption energies are instead dominated by the concentration of defect sites on the surface.[116, 117, 118, 119, 120]

In complementary work, Wang et. al. demonstrated that it is also possible to switch the polarization of thin film ferroelectrics by changing the oxygen environment in order to favor one surface over the other.[121] They grew 10 nm $PbTiO_3$ thin films and varied the oxygen pressure from 10^{-7} to 10^{1} Torr at temperatures between 550 and 950 K. By monitoring the lattice constant, they showed that low oxygen pressure results in an oxygen vacancy-related surface reconstruction that stabilizes a negative polarization, while the surface observed under high oxygen pressure favors a positively-poled film.

Kolpak *et al.* used first principles density functional theory to investigate the effect of polarization on the adsorption of molecules to a Pt layer supported by $PbTiO_3$.[14] They find that binding energies and geometries as well as molecular dissociation energies are affected by polarization, and that these affects are strongest for a single monolayer of Pt covering the $PbTiO_3$ substrate. In addition, several experimental works on ferroelectric-supported metals, including $BaTiO_3$-supported Ni and $LiNbO_3$-supported Cu and Au, observed changes in catalytic activity correlated with the ferroelectric-paraelectric transition.[122, 123, 124, 125]

In this work, we use first principles density functional theory to investigate the effects of polarization on the (001) surface of $PbTiO_3$. We investigate the consequences of changing polarization on stoichiometric surfaces and we determine the thermodynamically stable (non-stoichiometric) surface structures as a function of the film polarization. We then consider the adsorption of CO_2 and H_2O to both stoichiometric and non-stoichiometric surfaces.

We focus our efforts on surfaces which may improve CO_2 and H_2O catalysis

because reactions involving these molecules are technologically important, especially to climate change. CO_2, which is produced by burning hydrocarbons, is a greenhouse gas which may contribute to global warming, and finding a way to use or capture CO_2 is a major technological goal.[126, 127] In addition, finding an efficient way to splitting H_2O into H_2 and and O_2 would be a important step towards replacing hydrocarbons with H_2 in energy applications.[128]

Finally, in addition to looking at the $PbTiO_3$ surface itself, we also consider the effects of adding a single epitaxial surface layer of several different materials in order to combine the high polarization of $PbTiO_3$ with a material that has superior catalytic properties. Unfortunately, many of the transition metals commonly used as catalysts are not thermodynamically stable as monolayer films on $PbTiO_3$. However, we find several alkali earth metals and metallic oxides which are stable on $PbTiO_3$ and may have enhanced catalytic properties.

This chapter is organized as follows: 8.1. Introduction, 8.2. Methods, 8.3. Stoichiometric Surfaces, 8.4. Non-Stoichiometric Surfaces, 8.5. Epitaxial Catalytic Layers, 8.6. Conclusions.

8.1 Methods

Our calculations are based on first-principles density functional theory calculations using a plane wave basis set.[20, 21] We use the PW91 GGA to approximate the exchange correlation function,[33] and ultrasoft pseudopotentials to eliminate core electrons[35, 129].

We perform calculations in a slab geometry, with the (001) surface of $PbTiO_3$ perpendicular to the z direction (see Fig. 8.11). We use a dipole correction to eliminate spurious electrostatic coupling between periodic copies in the z direction.

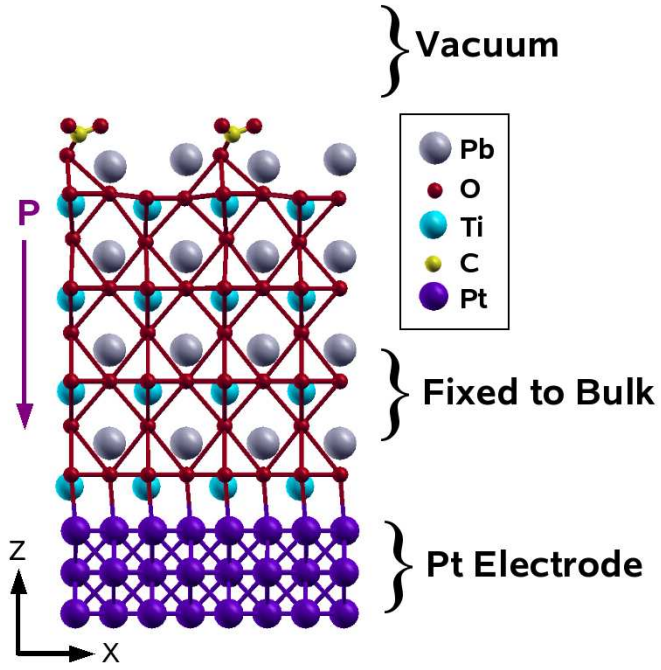

Figure 8.1: (Color online) Schematic of simulation cell, shown for a negatively-poled PbO-terminated surface with 0.5 ML CO_2. We use a slab geometry in the z direction, with vacuum above the surface and a Pt electrode on the opposite side of the $PbTiO_3$. The O−O bonds show octahedral cages around Ti.

In order to simulate thick slabs of $PbTiO_3$, our unit cell consists of 3.5-4 unit cells of $PbTiO_3$, with 3 layers of Pt serving as a bottom electrode to provide an electron reservoir (see Fig. 8.1). We find that adding additional $PbTiO_3$ or Pt layers has no effect on CO_2 binding energies to within 0.01 eV.

We only consider polarization in the z direction, perpendicular to the surface. We fix our in-plane lattice constant to that of $SrTiO_3$, as that is known experimentally to fix the polarization to lie in the z direction.[130] In order to simulate the polarization of a thicker slab than we can easily calculate, we fix the second and third atomic planes of $PbTiO_3$ from the bottom to their bulk values (the rest of the $PbTiO_3$ and Pt can relax). We find that this method is sufficient to describe the surface of a thick polarized $PbTiO_3$ slab (see Fig. 8.2), despite the fact that a stoichiometric polarized slab with less than 10 unit cells of $PbTiO_3$ and is higher energy than the equivalent

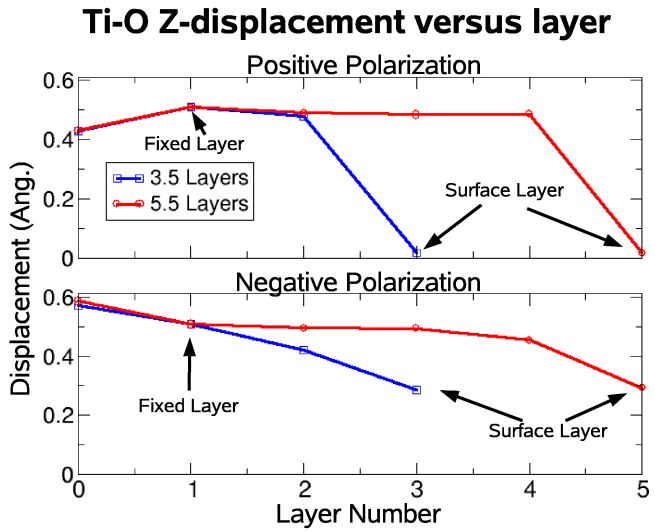

Figure 8.2: (Color online) Average absolute value of Ti-O z-displacement in each layer for positively-poled and negatively-poled TiO_2-terminated surfaces. We compare slabs with 3.5 unit cells (blue squares) and 5.5 unit cells (red circles) of $PbTiO_3$, and find similar surface geometry.

paraelectric slab.

When searching the phase space of atomic reconstructions, the possible reconstructions we consider are 0.5-2 ML adsorbed O and 0.5-1 ML O vacancies. In addition, for the PbO terminated surface, we consider Pb-vacancies, and for the TiO_2-terminated surface, we consider Ti vacancies. These calculations are all done in a c(2×2) unit cell, which allows for octahedral rotations and tilting. After using these initial calculations to get a rough idea of the phase space, we also considered larger unit cells and reconstructions for relevant surfaces (see, for example, the 4×1 reconstruction in Fig. 8.11). After determining the most stable surface for each polarization direction, we investigate CO_2 and H_2O binding sites by starting our relaxations with the molecules in several orientations (including disassociated) near each of the exposed atoms on the surface.

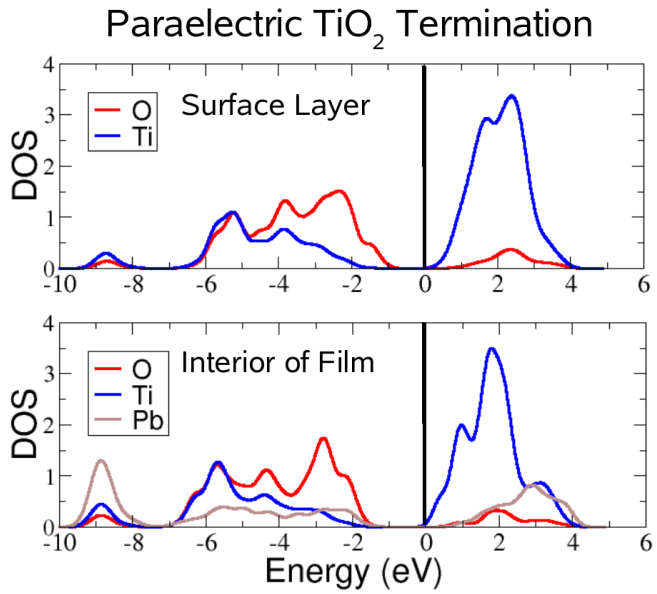

Figure 8.3: (Color online) Projected density of states (DOS) for the TiO_2-terminated paraelectric surface. The energy is relative the Fermi level. The top panel shows the DOS for the surface atoms, and the bottom panel shows DOS for bulk atoms.

8.2 Stoichiometric Surfaces

We begin by examining the electronic structure of stoichiometric TiO_2-terminated $PbTiO_3$. For the paraelectric surface, we find that the surface states are similar to the bulk-like region in the interior of the film, albeit with a reduced band gap due to the lower coordination number of surface atoms (see Fig. 8.3). In contrast, both the positively-poled and negatively-poled surfaces undergo electronic reconstructions in order to cancel the depolarizing field arising from the polarization charge ($\sigma = \vec{P} \cdot \hat{z}$, see schematic in Fig. 8.4). When limited to a stoichiometric surface, this is the only possible charge compensation mechanism; however, we consider atomic reconstructions in the following section.

On the positively-poled surface, electrons move from the bottom electrode to the unoccupied *d*-states on the surface Ti, which form the bottom of the conduction band

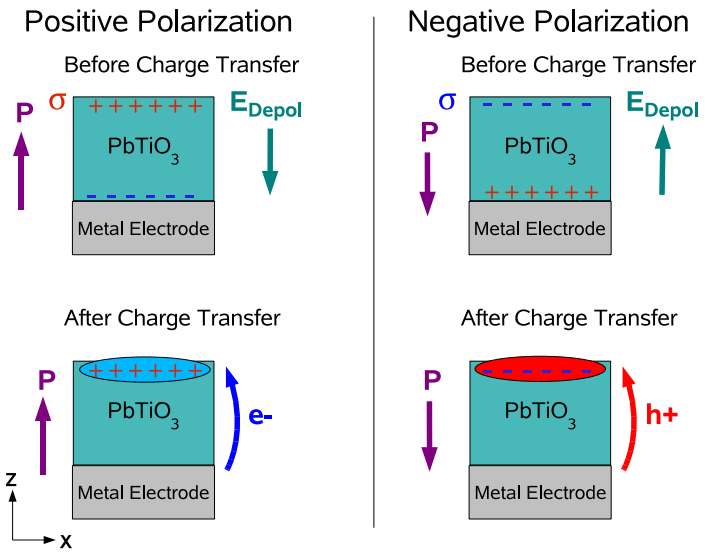

Figure 8.4: (Color online) Schematic of electronic reconstructions. For both the positively-poled (left) and negatively-poled (right) surfaces, the polarization creates a surface charge (σ) which results in a long range depolarization field (E_{Depol}). In order to reduce this field, either electrons (positive surface) or holes (negative surface) transfer from the electrode to normally unoccupied surface states, modifying surface chemistry.

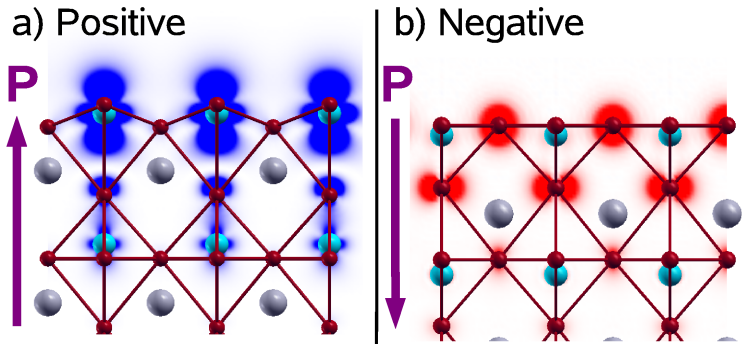

Figure 8.5: (Color online) Integrated local density of states (DOS) for a) positively-poled and b) negatively-poled TiO_2-terminated surface. The positive surface (a) is integrated from the top of the conduction band to the Fermi level, and shows electrons in the Ti d-orbitals on the surface. The negative surface (b) is integrated from the Fermi level to the top of the valence band, and shows holes in the p_{xy}-orbitals on the surface O. Atomic colors are the same as Fig. 8.1.

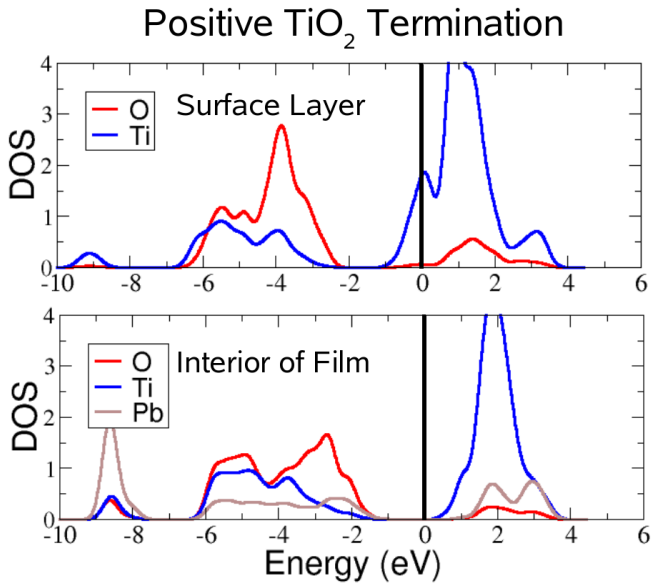

Figure 8.6: (Color online) Projected density of states (DOS) for the TiO_2-terminated positively-poled surface. The energy is relative the Fermi level. The top panel shows the DOS for the surface atoms, and the bottom panel shows DOS for bulk atoms. Electrons screen the surface charge by moving into the Ti conduction band states, as seen in the top panel (see also Fig. 8.5 a).

(see Figs. 8.6 and 8.5 a). This charge transfer screens the positive surface charge, σ, and for a thick film will eliminate the depolarizing field across the $PbTiO_3$. The negatively-poled surface has a similar electronic reconstruction; however, in this case, holes must move from the bottom electrode to the surface oxygen p-states, which form the top of the valence band, in order to screen the negative surface charge (see Figs. 8.7 and 8.5 b). This transfer of charges on both surfaces reduces the long range depolarization field and stabilizes the ferroelectric distortion for thick films.

We note that the positively-poled surface has a minor reconstruction, where half of the surface oxygen atoms are raised above the surface Ti, instead of below it like they would be in the bulk (see Fig. 8.5a). This alternating of the surface O results in the surface layer having almost no net Ti-O displacement along the z direction, as

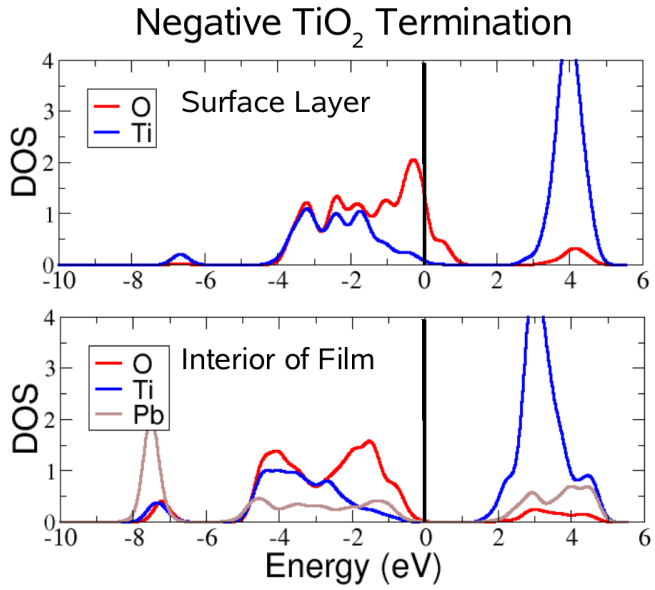

Figure 8.7: (Color online) Projected density of states (DOS) for the TiO_2-terminated negatively-poled surface. The energy is relative the Fermi level. The top panel shows the DOS for the surface atoms, and the bottom panel shows DOS for bulk atoms. Holes screen the surface charge by moving into the O valence band states, as seen in the top panel (see also Fig. 8.5 b).

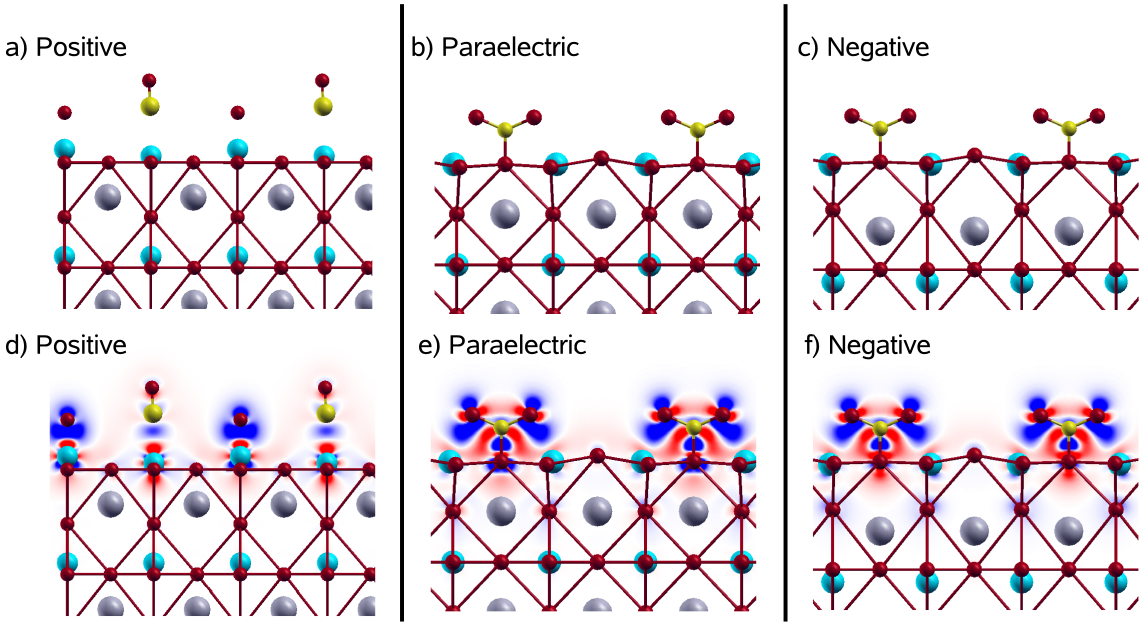

Figure 8.8: (Color online) Top: Binding geometry for 0.5 ML CO_2 on a stoichiometric TiO_2-terminated surface for a) positive, b) paraelectric, and c) negative polarizations. Bottom: Charge transfer plots for the surfaces in a-c. The background colors show how electrons rearrange when the CO_2 and the surface are allowed to interact; electrons move from red regions into blue regions. The positive surface (d) shows a transfer of electrons from surface Ti to the dissociated CO and O, while the paraelectric (e) and negative (f) surfaces show covalent bond formation.

Table 8.1: Binding energy of 0.5 ML CO_2 on stoichiometric TiO_2-terminated surface. See Fig. 8.8.

Polarization	Geometry	Binding Energy (eV)
Paraelectric	$(CO_3)^{2-}$	1.0
Negative	$(CO_3)^{2-}$	0.3
Positive	Disassociated	2.4

the two types of surface O have large but opposite displacements in the z direction (see Fig. 8.2). However, this reconstruction is only 0.06 eV/1×1 lower in energy than a more bulk-like configuration with both O below the surface Ti.

The polarization-induced electronic reconstruction has a large effect on both the CO_2 binding mode and binding energy (see Table 8.1 and Fig. 8.8). In the paraelectric case, the CO_2 forms a covalent bond with an O^{2-} on the surface, forming a carbonate $(CO_3)^{2-}$, as shown in Fig. 8.8b. The electrons on the carbonate anion are localized between the carbon atom and a surface oxygen; additional interactions between the oxygen p states in the CO_2 and surface Ti also occur, as illustrated by the charge density plot in Fig 8.8e. This carbonate bonding geometry and covalent bond formation is a typical binding mode for CO_2 to an oxide surface,[131] in this case resulting in a moderate binding energy of 1.0 eV (see Table 8.1). The negatively-poled surface also forms a carbonate (see Fig. 8.8 c and f); however, the binding energy is reduced relative to the paraelectric case (see Table 8.1), due to holes on the negatively-poled surface which are forced to move to the normally closed shell $(CO_3)^{2-}$, reducing its formation energy.

In contrast to the paraelectric and negatively-poled cases, CO_2 adsorption on the surface of the positively poled-film leads to dissociation and formation of CO and atomic O, both of which bind to surface Ti cations, as illustrated in Fig. 8.8c. This bonding mode is primarily a charge transfer interaction driven by the screening electrons in the Ti conduction band states at the surface (see Fig. 8.5a); these

electrons lower their energy by transferring to the antibonding C-O π state of CO_2, weakening a C-O bond and thus leading to dissociation. The charge transfer is clearly observed in Fig. 8.8d, which shows electrons leaving the red regions around the Ti and moving to the blue regions around the adsorbed O and CO. The dissociative adsorption of CO_2 on the positively poled surface is exothermic by 2.4 eV, which is significantly more favorable than the carbonate binding mode seen on the paraelectric and negatively-poled surfaces (see Table 8.1).

These calculations suggest that a switchable stoichiometric TiO_2-terminated $PbTiO_3$ surface would be very useful for CO_2 catalysis. First, the positively-poled surface could be used to bind and dissociate the CO_2 molecule. Then, the the polarization could be flipped, and the negatively-poled surface would release the products. However, this strong binding of the CO_2 to the positively-poled surface is partially due to the unstable state the surface is in prior to the interaction with the molecule. Instead, it is likely that the surface will reconstruct in order to reduce the number of electrons in the conduction band, possibly interfering with this promising result.[132] We investigate the effect of such atomic reconstructions in the following section.

8.3 Non-Stoichiometric Surfaces

8.3.1 Surface Thermodynamics

In order to compare the relative thermodynamic stabilities of non-stoichiometric $PbTiO_3$ surfaces, we compare the zero temperature surface free energy per area

$$F_{surf}(\mu_{Pb}, \mu_{Ti}, \mu_0) = E_{Tot} - N_{Pb}\mu_{Pb} - N_{Ti}\mu_{Ti} - N_O\mu_O \tag{8.1}$$

Table 8.2: DFT formation energies and experimental $\Delta_f H^0$ of various compounds. DFT formation energies are relative to bulk crystals at zero temperature for all elements except O, which is relative to a isolated atomic O_2 molecule. We also report the atomization energy of O_2, which is 6.64 eV in DFT, as compared to 5.23 in experiment.[133]

Compound	DFT Formation Energy (eV)	Experimental $\Delta_f H^0$
PbO	-2.59	-2.27 [134]
TiO_2	-9.85	-9.73 [134]
$PbTiO_3$	-12.77	-12.42 [135]
SrO	-5.87	-6.14 [134]
RuO_2	-2.85	
Rb_2O	-3.09	

where E_{Tot} is the total energy of the surface per unit area, N_i is the number of atoms of species i, and μ_i is the chemical potential of species i (the possible species are Pb, Ti, and O). The chemical potential of a species is the energy required to take an atom of that type from a reservoir and add it to the surface. We assume that bulk $PbTiO_3$ is stable in our system; therefore, the relevant region of phase space is that in which $PbTiO_3$ is stable with respect to the formation of compounds like PbO and TiO_2 (see Table 8.2). We use DFT to calculate the formation energy of these bulk compounds.

Our first requirement is that $PbTiO_3$ be in equilibrium with our reservoirs, which means adding or subtracting a full unit cell of $PbTiO_3$ from the surface does not change the surface free energy. This places the constraint that

$$E_{PbTiO_3} = \mu_{Pb} + \mu_{Ti} + 3\mu_O, \tag{8.2}$$

which allows us to eliminate μ_{Ti} and only consider the two dimensional phase space (μ_O, μ_{Pb}). In addition, we require that our surfaces are stable with respect to the formation of bulk Pb, Ti, TiO_2, and PbO, which adds the following constraints:

$$\mu_{Pb} \leq E_{Pb} \tag{8.3}$$

$$\mu_{Ti} = E_{PbTiO_3} - \mu_{Pb} - 3\mu_O \leq E_{Ti} \tag{8.4}$$

$$\mu_{Pb} + \mu_O \leq E_{PbO} \tag{8.5}$$

$$\mu_{Ti} + 2\mu_O = E_{PbTiO_3} - \mu_{Pb} - \mu_O \leq E_{TiO_2}. \tag{8.6}$$

In addition to the above limits, we require that the oxygen chemical potential corresponds to a gas with a temperature and pressure that is achievable under typical experimental conditions. This places the additional limit that

$$\mu_O \leq \frac{1}{2} E_{O_2}. \tag{8.7}$$

Any thermodynamically stable surface must have the lowest free energy at a given set of (μ_O, μ_{Pb}) which is allowed by the above constraints. The allowed region of phase space corresponds to the area inside the red lines in the phase diagrams shown in Figs. 8.9, 8.10, and 8.12. In order to improve comparison with experiment, we also apply a correction to the formation energy of an O_2 molecule from two O atoms, which is well known to be overestimated in GGA,[136] by referencing μ_0 to the energy of atomic oxygen in DFT plus one half of the experimental formation energy of O_2, rather than the DFT formation energy. This correction has no effect on the relative stability of structures in DFT, but improves the comparison with experimental oxygen chemical potentials.

8.3.2 Bare Surfaces

We use the methods in section 8.3.1 to find the most stable stoichiometry and geometry of the surface throughout the range of chemical potentials in which $PbTiO_3$ is stable. In agreement with previous work,[137] we find that the surface is always PbO-terminated; however, by expanding our phase space to include atomic reconstructions, we find that the stoichiometry of the top-most PbO layer changes in response to the polarization in order to compensate the surface charge and eliminate the depolarization field.

We begin by looking at the paraelectric surface. Fig. 8.9 shows that except for regions of very high oxygen chemical potential, which causes O_2 molecules adsorb to the surface, the paraelectric surface is terminated by a stoichiometric charge neutral PbO layer, as expected for a system with no polarization-induced surface charge. We find that the system does have a $c(2 \times 2)$ reconstruction due to TiO_6 octahedral rotations in the second atomic layer, consistent with experiment.[138]

The situation is very different for the polarized surfaces, as neither the negatively-poled nor the positively-poled surfaces are terminated by a stoichiometric PbO layer for any chemical potentials. For the negatively-poled surface, this can be seen in Fig. 8.10, which shows that neither stoichiometric termination is ever the lowest energy structure at any combination of Pb and O chemical potentials. Instead of forming a stoichiometric termination, which requires an electronic reconstruction to cancel the depolarizing field (see section 8.2 and Figs. 8.4, 8.5b and 8.7), the system undergoes an atomic reconstruction. Specifically, over a wide range of μ_O, the system forms oxygen vacancies on the surface. These oxygen vacancies act as positively charged defects which serve to cancel the depolarizing field through the substrate in the same way that the stoichiometric negatively-poled surface accumulates holes. Equivalently,

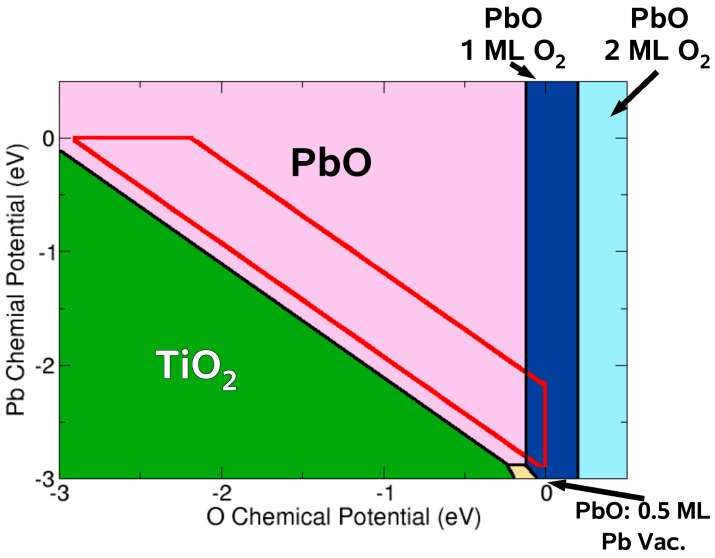

Figure 8.9: (Color online) Phase diagram of the paraelectric surface as a function of μ_O and μ_{Pb}. Each colored region is the thermodynamically stable structure for those chemical potentials. The physically allowed region is inside the red lines. The only stable structure in the majority of phase space is the stoichiometric PbO termination.

the oxygen vacancies can be viewed as electron donors, with the donated electrons filling in the holes caused by the depolarization field.

Over most of the relevant range of chemical potentials, the negatively poled surface has 0.5 ML oxygen vacancies (see the large light green region in the center of 8.10). Of the structures we have tried (2×1, c(2×2), 4×1, c(4×2) and 2×2), the lowest energy configuration is for the vacancies to arrange themselves into a 4×1 pattern as shown in Fig. 8.11. This pattern allows the three Pb^{2+} with surface O neighbors to break symmetry and decrease their distance from two of the O by 0.4-0.5 Å. Also, the surface Pb with no surface O neighbors moves towards the bulk, decreasing its distance to its second layer O neighbors by 0.2 $\AA$. Relative to the c(2×2) reconstruction, where each Pb also breaks symmetry, but only has only one close O neighbor, this reconstruction is 0.2 eV/u.c. more stable. The reconstruction is consistent with the experimental observation of a 4×1 reconstruction on the

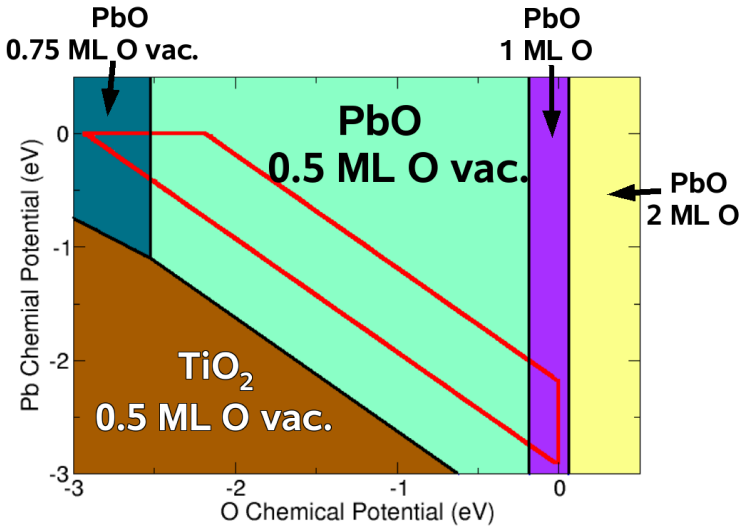

Figure 8.10: (Color online) Phase diagram of negatively poled surface as a function of μ_O and μ_{Pb}. Each colored region is the thermodynamically stable structure for those chemical potentials. The physically allowed region is inside the red lines. Stable structures are all PbO terminated, and have 0.75 ML O vacancies, 0.5 ML O vacancies (see Fig. 8.11), and 1.0 ML adsorbed O (at very high μ_O).

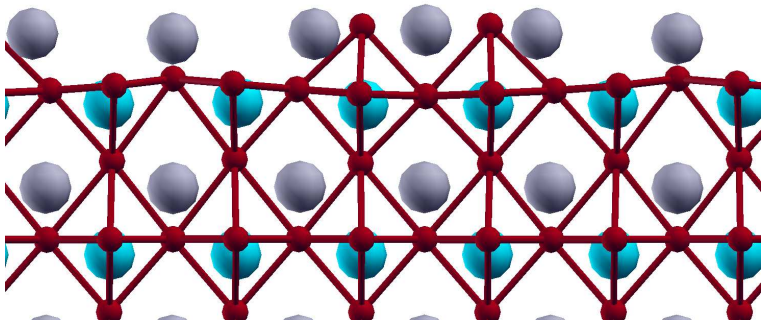

Figure 8.11:]
(Color online) Atomic structure of negatively-poled PbO terminated surface with 0.5 ML vacancies arranged into a 4×1 reconstruction. This structure corresponds to the green region in the center of Fig. 8.10.

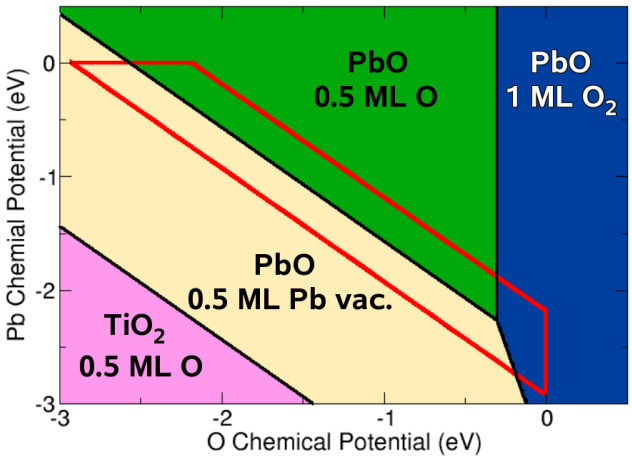

Figure 8.12: (Color online) Phase diagram of the positively-poled surface as a function of μ_O and μ_{Pb}. Each colored region is the thermodynamically stable structure for those chemical potentials. The physically allowed region is inside the red lines. Stable structures are all PbO terminated, and have 0.5 ML adsorbed O (see Fig. 8.13a and b), 0.5 ML Pb vacancies (see Fig. 8.13c), and 1 ML adsorbed O_2 (at very high μ_O).

negatively-poled surface.[121]

The positively-poled surface is similar to the negatively-poled surface in that the stoichiometric surface is never thermodynamically stable (see Fig. 8.12). This surface, which prior to reconstruction would have extra electrons in the conduction band (see Figs. 8.4, 8.5a, 8.6), reconstructs to have either extra O adsorbed on the surface (high μ_O, high μ_{Pb}), or Pb vacancies (low μ_O, low μ_{Pb}) (see Fig. 8.13). The extra O atoms act as an electron acceptors and the Pb vacancies act as hole donors, both of which reduce the number of electrons in the conduction band while still compensating the depolarization field. The surface with extra oxygen (see Fig. 8.13a-b) has an interesting reconstruction, where each Pb atom moves 0.5 unit cell in the y direction, which reduces its distance to the surface O while maintaining a large displacement in the z direction.

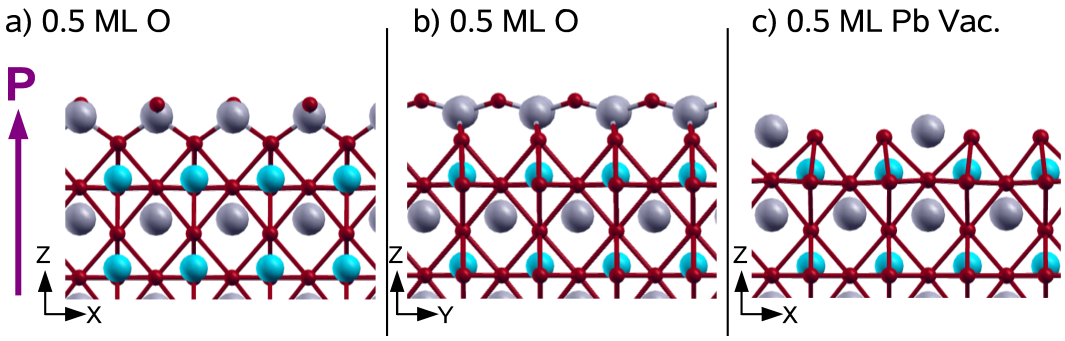

Figure 8.13: (Color online) Selected thermodynamically stable structures for the positively-poled surface. a) and b) are two views of the PbO surface with 0.5 ML adsorbed oxygen, which corresponds to the dark green triangular region in the upper part of Fig. 8.12. The Pb atoms have left their bulk positions and moved half a unit cell in the y direction, which results in an shorter Pb-O distance which is closer to bulk PbO. The adsorbed O is between two Pb. c) Shows the PbO surface with 0.5 ML Pb vacancies, which corresponds to the orange region in Fig. 8.12

Table 8.3: Binding energy of 0.5 ML CO_2 to thermodynamically stable surfaces.

Polarization	Termination	Stoich (ML)	Binding Geom.	Fig.	E_{bind}(eV)
Positive	PbO	+0.5 O	Physi.	8.14a	0.13
Positive	PbO	-0.5 Pb	$(CO_3)^{2-}$	8.14b	0.66
Negative	PbO	-0.5 O	$(CO_3)^{2-}$	8.14c	0.50
Paraelectric	PbO	0	$(CO_3)^{2-}$	8.14d	0.29

8.3.3 CO_2 binding

Armed with knowledge of how polarization effects surface geometry and stoichiometry, we investigate the effect of these changes on surface chemistry and reactivity. Specifically, we will again look at CO_2 binding to the surface. We consider the binding of CO_2 to the four surfaces which are stable in large regions of phase space. The results are summarized in Table 8.3.

Allowing atomic reconstructions generally reduces the largest CO_2 binding energies (compare Tables 8.1 and 8.3). In particular, the very large binding energy associated with the charge transfer binding mode of the the positively poled TiO_2-terminated surface does not occur on either of the thermodynamically stable

positively-poled surfaces. On the stoichiometric surface, this binding mechanism is driven by the electrons in high energy Ti d-states, and because the atomic reconstructions eliminate these high energy electrons, the related binding mode is also suppressed.

While most of the surfaces demonstrate the typical carbonate binding geometry, with the CO_2 forming a covalent bond with one of the exposed oxygen atoms (see Fig. 8.14), there is still significant variation in the binding energy with polarization. In particular, the positively-poled surface demonstrates the importance of atomic geometry and stoichiometry to molecular binding. The positively-poled surface with adsorbed oxygen, which occurs for surfaces with high μ_O and high μ_{Pb} (see Figs. 8.12 and 8.13a,b), has no chemisorption mode for CO_2 binding because the unusual positions of the surface Pb and adsorbed oxygen prevent carbonate formation. On the other hand, the positively-poled surface with Pb vacancies has enough room for the CO_2 to displace a surface Pb atom and reach a stable binding site (compare Fig. 8.14 a and b).

Table 8.3 suggests the possibility of using thermodynamically stable $PbTiO_3$ surfaces to bind and release CO_2 by switching the polarization. In particular, in the part of the phase diagram with high μ_O and high μ_{Pb}, switching the polarization will cycle between the negatively-poled surface with 0.5 ML oxygen vacancies , which forms a covalent bond with CO_2 (Fig. 8.14c), and the positively-poled surface with 0.5 ML added oxygen , which binds CO_2 only via weaker physisorption (see Fig. 8.14a). However, while these differences in binding with polarization are interesting as a proof of principle, the low total magnitude of the binding limits potential applications. In particular, attempting to use this surface for to bind and release CO_2 will require a sensitive control of relatively low temperatures of about 180 K.[139] Therefore, in section 8.4, we consider other materials in the hope of finding a larger

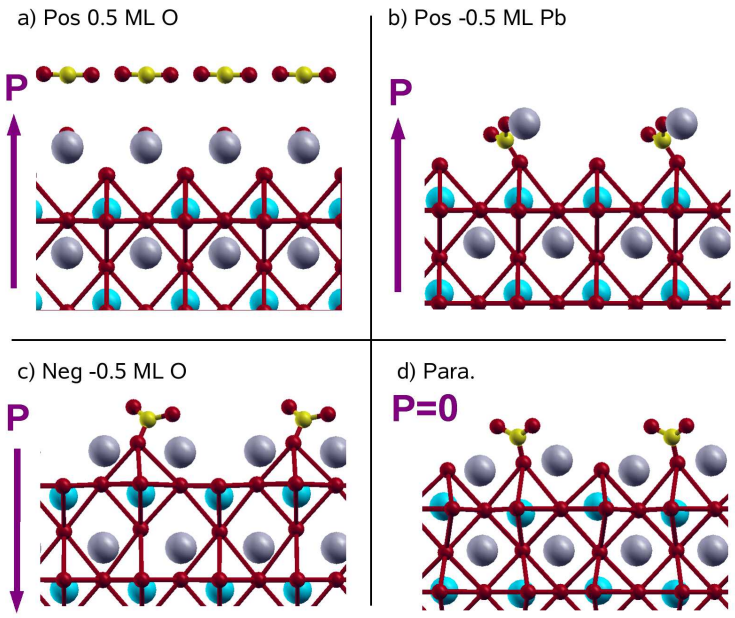

Figure 8.14: (Color online) Binding of 0.5 ML CO_2 to selected thermodynamically stable surfaces (see Table 8.3). a) Physisorption to positively-poled surface with 0.5 ML O. b) Carbonate bonding to positively-poled surface with 0.5 ML Pb vacancies. c) Carbonate bonding to negatively-poled surface with 0.5 ML oxygen vacancies. d) Carbonate bonding to stoichiometric PbO-terminated paraelectric surface.

effect.

8.3.4 H_2O Binding

In addition to CO_2 binding, we also consider the binding of gas phase H_2O molecules to the thermodynamically stable $PbTiO_3$ surfaces. Like CO_2, both the binding energy and binding mode of H_2O depend on the polarization direction and oxygen coverage. The results are summarized in Table 8.4.

The paraelectric PbO-terminated surface has two competitive H_2O binding modes. The most favorable binding mode for this surface has an H_2O molecule forming a hydrogen bond to a surface oxygen atom, with a binding energy of 0.76 eV (see Fig. 8.15 a). The H-O bond length for the hydrogen bond is 1.6 Å, as opposed to a covalent bond distance of 1.0 Å. The other binding mode, which is 0.20 eV less stable,

Table 8.4: Binding energy of 0.5 ML H_2O to several surfaces using both a disassociated geometry and a hydrogen-bonded geometry. The top three surfaces are thermodynamically stable, the bottom two are included for comparison.

Polarization	Termination	Stoich. (ML)	Disassociated Binding (eV)	H-Bond Binding (eV)	Fig.
Paraelectric	PbO	0	0.56	0.76	8.15a,b
Positive	PbO	+0.5 O	0.76	0.49	8.15c
Negative	PbO	-0.5 O	1.14	0.20	8.15d
Positive	PbO	0	0.04	0.18	
Negative	PbO	0	1.05	0.64	

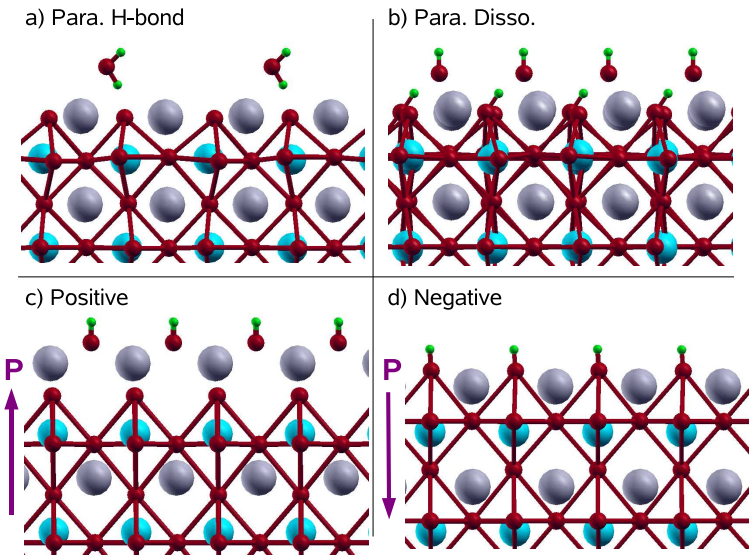

Figure 8.15: (Color online) Binding of 0.5 ML H_2O to selected thermodynamically stable surfaces (see Table 8.4). H is in green (other colors the same as Fig. 8.1). a) Hydrogen bonding to paraelectric surface. b) Disassociated bonding to paraelectric surface. c) Disassociated bonding to positively-poled surface with 0.5 ML adsorbed oxygen. d) Disassociated bonding to negatively-poled surface with 0.5 ML oxygen vacancies.

again has two covalent H-O bonds plus a hydrogen bond; however, in this case, the H_2O dissociates and the H atom binds covalently to a surface oxygen (see Fig. 8.15 b).

In contrast to the paraelectric surface, the thermodynamically stable negatively-poled surface with 0.5 ML oxygen vacancies shows a strong preference for the dissociated binding geometry (see Fig. 8.15 d and Table 8.4). Like the dissociated binding mode on the paraelectric surface, the dissociated H again bonds to a surface O, forming an OH. However, instead of forming a hydrogen bond with the surface, the remaining OH fills in the oxygen vacancy site. The end result is the same as a stoichiometric PbO-terminated surface with a additional 1 ML atomic H bonded to the surface oxygen. The change from $O^{2-} + H_2O \rightarrow 2\ (OH)^-$ results in a strong binding energy of 1.14 eV.

Interestingly, the low energy binding mode of H_2O to the thermodynamically stable positively-poled surface with 0.5 ML adsorbed O is very similar to the binding mode of the negatively-poled surface (see Fig. 8.15 c). Again, the H_2O dissociates, and the H bonds to the extra surface O atom. The $(OH)^-$ then fills in the empty O adsorption site, between two Pb atoms, resulting in a surface with a 1x1 reconstruction and 1 ML adsorbed $(OH)^-$. Much like the negatively-poled surface, the end result is $O^{2-} + H_2O \rightarrow 2\ (OH)^-$, which results in a more stable system and a binding energy of 0.76 eV. The difference between the two polarizations is that the negatively-poled surface has 1 ML less oxygen than the positively-poled surface, due to the differing surface charges.

These surfaces are potentially useful because they show that a) one can dissociate H_2O into OH by switching between a paraelectric surface and either polarized surface, and b) one can change the binding energy of the dissociated H_2O by flipping the polarization; however, more work must be done in order to understand how these

changes will affect practical catalytic reactions.

8.4 Epitaxial Catalytic Layers on $PbTiO_3$

While our results for CO_2 adsorption on $PbTiO_3$ are very interesting as a proof of principle, we attempt to improve the surface's catalytic properties. In particular, we would like a surface that a) is thermodynamically stable, b) has strong CO_2 binding for at least one polarization, and c) shows a large change in binding energy with polarization. Preferably, this material will be metallic, so that the Fermi level on the surface can change with polarization, altering the binding energy, without changing the stoichiometry of the surface.

Most of the typical transition metals used for catalytic applications are not thermodynamically stable on a $PbTiO_3$ surface. These transition metals have large cohesive energies, and prefer to aggregate into bulk-like clusters on the surface. For instance, on the TiO_2-terminated surface, a monolayer of Pt is unstable with respect to the formation of bulk Pt by 0.6 eV/Pt for the positively-poled surface and 1.2 eV/Pt for a negatively-poled surface. We consider two possible solutions: a) $SrRuO_3$, a metallic oxide with a perovskite structure that matches $PbTiO_3$, and b) Rb, an Alkali metal with relatively low cohesive energy.

We first considered adding a single layer of RuO_2 to a PbO terminated surface, but this turns out to be unstable with respect to the formation of bulk RuO_2. However, adding a full layer of $SrRuO_3$ to a TiO_2-terminated substrate, with the RuO_2 layer on the surface, is stable for all three polarizations. Unfortunately, this surface does not have particularly interesting CO_2 binding properties, as the binding energy is relatively weak and varies only 0.1 eV between positive and negative polarization (see Table 8.5 and Fig. 8.17a). However, the change in oxygen binding is much larger, on

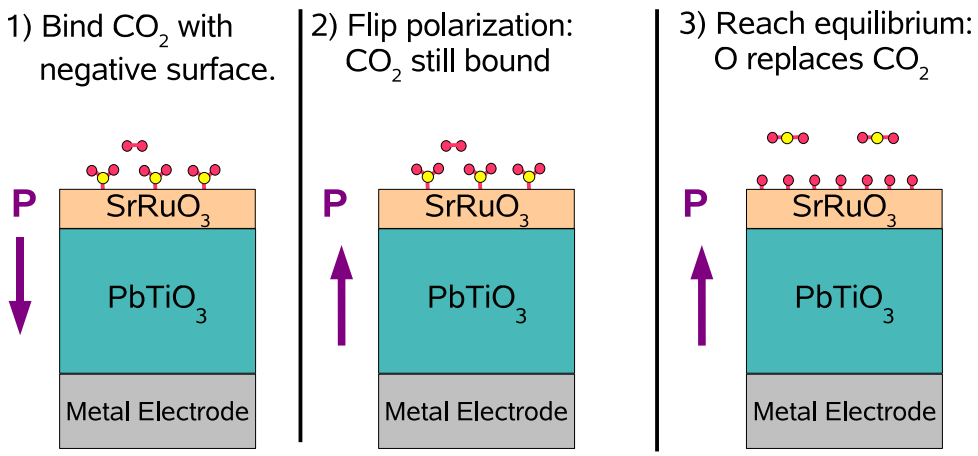

Figure 8.16: (Color online) Possible method for reversibly binding CO_2 to a $SrRuO_3$ (or SrO) monolayer on $PbTiO_3$. Step 1: The CO_2 is bound to the negatively-poled surface, which is stable at low O_2 pressure. Step 2: Flip the polarization. The CO_2 has a similar binding energy for either polarization; however, the positively-poled stoichiometric surface is not thermodynamically stable for experimentally realizable oxygen chemical potentials. Step 3: The system reaches thermodynamic equilibrium, and oxygen replaces the CO_2. To get back to the initial configuration, simply flip the polarization back.

the order of 1 eV, and it is likely the positively-poled surface will be covered in excess oxygen, eliminating all CO_2 binding sites. This suggests that it would be possible to bind CO_2 with the negatively poled surface, and then release it by flipping the polarization, causing oxygen to replace the CO_2 (see Fig. 8.16).

We also consider adding a single layer of SrO to a TiO_2-terminated $PbTiO_3$ substrate, without a RuO_2 layer. This configuration is thermodynamically stable with respect to SrO formation, and promisingly, CO_2 binds strongly to this surface. All three polarizations bind in the $(CO_3)^{2-}$ geometry and have a binding energy above 1.3 eV (see Table 8.5 and Fig. 8.17b). However, the binding of O to this surface is very strong, especially for the positively-poled surface, and it is again likely the positively-poled surface will be covered in oxygen. Therefore, this surface is also a candidate for the cycle proposed in Fig. 8.16.

Finally, we tried adding 0.5 ML Rb to the $PbTiO_3$ surface, in a c(2×2) configura-

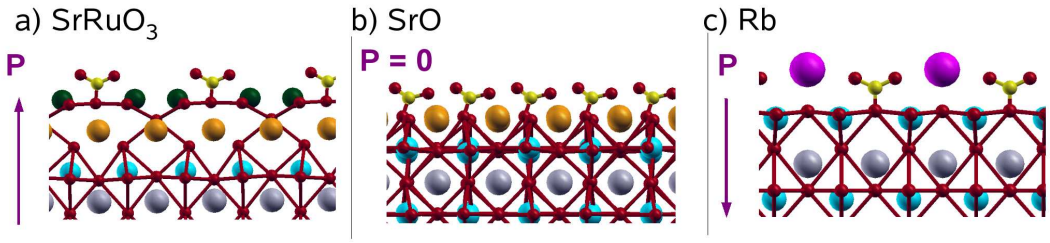

Figure 8.17: (Color online) Binding of 0.5 ML CO_2 to selected surfaces. Ru is in dark green, Sr is in orange, Rb is in pink (other colors the same as Fig. 8.1). a) Positively-poled $SrRuO_3$ surface. b) Paraelectric SrO surface c) Negatively-poled surface with 0.5 ML Rb.

tion. The Rb was stable with respect to the formation of bulk Rb on both stoichiometric terminations of the $PbTiO_3$ surface for all three polarizations; however, the positively-poled surface strongly prefers to oxidize, and form a layer of rubidium oxide on the surface. We focus our attention on the TiO_2-terminated negatively-poled and paraelectric surfaces with 0.5 ML Rb, which our calculations predict will be stable under realistic conditions. We find that the addition of Rb increases the binding of CO_2 to these surfaces (see Fig. 8.17c). While both polarizations bind the CO_2 in a $(CO_3)^{2-}$ geometry regardless of the presence of the Rb, the extra interaction with the Rb increases the binding of CO_2 by 1.2 eV for the negatively-poled surface and 0.8 eV on the paraelectric surface, making Rb an interesting candidate for increased CO_2 binding (see Table 8.5 as compared with Table 8.1).

8.5 Conclusions

We have examined the effects of polarization on the electronic structure, stoichiometry, geometry, and reactivity of the $PbTiO_3$ surface. We find that polarization has the largest effect on the stoichiometric TiO_2-terminated surface. This surface displays an electronic reconstruction, with electrons or holes moving to compensate the polarization-induced surface charge. These electrons and holes have a large effect on

Table 8.5: Binding Energy of 0.5 ML CO_2 to various surfaces. The positively-poled surfaces in all three cases will bind oxygen instead of CO_2 for realistic oxygen chemical potentials; results are included for comparison purposes.

Termination	Monolayer	Polarization	Binding Energy (eV)	Fig.
TiO_2	$SrRuO_3$	Positive	0.64	8.17 a
TiO_2	$SrRuO_3$	Negative	0.74	
TiO_2	$SrRuO_3$	Paraelectric	0.68	
TiO_2	SrO	Positive	1.34	
TiO_2	SrO	Negative	1.61	
TiO_2	SrO	Paraelectric	1.48	8.17 b
TiO_2	Rb	Positive	2.27	
TiO_2	Rb	Negative	1.35	8.17 c
TiO_2	Rb	Paraelectric	1.80	

CO_2 binding geometry and energy.

Polarization also greatly affects the thermodynamic stability of various surface stoichiometries and geometries. The surface always prefers to screen the depolarization field with atomic reconstructions rather than electronic reconstructions. These atomic reconstructions also affect both CO_2 and H_2O binding by changing both the binding energy and the availability of binding sites.

These results also have a variety of potential applications. If the stoichiometric TiO_2-terminated surface can be stabilized, the positively-poled surface would be very interesting as a way to disassociate CO_2. More realistically, the thermodynamically stable PbO-terminated surfaces also display differences in binding energies of CO_2 and H_2O. However, more work must be done to increase the magnitude of binding for CO_2 and to learn how to take advantage of the dissociation of H_2O when the surface becomes polarized. Finally, by engineering the $PbTiO_3$ by adding monolayers of other oxides to the surface, it is possible to both increase the binding of CO_2 to the surface and also achieve differences in binding with polarization. In particular, the variation of oxygen coverage with polarization provides a method for controlling the availability of CO_2 binding sites.

Chapter 9

Resonant Phonon Coupling

9.1 Introduction

Advancements in crystal growth techniques such as molecular beam epitaxy (MBE) and pulsed laser deposition (PLD) now enable control of interfaces between complex oxides at an atomic scale, resulting in an unprecedented ability to use interface effects to probe and modify material properties. While this freedom has commonly been used to modify the static properties of a material (e.g. strain engineering[140]), rarely has the direct *dynamic* coupling between atoms at an interface been used to modulate the electronic properties of one of the materials.

In this work, we investigate the resonant coupling of phonons across an epitaxial interface between a $La_{1-x}Sr_xMnO_3$ (LSMO) thin film and a $SrTiO_3$ (STO) substrate. LSMO, a colossal mangetoresitive (CMR) manganite, has a very strong interplay between its atomic structure and transport properties.[17, 18] Mobile electrons in LSMO are largely confined to localized Mn-d orbitals, and hop between these orbitals via overlap with neighboring oxygen atoms; therefore, the electronic structure and transport properties of LSMO are strongly influenced by changes in

the Mn-O bond length and bond angle. This strong dependence on atomic structure has been exploited previously to control CMR films via strain as well as coherent photoexcitation of a vibrational mode.[141, 142]

We seek to modify the atomic structure at the interface by coupling the motion of MnO_6 octahedral cages through the interface to TiO_6 octahedral cages in the STO substrate. In particular, we take advantage of the phonon-softening phase transition at T_c=108 K in STO (see Fig. 9.1). Above the phase transition temperature, STO is a cubic perovskite, but below T_c, the octahedral cages of STO become frozen in a antiferrodistortive pattern (AFD), resulting in a tetragonal distortion of the unit cell and non-zero average octahedral rotation angle. At temperatures just above and just below the phase transition, the phonon frequencies corresponding to rotations of the octahedral cage (Γ_{25} (111))[143, 144] approach zero, and therefore the occupation of this mode and the correlation length associated with it diverge. In order to investigate the coupling of this phonon mode across the interface and into an LSMO thin film, our experimental colleagues have grown LSMO thin films on STO and performed transport measurements.[145] They find a large cusp in the resistivity of the LSMO near the STO phase transition, in addition to a decreased magnetic moment, both of which are attributed to phonon coupling across the interface.

In order to confirm and clarify the proposed explanation of the experimental results, we use first principles theory to understand this interface at the atomic scale. First, we use supercell calculations to directly observe octahedral coupling across the interface. In addition, we build a first principles based model of atomic motion at the interface between LSMO and STO, and then perform finite temperature Monte Carlo sampling to investigate the effects of temperature on atomic motion at the interface. We show that the phonon mode with diverging correlation length extends from STO into LSMO, with a decay length in agreement with experimental measurements of the

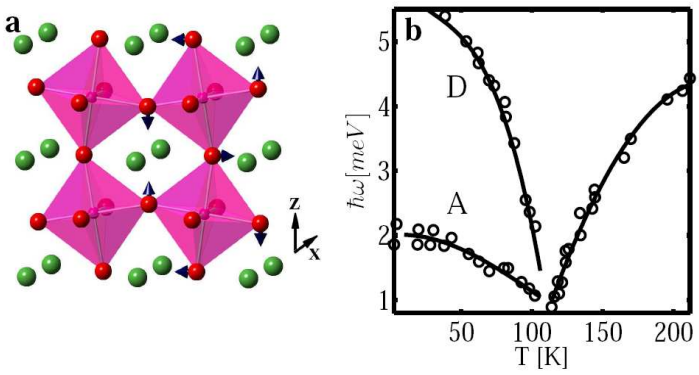

Figure 9.1: (Color online) Phonon softening in STO. a) Atomic displacements associated with the Γ_{25} octahedra rotation phonon mode. The octahedra rotate around the x axis in this example. z is the direction normal to the substrate-film interface. b) Energy of the phonon mode, showing the softening around the STO transition temperature.[144] Lines are a guide to the eye. Below the structural phase transition the mode splits due to the breaking of cubic symmetry. A and D indicate the mode's polarization, normal to the tetragonal axis and parallel to it, respectively.

resistivity changes. In addition, we rule out static structural changes at the interface as the driving force for the observed resistivity cusp, confirming our explanation that the increased resistance near T_c is due to dynamic phonon coupling.

9.2 Experiments

We briefly describe the key parts of the experiments of our collaborators, Y. Segal, C. A. F. Vaz, J. D. Hoffman, F. J. Walker, and C. H. Ahn, which are presented in more detail elsewhere.[146] They grow thin films of $La_{0.53}Sr_{0.47}MnO_3$ by molecular beam epitaxy on TiO_2-terminated STO (001) substrates. Then, they overlay the ferroelectric $PbZr_{0.2}Ti_{0.8}O_3$ (PZT), which is used to provide gate modulation of the number and distribution of charge carriers in the LSMO, although the phonon coupling effects are seen without the PZT layer. The LSMO is coherently strained to the STO, resulting in an A-type antiferromagnetic (AFM) metallic state (which is not seen in bulk LSMO, but is consistent with previous experiments).[140, 141] Using X-ray diffraction, they confirm that the films are under tensile strain, with c/a = 0.975.[141]

The major results of the experiments are presented in Fig. 9.2. Panel a shows the resistivity for a 11 u.c. $La_{0.53}Sr_{0.47}MnO_3$ film, as well as the magnetization for a 15 u.c. film. The resistivity plot shows a metal-insulator transition at 250 K, which is typical of LSMO, and also the resistivity peak at 108 K, which is correlated with the phonon softening transition in STO. Panel b, which is for a thicker 12 u.c. film, demonstrates that the cusp at 108 K is still present but diminished in a thicker film, confirming that the cusp is an interface effect (see also Ref. [147], which shows a much smaller effect for a thick film). Finally, panel c shows the effect of the polarization state of the PZT on the resistivity. When the PZT is in the depletion

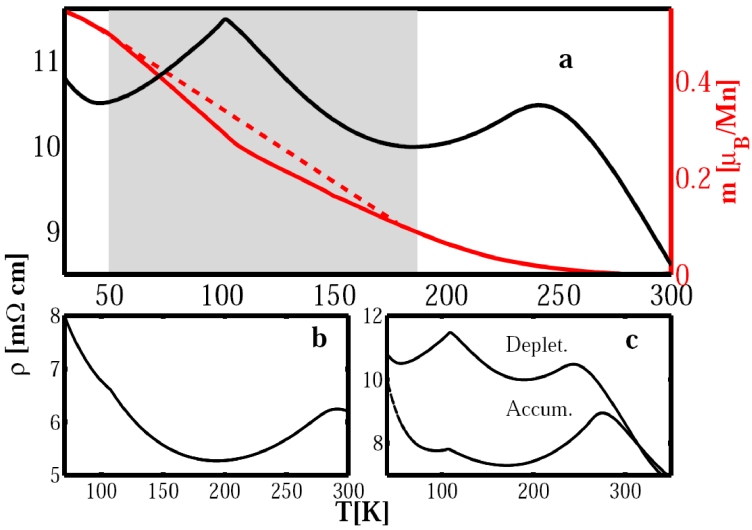

Figure 9.2: (Color online) Experimental results showing enhanced phonon-scattering. a) Left axes: Resistivity of 11 u.c. $La_{0.53}Sr_{0.47}MnO_3$ film showing a strong cusp at 108 K. The PZT layer is in the depletion state. Right axis: Magnetic moment of a 15 u.c. $La_{0.55}Sr_{0.45}MnO_3$ film. The moment is measured along the [100] direction under an applied magnetic field of 1kOe. A dip in the moment is observed, overlapping the temperature range of the resistivity cusp (emphasized by gray box). The dashed line is a linear interpolation between the edges of the dip region. b) Resistivity of a 12 u.c. $La_{0.53}Sr_{0.47}MnO_3$ film in the depletion state. c) The resistivity of the 11 u.c. film for the two polarization states of the PZT.

state, charge carriers (holes) are pushed towards the STO-LSMO interface, which increases the size the resistivity cusp. Conversely, in the accumulation state, holes are removed from the interface, which reduces the size of the cusp.[15] These results are also consistent with the increase in resistivity being confined to a few layers near the interface, rather than being dispersed throughout the film, as the effect is maximal when carriers are confined near the interface.

9.3 Zero Temperature Structures

9.3.1 Methods

In order to understand the microscopic origin of the coupling between LSMO and STO at the STO phase transition temperature, we perform first principles density functional theory[20, 21] calculations using the spin-polarized PBE GGA functional[28] and ultrasoft pseudopotentials.[35] For Mn, we include semicore $3s^2 3p^6$ projectors, in addition to valence projectors for the following valence configuration: $4s^2 3d^3 4p^0$. Cutoff radii are $r_s = r_p = r_d = 1.4$ Bohr, with a non-local core correction radius of 0.5 Bohr,[81] which we find to be necessary to converge differences in magnetic ordering.[148] Other pseudopotentials are described in the chapter 6. Regarding the La pseudopotential, we note that while the behavior of the LSMO is qualitatively the same for any reasonable choice of pseudopotential, the energy of octahedral rotations depends surprisingly sensitively (up to 20%) on the details of the La pseudopotential, and in particular the description of the f states. We carefully consider the logarithmic derivatives when generating the pseudopotentials, and choose $r_{local} = 3.0$ Bohr, as well as add a second projector to the f channel in our La pseudopotential in order to improve its description. Removing the f states entirely, as is sometimes done, increases the stability of octahedral rotations relative to tetragonal LSMO, and tends

to worsen the description of $LaMnO_3$.[149]

For computational ease, we represent $La_{0.5}Sr_{0.5}MnO_3$ by using the virtual crystal approximation to create an atom which is a 50%/50% mixture of La and Sr[150, 151]. We find an upper bound to the error in this approximation by calculating the ground state octahedral rotations of several ordered supercells of $La_{0.5}Sr_{0.5}MnO_3$ with separate La and Sr atoms. We find that the virtual crystal approximation captures the average behavior of these supercell calculations well, with errors of less than 2° in rotation angle and 35 meV (less for more disordered supercells) in the energy difference between the undistorted tetragonal and fully relaxed phases.

9.3.2 Bulk Strained LSMO

We begin by examining the ground state of bulk LSMO which has been epitaxially strained along the x and y directions to the theoretical STO lattice constant. This puts the LSMO under tensile strain and results in a c lattice constant 0.961 times the STO lattice constant, in good agreement with experiment. At this strain, we find that the system has an A-type AFM metallic state, in agreement with both experiment and previous theory,[141, 152] but the difference between ferromagnetic and antiferromagnetic ordering is only 14 meV/Mn. We also note that the magnetic ordering has only a small effect on the amplitude and energy of octahedral rotations. For example, relaxing the pseudo-cubic tetragonal structure lowers the energy of the ferromagnetic (FM) system by 68 meV/Mn, versus 53 meV/Mn for the AFM system. Also, the lowest energy rotation pattern is the same for either magnetization, and the rotation angles are very similar.

Bulk strained A-type AFM LSMO favors antiferrodistortive (AFD) octahedral rotations around both the x and y axes (around the $x = y$ or $x = -y$ line in the xy plane), which lowers the energy of the system by 53 meV/Mn. When limited to

rotation around either the x or y axis, the amplitude of rotations is 8°; however, the system can lower its energy by an additional 3 meV/Mn by instead rotating around both x and y by 6° (see Fig. 9.4). While also lower in energy than the undistorted tetragonal phase, rotations around the z axis are much less favorable energetically and the ground state structure has no z rotation. Both the energy and magnitude of the AFD rotations in LSMO are much larger than in STO, which has an rotation angle of 5.1° in GGA, and an energy lowering of 7 meV/Ti relative to the cubic phase. It is known that approximations based on the local density approximation (LDA) overestimate the equilibrium rotation angle of the oxygen octahedra in STO, which is only 2.1° experimentally,[153, 154] and in addition LDA incorrectly predicts a ferroelectric ground state for STO, at least when treating the atomic positions classically.[155] It is believed that both of these differences are related to quantum fluctuations in the oxygen position, as a full quantum statistical mechanics treatment of the low energy excitations of STO shows that the ferroelectric transition is suppressed down to <5 K, correctly predicting STO to be an incipient ferroelectric.[155, 153, 156] We artificially eliminate the ferroelectric state in our calculations by imposing symmetry along the z direction, as the ferroelectric state is not relevant at temperatures near the AFD phase transition at 108 K.

9.3.3 Supercell Calculations

In order to study how the LSMO octahedral rotations couple to the weaker rotations in STO, we perform supercell calculations of 4 layers of STO and 6 layers of LSMO in the z direction, with a $\sqrt{2} \times \sqrt{2}$ cell in the xy plane to accommodate AFD rotations. We fix the in-plane lattice constant to the theoretical lattice constant of STO. We consider both the TiO_2-$La_{0.5}Sr_{0.5}O$ interface as well as the SrO-MnO_2 interface, and we find that the resulting octahedral rotations are qualitatively the same. In Fig. 9.3

we show results for an averaged interface, with a virtual $Sr_{0.25}La_{0.75}$ layer of atoms at the interface, which results in a stoichiometric and symmetric $La_{0.5}Sr_{0.5}MnO_3$ film in our supercell.

In our calculations, we find that the AFD pattern of octahedral rotations is always continued through the interface, confirming the coupling between the STO and LSMO octahedra. As discussed in Sec. 9.3.2, the octahedral rotations of LSMO have a deeper energy well than the rotations of STO; therefore, the preference of LSMO for simultaneous rotations around the x and y axes forces the lowest energy interface to have both LSMO and STO rotated around the x and y axis, with little z rotation. Both the LSMO and STO rotation angles approach bulk-like values away from the interface and the average of their bulk values near the interface. This xy orientation for the interface octahedra is consistent with strong phonon coupling between the two materials. This is due to the fact that octahedral rotations around the x or y axis are propagated by first nearest neighbor oxygen motion across the interface. This is in contrast to rotations around the z axis, perpendicular to the interface, which are propagated between TiO_2 and/or MnO_2 layers in the z direction only by weaker second nearest neighbor oxygen interactions.

In order to look at how distortions in the STO propagate into the LSMO, we fix the center SrO layer and the surrounding two TiO_2 layers of STO in our supercells to have AFD distortions with $\theta_x = 2.5\text{-}10^\circ$ and $\theta_y = \theta_z = 0^\circ$, and we see how these distortions propagate through the interface and into the LSMO (see Fig. 9.3). We find that larger x axis rotations in the STO result in larger x axis rotations and smaller y axis rotations in the interfacial LSMO layers; however, the LSMO returns to its bulk rotation angles with a decay length of 1-2 unit cells. This rapid decay of the interfacial octahedral rotations away from the interface is consistent with the localized interface effect observed in experiment.

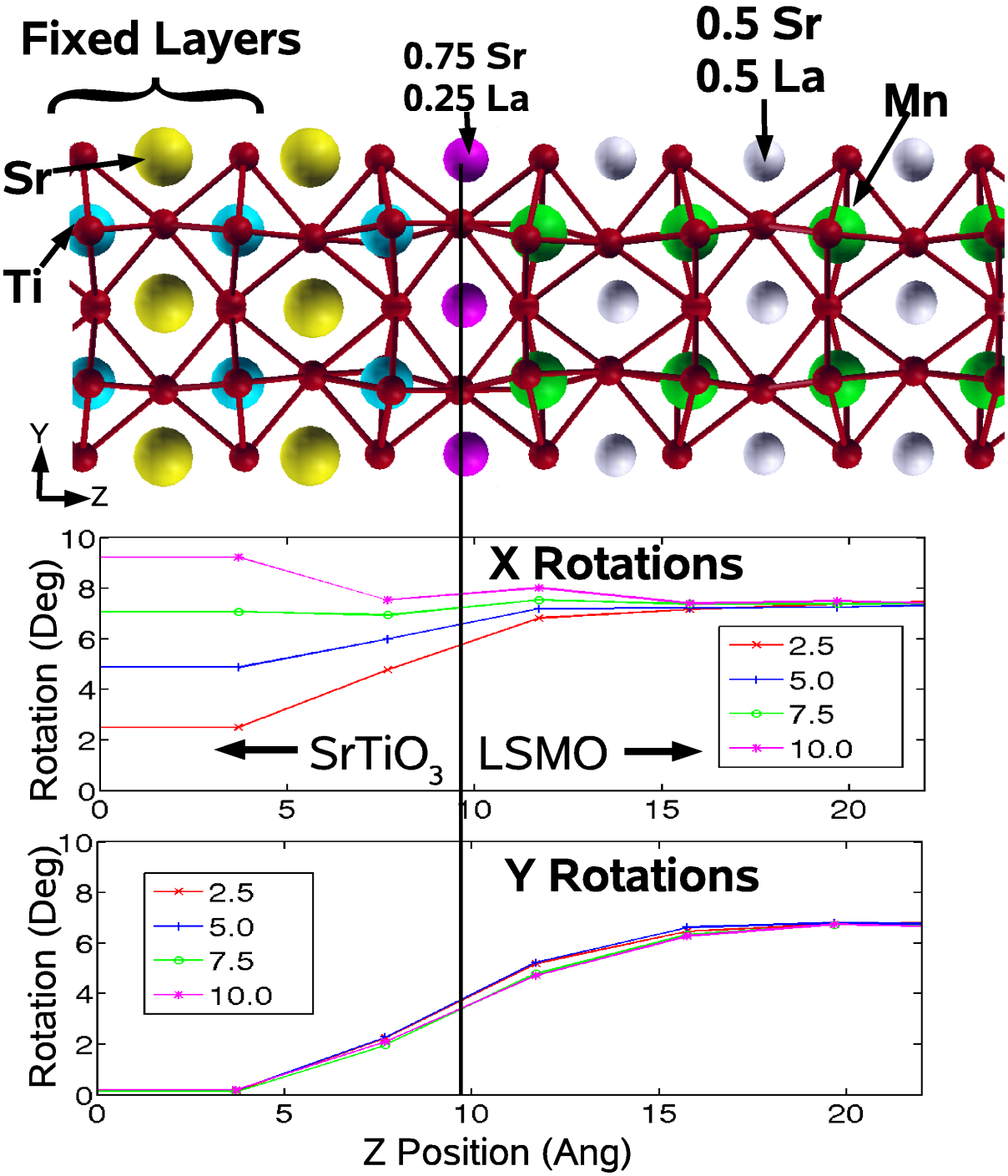

Figure 9.3: (Color online). Top: Side view of interface geometry, with octahedral oxygen cages drawn. z-direction is to the right. STO is on the left, LSMO on the right. The two TiO_2 layers and one SrO layer to the left are fixed to 5° x-axis rotation (out of page), the rest are free. Middle and bottom: average x-axis and y-axis octahedral rotations for 2.5-10° fixed STO. The data in middle and bottom panels line up with ball and stick model above.

9.4 Finite Temperature Calculations

9.4.1 Model of Octahedral Rotations

Having confirmed the coupling between STO and LSMO octahedra at zero temperature, we construct an *ab initio* classical model of octahedral rotations that we can use to calculate the effects of temperature on the atomic structure and vibrations at the interface. Our model consists of a Taylor expansion of the energy in terms of distortions of the cubic (STO) or tetragonal (LSMO) high temperature structures. Our degrees of freedom the are oxygen positions (in all three spatial directions) as well as a local strain variable that allows for changes in the size of the unit cell. The strain degrees of freedom are necessary to properly capture the AFD phase transition of STO.[155, 153] The form our expansion is:

$$E = \sum_{ij}\sum_{uv} K_{iujv}x_{iu}x_{jv} + \gamma_{iuv}x_{iu}^2x_{jv}^2 + \sum_{\alpha\beta} k_{\alpha\beta}s_\alpha s_\beta + \delta_{iu\alpha}s_\alpha x_{iu}^2 \tag{9.1}$$

where i and j run over the oxygen degrees of freedom unit cells, u and v run over the x,y, and z coordinates, and α and β run over the stress degrees of freedom. x_{iu} is an oxygen displacement from its undistorted position, K_{ijuv} is a harmonic spring constant between two oxygen displacements, γ_{iuv} is a local anharmonic (4^{th} order) interaction between oxygen displacements oxygen displacements on the same atom, s_α is a strain degree of freedom, $k_{\alpha\beta}$ is a harmonic interaction between strain degrees of freedom, and $\delta_{iu\alpha}$ is the lowest order interaction between oxygen displacement and strain.

The local strain degrees of freedom s_α correspond to the difference between the length of the unit cell and its equilibrium (cubic) length. Because we keep track of the differences between unit cells, our calculations implicitly include a homogeneous

strain degree of freedom, *i.e.* the size of the unit cell can change. We do not allow for changes in angle between our lattice vectors, which is consistent with experiment. Also, we do not include interactions between the LSMO oxygen degrees of freedom and the strain, which allows us to only use $SrTiO_3$ elastic constants and keep the size of the unit cell fixed to $SrTiO_3$, like it is in experiment, where the LSMO is strained to a much larger $SrTiO_3$ substrate. Our treatment of strain also ignores the anharmonic terms which must be included for a true rotationally invariant description of the strain[157]. These terms, like the anharmonic oxygen interactions, would cause phonons in this model to have a finite lifetime.

All of the coupling constants are fit from bulk first principles calculations of STO and LSMO. The bulk LSMO is strained in the x and y directions to the STO lattice constant, and allowed to relax in the z direction. K_{ijuv} is fit from DFT perturbation theory,[37, 38] and the rest of the parameters are least squares fits to bulk calculations with finite oxygen and unit cell displacement. For example, Fig. 9.4 shows the rotation of LSMO octahedra around the x and $x+y$ axes, which allows us to fit γ_{ij}.

For interactions between oxygens across the LSMO/STO interface, we average the K_{ijuv} for bulk LSMO and STO. In order to test this approximation, we calculate spring constants at the Bloch wave vector k=Γ in reciprocal space for a 4 layer supercell (2 layers STO, 2 layers LSMO), and compare to the prediction of our model. We find reasonable agreement; the large matrix elements at the interface are usually within 10% of the average of the bulk materials. We also tested alternate approximations for the spring constants at the interface (e.g. we used STO spring constants at the interface), and we find that the results of our finite temperature calculations are not very sensitive to this approximation.

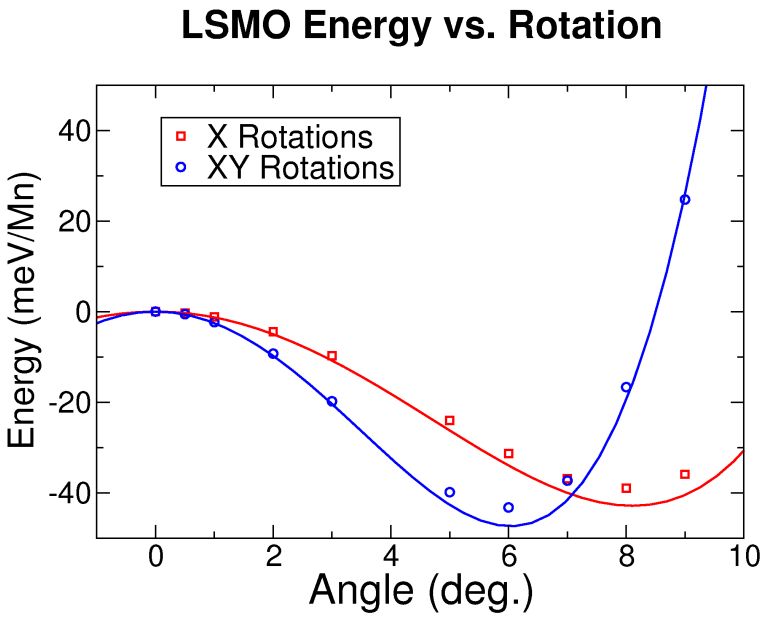

Figure 9.4: (Color online) Energy difference between tetragonal LSMO and LSMO with rigidly rotated octahedra, showing half of the double-well structure. The symbols show the first principles results, and the lines show the fit of our classical energy model (see Eq. 9.1). Each curve is a one parameter fit, as the harmonic part of the model not fit but given by perturbation theory calculations. Rotations around the $x + y$ axes by 6° each are slightly more favorable than rotations just around x or y. (The energy can be lowered by another 10 meV if the octahedra are not forced to rotate rigidly, because the tetragonal unit cell breaks symmetry between different oxygen.)

9.4.2 Monte Carlo Sampling

Using our model for octahedral rotations, we calculate the properties of the LSMO STO interface at finite temperature by sampling the partition function by using classical Monte Carlo techniques and the Metropolis algorithm.[48, 49] We use an ordered starting configuration for the oxygen, with the oxygen arranged into a low energy AFD pattern, and allow for thermalization before sampling. Rather than using completely random trial steps, we choose our new configurations based our knowledge of the energy landscape in order to improve our the acceptance rate for trial steps and accelerate the calculation. Starting from configuration $\vec{q}_j$, a new configuration $\vec{q}_i$ is chosen according to the discrete time Langevin equation which is also the equation for classical Brownian motion:

$$\vec{q}_i = \vec{q}_j + \tau(-\beta \nabla E(\vec{q}_i) + \sqrt{\frac{2}{\tau}}\vec{g}) \tag{9.2}$$

where β is the inverse temperature, τ is a time step, and $\vec{g}$ is a random Gaussian distributed vector with zero mean and unit variance along each axis with probability density in d dimensions

$$P(g) = (2\pi)^{-d/2} \exp(-g^2/2). \tag{9.3}$$

This choice leads to a proposal probability for a step from i to j equal to

$$c(ij) = C \exp\left(\frac{-(\vec{q}_i - \vec{q}_j + \beta\tau\nabla E(\vec{q}_j))^2}{4\tau}\right) \tag{9.4}$$

as per Sec. 2.5, where C is a normalization constant.

We actually use three separate time steps τ in Eq. 9.2: one for stress degrees of

freedom, one for oxygen motion in the direction of the nearest neighbor Ti or Mn (the hard or stiff direction) and one for all other oxygen motion (the easy directions). This allows us to adjust each time step separately to accept 50% of trial moves, which gives us the best performance in terms of sampling the phase space with the fewest number of iterations. Trial steps are accepted with a probability of $a(ij)$ according to the generalized Metropolis criteria, which preserves detailed balance:[50]

$$a(ij) = \min\left[1, \frac{c(ji)}{c(ij)}\, exp(-\beta(E_i - E_j))\right] \tag{9.5}$$

$$c(ji)/c(ij) = \exp\Big(-\frac{1}{4\tau}[(\vec{q}_j - \vec{q}_i + \beta\tau\nabla E(\vec{q}_i))^2 - (\vec{q}_i - \vec{q}_j + \beta\tau\nabla E(\vec{q}_j))^2]\Big), \tag{9.6}$$

We perform our Monte Carlo sampling in a $10 \times 10 \times 100$ perovskite supercell which has 60 layers of STO and 40 layers on LSMO along the z direction, and periodic boundary conditions in all three directions. The periodic boundary conditions along the z direction allow us to avoid dealing with a surface which our model is not designed to handle correctly. We find that using a larger unit cell in the x and y directions makes our computed phase transition sharper but has little effect on either the qualitative behavior of the system or the critical temperature of STO, T_c, which we find to be 110 K. This compares surprisingly well with the experimental value of 108 K, given that we have ignored both quantum fluctuations as well as the ferroelectric modes of STO.[156]

9.4.3 Effect of Temperature on Interface Structure

Using our model of octahedral rotations, we can analyze the effects of temperature on the average rotation angles. Results are presented in Fig. 9.5 as well as table 9.1. At low temperatures ($T = 0.3T_c$) (see Fig. 9.5a), the STO far from the interface

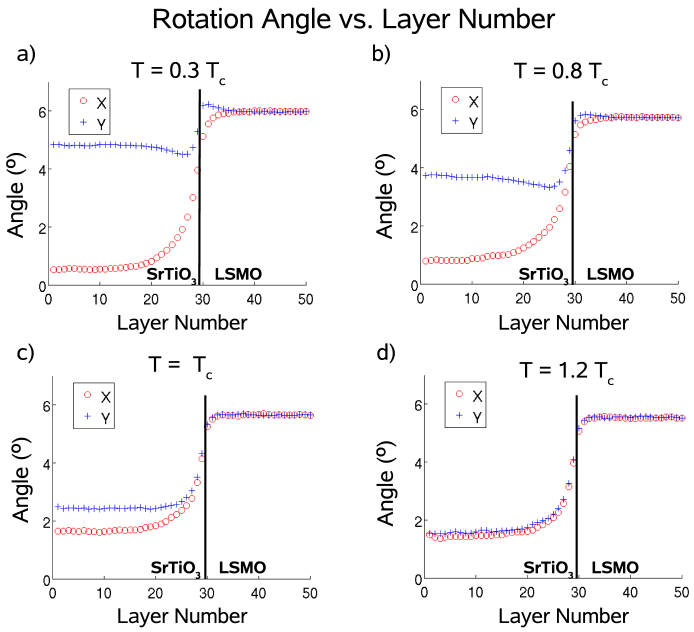

Figure 9.5: (Color online) Mean rotation angle versus layer number for four temperatures: a) 0.3 T_c b) 0.8 T_c c) T_c d) 1.2 T_c. The layers with number ≤ 60 are $SrTiO_3$, and ≤ 61 are LSMO.

is very close to being in its ground-state configuration, which consists of octahedral rotations of 5.1° around the y axis, and no average rotation in the other directions. The LSMO is also in its ground state, which consists of rotations around both the x and y axes. Near the interface, the TiO_6 octahedral in the STO are forced to line up with the MnO_6 octahedra in the LSMO, as we saw in our supercell calculations (see Fig. 9.3). In the STO, this causes the x component of the STO rotations to increase dramatically near the interface, with a fairly slow decay into the STO bulk. In the LSMO, the broken symmetry of the STO causes the y rotations to increase and the x rotations to decrease; however, this effect decays rapidly away from the interface, as we also saw in our supercell calculations.

At temperatures approaching T_c (see Fig. 9.5b), the interface looks similar to the

Table 9.1: LSMO rotation angles and the resulting conductivities normalized to the xx or yy the conductivity of tetragonal (unrotated) LSMO (σ_T, for $\theta_x = \theta_y = 0$). Rotation angles θ_x and θ_y are calculated for the LSMO layer at the interface with STO by Monte Carlo. Below the STO phase transition temperature, the STO breaks symmetry, resulting in different θ_x and θ_y values; however, the resulting change is conductivity is very small.

T/T_c	θ_x	θ_y	σ_{xx}/σ_T	σ_{yy}/σ_T	σ_{zz}/σ_T
0.8	5.73	5.21	0.91	0.89	0.18
1.0	5.34	5.34	0.89	0.89	0.18
1.2	5.20	5.20	0.90	0.90	0.19

low temperature interface (Fig. 9.5a). In the bulk-like regions, the mean rotation angles of both materials have decreased slightly, due to increased vibrational free energy favoring the cubic phase. At the interface, there is a decrease in symmetry breaking, which is due to the lower difference in free energy of the STO between x and $x + y$ rotations. At the critical temperature (see Fig. 9.5c), the symmetry breaking at the interface is essentially gone (the remaining symmetry breaking is due to the computational difficulty in sampling the full partition function near the critical temperature, where the barrier to switch states is very high). However, there is only a small change in the mean rotation angle for LSMO, even at the interface, as compared to $T = 0.8T_c$ (see Fig. 9.5b-c and table 9.1). This relatively small change in the LSMO rotation angle is due to the fact that the octahedral rotations in LSMO are much stronger than STO, leading the LSMO rotations to dominate the STO at the interface. For temperatures above the critical temperature (see Fig. 9.5d), there is again little change in the LSMO. The nonzero average AFD distortion in STO above T_c is due to the LSMO breaking the symmetry between $+x$ and $-x$ (and also $+y$ and $-y$) at the interface; without the LSMO, the bulk STO rotation angles would be zero.

9.4.4 How Structural Changes Modulate Conductivity

We consider two mechanisms whereby the phase transition in STO could increase the resistance in LSMO: a static change in interface structure or a phonon-driven change in electron scattering (a change in the relaxation time τ). First we look at whether the static structural changes in the LMSO at the interface around T_c (see Sec. 9.4.3) account for the observed resistance cusp, assuming the τ is constant. In the next section, we consider the influence of a dynamic phonon coupling which would modify τ.

We calculate the conductivity for bulk strained LSMO using the standard semi-classical formula for conductivity under the relaxation time approximation[25]:

$$\sigma_{ij} \propto \tau \sum_n \int d^3k \, v_i^n(\mathbf{k}) v_j^n(\mathbf{k}) (-f'(\epsilon_n(\mathbf{k})) \tag{9.7}$$

where σ_{ij} is the conductivity tensor, $v_i^n(\mathbf{k}) = \frac{\partial \epsilon_n(\mathbf{k})}{\partial k_i}$, the derivative of the band energy, is the electron velocity in effective mass theory, $f'(x)$ is the derivative of the Fermi function, and τ is the relaxation time, which is assumed to be constant.

We implement this expression numerically by first computing a real-space tight-binding Hamiltonian, $H_{mn}(\mathbf{R})$ in the maximally localized Wannier function [46] basis which reproduces the Mn-d bands near the Fermi level. Using this real-space Hamiltonian, we can then take a Fourier transform and calculate $\epsilon_n(\mathbf{k})$ and $v_i^n(\mathbf{k})$ on a fine mesh in reciprocal space:

$$H(\mathbf{k}) = \sum_{\mathbf{R}} H(\mathbf{R}) \mathbf{e}^{\mathbf{ik}\cdot\mathbf{R}} \tag{9.8}$$

$$H(\mathbf{k})\psi_{n\mathbf{k}} = \epsilon_n(\mathbf{k})\psi_{\mathbf{nk}} \tag{9.9}$$

$$v_i^n(\mathbf{k}) = \frac{\partial \epsilon_n(\mathbf{k})}{\partial k_i} = \psi_{n\mathbf{k}}^\dagger \frac{\partial H(\mathbf{k})}{\partial k_i} \psi_{n\mathbf{k}} \tag{9.10}$$

$$\frac{\partial H(\mathbf{k})}{\partial k_i} = i\sum_{\mathbf{R}} R_i H(\mathbf{R}) \mathbf{e}^{\mathbf{ik\cdot R}} \tag{9.11}$$

In addition to being a computationally inexpensive method to interpolate the band structure on a very find k-space mesh (32 k-points along each direction in reciprocal space are required to converge σ_{ij}), our Wannier function formalism allows us take the derivative $\frac{\partial \epsilon_n(\mathbf{k})}{\partial k_i}$ analytically (see Eq. 9.11), which simplifies our calculations.

We calculate conductivities for several different rotation angles above and below T_c; the results are summarized in table 9.1. We find that the differences in conductivity due to interfacial structure changes near the STO phase transition are too small to explain the observed conductivity changes (see Fig. 9.2). In order to understand this result microscopically, we compute Mn-O-Mn overlaps and hopping matrix elements, and we find that they change only by 1-2 % due to the static structural changes, explaining the lack of change in the conductivity.

Separately, the symmetry breaking caused by the STO phase transition is present for all temperatures below the phase transition and increases for lower temperatures (see Fig. 9.5a,b); however, the resistivity cusp seen experimentally is present only for temperatures close to T_c (both above and below T_c). Therefore, both the small size of the change in resistivity at $T = T_c$ as well as persistence of the change at all temperatures below T_c rule out static structural changes as the cause of the resistivity cusp; therefore, we now consider the effect of electron-phonon scattering.

9.4.5 Correlations and Phonons

In this section, we investigate the second mechanism for changes in LSMO resistivity, which is a change in τ, the relaxation time, due to increased electron-phonon scattering near the phase transition. In order to examine the penetration of STO phonon modes into the LSMO, we use our finite temperature sampling of the interface to

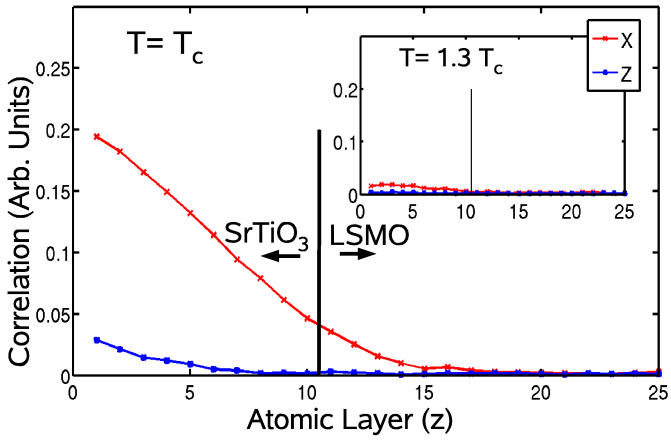

Figure 9.6: (Color online) Correlation of layers near the interface with bulk STO layers at $T = T_c$. At the phase transition, the correlation length in the STO diverges, and correlations decay into the LSMO. Inset: At $T = 1.3\,T_c$, correlations no longer extend significantly into the LSMO. See Fig. 9.7 for full temperature variation of interface region.

calculate the correlation $C_{ij} =< x_i x_j > - < x_i >< x_j >$ between oxygen octahedra in different layers along the z direction. Near the STO phase transition (at $T_c =$ 110 K in the model), when the correlation length in STO diverges, we find that the LSMO near the interface becomes correlated with bulk STO (see Fig. 9.6). The fact that correlations extend from bulk STO into the LSMO indicates that phonon modes associated with the AFD rotation in STO, which have frequencies approaching zero as $T \to T_c$, extend into the LSMO with a decay length of 2.2 unit cells, which we get by fitting to an exponential. In Fig. 9.7, we again show the correlation of interface layers with bulk STO, but here we plot the correlation as a function of temperature, which highlights the fact that this correlation is only present near the phase transition.

While non-linear terms will become increasingly important near the T_c, experimentally, phonons can be measured very close to the phase transition[143, 144]. Therefore, we assume that at any given temperature, the free energy can be expanded

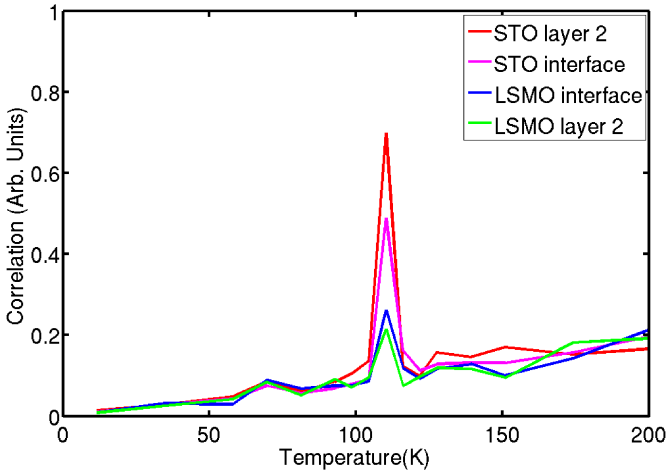

Figure 9.7: (Color online) Correlation of the two STO layers and two LSMO layers closest to the interface with bulk STO as a function of temperature. See Fig. 9.6 for spatial variation across the interface region.

around its equilibrium structure with an effective harmonic description $F(T) = \frac{1}{2}\mathbf{x}^\dagger K_{eff}(T)\mathbf{x}$, and that the eigenvalues of $K_{eff}(T)$, which are proportional to the effective phonon frequencies squared, are all real and positive. Then, we can relate these eigenvalues to the correlation matrix, C_{ij}, which we can calculate at finite temperature with Monte Carlo sampling:

$$\mathbf{C} = \frac{1}{Z}\int d\mathbf{x}\,\mathbf{x}\mathbf{x}^\dagger \exp(-\beta\mathbf{x}^\dagger K_{eff}\mathbf{x}/2) \tag{9.12}$$

$$= \mathbf{V}\mathrm{diag}(\frac{1}{\beta m\omega^2})\mathbf{V}^\dagger \tag{9.13}$$

where $\mathbf{V}$ and ω are the eigenvectors and vibrational frequencies of $K_{eff}(T)$, m is the mass of oxygen, Z is the partition function, and β is the inverse temperature. Eq. 9.13 shows that the eigenvectors of C_{ij} are the same as the eigenvectors of $K_{eff}(T)$, and the eigenvalues of C_{ij} are inversely related to the square of the vibrational frequencies. Using this relationship we simply diagonalize our calculated C_{ij} matrix and find the mode with the highest eigenvalue, which therefore has longest correlation

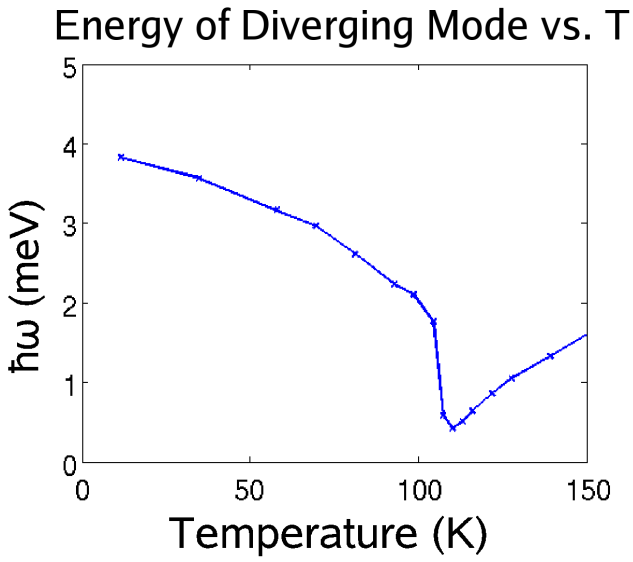

Figure 9.8: (Color online) Energy ($\hbar\omega$) of the lowest energy mode in the interface system as a function of temperature. Compare to Fig. 9.1, which shows experimental results for diverging phonon modes in STO.

length and lowest frequency in our system (see Fig. 9.8). Due to the size of the matrices involved, we take advantage of the Bloch character of our supercell and only consider modes of C_{ij} with the appropriate wave-vector to correspond to an AFD mode. The frequency of this mode clearly approaches zero at $T_c = 110$ K; however, it remains finite due to the limited size of our simulation cell.

We look at the spatial extent of this mode in the z direction at $T = T_c$ in Fig. 9.9. First, we note that the mode alternates in sign for both x and z rotations (y rotations are very similar to x and are not shown), indicating that it is an AFD mode. Second, while the mode is predominantly localized in the STO, the rotations in the x direction decay exponentially into the LSMO, with a decay length of 2.3 unit cells, which we calculate by fitting an exponential to the absolute value of the eigenvector as it decays into the LSMO.

This mode will have diverging phonon occupation as $T \to T_c$, resulting in greatly increased scattering of electrons in the LSMO layers close to the interface. The

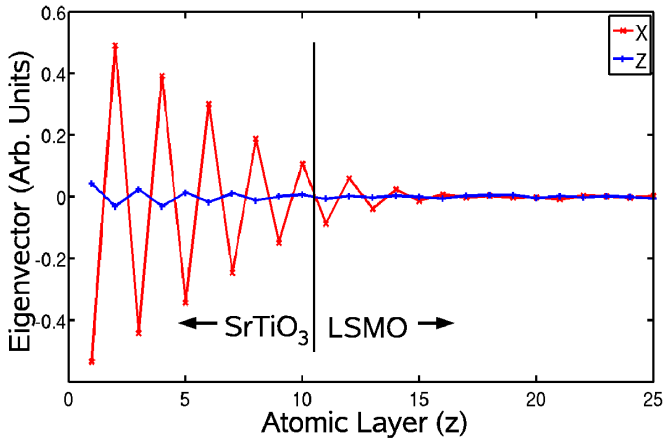

Figure 9.9: (Color online) Spatial profile of the eigenvector with the lowest frequency near the interface at $T = T_c$. The eigenvectors of x (and y, not shown) octahedral rotations extend from STO across the interface and into the the LSMO.

scattering will be proportional to $ne^{-2z/\lambda}$, where n is the Boson occupation number for the diverging mode, λ is the decay length of the mode amplitude, and z is the distance from the interface (the factor of 2 is due to squaring the eigenvector).[158] This decay length can be fit to the experimental resistivity measurements with the following form:[159]

$$\sigma = \sum_{z \in layers} (\rho_{base} + cne^{-2z/\lambda})^{-1} \tag{9.14}$$

where ρ_{base} is the unperturbed LSMO resistivity, fit by passing a smooth line below the cusp, and c is a constant related to the electron-phonon matrix element, which is also fit to the data. This form fits the observed resistivity cusp well (see Fig. 9.10), with a decay length of 1.8 unit cells, in good agreement with the theoretical decay length of 2.3 unit cells.

The large resistivity cusp observed experimentally requires a strong electron-phonon coupling, because as we have shown, the phonon modes decay within 1-3 layers of the interface. This strong electron-phonon coupling seems to be related to

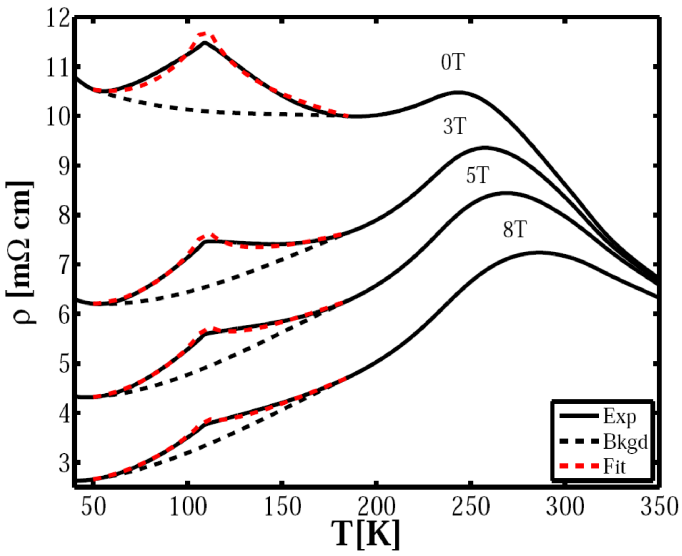

Figure 9.10: (Color online) Resistivity of an 11 u.c. film of $La_{0.53}Sr_{0.47}MnO_3$ as a function of temperature, for several out-of-plane magnetic values, with the PZT layer in the depletion state. Black dashed lines are interpolations excluding the cusp, and red dashed lines are fits to phonon coupling (see Eq. 9.14).

the A-type AFM ordering near x=0.5 doping, as the resistivity cusp is much smaller for dopings of x=0.2, where the LSMO is ferromagnetic.[15] Also, the size of the resistivity cusp is reduced by a strong out-of-plane magnetic field (see Fig. 9.10), which tends to favor a ferromagnetic alignment of spins in the z direction. However, the specific mechanism relating the phonons, magnetic ordering, and conductivity is still unclear.

9.5 Summary

We use first principles calculations to analyze the atomic behavior of the interface between LSMO and STO, which has a large increase in resistivity at the phase transition temperature of the STO substrate related to octahedral rotations. Using supercell calculations, we find these octahedral rotations couple from the STO into the LSMO. We build a classical model of oxygen motion at the interface which we use to analyze

the finite temperature behavior of the interface. We find that static changes in interface structure are too small to explain the resistivity changes; however, at the STO phase transition, phonon modes with diverging occupation decay significantly into the LSMO. These phonon modes will result in increased electron-phonon scattering near the STO phase transition, explaining the experimental observations.

Our results provide insight into the nature of conduction at the LSMO interface. They show that the interfacial layers of the film contribute to the conduction, and that the two-dimensional conduction in thin films with 50% doping is especially sensitive to electron-phonon scattering.

Chapter 10

Conclusions and Outlook

I have presented the results of a series of first principles calculations and models for a variety of surfaces and interfaces. A brief summary of the results and possibilities for future research on each of the topics I have investigated follows.

10.1 Epitaxial Oxide Growth on Semiconductors

I have presented investigations of Sr on both Ge and Si substrates and have found results in agreement with experimental RHEED, XRD, and STM measurements. At high deposition temperatures, both systems form non-stoichiometric Ge/Si structures at low Sr coverage. In addition, I have looked at the phase diagram of La on Si, and found that the surface will form silicides for La coverages above 0.2 ML, and that this will hinder oxide growth. Finally, using my knowledge of the surface structures, I looked at the initial SrO-Si interface, and then proposed a method for growing $LaAlO_3$ on Si.

One possible extension of this work would be to investigate the precise series of growth steps which are used to grow $SrTiO_3$ epitaxially on Si. One method for growing $SrTiO_3$ films on Sr+Si surfaces is to start depositing SrO layers at low tempera-

ture first, and then deposit Ti on top[160], after which the film is annealed at a carefully controlled temperature to crystallize the $SrTiO_3$ while avoiding SiO_2 and $TiSi_2$ formation.[160, 161, 162] In other growth procedures, the SrO and TiO_2 layers are co-deposited or alternated, but similar precise temperature control is necessary.[110, 52] Understanding the kinetics of this reaction may help in growth optimization as well as inform the search for growth procedures for other oxides. Understanding the growth kinetics of my proposed $LaAlO_3$ structures would also help predict a precise combination of temperatures and deposition orders which would result in good interfaces (or show that there is no temperature window where epitaxial interfaces are possible).

10.2 Ferroelectric Surfaces

I have calculated the dependence of the surface stoichiometry of $PbTiO_3$ on polarization, and I have also investigated how these changes in the surface modify the surface chemistry.

While I have made an attempt to find a surface layer to cap the $PbTiO_3$ surface that will enable useful polarization-dependent chemistry, thus far the results have been mixed. In particular, the materials I have looked at thus far, like the bare $PbTiO_3$ surface, tend to change oxygen stoichiometry with polarization. While this stoichiometry change can also modify the binding of small molecules to the surface, it would be desirable to find a material that has surface chemistry that changes with polarization without changing stoichiometry, which will make the system less dependent on the thermodynamics and kinetics of oxygen adsorption/desorption. One possible solution to this problem would be to find a metallic perovskite which is stable on either $PbTiO_3$ or another ferroelectric and which has more interesting

surface chemistry than $SrRuO_3$. Another method would be to find a way to add a more traditional transition metal catalyst to the surface in a thermodynamically stable manner. It may be necessary to consider other ferroelectrics, like $BaTiO_3$, which have a smaller polarization than $PbTiO_3$, and therefore may have a surface that is easier to engineer, while still producing interesting effects.

In a related area, more work can be done on the understanding thin film chemical sensing applications for ferroelectric surfaces.[121] Whereas I have tried to simulate thick $PbTiO_3$ substrates, these applications involve at thin film effects where the presence or absence of a particular adsorbate will change the relative surface energy of different polarizations, which can then drive a change in the polarization state of the thin film.

10.3 Interface Phonon Coupling

I have created a first principles model of octahedral rotations at the interface between LSMO and $SrTiO_3$ and used it to analyze the coupling of these rotations from $SrTiO_3$ into LSMO at the $SrTiO_3$ phase transition temperature.

There are several possibilities for improving my model of octahedral rotations. Some improvements which would improve the quantitative accuracy of the model include explicit calculation of the real space spring constants and anharmonic terms for the at the interface between $SrTiO_3$ and LSMO (eliminating an approximation of my model), and also improving the fitting of anharmonic terms in the bulk to better reproduce the ground state phonon frequencies. In addition, the model could be improved by including the full range of atomic motions, including the ferroelectric distortions in $SrTiO_3$ and by moving to a quantum description of the statistical mechanics, which is important for $SrTiO_3$[155, 153, 156].

A more advanced topic would be to calculate electron-phonon matrix elements in LSMO and use the eigenvectors and eigenvalues of the correlation matrix to calculate the change in conductivity in the LSMO film, which would then provide a more direct comparison between theory and experiment. One difficulty in this computation is the inadequacy of current electronic structure methods to quantitatively (and sometimes qualitatively) describe the electronic structure and conduction in LSMO, a strongly correlated material. In addition, there are many unexplained features of the LSMO interface, such as the 'dead layer' effect[163, 164], as well as questions about the bulk conductivity, which would have to be answered before such a calculation could be reliable.

Bibliography

[1] B.D. Fahlman. *Materials Chemistry*. 2007.

[2] *International Technology Roadmap for Semiconductors*. 2007.

[3] G. D. Wilk and R. M. Wallace. *Appl. Phys. Lett.*, 74:2854, 1999.

[4] John E. Northrup, Mark S. Hybertsen, and Steven G. Louie. *Phys. Rev. Lett.*, 66(4):500–503, 1991.

[5] G.E. Moore. *Electronics Mag.*, page 4, 1965.

[6] J.W. Reiner, A.M. Kolpak, Y. Segal, K.F. Garrity, S. Ismail-Beigi, C.H. Ahn, and F.J. Walker. *Adv. Mat.*, 22:2919, 2010.

[7] G. D. Wilk, R. M. Wallace, and J. M. Anthony. *Journal of Applied Physics*, 89(10):5243–5275, 2001.

[8] J. Mannhart C. H. Ahn, J. M. Triscone. *Nature*, 424:1015, 2003.

[9] J. M. Triscone C. H. Ahn, K.M. Rabe. *Science*, 303:488, 2004.

[10] J. W. Reiner, K. F. Garrity, F. J. Walker, S. Ismail-Beigi, and C. H. Ahn. *Phys. Rev. Lett.*, 101:105503, 2008.

[11] C. Noguera. *J. Phys.-Condens. Mat.*, 12:R367, 2000.

[12] G. Parravano. *J. Chem. Phys.*, 20:342, 1952.

[13] K. F. Garrity, Kolpak A. M., S. Ismail-Beigi, and E. I. Altman. *Adv. Mat.*, 22:2969–2973, 2010.

[14] A. M. Kolpak, I. Grinberg, and A. M. Rappe. *Phys. Rev. Lett.*, 98:166101, 2007.

[15] C. A. F. Vaz, J. Hoffman, Y. Segal, J. W. Reiner, R. D. Grober, Z. Zhang, C. H. Ahn, and F. J. Walker. *Phys. Rev. Lett.*, 104:127202, 2010.

[16] A. Ohtomo and H. Y. Hwang. *Nature*, 427:423, 2004.

[17] M. B. Salamon and M. Jaime. *Rev. Mod. Phys.*, 73:583, 2001.

[18] Y. Tokura. *Rep. Prog. Phys.*, 69:797, 2006.

[19] Kevin F. Garrity, Myrtle-Rose Padmore, Yaron Segal, J.W. Reiner, F.J. Walker, C.H. Ahn, and S. Ismail-Beigi. *Surface Science*, 604(9-10):857 – 861, 2010.

[20] P. Hohenberg and W. Kohn. *Phys. Rev.*, 136:B864, 1964.

[21] W. Kohn and L. Sham. *Phys. Rev.*, 140:A1133, 1965.

[22] R.O. Jones and O. Gunnarsson. *Rev. Mod. Phys.*, 61:689, 1989.

[23] U. von Barth and L. Hedin. *J. Phys. C.*, 5:1629, 1972.

[24] A.K. Rajagopal and J.Callaway. *Phys. Rev. B.*, 7:1912, 1973.

[25] Neil W. Ashcroft and N. David Mermin. *Solid State Physics*. Brooks Cole, 1976.

[26] D.M. Ceperley and B.J. Alder. *Phys. Rev. Lett.*, 45:556, 1980.

[27] J.P. Perdew and A. Zunger. *Phys. Rev. B*, 23:5048, 1981.

[28] John P. Perdew, Kieron Burke, and Matthias Ernzerhof. *Phys. Rev. Lett.*, 77:3865–3868, 1996.

[29] S. Ismail-Beigi. Theory of solids lecture notes, 2006.

[30] K. Burke, J.P. Pewdew, and M Ernzerhof. *Inter. Jour. Quan. Chem.*, 61:287, 1997.

[31] D. C. Langreth and M. J. Mehl. *Phys. Rev. B*, 28:1809, 1983.

[32] A. D. Becke. *Phys. Rev. A*, 38:3098, 1988.

[33] J. P. Perdew, J. A. Chevary, S. H. Vosko, K. A. Jackson, M. R. Pederson, D. J. Singh, , and C. Fiolhais. *Phys. Rev. B*, 48:4978, 1993.

[34] N. Troullier and Jos Luriaas Martins. *Phys. Rev. B*, 43:1993–2006, 1990.

[35] D. Vanderbilt. *Phys. Rev. B*, 41:7892, 1990.

[36] M. Scheffler M. Fuchs. *Comp. Phys. Comm.*, 119:67, 1999.

[37] S. Baroni, P. Giannozzi, and A. Testa. *Phys. Rev. Lett.*, 58:1861, 1987.

[38] P. Giannozzi, S. de Gironcoli, P. Pavone, and S. Baroni. *Phys. Rev. B*, 43:7231, 1991.

[39] S. de Gironcoli. *Phys. Rev. B*, 51:6773, 1995.

[40] H. Jonsson, G. Mills, and K. W. Jacobsen. In B. J. Berne, G. Ciccotti, and D. F. Coker, editors, *Classical and Quantum Dynamics in Condensed Phase Simulations*, page 385. World Scientific, 1998.

[41] G. Henkelman, B. P. Uberuaga, and H. Jonsson. *J. Phys. Chem.*, 113(22), 2000.

[42] C. Wert and C. Zener. *Phys. Rev.*, 76:1169, 1949.

[43] G.H. Vineyard. *J. Phys. Chem. Solids*, 3:121, 1957.

[44] W. Kohn. *Phys Rev.*, 115:809, 1959.

[45] S. Ismail-Beigi and T. Arias. *Phys Rev. Lett.*, 82:2127, 1999.

[46] A. A. Mostofi, J. R. Yates, Y.-S. Lee, I. Souza, D. Vanderbilt, and N. Marzari. *Comput. Phys. Commun.*, 178:685, 2008.

[47] R. D. King-Smith amd D. Vanderbilt. *Phys. Rev. B*, 47:1651, 1993.

[48] N. Metropolis, A. W. Rosenbluth, M. N. Rosenbluth, A. H. Teller, and E. Teller. *J. Chem. Phys.*, 21:1087, 1953.

[49] D. Frenkel. *Computational Soft Matter: From Synthetic Polymers to Proteins.* John von Neumann Institute for Computing, 2004.

[50] B.L. Hammond, W.A. Lester Jr., and P.J. Reynolds. *Monte Carlo methods in Ab Initio quantum chemistry.* World Scientific Publishing Co., 1994.

[51] John Robertson. *Reports on Progress in Physics*, 69(2):327–396, 2006.

[52] R. A. McKee, F. J. Walker, and M. F. Chisholm. *Phys. Rev. Lett.*, 81(14):3014–3017, Oct 1998.

[53] R. A. McKee, F. J. Walker, M. Buongiorno Nardelli, W. A. Shelton, and G. M. Stocks. *Science*, 300(5626):1726–1730, 2003.

[54] Clemens J. Först, Christopher R. Ashman, Karlheinz Schwarz, and Peter E. Blöchl. *Nature*, 427(1):53, 2004.

[55] A.M. Kolpak, F.J. Walker, J.W. Reiner, Y. Segal, D. Su, M.S. Sawicki, C.C. Broadbridge, Z. Zhang, Y. Zhu, C.H. Ahn, and S. Ismail-Beigi. *Phys. Rev. Lett.*, 105(21):217601, Nov 2010.

[56] D. O. Klenov, D. G. Schlom, Hao Li, and Susanne Stemmer. *Jpn. J. Appl. Phys., Part 2*, 44:L617, 2005.

[57] Christopher R. Ashman, Clemens J. Först, Karlheinz Schwarz, and Peter E. Blöchl. *Phys. Rev. B*, 69(7):075309, Feb 2004.

[58] A. A. Stekolnikov, K. Seino, F. Bechstedt, S. Wippermann, W. G. Schmidt, A. Calzolari, and M. Buongiorno Nardelli. *Physical Review Letters*, 98(2):026105, 2007.

[59] Nicolas Mounet and Nicola Marzari. *Phys. Rev. B*, 71:205214, 2005.

[60] J. Lettieri, J. H. Haeni, and D. G. Schlom. *J. Vac. Sci. Tech. A*, 20(4):1332–1340, 2002.

[61] W. C. Fan, N. J. Wu, and A. Ignatiev. *Phys. Rev. B*, 42(2):1254–1257, Jul 1990.

[62] R. Z. Bakhtizin, J. Kishimoto, T. Hashizume, and T. Sakurai. *J. Vac. Sci. Technol. B*, 14(2):1000, 1996.

[63] Wenhan Du, Bing Wang, Lei Xu, Zhenpeng Hu, Xuefeng Cui, B. C. Pan, Jinlong Yang, and J. G. Hou. *J. Phys. Chem.*, 129:164707, 2008.

[64] D. J. Chadi. *Phys. Rev. Lett.*, 59:15, 1987.

[65] A. Ramstad, G. Brocks, and P. J. Kelly. *Phys. Rev. B*, 51:14504, 1995.

[66] J. Wang, T.A. Arias, and J. D. Joannopoulos. *Phys. Rev. B*, 47:16, 1993.

[67] A.P. Smith and H. Jonsson. *Phys. Rev. Lett.*, 77:7, 1996.

[68] J Tersoff and D. R. Hamann. *Phys. Rev. Lett.*, 50:1998, 1983.

[69] J. Tersoff and D. R. Hamann. *Phys.Rev. B*, 31:805, 1985.

[70] X. Hu, X. Yao, C. A. Peterson, D. Sarid, Z. Yu, J. Wang, D. S. Marshall, R. Droopad, J. A. Hallmark, and W. J. Ooms. *Surface Science*, 445(2-3):256 – 266, 2000.

[71] Kaoru Ojima, Masamichi Yoshimura, and Kazuyuki Ueda. *Surface Science*, 491(1-2):169 – 174, 2001.

[72] J. W. Reiner, Y. Segal, K. F. Garrity, H. Hong, S. Ismail-Beigi, C. H. Ahn, and F. J. Walker. volume 27, pages 2015–2019. AVS, 2009.

[73] K.F. Garrity and S. Ismail-Beigi. *Phys. Rev. B.*, 80:085306, 2009.

[74] J. W. Reiner, F. J. Walker, and C. H. Ahn. *Science*, 323(5917):1018–1019, February 2009.

[75] R.A. McKee, F.J. Walker, M.B. Nardelli, W.A. Shelton, and G.M. Stocks. *Science*, 300:1726, 2003.

[76] M Sokolowski, T Koch, and H Pfnür. *Surf. Sci.*, 243(1-3):261 – 272, 1991.

[77] Y. Segal, J. W. Reiner, A. M. Kolpak, Z. Zhang, S. Ismail-Beigi, C. H. Ahn, and F. J. Walker. *Phys. Rev. Lett.*, 102(11):116101, Mar 2009.

[78] M. P. Warusawithana, C. Cen, C. R. Sleasman, J. C. Woicik, Y. L. Li, L. F. Kourkoutis, J. A. Klug, H. Li, P. Ryan, L. P. Wang, M. Bedzyk, D. A. Muller, L. Q. Chen, J. Levy, and D. G. Schlom. *Science*, 324(5925):367–370, 2009.

[79] C. Kittel. *Introduction to Solid State Physics*. John Wiley, 2005.

[80] R. A. McKee, F. J. Walker, and M. F. Chisholm. *Science*, 293:468, 2001.

[81] Steven G. Louie, Sverre Froyen, and Marvin L. Cohen. *Phys. Rev. B*, 26:1738, 1982.

[82] J. P. Perdew, R. G. Parr, M. Levy, and J. L. Balduz. *Phys. Rev. Lett.*, 49:1691, 1982.

[83] J. P. Perdew and M. Levy. *Phys. Rev. Lett.*, 51:1884, 1983.

[84] L. J. Sham and M. Schluter. *Phys. Rev. Lett.*, 51:1888, 1983.

[85] L. Hedin. *Phys. Rev.*, 139:A796, 1965.

[86] W.G. Aulbur, L. Jonsson, and J.W. Wilkins. *Solid State Physics*, 54:1, 2000.

[87] D. Kumah, J.W. Reiner, J. Ngai, Y. Segal, A.M. Kolpak, D. Qiu, S. Ismail-Beigi, C.H. Ahn, F.J. Walker, D. Su, Y. Zhu, and Z. Zhang. *APS March Meeting Talk*, 2011.

[88] Schlom-D.G. Chambers S.A. Cicerrella E. Freeouf J.L. Hollnder B. Schubert J. Edge, L.F. *Applied Physics Letters*, 84(5):726–728, 2004. cited By (since 1996) 90.

[89] W.F. Xiang, H.B. Lu, Z.H. Chen, X.B. Lu, M. He, H. Tian, Y.L. Zhou, C.R. Li, and X.L. Ma. *Journal of Crystal Growth*, 271(1-2):165 – 170, 2004.

[90] J. W. Reiner, A. Posadas, M. Wang, M. Sidorov, Z. Krivokapic, F. J. Walker, T. P. Ma, and C. H. Ahn. *Journal of Applied Physics*, 105(12):124501, 2009.

[91] C. Merckling, G. Delhaye, M. El-Kazzi, S. Gaillard, Y. Rozier, L. Rapenne, B. Chenevier, O. Marty, G. Saint-Girons, M. Gendry, Y. Robach, and G. Hollinger. *Microelectronics Reliability*, 47(4-5):540 – 543, 2007. 14th Workshop on Dielectrics in Microelectronics (WoDiM 2006).

[92] Y. Y. Mi, Z. Yu, S. J. Wang, P. C. Lim, Y. L. Foo, A. C. H. Huan, and C. K. Ong. *Applied Physics Letters*, 90(18):181925, 2007.

[93] Dmitri O. Klenov, Darrell G. Schlom, Hao Li, and Susanne Stemmer. *Japanese Journal of Applied Physics*, 44(20):L617–L619, 2005.

[94] Clemens J. Först, Karlheinz Schwarz, and Peter E. Blöchl. *Phys. Rev. Lett.*, 95(13):137602, Sep 2005.

[95] Christopher R. Ashman, Clemens J. Först, Karlheinz Schwarz, and Peter E. Blöchl. *Phys. Rev. B*, 70(15):155330, Oct 2004.

[96] I. Devos and P. Boulenc. *Appl. Phys. Lett.*, 90:072906, 2007.

[97] A. A. Knizhnik, I. M. Iskandarova, and B. V. Potapkin A. A. Bagaturyants, L. R. C. Fonseca, and A. Korkin. *Phys. Rev. B*, 72:235329, 2005.

[98] C.X. Zhu, S. Misawa, S. Tsukahara, A. Kawazu3, and S.J. Pang1. *Appl. Phys. A*, 68:145, 1999.

[99] C. Zhu, S. Misawa, and S. Tsukahara. *J. Appl. Phys.*, 80:4205, 1996.

[100] J.H. Seo, J.Y. Park, S.K. Jung, K.-H. Yoo, C.N. Whang, S.S. Kim, D.S. Choi, and K.H. Chae. *Chem. Phys. Lett.*, 417:72, 2006.

[101] C. Zhu, A. Kawazu, S. Misawa, and S. Tsukahara. *Phys. Rev. B.*, 59:9760, 1999.

[102] J.J. Lander and J. Morrison. *Surf. Sci.*, 29:553, 1964.

[103] G. Brocks, P. J. Kelly, and R. Car. *Phys. Rev. Lett.*, 25:2786, 1993.

[104] Y. Umeno and T. Kitamura. *Modelling Simul. Mater. Sci. Eng.*, 12:1147, 2004.

[105] G. Brocks, P. J. Kelly, and R. Car. *J. Vac. Sci. Technol B*, 12:2705, 1994.

[106] F. Amy, A. S. Wan, A. Kahn, F. J. Walker, and R. A. McKee. *J. Appl. Phys.*, 96:1635, 2004.

[107] C. J. Forst, C. R. Ashman, K. Schwarz, and P. E. Blochl. *Nature*, 427:53, 2004.

[108] Sanghun Jeon, F.J. Walker, C.A. Billman, R.A. McKee, and Hyunsang Hwang. *Electron Device Letters, IEEE*, 24(4):218 – 220, 2003.

[109] S. A. Chambers, Y. Liang, Z. Yu, R. Droopad, and J. Ramdani. *J. Vac. Sci. Technol. A*, 19:934, 2001.

[110] M. El Kazzi, G. Delhaye, C. Merckling, E. Bergignat, Y. Robach, G. Grenet, and G. Hollinger. *J. Vac. Sci. Tech A*, 25(6):1505–1511, 2007.

[111] Shao-Bo Mi, Chun-Lin Jia, Venu Vaithyanathan, Lothar Houben, Jürgen Schubert, Darrell G. Schlom, and Knut Urban. *Applied Physics Letters*, 93(10):101913, 2008.

[112] T. Bligaard, J.K. Nrskov, S. Dahl, J. Matthiesen, C.H. Christensen, and J. Sehested. *Journal of Catalysis*, 224(1):206 – 217, 2004.

[113] Sren Dahl, Ashildur Logadottir, Claus J. H. Jacobsen, and Jens K. Nrskov. *Applied Catalysis A: General*, 222(1-2):19 – 29, 2001.

[114] Y. Yun and E. I. Altman. *J. Am. Chem. Soc.*, 129:15684, 2007.

[115] Y. Yun, L. Kampschulte, D. Liao, M. Li, and E. I. Altman. *J. Phys. Chem. C*, 111:13951, 2007.

[116] J. Garra, J.M. Vohs, and D.A. Bonnell. *Surface Science*, 603(8):1106 – 1114, 2009.

[117] J. Garra, J. M. Vohs, and D. A. Bonnell. *Surf. Sci.*, 603:1106, 2009.

[118] D. Li, M. H. Zhao, J. Garra, A. M. Kolpak, A. M. Rappe, D. A. Bonnell, and J. M. Vohs. *Nat. Mater.*, 7:473, 2008.

[119] M. H. Zhao, D. A. Bonnell, and J. M. Vohs. *Surf. Sci.*, 602:2849, 2008.

[120] M. H. Zhao, D. A. Bonnell, and J. M. Vohs. *Surf. Sci.*, 603:284, 2009.

[121] R. V. Wang, D. D. Fong, F. Jiang, M. J. Highland, P. H. Fuoss, C. Thompson, A. M. Kolpak, J. A. Eastman, S. K. Streiffer, A. M. Rappe, and G. B. Stephenson. *Phys. Rev. Lett.*, 102:047601, 2009.

[122] C. Park and R. T. K. Baker. *Chem. Mater.*, 14:273, 2002.

[123] C. Park and R. T. K. Baker. *J. Phys. Chem. B*, 104:4418, 2000.

[124] Y. Inoue and Y. Watanabe. *Catal. Today*, 16:487, 1993.

[125] N. Saito, Y. Yukawa, and Y. Inoue. *J. Phys. Chem. B*, 106:10179, 2002.

[126] IPCC. *Climate Change 2007: The Physical Science Basis*. 2007.

[127] Bert Metz, Ogunlade Davidson, Heleen de Coninck, Manuela Loos, and Leo Meyer. *IPCC Special Report: Carbon Dioxide Capture and Storage*. 2005.

[128] D.W. Oxtoby. *Principles of Modern Chemistry (5th ed.)*. 2002.

[129] For Pb, we include $5d$, $6s$, and $6p$ projectors with cutoff radii r_d=2.3 and r_s=r_p=2.3 Bohr. For Ti, we include semicore $3s$ and $3p$ projectors as well as $3d$, $4s$, and $4p$. Cutoff radii are r_s=r_p=1.8 Bohr, and r_d=2.0 Bohr. For O, we include $2s$ and $2p$ projectors with r_s=r_p=1.3 Bohr. For H, we include a $1s$ projector with r_s=0.9 Bohr. For Sr, we include $4s$ and $4p$ semicore states, as well as $4d$, $5s$, and $5d$ state with r_s=1.3 Bohr and r_p=r_d=2.2 Bohr. For Ru, we include $4d$, $5s$, and $5p$ projectors with r_d=2.0 Bohr and r_s=r_p=2.2 Bohr. For Rb, we include $4s$ and $4p$ semicore states plus $4d$, $5s$, and $5p$ projectors with r_s=1.8 Bohr, r_p=2.0 Bohr, and r_d=2.2 Bohr. For Ba, we include $5s$ and $5p$ semicore states in addition to $5d$, $6s$ and $6p$ projectors, with r_s=2.4 Bohr, r_p=2.0 Bohr, and r_d=2.2 Bohr.

[130] Sriram Venkatesan, Ard Vlooswijk, Bart J. Kooi, Alessio Morelli, George Palasantzas, Jeff T. M. De Hosson, and Beatriz Noheda. *Phys. Rev. B*, 78:104112, 2008.

[131] H. J. Freund and M. W. Roberts. *Surface Science Reports*, 25(8):225 – 273, 1996.

[132] Sergey V. Levchenko and Andrew M. Rappe. *Phys. Rev. Lett.*, 100(25):256101, Jun 2008.

[133] Y. Zhang and W. Yang. *Phys. Rev. Lett.*, 80:890, 1998.

[134] *NIST Chemistry WebBook*. 2010.

[135] M. M. Lenkcka and R. E. Riman. *Chem. Mater.*, 5:61, 1993.

[136] Eric J. Walter and Andrew M. Rappe. *Surface Science*, 427-428:11 – 14, 1999.

[137] B. Meyer, J. Padilla, and David Vanderbilt. *Faraday Discuss.*, 114:395, 1999.

[138] A. Munkholm, S. K. Streiffer, M. V. Ramana Murty, J. A. Eastman, Carol Thompson, O. Auciello, L. Thompson, J. F. Moore, and G. B. Stephenson. *Phys. Rev. Lett.*, 88(1):016101, Dec 2001.

[139] P.A. Redhead. *Vacuum*, 12:203, 1962.

[140] O. Chmaissem, B. Dabrowski, S. Kolesnik, J. Mais, J. D. Jorgensen, and S. Short. *Phys. Rev. B*, 67:094431, 2003.

[141] Y. Konishi, Z. Fang, M. Izumi, T. Manako, M. Kasai, H. Kuwahara, M. Kawasaki, K. Terakura, and Y. Tokura. *J. Phys. Soc. Japan*, 68:3790, 1999.

[142] M. Rini, R. Tobey, N. Dean, J. Itatani, Y. Tomioka, Y. Tokura, R. W. Schoenlein, and A. Cavalleri. *Nature*, 449:72, 2007.

[143] P. A. Fleury, J. F. Scott, and J. M. Worlock. *Phys. Rev. Lett*, 21:16, 1968.

[144] J.F. Scott. *Rev. Mod. Phys.*, 46:83, 1974.

[145] Y. Segal, K. F. Garrity, C. A. F. Vaz, J. D. Hoffman, F. J. Walker, S. Ismail-Beigi, and C. H. Ahn. *Submitted to Phys. Rev. Lett.*, 2011.

[146] C. A. F. Vaz, Y. Segal, J. D. Hoffman, F. J. Walker, and C. H. Ahn. *J. Vac. Sci. Technol. B*, 28:C5A6, 2010.

[147] T. S. Santos, S. J. May, J. L. Robertson, and A. Bhattacharya. *Phys. Rev. B.*, 80:155114, 2009.

[148] Dirk Porezag, Mark R. Pederson, and Amy Y. Liu. *Phys. Rev. B*, 60:14132, 1999.

[149] H. Sawada, Y. Morikawa, K. Terakura, and N. Hamada. *Phys. Rev. B.*, 56:12154, 1997.

[150] L. Nordheim. *Ann. Phys. (Leipzig)*, 9:607, 1931.

[151] D. Vanderbilt. *Phys. Rev. B*, 61:7877, 2000.

[152] Z. Fang, I.V. Solovyev, and K. Terakura. *Phys. Rev. Lett.*, 84:3169, 2000.

[153] N. Sai and D. Vanderbilt. *Phys. Rev. B.*, 62:13942, 2000.

[154] E. Courtens. *Phys. Rev. Lett.*, 29:1380, 1972.

[155] W. Zhong and D. Vanderbilt. *Phys. Rev. Lett.*, 74:2587, 1995.

[156] W. Zhong and D. Vanderbilt. *Phys. Rev. B.*, 53(9):5047, 1996.

[157] P.N. Keating. *Phys. Rev.*, 145:637, 1966.

[158] J. M. Ziman. *Electrons and Phonons*. Oxford Press, 1960.

[159] T. von Waldkirch, K. A. Mller, and W. Berlinger. *Phys. Rev. B*, 7:1052, 1973.

[160] D. M. Schaadt, E. T. Yu, V. Vaithyanathan, and D. G. Schlom. *J. Vac. Sci. Technol. B*, 22:2030, 2004.

[161] V. Shutthanandan, S. Thevuthasan, Y. Liang, E. M. Adams, Z. Yu, and R. Droopad. *Appl. Phys. Lett.*, 80:1803, 2002.

[162] M. G. Blamire, J. L. MacManus-Driscoll, N. D. Mathur, and Z. H. Barber. *Adv. Mater.*, 21:3827, 2009.

[163] J. Z. Sun, D. W. Abraham, R. A. Rao, and C. B. Eom. *Applied Physics Letters*, 74(20):3017–3019, 1999.

[164] K. H. Mller, K. Drr, T. Walter, M. Sahana, K. Brand, and L. Schultz. *Journal of Magnetism and Magnetic Materials*, 242-245(Part 1):447 – 449, 2002.